Cement-based materials with hydrophobic micro-textured surface

By

Shiying Zheng

A thesis submitted in fulfilment of the requirements for the degree of Doctor of Philosophy

Department of Civil and Environmental Engineering

Imperial College London

December 2022

Declaration

I, Shiying Zheng, confirmed that this thesis has been composed by myself and is all my own work except where otherwise stated and referenced. This thesis is submitted for the Degree of Doctor of Philosophy Imperial College London and has not been submitted for any other degree or professional qualification.

The copyright of this thesis rests with the author. Unless otherwise indicated, its contents are licensed under a Creative Commons Attribution-Non Commercial 4.0 International Licence (CC BY-NC).

Under this licence, you may copy and redistribute the material in any medium or format. You may also create and distribute modified versions of the work. This is on the condition that: you credit the author and do not use it, or any derivative works, for a commercial purpose.

When reusing or sharing this work, ensure you make the licence terms clear to others by naming the licence and linking to the licence text. Where a work has been adapted, you should indicate that the work has been changed and describe those changes.

Please seek permission from the copyright holder for uses of this work that are not included in this licence or permitted under UK Copyright Law.

Shiying Zheng

December 2022

Abstract

The use of hydrophobic additives is a relatively new development within the field of durability design of concrete structures. This approach relies mainly on chemical modification of the cement paste matrix. Another promising, but less well-studied approach is by adopting the Cassie-Baxter mechanism. This can be achieved by creating a suitable micro texture on the surface of the cementitious material, which traps air when in contact with water leading to the separation between water and solid. The focus of this study is to develop concretes with hydrophobic micro textured surfaces and to study the properties and durability of such concretes. Hydrophobic Precipitated Calcium Carbonate (HPCC) made by dry ball milling calcium carbonate and stearic acid is used to enhance hydrophobicity of the textured surfaces.

The effects of HPCC on the wettability and mass transport properties of cementitious materials were investigated. By adopting soft lithography, micro textures on hydrophobic lotus and taro leaves were transferred onto the surfaces of cementitious samples. Furthermore, research on developing hydrophobic surfaces using a fine microgrid to mimic the micro texture of hydrophobic plant leaves was undertaken. The hydrophobicity of micro textured surfaces was enhanced by adding HPCC into cementitious mixture or by coating the surface with Polydimethylsiloxane (PDMS). Water contact angle measurements were carried out to determine the effect of surface micro textures on wettability and imbibition experiments were carried out to determine the effect they have on water transport properties. Optical microscopy was used to observe the formation and evolution of air trapped between the micro texture. Furthermore, their durability and hydrophobicity when exposed to a range of conditions were investigated. Changes in morphology due to continuous hydration, atmospheric carbonation and abrasion, and wettability of deteriorated textured surfaces were investigated.

The research was successful in developing cementitious materials with micro textured surfaces that displayed hydrophobicity, high water contact angle and strong adhesion between droplets and substrate. The addition of HPCC to both micro textured and non-textured samples showed decreasing wettability with increasing HPCC content. For example, taro textured cementitious samples containing 16% HPCC had a water contact angle of 143˚, compared to 123˚ for taro textured samples without HPCC. Furthermore, micro textured samples containing 16% HPCC showed around 40% reduction in water sorptivity while the textured samples with PDMS coating showed a reduction of 70% compared to non-textured samples. The decrease in water absorption is mainly due to formation of trapped air cushions when the sample is submerged underwater. However, samples containing less than 8% HPCC

do not form such air cushion, and therefore, are less effective in decreasing water absorption. This indicates that the performance of micro textures is related to HPCC content.

Durability studies showed that abrasion and efflorescence could affect the morphology of textured surfaces and increase their wettability. In contrast, the influence of continuous hydration and carbonation was negligible. Replacing 10% wt. of cement with silica fume can prevent efflorescence and increase the abrasion resistance of surface textures, which yielded a more durable textured surface. PDMS coating on micro textured surfaces was resistant to cyclic wetting and elevated temperature of 50˚C, indicating that the coating was stable and capable of providing long-term protection to cementitious materials. Overall, this research has shown that the combination of hydrophobic treatments (HPCC / PDMS coating) and micro-textured surfaces is a promising approach to deliver innovative hydrophobic concrete for durable structures.

Acknowledgements

I would like to thank Dr Hong Wong and Prof Chris Cheeseman for their helpful discussion and guidance. Their support is extremely valuable throughout this work. I am also grateful to them for allowing me the freedom to steer the direction of the thesis. I would also like to thank Andrew Morris and Dr Marcus Yio for their assistance in the lab work.

I would like to give thanks to my family for their understanding and support throughout my PhD study. The greatest thanks must go to my parents. This PhD would not have been possible without their continuous support and encouragement.

I would also like to acknowledge the friends I have made over the course of my study for their company, help, and keeping my mind fresh. Thank you for all the support that you have provided me with.

Notation

A	Cross-section area of the sample (m^2)
A_s	i-intercept of sorptivity curve
ATR	Attenuated Total Reflectance
A_{SL}	Area of interface between solid and liquid (m^2)
BSE	Backscattered electron
C_1	Concentration of oxygen in the nitrogen stream at 1 bar (m^3/m^3)
C_2	Concentration of oxygen in the oxygen stream at 1 bar (m^3/m^3)
C_2S	$2CaO . SiO_2$
C_3S	$3CaO . SiO_2$
C_3A	$3CaO . Al_2O_3$
C-S-H	Calcium silicate hydrates
D	Oxygen diffusivity coefficient (m^2/s)
DEF	Delayed ettringite formation
EDX	Energy-dispersive X-ray spectroscopy
f_i	Area fraction of phase i
FTIR	Fourier-transform infrared spectroscopy
g	Gravitational acceleration (m/s^2)
G	Gibbs surface energy of drop (J)
G_0	Percentage of oxygen in initial nitrogen stream
G_1	Percentage of oxygen in outflow stream
l	Length of wetted area (m)
L	The sample length (m)
L_c	Capillary length of water (m)
i	Cumulative water absorption (mm)
i_e	Amount of water being absorbed at equilibrium (m)
k	Oxygen permeability coefficient (m^2)
k_m	Measured permeability coefficient (m^2)
k_{int}	Intrinsic permeability coefficient (m^2)
K	Permeability of wetted region
P_0	Atmospheric pressure (bar)
P_1	Pressures on the inflow face (bar)
P_1^*	Pressure of oxygen stream (bar)
P_2	Pressures on outflow face (bar)
P_m	Average of pressure at inflow and outflow faces (bar)
P_a	Air pressure ahead of waterfront (Pa)

P_f	Capillary pressure (Pa)
ΔP	Pressure difference between oxygen and nitrogen stream (bar)
∇P	Pressure gradient (Pa/m)
PCC	Precipitated calcium carbonate
PDMS	Polydimethylsiloxane
PSA	Paper sludge ash
q	Gas flux per unit area (m/s)
Q	Oxygen diffusion rate at a pressure of 1 bar (m^3/s)
R_1	Flow rate of nitrogen stream (mL/min)
R_2	Flow rate of oxygen stream (mL/min)
R_f	Roughness factor
R^2	Coefficient of determination
RH	Relative humidity
S	Sorptivity ($mm/min^{0.5}$)
S'	Sorptivity under water pressure ($mm/min^{0.5}$)
SEM	Scanning electron microscope
SF	Silica fume
t	Elapsed time (min)
t_h	Thickness of sample (m)
T	$=S^2t/i_e^2$
T'	$= S'^2t/i_e^2$
V	Volume of water drop (µl)
w_n	Geometric parameter relating to n-folding scale roughness
x_e	Length of wetting area at equilibrium (m)
X	$= i/i_e$
γ_i	Surface tension of material i (J/m^2)
γ_{ij}	Interfacial tension between medium i and medium j (J/m^2)
γ_{LG}	Interfacial tension between liquid and gas (J/m^2)
γ_{SL}	Interfacial tension between solid and liquid (J/m^2)
γ_{SG}	Interfacial tension between solid and gas (J/m^2)
θ_{app}	Apparent contact angle (º)
θ_A	Advancing contact angle (º)
θ_C	Contact angle predicted by the Cassie-Baxter equation (º)
θ_R	Receding contact angle (º)
$\Delta\theta_H$	Difference between the advancing angle and receding angle (º)
$\theta_{n,\ n+1}$	Contact angle on a surface with n-folding, n+1-folding length scale roughness (º)
θ_w	Contact angle predicted by the Wenzel equation (º)

θ_Y	Young's contact angle (º)
μ	Viscosity of fluid (Pa*s)
ρ_w	Density of water (kg/m^3)
Φ	Porosity of material
λ	$=i_e/\Phi L$

Contents

1 Introduction 20

1.1 Background 20

1.2 Objectives 22

1.3 Thesis outline 22

2 Literature review 24

2.1 Wetting and contact angle 24

2.1.1 Surface tension 24

2.1.2 Wettability and Young's equation 25

2.1.3 The Wenzel state 26

2.1.4 Contact angle hysteresis 27

2.1.5 The pinning of three-phase contact line 28

2.1.6 The Cassie state 29

2.1.7 Cassie-Baxter wetting state on textured hydrophilic surface 30

2.1.8 Condensation on textured surfaces 31

2.2 Capillary absorption of cementitious materials 31

2.3 Water ingress and degradation of concrete 33

2.3.1 Carbonation 33

2.3.2 Freezing and thawing 33

2.3.3 Alkali–silica reaction 34

2.3.4 Chloride ingress 34

2.3.5 Sulfate attack 35

2.3.6 Acid attack 36

2.4 Hydrophobic surfaces 36

2.5 Reducing water ingress in cementitious materials 40

2.6 Water resisting agents 41

2.7 Hydrophobic calcium carbonate 45

2.8 Concrete with micro textured surfaces 49

2.9 Summary 50
3 Methodology 52
3.1 Sample preparation 52
3.1.1 Materials 52
3.1.2 Preparation of master pattern mould 53
3.1.3 Mix proportions 53
3.1.4 Sample batching, mixing and curing 55
3.2 Workability, strength and hydration 55
3.2.1 Workability 55
3.2.2 Compressive strength 55
3.2.3 Degree of hydration 56
3.2.4 Isothermal calorimetry 56
3.3 Mass transport properties 56
3.3.1 Water absorption 56
3.3.2 Water vapour absorption 57
3.3.3 Oxygen diffusivity 57
3.3.4 Oxygen permeability 59
3.4 Surface properties 62
3.4.1 PDMS residue 62
3.4.2 Static water contact angle 63
3.4.3 Contact angle hysteresis 64
3.5 Scanning electron microscopy 65
3.5.1 Observations of surface textures 65
3.5.2 Sample preparation for BSE imaging 66
3.5.3 BSE imaging 67
3.6 Durability of micro textures 68
3.6.1 Abrasion resistance 68
3.6.2 Exposure to humid environment 69

3.6.3 Carbonation 69
3.7 Summary 70
4 Development of hydrophobic cement-based materials 72
4.1 Introduction 72
4.2 Experimental 74
4.3 Hydrophobic precipitated calcium carbonate 77
4.3.1 Particle size 78
4.3.2 Workability 81
4.3.3 Strength and cement hydration 81
4.3.4 Microstructure 83
4.4 Hydrophobic micro textured surfaces transferred from plants 86
4.4.1 Fidelity of reproduced surface structure using soft lithography 91
4.4.2 PDMS residue 94
4.5 Coating micro textured surfaces 95
4.5.1 PDMS residue 97
4.6 Hydrophobic microgrid patterned surface 98
4.7 Wettability of hydrophobic cementitious materials 104
4.7.1 Water contact angle 104
4.7.2 Contact angle hysteresis 105
4.7.3 Motion of water droplets 106
4.7.4 Discussion 110
4.8 Conclusion 114
5 Mass transport properties of hydrophobic cementitious materials 116
5.1 Introduction 116
5.2 Experimental 118
5.3 Trapped air cushion 122
5.4 Water sorptivity 128
5.5 Influence of hydrostatic pressure 133

5.5.1 Hydraulic pressure to break down metastable Cassie-Baxter state 133
5.5.2 Imbibition with air trapping under hydrostatic pressure 133
5.5.3 Water absorption under hydraulic pressure 136
5.6 Total water absorption 138
5.7 Gas transport properties 139
5.8 Water vapour absorption 141
5.9 Conclusion 144
6 Durability of hydrophobic cement-based materials 146
6.1 Introduction 146
6.2 Experimental 147
6.3 Abrasion resistance 149
6.4 Acid leaching 153
6.5 Cyclic wetting and drying 154
6.6 Influence of humid environment 163
6.7 Carbonation 170
6.8 Conclusion 171
7 Conclusions and future work 173
7.1 General conclusions 173
7.2 Opportunities for future work 175
8 Reference 178
Appendix I 197

List of Tables

Table 2.1 Summary of selected studies on the effects of hydrophobic agents on concrete performance. 42

Table 3.1 Oxide composition and loss of ignition (LOI) for CEM I and SF. 52

Table 4.1 Summary of mix proportions. 74

Table 4.2 Compressive strength (MPa) of cementitious materials containing various amounts of HPCC. Standard errors are showed in brackets. 82

Table 4.3 Influence of HPCC on degree of cement hydration. 83

Table 4.4 Water contact angles measured on the prepared cementitious samples. The numbers in brackets indicate standard error. 104

Table 5.1 Summary of water sorptivity ($\times 10^{-2}$ mm/min$^{0.5}$). 128

Table 5.2 Total water absorption of cementitious samples containing different amounts of HPCC. 138

Table 6.1 Summary of mix proportions. 148

Table 6.2 Summary of water contact angles of textured surfaces subjected to different exposure time to 98% RH. 169

Table 6.3 Water contact angles of textured mortars before and after carbonation. 170

List of Figures

Figure 2.1 Origin of surface tension. Molecules on surface experience an inward attraction (Higham, 2023). 24

Figure 2.2 A liquid drop is placed against a solid surface. γ_{LG} is the interfacial tension of the liquid-gas interface. γ_{SL} is the interfacial tension of the solid-liquid interface. γ_{SG} is the interfacial tension of the solid-gas interface...... 26

Figure 2.3 Surface tension vectors at three-phases interline. (a) The underlying solid surface slowly deforms along the three phases boundary and approaches equilibrium geometry. (b) At equilibrium, the interfacial tensions should balance each other. 26

Figure 2.4 The pinning of contact line on a heterogeneous surface consisting of hydrophobic and hydrophilic patches. Left: Profile of a liquid drop on the surface. Right: Imagined transition region at the interface of hydrophilic material (contact angle of θ_1) and hydrophobic material (contact angle of θ_2). The chemical composition varies in gradient from left to right. The contact angle within this region is between θ_1 and θ_2...... 28

Figure 2.5 Close-up view of contact line moving uphill along the upstream surface and pinned around the sharp edge. θ_{app} stands for the apparent contact angle and θ_0 stands for the Young's contact angle. 28

Figure 2.6 A hierarchical structure made of hydrophilic material. (a) Schematic close-up view of structure. (b) The change in system energy during the water-air interface move downward along a groove. 31

Figure 2.7 SEM images showing the surface characteristics of (a) lotus, (b) Euphorbia myrsinites, and Salvinia oblongifolia. The insets show nanoscale wax crystals. Adapted from Koch & Barthlott (2009)...... 37

Figure 2.8 Schematic illustration of ball mill. Adapt from Faraji, Kim & Kashi, (2018). 45

Figure 2.9 Adsorption of stearic acid molecules on the surface of calcium carbonate filler after dry milling (Mihajlović *et al.*, 2013). 47

Figure 2.10 Surface roughness produced through (a) applying micro particles on concrete surfaces (post-casting treatment) adapted from Flores-vivian et al., (2013) and (b) lithography (pre-treatment) adapt from Horgnies & Chen, (2014). 49

Figure 3.1 Sample designation..... 55

Figure 3.2 Experimental arrangement for water absorption. Adapted from Wong (2006). 57

Figure 3.3 Schematic diagram of the diffusion test set up adapted from Wong (2006). 59

Figure 3.4 Schematic diagram of the permeability test set up adapted from Wong (2006). . 60

Figure 3.5 An example of applying Klinkenberg correction for gas slippage to determine the intrinsic permeability coefficient. 62

Figure 3.6 An example of FTIR spectrum showing PDMS grafted on paste containing 10%SF. 63

Figure 3.7 Left: Photograph shows a water droplet sitting on a lotus textured surface (P-L-0%H-0%SF). Right: The droplet was analysed using Laplace-Young fitting to obtain the contact angle. 64

Figure 3.8 Top: SEM image of a cement paste sample cast against a PDMS coated nylon microgrid; Bottom: Cross section profile of fabricated texture reconstructed by 3D map software. 66

Figure 3.9 (a) Cumulative brightness histogram versus grey value. The red dash line indicates inflection point determined by overflow method. (b) Segmented pores. (c) Brightness histogram for cement paste showing a distinct peak for anhydrous cement. (d) Segmented anhydrous cement. 68

Figure 3.10 Schematic diagram of test arrangement for determining abrasion resistance. .. 69

Figure 4.1 Illustration of how the distance between adjacent textures, and height and diameter of individual texture (papillae) are measured. 76

Figure 4.2 Ball mill equipment. Left: (1) porcelain ball milling shell (2) milling media (3) clamp (4) milling shell lid (5) rubber ring. Right: ball mill roller. 78

Figure 4.3 Particle size distribution and cumulative volume of HPCC determined using laser diffraction granulometry. 79

Figure 4.4 SEM image of HPCC taken at (a) 1000x and (b) 10,000x magnification. 79

Figure 4.5 Effect of HPCC content on slump 81

Figure 4.6 Isothermal calorimetry curves for pastes containing 0%, 4%, 8%, and 16% HPCC. 82

Figure 4.7 The porosity of cementitious samples with various amount of HPCC. 84

Figure 4.8 BSE scanning electron micrographs of impregnated paste (a) and mortars (b) with 16% HPCC (3 days, w/c 0.4), at 100x magnification. 84

Figure 4.9 A water droplet is encased in a sheath of HPCC as it rolls over a glass surface. 85

Figure 4.10: SEM image of surface texture on lotus leaf (left) and taro leaf (right). 87

Figure 4.11 Preparation of mould for soft lithography and the produced PDMS mould. 87

Figure 4.12 Formation of a PDMS mould from a plant leaf and reproducing the texture onto a cementitious material sample. 88

Figure 4.13 SEM image of PDMS master mould showing a negative template of lotus (left) and taro (right) leaf texture. 89

Figure 4.14 Left: lining the PDMS master on the bottom of steel mould. Right: The appearance of sample surface (M-L-0%H-0%SF) cast against the PDMS mould. 89

Figure 4.15 SEM images of the replicated surface textures on mortar samples. (Left) Lotus textured surface (Right) Taro textured surface. 90

Figure 4.16 Void space within the microstructure of lotus textured mortar (left) and taro textured mortar (right). 91

Figure 4.17 Schematic showing blockage of the PDMS mould by large cement grains forming a hollow texture (left) rather than a solid texture (right). The hollow texture is prone to damage as shown in Figure 4.16. 91

Figure 4.18 Cross section profiles of lotus papillae: (a) original lotus leaf, and (b) reproduced on a mortar sample using soft lithography. 92

Figure 4.19 Distribution of original and reproduced papillae dimensions: (a) separation distance, (b) diameter, (c) height. 93

Figure 4.20 Examples of flawed surface textures made using the same PDMS mould after 3 cycles of casting (left) and after 5 cycles (right). 94

Figure 4.21 FTIR spectrum of PDMS and of cement paste interface. The spectra were taken from 500 cm^{-1} to 4000 cm^{-1} at a resolution of 4 cm^{-1}. 95

Figure 4.22 PDMS molecules coating the surface of SF mortar through grafting reaction. .. 96

Figure 4.23 The transfer of PDMS molecules on to the surface of SF. 96

Figure 4.24 SEM images of lotus textured mortars (a) 20% SF, 28 days; (b) 10% SF, 28 days.

.....97

Figure 4.25 Comparison of FTIR spectrums obtained from PDMS and paste samples with or without 10% SF cast against PDMS mould. 98

Figure 4.26 A schematic illustration of a textured surface created by casting cementitious material in a mould embossed with a microgrid. 99

Figure 4.27 Left: microgrid obtained by dismantling nylon bag. Right: SEM showing the texture and dimensions of the microgrid. 100

Figure 4.28 A comparison of the FTIR spectrums from nylon microgrid, PDMS and PDMS coated nylon microgrid. 101

Figure 4.29 The surface appearance of samples cast against nylon microgrid. (a) P-0%H-0%SF and (b) P-0%H-20%SF, cast against uncoated nylon microgrid. (c) and (d): top view and side view of P-0%H-0%SF cast against a PDMS coated nylon microgrid. 102

Figure 4.30 Comparison of FTIR spectrums obtained from PDMS and paste samples with or without 10% SF cast against PDMS modified microgrid. 103

Figure 4.31 Water droplet pinned on M-L-0%H-10%SF when the sample was rotated by 90° (b) and 180° (c). 106

Figure 4.32 Motion space of falling droplets for micro textured mortars (0%SF, 3 days old) with various amounts of HPCC. 107

Figure 4.33 Examples of wetting behavior of water droplets dropped from (a) 4 cm and (b) 30 cm above a M-L-0%H-0%SF surface inclined at 30°. 108

Figure 4.34 (a) A water droplet dropped from a height of 4 cm became pinned on M-MP-0%H-0%SF inclined at 30° after rolling over a short distance. (b) A water droplet dropped from the same height rolled across M-MP-16%H-0%SF surface inclined at 30°. 109

Figure 4.35 Motion space of falling droplets for PDMS coated micro textured mortars (0%HPCC, 10%SF, 28 days old). 110

Figure 4.36 Two examples of "energy-stable configuration" to maintain the Cassie-Baxter wetting state on a roughened hydrophilic surface: (a) mushroom-shaped element. (b) nail-head-shaped element. 112

Figure 4.37 SEM image of deformed cell walls of a dried taro leaf. Red arrows show the energy-stable features for contact line pinning. 113

Figure 5.1 Experimental arrangement using an optical microscope and digital image processing to study the air cushion trapped between surface textures of cementitious materials. 119

Figure 5.2 Schematic diagram showing the light propagating paths through water and reflected at the trapped air/water interface. 119

Figure 5.3 Low pressure water absorption apparatus. The exposed surfaces are placed face downward on plastic strips. Red lines represent the surfaces sealed with waterproof tape. 121

Figure 5.4 Optical microscope images of the evolution of air cushion on a MP-8%H sample at the same location. Time counting began when the surface was immersed in water. 123

Figure 5.5 (a-f) Sequence of images showing the air cushion on a MP-16%H sample slowly disappearing through dissolution. (g) Graph shows the fractional area of air cushion decreases with time. Multiple wetting experiments show repeatable behavior. 124

Figure 5.6 (a-d) Optical microscope images of trapped air cushion on a PDMS coated microgrid patterned mortar (M-MP-0%H-10%SF). (e) Graph shows the area fraction of air cushion decreases with time. Cyclic wetting and drying experiments show similar behaviour. 126

Figure 5.7 Optical microscope images of an air bubble (top right corner) growing rapidly on a PDMS coated microgrid patterned mortar (MP-0%H-10%SF) sample, engulfing the surrounding air cushion. 127

Figure 5.8 Water absorption curves for uncoated non-textured samples with different HPCC contents. Left: paste; Middle: mortar; Right: concrete..... 129

Figure 5.9 Water absorption curves for micro textured pastes with different HPCC contents. Left: Lotus; Middle: Taro; Right: microgrid pattern. 130

Figure 5.10 Absorption curves for uncoated micro textured mortars with different HPCC contents. Left: Lotus; Middle: Taro; Right: Microgrid pattern. 130

Figure 5.11 Water absorption curves for PDMS coated micro textured mortar with different HPCC contents. Left: Lotus; Middle: Taro; Right: Microgrid pattern. 131

Figure 5.12 Progressive development of build-up air pressure P_a in a bulk sample of length L ($t_2 > t_1$). $P_0+\rho_w gh$ is pressure on the inflow surface and P_f is capillary pressure. 134

Figure 5.13. The family of curves of equation 5.4 with different values of λ in the range of 0.5

to 1. The results are insensitive to the value of λ for small T*, whereas it will cause great difference at longer times.* 136

Figure 5.14 Sorptivity values and water absorption curves for samples tested under 2452 Pa water pressure. 137

Figure 5.15 Water absorption and porosity of cement matrix. The results have been corrected for aggregate and HPCC content to account for the dilution effect. 139

Figure 5.16 Effect of HPCC on gas diffusivity and gas permeability of non-textured cementitious samples at 3 days. 140

Figure 5.17 Mass gain of mortar samples containing (a) 0% HPCC and (b) 16% HPCC exposed to 98% RH. 142

Figure 5.18 Mass gain of SF-containing mortar samples containing (a) 0% HPCC and (b)16% HPCC exposed to 98% RH. 142

Figure 5.19 Moisture transport in a capillary pore with two narrow constrictions. Black solid circles represent water molecules. 144

Figure 6.1 Water contact angle versus pulling distance for textured pastes and mortars. Error bars represent standard error. 150

Figure 6.2 (a) and (c). Surface topography and profile of a P-MP-0%H-0%SF-3d sample. (b) and (d) Surface topography and profile after pulling through 100 cm on a 1200-grit SiC paper. 151

Figure 6.3 Water contact angle versus pulling distance for textured samples made of SF-containing mortar. Error bars represent standard error. 152

Figure 6.4 Silicon and calcium maps of a textured paste (P-L-0%H-0%SF) after acid leaching. 153

Figure 6.5 Scanning electron micrographs of textured pastes leached at a pH of 2 for 7 days. (a) P-L-0%H-0%SF, (b) P-T-0%H-0%SF, (c) P-MP-0%H-0%SF. 153

Figure 6.6 Sorptivity of paste samples subjected to cyclic wetting and drying (a) Non-textured, (b) Lotus textured, (c) Taro textured, (d) Microgrid patterned. Error bars represent standard deviation. 155

Figure 6.7 Example of cumulative water uptake plots for paste samples containing various amount of HPCC at the 1st, 3rd, and 5th wetting cycle. 157

Figure 6.8 Cracks on a P-L-16%H-0%SF-3d after subjected to cyclic wetting. Left: large cracks seen by the naked eye. Right: micro cracks seen under a SEM. 158

Figure 6.9 Sorptivity of uncoated mortar samples subjected to cyclic wetting and drying (a) Nontextured, (b) Lotus textured, (c) Taro textured, (d) Microgrid patterned. Error bars represent standard deviation. 160

Figure 6.10 Sorptivity of PDMS coated mortar samples subjected to cyclic wetting and drying (a) Nontextured, (b) Lotus textured, (c) Taro textured, (d) Microgrid patterned. Error bars represent standard deviation. 162

Figure 6.11 (a)-(l) Micro textured pastes and mortars subjected exposure to 98% RH for 1 and 3 months. (m) XRD analysis of surface exposed for 1 month. (n) XRD analysis of surface exposed for 3 months. 166

Figure 6.12 SEM images of (a) M-L-0%H-10%SF-28d (b) M-T-0%H-10%SF-28d (c) M-MP-0%H-10%SF-28d exposed to 98% RH for 3 months. 167

Figure 6.13 XRD spectrums of SF-containing textured surface after (a) 1 month and (b) 3 months exposure to 98% RH. 168

Figure 6.14 Raman spectrums of micro textured mortar surfaces before and after carbonation. Left: M-L-0%H-0%SF-3d; Right: M-L-0%H-10%SF-28d. 170

Figure 7.1 Schematic illustration of (a) a grid-like micro texture and (b) the mold used to fabricate the desired surface. 177

Figure A.0.1 Two-dimensional sinusoidal profile of a papilla (side view). The equation at the top right corner defines the sinusoidal waveform. 197

Figure A.0.2 Progressive penetration of liquid. The contact angle maintains θ_Y against the side of papillae throughout the whole wetting process. Solid line represents the outline of papillae. Dashed lines represent tangents. Dotted lines represent the water-gas interface. The insert on the right shows that the water front moves downward by a distance of ds. Correspondingly, the water-gas interfacial area decreases ds'. 198

1 Introduction

1.1 Background

Since the lotus leaf effect was explained in 1992 (Ensikat *et al.*, 2011), hydrophobic surfaces have received much attention. Remarkable achievements that relate to hydrophobic surfaces have been made in recent decades. This type of surface can either be natural or man-made, and is able to repel water when the surface is wetted (Neinhuis and Barthlott, 1997b). A waterdrop can stand on the surface without being absorbed by capillary suction, and the waterdrop can roll off when the surface is inclined. Such surface characteristic makes it very effective for resisting water ingress, which is important for many applications of concrete and the long-term durability of structures that are exposed to harsh environments. This is because concrete is a porous material containing many open pores that provide paths for the absorption of water and penetration of aggressive species from the external environment, causing a range of degradation mechanisms. Therefore, developing concrete with hydrophobic surfaces is potentially a viable solution to overcome the high sorption of concrete. It is also potentially an approach to develop self-cleaning properties on cementitious materials.

Various approaches have been attempted to achieve hydrophobicity in mortars and concretes. Wong *et al.* (2015) replaced part of cement with hydrophobic powder that was made by dry milling paper sludge ash (PSA) and stearic acid. The water absorption, sorptivity, and electrical conductivity of concrete blended with the hydrophobic PSA were significantly decreased. Qu and Yu (2018) adopted GGBS instead of PSA to make hydrophobic powder. The concrete made by replacing 15% GGBS hydrophobic powder had a water contact angle of 92°. Both chloride penetration depth and water absorption were significantly decreased. Di Mundo, Petrella and Notarnicola (2018) made a hydrophobic concrete by replacing conventional aggregates with tyre rubber grains. The samples with tyre rubber grains showed hydrophobicity, and the smaller the grains used, the higher the water contact angle observed. For samples containing tyre rubber grains smaller than 2 mm, a water contact angle of 125° was achieved.

Commercially available hydrophobic additives such as ‘Vandex’ are described as capillary active and are claimed to reduce capillary pore diameter and as a result, cause a reduction in water absorption. Concrete with 5% Vandex by weight of cement was reported to show 50% lower capillary absorption and 40% lower water penetration than the control (The Concrete Society, 2013). Another commercially available water-resisting additive is ‘Hycrete’ (disodium tetrapropenyl succinate) and this is claimed to be effective in decreasing water permeability.

However, studies have found that Hycrete has an air entraining effect and this lowers the strength of the concrete (The Concrete Society, 2013).

In addition, some researchers have attempted to achieve the Cassie-Baxter state by creating a layer of micro textures on the surface of concrete. Such textures have characteristic size in the range of microns because the contribution of roughness on hydrophobicity is only effective at the scale of microns and below (Zheng & Lü, 2013).

Horgnies and Chen (2014) were the first to introduce a physical hydrophobic surface onto concrete. A micro texture was produced by casting concrete against a mold embedded with a pattern consisting of conical shaped features. They showed that the micro texture of the mold was successfully transferred to the surface of concrete. Liu *et al.* (2017) adopted soft lithography to transfer the microstructure of lotus leaf to the surface of cement paste sample. A negative template of the lotus leaf microstructure was made by soft lithography and then cement paste was cast against the template. A layer of closely packed papillae made of cement paste was observed on the sample surface when viewed under a microscope.

The hydrophobic cementitious materials produced from the previously mentioned methods are innovative, but there are some drawbacks related to these methods. For example, partially replacing cement with additives such as rubber crumbs lead to a decrease in strength of the concrete. In some cases, the hydrophobic agent itself such as silicone may cause some degree of retardation in cement hydration. Soluble soaps, mineral oil, and waxes may result in air entrainment due to their surfactant properties, and therefore the maximum dosage of 0.2% by weight of cement was recommended (Hewlett, Justnes & Edmeades, 2019). The development of micro textured cementitious surfaces that demonstrate hydrophobicity is a new route to hydrophobic concrete. However, there were only a few studies focused on this area and these have mainly focused on its influence on wettability (Liu *et al.*, 2017; Horgnies & Chen, 2014; Gao *et al.*, 2019). No studies have been carried out on the long-term performance of the hydrophobic surfaces.

Therefore, this research aims to address these limitations by producing various types of micro texture on the surfaces of cementitious samples and studying their durability against repeated wetting-drying cycles and other forms of degradation such as carbonation and abrasion. Concrete with micro textured surfaces will be prepared by replicating the surface textures of natural materials (e.g. lotus leaf) or manufactured materials such as microgrid with the appropriate pattern and size. A hydrophobic powder made by dry ball milling precipitated calcium carbonate and stearic acid will be used to enhance the performance of the micro textured surface. The hydrophobic powder acts as surface modification agent by altering the

chemical nature of both the outer surface of samples and the inner walls of capillary pores. Therefore, the hydrophobic concrete of this type will have hydrophobicity that arise from both the Cassie-Baxter mechanism and chemical heterogeneity.

1.2 Objectives

The aim of this research is to create concrete with hydrophobic surfaces that is durable and highly resistant to water ingress by capillary absorption. The surfaces are made by combining micro textures with admixed hydrophobic precipitated calcium carbonate (HPCC). Several methods for creating the micro textures and their durability are tested. In addition, the feasibility for large-scale application of micro textured surface is evaluated. This aim will be accomplished by:

a) Investigating the properties of HPCC and how the HPCC would affect the properties of cementitious materials including: workability, degree of hydration, strength, microstructure, wettability and water absorption.

b) Developing methods to produce micro textures using synthetic materials or by reproducing micro textures of natural material (e.g. taro and lotus leaves) on the surface of cementitious materials to induce hydrophobicity.

c) Studying the performance of cement-based materials containing hydrophobic micro textures and HPCC.

d) Determining the durability of hydrophobic micro textured surfaces, in particular when samples are exposed to cyclic wetting/drying, abrasion, continuous hydration, and carbonation.

e) Understanding which factor has the most significant influence and developing methods to enhance the durability of the hydrophobic micro textured surfaces.

1.3 Thesis outline

This thesis is divided into seven chapters. The introduction is set out in Chapter 1 along with the aims of this research and thesis outline. Chapter 2 summarizes the key literature related to the scope of this thesis. This includes a review of surface wetting mechanisms and recent published work on hydrophobic concrete. Chapter 3 provides a detailed description of experimental approaches, test procedures and instruments that are used in this research.

The main results are presented in the next three chapters. In Chapter 4, methods to produce hydrophobic cementitious materials are investigated. The HPCC is examined to obtain an

overall particle size distribution and to identify the structure and morphology of individual particle. The influence of HPCC on the workability, degree of hydration, strength, and microstructure of cementitious samples is investigated. One of the critical tasks is to replicate the surface texture of plant leaves and to study the effect of the reproduced surface textures on the performance of cementitious samples. Soft lithography is shown to be effective in transferring the surface textures of plant leaves with high fidelity onto cementitious samples. In addition, a new method to fabricate a micro texture on cementitious samples using nylon microgrids is investigated. This method produces an array of micro posts on the surface. Chapter 4 also contains an investigation on enhancing the hydrophobicity of micro textured samples through PDMS coating. Silica fume (SF) was used as a supplementary cementitious material to facilitate the transfer of PDMS molecules. The effect of the surface textures on wettability of cementitious samples were studied.

Chapter 5 presents the mass transport properties of the hydrophobic cementitious samples developed in Chapter 4. Transport properties such as water sorptivity, water absorption, water vapor diffusion and gas permeation are tested. The stability of air cushion between micro posts is investigated using an optical microscope to observe its evolution over time. Results from the observation are used to explain the large decrease in water sorptivity observed on micro textured samples containing 16% HPCC and PDMS coating.

The durability of the micro textures is reported in Chapter 6, including their resistance to cyclic wetting/drying, abrasion, acid leaching, and long-term exposure to high humidity and carbonation. Textured samples are imaged before and after being subjected to these exposure conditions to observe changes in surface morphology. It is found that efflorescence induces the most detrimental effect on the durability of micro textures. Samples with the large microgrid pattern are more durable when subjected to these conditions compared to those with textures derived from plant leaves.

Finally, Chapter 7 presents key conclusions drawn from this work and recommendations for further research.

2 Literature review

This chapter presents a literature review on subjects relevant to the scope of this thesis. The mechanism of surface wetting is first summarised to help understand the way in which water interacts with a solid surface, and the models used to predict this. Subsequently, capillary absorption and degradation of cementitious materials related to water ingress are presented. Finally, methods to fabricate hydrophobic surfaces and recent developments in water-resisting cementitious materials are reviewed.

2.1 Wetting and contact angle

2.1.1 Surface tension

The surface tension stems from unbalanced intermolecular forces at boundary. A molecule in the interior of liquid drop experiences symmetric intermolecular forces that stem from hydrogen bond, permanent dipole-dipole interaction, and London dispersion attraction. In contrast, for a molecule at the surface of the drop, the molecule is partially surrounded by others. Therefore, the molecule undergoes a net force directed only toward the interior of the drop because the air cannot provide an equal force outward to balance the attraction of liquid molecules (Figure 2.1). Therefore, molecules at the surface tend to be drawn inward toward the interior and seeking for a minimum surface area to lower its energy (Berg, 2010).

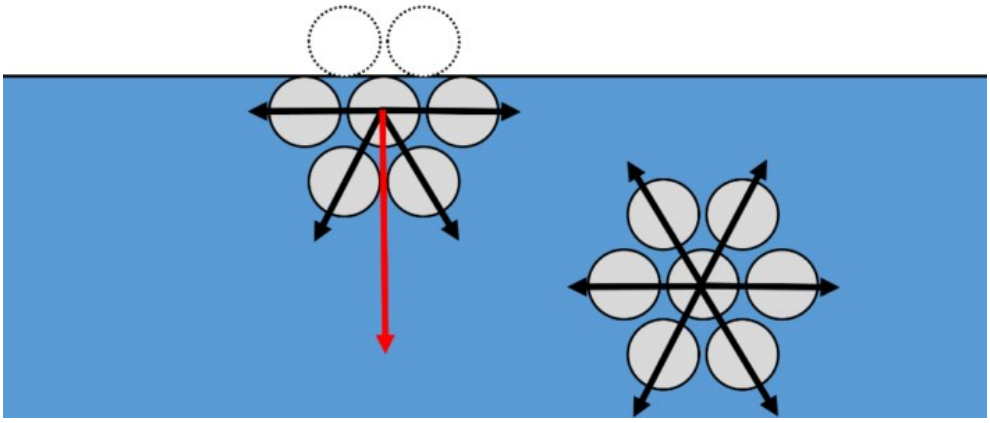


Figure 2.1 Origin of surface tension. Molecules on surface experience an inward attraction (Higham, 2023).

When two surfaces are brought into contact, the net pulling-inward intermolecular force is partially compensated by attraction from another substance (Nosonovsky & Ramachandran, 2015). Therefore, the interfacial surface tension can be described as a net force pulling the interface towards the substance that possesses greater surface tension.

2.1.2 Wettability and Young's equation

In most instances, different liquids exhibit different wetting behaviour when they adhere to a given solid surface. This is because interfacial tension determines the wetting behaviour of a liquid drop on a surface. The contact angle, which is a macroscopic quantity, provides a useful parameter to measure this wetting behaviour. When a drop of liquid deposits upon a solid surface, it may ball up and remain a drop, or spread out and wet the surface. The degree of wetting varies depending on the characteristics of the liquid and solid. The equilibrium shape of the liquid drop can be determined by minimising the surface energy for the overall system (Adamson & Gast, 1997; Bico, Thiele & Quéré, 2002).

Consider a water drop placed against a flat surface and the drop maintains a shape of a spherical cap (Figure 2.2). A small displacement of liquid interline, A_{SL}, leads to a change in the area of solid surface contacting with liquid, ΔA_{SL}, and a change in system surface energy, ΔG that can be expressed as (Israelachvili, 2011):

$$\Delta G = \Delta A_{SL}(\gamma_{SL} - \gamma_{SG}) + \Delta A_{SL}\gamma_{LG}\cos\theta_Y \quad \text{(eqn. 2.1)}$$

The first term refers to a change in solid-liquid interfacial energy due to an increase in the solid-liquid interface. The second term refers to a change in liquid-vapor interfacial energy.

At equilibrium, the limit of ΔG should equal to zero as ΔA_{SL} approaches zero:

$$\lim_{\Delta A_{SL}\to 0} \frac{\Delta G}{\Delta A_{SL}} = 0 \qquad \text{(eqn. 2.2)}$$

Therefore, the contact angle at equilibrium can be represented as a function of interfacial tensions.

$$\cos\theta_Y = \frac{(\gamma_{SG} - \gamma_{SL})}{\gamma_{LG}} \qquad \text{(eqn. 2.3)}$$

The expression above is the well-known Young's equation (Young, 1805). It should be pointed out that Figure 2.2 shows a mechanically stable, but nonequilibrium configuration of a liquid drop on a surface. To achieve a state of equilibrium, the vector sum of all forces should be zero, i.e. $\overrightarrow{\gamma_{LG}} + \overrightarrow{\gamma_{SL}} + \overrightarrow{\gamma_{SG}} = 0$. But the forces in Figure 2.2 is unbalanced because of a lack of a normal force to balance the upward force of $\gamma_{LG}\sin\theta$. This upward force causes the surface to bulge upward to release the high local stress on the solid surface (Israelachvili, 2011). See Figure 2.3.

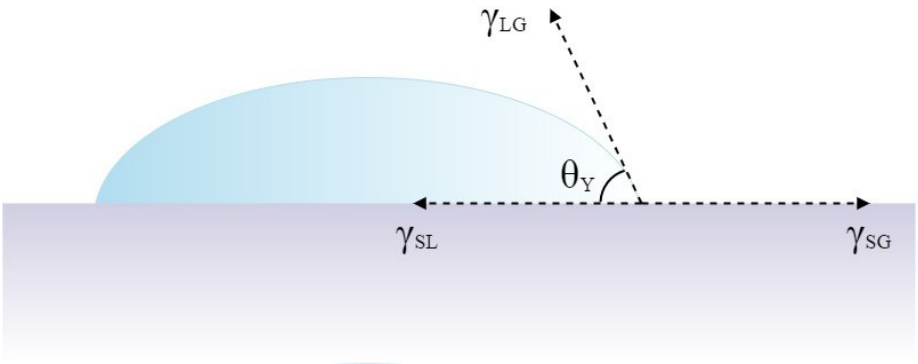


Figure 2.2 A liquid drop is placed against a solid surface. γ_{LG} is the interfacial tension of the liquid-gas interface. γ_{SL} is the interfacial tension of the solid-liquid interface. γ_{SG} is the interfacial tension of the solid-gas interface.

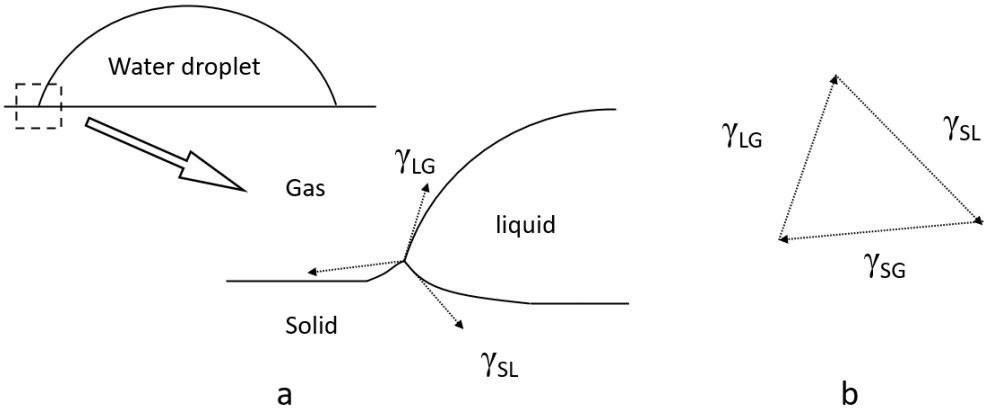


Figure 2.3 Surface tension vectors at three-phases interline. (a) The underlying solid surface slowly deforms along the three phases boundary and approaches equilibrium geometry. (b) At equilibrium, the interfacial tensions should balance each other.

2.1.3 The Wenzel state

It should be noted that the Young's equation is based on an oversimplified model. Its validity requires not only that the substrate be made of a homogeneous material, but also that the influence of roughness is neglected. The texture or roughness of a surface will play a vital role in influencing the actual contact angle. Wettability tends to be magnified when the roughness of the surface is considered (Wenzel, 1936).

Therefore, the Wenzel model introduces a roughness factor "R_f" to accommodate the influence of roughness. The roughness factor can be regarded as a coefficient to correct the calculated contact angle for a non-flat surface owing to the increased in surface area. The Wenzel's equation is as follows:

$$\mathrm{R}_f\gamma_{SG} = R_f\gamma_{SL} + \gamma_{LG}\cos\theta_w \qquad \text{(eqn. 2.4)}$$

$$\cos\theta_w = \frac{R_f(\gamma_{SG}-\gamma_{SL})}{\gamma_{LG}} = R_f\cos\theta \qquad \text{(eqn. 2.5)}$$

Where θ_w is the contact angle of a droplet on the rough surface and R_f is the roughness factor, which is defined as the ratio of the actual surface area to the apparent surface area. If the roughness factor equals to unity, then the Wenzel model will be perfectly equivalent to the Young's equation. However, the roughness factor is always greater than one in practice, and therefore, hydrophilicity or hydrophobicity will be amplified for a rough surface compared to the Young's equation (Quéré, 2008).

2.1.4 Contact angle hysteresis

The ability of a liquid drop to move on a solid surface is determined by the contact angle hysteresis. When slowly inject a small amount of water into a drop, the three-phase interline remains fixed so that the apparent contact angle keeps increasing until the contact line advances. The angle just before the contact line starts moving is referred to as the advancing contact angle, θ_A. Similarly, when liquid is gradually withdrawn from the drop, the contact line remains pinned and the angle just before the contact line jumps to a new equilibrium state is referred to as the receding contact angle, θ_R (McHale, Shirtcliffe & Newton, 2004). The difference between advancing angle and receding angle is known as contact angle hysteresis:

$$\Delta\theta_H = \theta_A - \theta_R \qquad \text{(eqn. 2.6)}$$

Another equivalent approach to estimate the advancing angle and the receding angle is to measure the contact angles of a drop resting on a tilted surface. In this case, the leading edge angle just before the drop set in motion refers to as the advancing angle and the tailing edge angle refers to as the receding angle.

2.1.5 The pinning of three-phase contact line

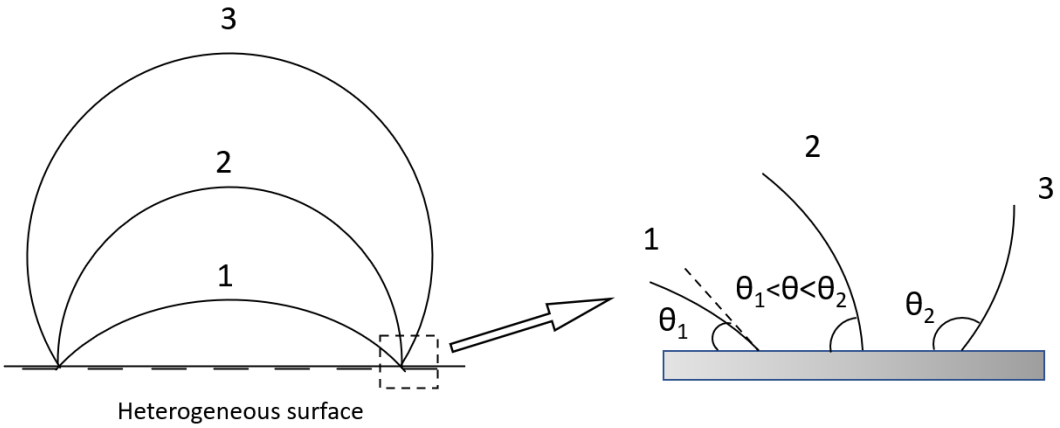


Figure 2.4 The pinning of contact line on a heterogeneous surface consisting of hydrophobic and hydrophilic patches. Left: Profile of a liquid drop on the surface. Right: Imagined transition region at the interface of hydrophilic material (contact angle of θ_1) and hydrophobic material (contact angle of θ_2). The chemical composition varies in gradient from left to right. The contact angle within this region is between θ_1 and θ_2.

The pinning of three-phases contact line arises from either chemical heterogeneity or surface roughness. For chemical heterogeneity, when a droplet is placed on a micro textured surface made of alternate patches of hydrophobic and hydrophilic material, the contact line will be pinned at the interface of these two different materials (Figure. 2.4). The contact angle can take any value between θ_1 and θ_2 and the contact line can only advance when the contact angle exceeds θ_2 to pass the hydrophobic patch (Gao & Mccarthy, 2006).

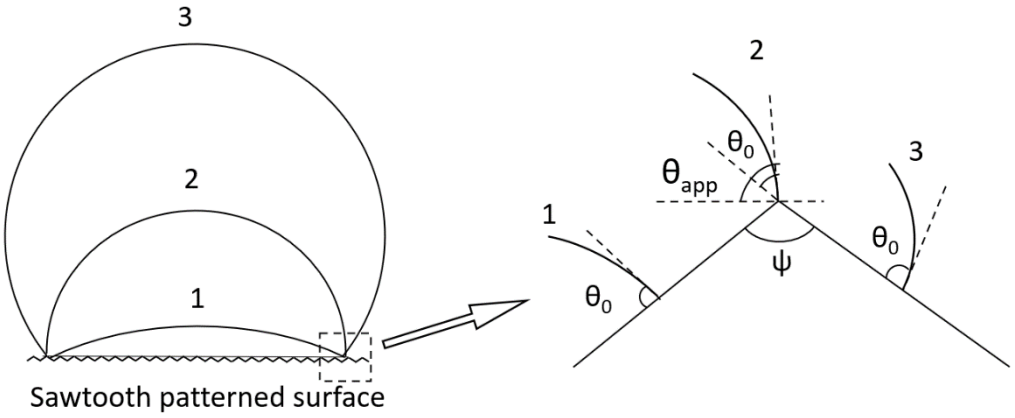


Figure 2.5 Close-up view of contact line moving uphill along the upstream surface and pinned around the sharp edge. θ_{app} stands for the apparent contact angle and θ_0 stands for the Young's contact angle.

Another cause of the pinning effect arises from surface roughness. Figure 2.5 is a close-up view of contact line moving across a rough surface consisting of a sawtooth pattern. When the contact line moves upward, the contact line will advance at a finite rate and stop at the sharp edge. To cross over the edge, the contact angle against the downstream surface of sawtooth pattern must equal to the Young's contact angle so that the interfacial tensions are in the state of equilibrium (Berg, 2010).

2.1.6 The Cassie state

Cassie and Baxter considered water droplets on a chemically heterogeneous surface and supposed the area fraction of surface components were known. The Cassie equation can then be demonstrated by system energy minimization (Bico, Thiele & Quéré, 2002; Israelachvili, 2011). Imagining a surface consisting of two types of materials for which the area fractions and surface energy are f_1 and f_2, and γ_{SG}^1 and γ_{SG}^2, respectively. A small displacement of contact line causes the change in system energy by ΔG that can be expressed as (Israelachvili, 2011; Bico, Thiele & Quéré, 2002):

$$\Delta G = f_1 \Delta A_{SL}(\gamma_{SL}^1 - \gamma_{SG}^1) + f_2 \Delta A_{SL}(\gamma_{SL}^2 - \gamma_{SG}^2) + \Delta A_{SL} \cos\theta_C \gamma_{LG} \qquad \text{(eqn. 2.7)}$$

At equilibrium,

$$\lim_{\Delta A_{SL} \to 0} \frac{\Delta G}{\Delta A_{SL}} = 0 \qquad \text{(eqn. 2.8)}$$

And

$$\cos\theta_C \gamma_{LG} = f_1(\gamma_{SG}^1 - \gamma_{SL}^1) + f_2(\gamma_{SG}^2 - \gamma_{SL}^2) \qquad \text{(eqn. 2.9)}$$

Or

$$\cos\theta_C = f_1 \cos\theta_1 + f_2 \cos\theta_2 \qquad \text{(eqn. 2.10)}$$

The contact angle is dependent on the fractions of different compositions.

If the droplet sits on the top of micro textured surface, leading to air gap across which water contact with air, the Cassie-Baxter equation (eqn. 2.10) reduced to $\cos\theta_C = f_1 \cos\theta_1 - f_2$ as the effective contact angle against air is 180˚. Herminghaus (2000) showed hierarchical structures were more efficient on decreasing wettability than single scale structures. The contact angle of a hierarchically structured surface that consists of textures at increasingly small scale can be determined by following linear recurrence relation:

$$\cos\theta_{n+1} = (1 - w_n)\cos\theta_n - w_n \qquad \text{(eqn. 2.11)}$$

In which $\cos\theta_{n+1}$ and $\cos\theta_n$ are two consecutive terms representing the contact angle of the corresponding scale and w_n is a geometric parameter. This recurrence relation is monotonic decreasing and approaches a limit of -1 as n approaches infinity. As a result, the contact angle of a droplet standing on a surface decorated by infinitely self-similar, iterated hierarchical structure can be 180° if do not consider the influence of gravity.

2.1.7 Cassie-Baxter wetting state on textured hydrophilic surface

The review in section 2.1.3 suggested that for a hydrophilic surface decorated by textures, the textures would lead to a lower water contact angle since the roughness can amplify its wettability. However, the Cassie-Baxter wetting state can also be established on a textured hydrophilic surface by adopting appropriate hierarchical roughness and overhanging structure to stabilize the three-phases contact line.

From the system energy point of view, certain types of surface structure, such as nail-head like and mushroom like structure, would create a high energy barrier to hinder the transition from the Cassie-Baxter wetting state to the Wenzel wetting state on a hydrophilic micro textured surface. For example, Cao, Hu & Gao (2007) studied the water contact angle on a roughened hydrogen-terminated surface. In the presence of protruding structures, the water contact angle varied between 139˚ and 162˚ depending on the distance between adjacent protruding elements, whereas in the absence of the protruding structure the water contact angle was 74˚. Nosonovsky & Bhushan (2007) gave a detailed explanation using an example texture shown in Figure 2.6. As penetration begins from the top of surface structures, the system's free energy begins to decrease and flatten out to reach a local minimum and then increase again. The difference in energy between a local minimum (a stable equilibrium) and the subsequent local maximum (a unstable equilibrium) represents an energy barrier. Nosonovsky & Bhushan (2007) noticed that stable equilibrium always found in a convex area whereas unstable equilibrium always found in a concave area. This finding agrees with the hypothesis made by Bormashenko *et al.* (2006), who suggested that a water-air interface can only be stable at locations where the angle made by liquid against solid was smaller than the Young's contact angle.

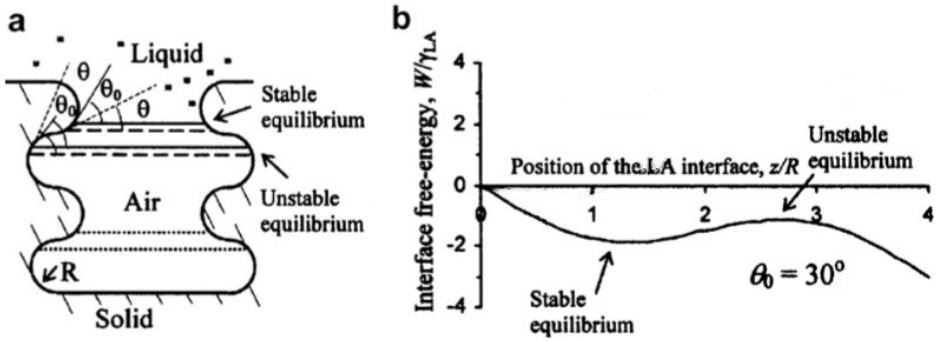


Figure 2.6 A hierarchical structure made of hydrophilic material. (a) Schematic close-up view of structure. (b) The change in system energy during the water-air interface move downward along a groove.

2.1.8 Condensation on textured surfaces

When a textured hydrophobic surface is exposed to condensation conditions, the surface wetting is governed by a different mechanism. Cheng *et al.* (2005) found strong adhesion between a condensed drop and a lotus leaf and the contact angle hysteresis changed significantly. Liu & Choi (2013) and Wier & Mccarthy (2006) demonstrated that the high contact angle accompanying a high contact angle hysteresis on lotus leaves probably involved a changes in wetting state as well as an increase in contact line length. Unlike in usual wetting situations, in which a water drop suspends on the top of surface structures, water vapour is able to fully wet wax tubules by infiltration. Evidence that this mechanism was involved in vapour condensation on the surface of lotus leaf was the observation that, in the case of condensation, the adhesion between water and papillae is much greater than that of dropping.

2.2 Capillary absorption of cementitious materials

Water absorption is defined as water flowing into pores of cementitious materials because of capillary force. When water contacts with a capillary pore, a meniscus forms due to surface tensions. For wetting of hydrophilic materials, such as cementitious materials, the curvature of meniscus is negative everywhere, which generates a negative Laplace pressure at the meniscus. It is this negative pressure causes water to be drawn into the pore from external source of water (Hall & Hoff, 2012d). Note that water adsorption would also occur when water in contact with the wall of capillary pore forming stable adsorptive structure with hydrogen bond. However, the adsorptive layer has only few molecular thick as attraction acting on molecules decrease with increasing distance from the wall. The main mass gain arises from the water ingress should therefore be attributed to water absorption.

The flow in cementitious materials can be described by the sharp front model, which is a simplified model used to study capillary absorption, first adopted by Green & Ampt (1911) in the study of soil physics. It is a valuable tool for predicting imbibition behaviour of complex system, such as layered materials, pressurized inflow, etc. This model assumes that unsaturated flow in porous materials is related to a constant capillary potential (Hall & Hoff, 2012c). The region behind the waterfront is assumed to be in a state of saturation with a step change at the waterfront. In the simplest situation in which the advancing waterfront is only driven by capillary suction, the Darcy's law can be reduced to

$$u = -K\nabla\psi = -K\frac{P_f}{l} \quad \text{(eqn. 2.12)}$$

in which K represents permeability of wetted region; P_f represents capillary pressure and l represents the length of wetted region. If the air in capillary pores is completely replaced with water, this relationship can be written as

$$\frac{di}{dt} = -K\Phi\frac{P_f}{i} \quad \text{(eqn. 2.13)}$$

In which l is replaced by a ratio of cumulative absorption per unit area, i, to the porosity, Φ. Therefore, by integrating this equation over the elapsed time, the cumulative water absorption is given by

$$i = \left(2K\Phi\left|P_f\right|\right)^{1/2}t^{1/2} \quad \text{(eqn. 2.14)}$$

Comparing this to the sorptivity relationship that is governed by the extended Darcy's law (Hall, 1989), sorptivity can be identified as $S=(2K\Phi|P_f|)^{1/2}$. Masoodi & Pillai (2013) compared the absorption data of polyethylene for three organic liquids with predictions using the sharp front model. The results showed a good fit between experiment data and model predictions. Hall & Hoff (2007) used the sharp front model to predict the process of capillary rise of water in walls and showed the predictions were satisfactory. Hall (1981) compared the shape of the water content profile of building materials over the entire absorption process. He found that the profile was stretched out as absorption continued, but basically remained a constant shape with 70% of the change in water content occurred within the first tenth of the profile. Data on the sorptivity of bricks indicated a good correlation between experiment result and prediction using the sharp front model (Hall, 1981). All these results indicated that the sharp water-front is a good approximation for the absorption behaviour of most building materials.

2.3 Water ingress and degradation of concrete

Concrete is a porous material by nature, which makes it vulnerable to be attacked both physically and chemically. According to The Concrete Society (2013), concrete degradation mechanisms that relies on the presence of water can be divided into 6 categories, including: chloride ingress, carbonation, sulfate attack, freezing and thawing, delayed ettringite formation, and alkali-silica reaction. The attack may target cement matrix itself, aggregate, or reinforcement and as a result, weakening the strength of concrete and leading to the failure of structure. Water can either participate in reaction or carry aggressive species into concrete through capillary suction. In this section, the mechanisms behind these deteriorations and the role of water in these deterioration process will be reviewed.

2.3.1 Carbonation

Carbonation of concrete relates to the diffusion of CO_2 (Groves, Rodway & Richardson, 1990). The CO_2 diffuses into concrete through pore system and dissolve in pore solution to create small amount of carbonic acid. The hydrogen ions generated by ionization of carbonic acid gradually dissolve calcium hydroxide, and carbonate ions combine calcium ions producing insoluble calcium carbonate (Mindess, 2019). As the CO_2 deplete calcium hydroxide on the surface of concrete, the 'front' moves downward to the reinforcement. Once the original alkalinity environment near reinforcement is destroyed by carbonic acid, the reinforcement is forced to exposed in a low PH environment, in which the passivate layer of ferric hydroxide on the reinforcement is activated and destroyed. Neville (2011) stated that the most rapid carbonation took place when the internal relative moisture ranged from 50% to 70%. High water content will slow down the rate of diffusion and therefore, less carbonation is observed at high water content. However, at high CO_2 concentration, C-S-H gel suffers decalcification in which calcium ions migrate from the inner C-S-H product to the outer product region and forming minute calcium carbonate crystals which build up in capillary pores (Groves, Rodway & Richardson, 1990).

The Concrete Society (2013) indicates that pore blocking type of water resisting treatment may improve the resistance of concrete to carbonation since the rate of gas diffusion is reduced due to pore blocking.

2.3.2 Freezing and thawing

Freezing and thawing damage is normally found on concrete very close to saturation (>90%) (Mindess, 2019). Water in pores experiences an increase in volume of 9% as it turns into ice, and this expansion results in a tensile stress build-up within cementitious materials. As the

pore water continues to freeze, micro cracks start to form when the pressure exceeds the tensile strength of concrete (Margi, 1998). The micro cracks will interconnect with each other to form a macro crack after multiple freezing and thawing cycles, leading to internal damage, or spalling.

Water enters concrete through capillary suction, and this is the major contributor to the freezing and thawing attack. Therefore, using water-resisting treatment in concrete may help concrete to maintain its internal relative humidity and keep the water content in cementitious materials under critical saturation level of 90% (The Concrete Society, 2013).

2.3.3 Alkali–silica reaction

Alkali-silica reaction is an internal chemical attack with the participation of reactive aggregate and alkali from cement. The depolymerization of reactive silica slowly occurs in pore solution and reaction with Na^+ and K^+ forms a low viscous alkali-silica gel. The gel can absorb water and expand, leading to the build-up of tensile stress, and eventually the cracking of concrete. This deterioration exhibits a distinct “map cracking” pattern and the cracks may be filled with gel as the reaction proceeds (Neville, 2011). Different from other type of chemical attack, alkali-silica reaction is slow, and may take decades to start showing signs of deterioration.

Use of water-resisting treatments may reduce the risk of alkali-silica reaction as this deterioration can be avoided by maintaining the water content of concrete below 75%.

2.3.4 Chloride ingress

Chloride ions normally enter concrete through diffusion and absorption. Water is the most common media carrying chloride ions into outer layers. The chemical action of chloride ion on concrete is mainly due to the binding between chloride ions and AFm phase in the cement matrix. Hydroxide, carbonate, and sulfate held by van der Waal force between the layer structure of AFm phase may be replaced by chloride ions (Galan, Glasser & Andrade, 2013). However, chloride ions have minor influence on the concrete itself.

Severe deterioration triggered by chloride ions arises from the corrosion of embedded reinforcement. The degradation of passive iron oxide coating on reinforcements starts at very low concentration of chloride by forming soluble iron-chloride complex (Rodrigues *et al.*, 2021). Once the passive coating is destroyed, the surface where exposed to pore solution will act as an anode and areas still covered by a passive coating will act as a cathode (Frankel, 1998). Therefore, a primary cell that is composed of large-scale cathode and small-scale of anode is formed. The corrosion rate is very large at the anode area leading to the ‘pitting corrosion’ (Tsutsumi, Nishikata & Tsuru, 2007). The chloride ions will move to where corrosion takes

place under the drive of the electric field and the content of chloride ions in concrete will increase over time as chloride is being constantly transported into concrete, which exacerbates the corrosion process.

Generally, corrosion of reinforcement requires an internal relative humidity above 60% to happen (Enevoldsen, Hansson & Hope, 1994; Mindess, 2019). In addition, how easy it is for chloride ions transport into concrete depends on to what extend water can penetrate the concrete. Water resisting treatment has been found effective on reducing both chloride penetration and chloride concentration on the surface of cementitious materials (Dai *et al.*, 2010). Case studies using a hydrophobic admixture (Caltite) reported structures containing Caltite remained in corrosion-free condition after 20 years and the chloride contents were significantly lower than that of controls (The Concrete Society, 2013).

2.3.5 Sulfate attack

Sulfate attack is normally found on foundation or underground construction where frequently or commonly submerge in underground water that is naturally high in sulfate ion. Monosulfoaluminate within cement matrix is able to react with sulfate ions forming ettringite (Hekal *et al.,* 2002), which leads to an expansion of 55% in volume. This type of deterioration manifests itself on the surface of concrete as cracking or spalling. At very high level of sulfate ion, deterioration caused by crystallization of gypsum is dominant, especially at area where experiences wetting-drying cycles. Evaporation reduces moisture content during drying cycles, which concentrate sulfate in pore solution then react with calcium hydroxide forming gypsum (Nehdi *et al.,* 2014). This is accompanied by an expansion of 120% in volume.

Magnesium sulfate is more damaging than other sulfate salt since it destroys C-S-H gel (Cohen and Bentur, 1988). Magnesium ions first react with calcium hydroxide to generate brucite which is a less soluble material. This reaction decreases PH value of pole solution, which destroys the original stable internal environment. Saturated brucite solution has a PH value lower than the PH required to stabilize ettringite and C-S-H gel. As a result, C-S-H gel starts to decompose and release calcium hydroxide when PH value is lower than 12.5 while the released calcium hydroxide again reacts with magnesium ion to generate brucite. Calcium and sulfate ions accumulate in the solution and eventually separate out as gypsum crystals (Margi, 1998). The decomposing process leads to a decreasing ratio of Ca/Si from 2.12 at PH of 12.5 to 0.5 at PH of 8.8.

Delayed ettringite formation is a sulfate deterioration that associates with internal sulfate attack. It happens in concrete that experiences elevated temperature shortly after casting, such as curing or internal heat of hydration. When the temperature is higher than 70˚C, ettringite

formed during hydration decomposes into monosulfate and releases sulfate and aluminate ions that are temperately absorbed by C-S-H gel (Taylor, Famy & Scrivener, 2001). These ions will be released again when the temperature cools down and involve in the reformation of secondary ettringite in the presence of significant moisture. The growth of secondary ettringite exerts pressure in confined paste structure which may lead to cracking, or the ettringite deposits in pre-existing cracks leading to its expansion (Diamond, 1996).

As all types of sulfate attack are associated with water that either act as a transport medium or are involved in reaction, it can be expected that applying a water resisting treatment will be beneficial. Gao *et al.*, (2022) concluded from tests on mortar containing hydrophobic mica powder that surface deterioration, diffusion depth and concentration of sulfate ion were decreased with the increase of hydrophobic powder content. Concrete coated with epoxy and ethyl silicate gave great resistance to sulfate attack after immersion for 120 days in 10% sodium sulphate solution, whereas uncoated concrete completely disintegrated after 105 days (Sakr & Bassuoni, 2018). Case study of hydrophobic admixture Caltite reported that concretes containing Caltite remained in sound condition after about 20 years exposed to groundwater (sulfate at 7200mg/L) (The Concrete Society, 2013).

2.3.6 Acid attack

Acid attack commonly happens in sewer pipe and on surfaces in contact with acid rain. The principal reaction of acid attack is the leaching of calcium hydroxide. However, if the acid is concentrated, calcium originally present within C-S-H gel may start to leach out (Baker & Bishop, 1997; Hinsenveld & Bishop, 1996; Du et al., 2014; Webster & Loehr, 1996). Du et al. (2014) reported that a significant increase in the amount of leachable calcium was observed when lowered the pH value of leachate from 4 to 2, indicating the attack of C-S-H gel. Many documents have reported a calcium-depleted zone on the exterior surface while the interior of samples was basically unaffected by acid solution (Torres et al., 2019; Fattuhi & Hughes, 1988; Chandra, 1988). The thickness of leached layer was 1 mm at most for leaching time up to 21 days in acid leachant with PH of 2-3 (Baker & Bishop, 1997).

2.4 Hydrophobic surfaces

Millions of years of natural evolution have optimized the surface morphology of some plants and animal skins to acquire water repellence. Neinhuis & Barthlott (1997) concluded that hierarchical structures were commonly observed on the surface of hydrophobic plant leaves after reviewing more than 200 plant species, of which leaves exhibited a water contact angle over 150°. The hierarchical structures consisted of plant tissues in micron and nano scale.

Some examples of hierarchical structure are given in Figure 2.7. Koch and Barthlott (2009) summarized that the hierarchical structures, such as the micro textures found on lotus leaves and taro plants, has a very dense arrangement of nano structure composed of cuticular wax covering bulges formed by epidermal cell.

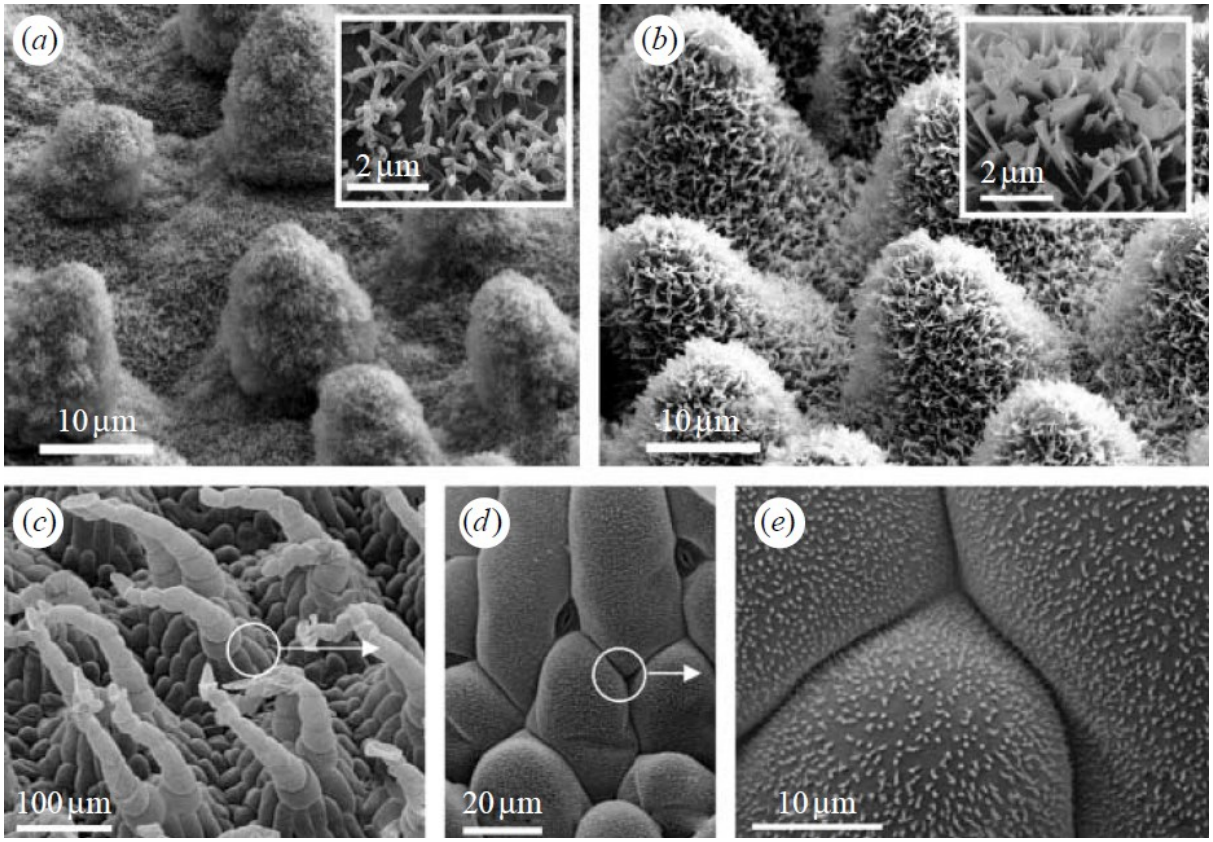


Figure 2.7 SEM images showing the surface characteristics of (a) lotus, (b) Euphorbia myrsinites, and Salvinia oblongifolia. The insets show nanoscale wax crystals. Adapted from Koch & Barthlott (2009).

The surface structure of plant leaves are generally classified in three levels: cell shape, cuticular fold and cuticular wax crystal (Wagner *et al.*, 2003). The papillose epidermal cells create bulges or cuticular folds in the micron scale on the surface of leaves. The outer cell wall are softened and the turgor pressure of contents act on the soft area to form a round bulge (Mauseth, 2008). Different degrees and shapes of bulges can be observed on different species. Trichomes may form if the softened outer cell walls experience severe bulging and stretching into hair-like structures (Figure 2.7 c).

Among all the plant species studied by Neinhuis & Barthlott (1997), the highest water contact angle was observed on a lotus leaf, which was 162°. In addition to the outstanding wettability, a lotus leaf also exhibited very low contact angle hysteresis. A water drop can roll off when

the surface was inclined with an angle of inclination 4°. Debris on the surface of lotus leaf will therefore adhere on the water drop and roll off because of weak van der Waals force between debris and surface (Ensikat *et al.*, 2011). Such self-cleaning phenomenon of lotus leaf is known as the “lotus effect”. The formation of high contact angle on lotus leaf is mainly caused by the morphology of the surface, on which closely packed papillae covered by a very dense wax tubules in the nano scale creating a hierarchical structure. Air is trapped in between these hierarchical structures forming a hybrid rough surface, which significantly decreases the water solid interface area, leading to a high water contact angle.

Several studies investigated the contribution of cuticular wax to the hydrophobicity of lotus leaf (Wagner *et al.*, 2003; Cheng *et al.*, 2006). FTIR measurements indicated a great deal of similarities in chemical components between cuticular wax on a lotus leaf and carnauba wax. Cheng *et al.*, (2006) tested the water contact angle of carnauba wax and found out that the carnauba wax was hydrophilic, with water contact angle of 74°. This can be supported by the observation that the cuticular wax contained many hydrophilic functional groups, such as carboxyl and hydroxyl (Wagner *et al.*, 2003). Therefore, these studies highlight the important contribution of micro textures at different length scales to hydrophobicity.

The hierarchical structure is not the only method to make a surface hydrophobic. For example, cabbage leaves are hydrophobic, but their surface lack hierarchical structure. The hydrophobicity of cabbage leaves is ascribed to the fact that its surface is covered by a thick layer of wax crystal. However, deterioration of hydrophobicity can be observed on mature leaves because of damage on the wax coverage (Koch & Barthlott, 2009). A leaf covering waxy trichomes also exhibit significant water-repellency. Gravity causes water drops to bend over trichomes, but the stiffness of trichomes hold and prevent droplets from contacting with the substrate. However, the hydrophobicity of trichomes is attributed to the presence of waxy crystal (Neinhuis & Barthlott, 1997a), and a lack of waxy crystal will decrease hydrophobicity. Waxy trichomes can hold water droplets for a long time even if the trichomes are loosely packed on a surface.

Hydrophobic surfaces have been engineered in a range of materials by exploited the lotus effect. To fabricate a surface that demonstrates self-cleaning, a textured surface that is capable of trapping air is required to achieve the Cassie-Baxter state. Soft lithography, which is a low-cost technology to replicate microstructures in the scale of nano to micron (Qin, Xia & Whitesides, 2010; Zhao, Xia & Whitesides, 1997), has been proved to be a facile method to fabricate a hydrophobic surface through transferring lotus leaf structure. Sun *et al.*, (2005) transferred the lotus leaf structure onto a PDMS surface using soft lithography. They first

fabricated a PDMS mould on which embedded with a negative pattern of lotus leaf structure. The mould was then coated with a layer of trimethylchlorosilane as release agent before casting PDMS polymer. Liu *et al.* (2006) adopted the similar method but they used the PDMS mould as a stamp to mould epoxy-based azo polymer ink into a lotus leaf structure. The resultant surface had a water contact angle of 154.6˚.

Other research on hydrophobic micro-textured surfaces has demonstrated that surface roughness can be fabricated on silicon wafer substrates, metal panels, and polymers using lithography, chemical etching, templating, and chemical vapor deposition (Oner & Mccarthy, 2000; Sun *et al.*, 2005; Guo, Liu & Su, 2011; Callies *et al.*, 2005; Ng *et al.*, 2016; Cao, Hu & Gao, 2007; Cha *et al.*, 2010; Crick & Parkin, 2009). Chemical vapor deposition has been used to prepare superhydrophobic rough surface (Crick & Parkin, 2009). Elastomer film deposited on a glass substrate consisted of agglomerate forming irregular roughness. The maximum water contact angle achieved by the elastomer film was 167˚ while a glass dip-coated with the same elastomer showed contact angle of 95˚. A studied carried out by Qian & Shen (2005) used metal plates as substrate and fluoroalkylsilane coating was applied. The metal plates were first roughed by dislocation etching and then submerged in fluoroalkylsilane solution to lower the surface energy. The resultant surface showed an increase in water contact angle from 98˚ to 150˚, with contact angle hysteresis of 7˚. Zhu *et al.* (2006) adopted photolithography to produce hydrophobic surfaces embedded with regular patterns with designed geometry. A silicon substrate was etched by inductively coupled plasma after photolithography, and surface coating was achieved by grafting Octadecyltrichlorosilane molecules onto the already roughed surface. The surface consisted of micro pillars with water-air contact faction of 0.95 showed contact angle of 160˚ and near zero contact angle hysteresis.

The hydrophobicity of an engineered micro-textured surface can be further enhanced by producing crystals in the nano scale on the top of the micro-texture. An example of the dual-scale structure fabrication used photolithography and plasma etching to fabricate designed micro textures on a silica wafer and then used chemical vapor deposition to generate silicon nanowires on the micro textured surface (Cao, Hu & Gao, 2007). The dual structure resulted in a contact angle to superhydrophobic regime (~160˚) even though silicon itself was a hydrophilic material. A study carried out by Hang *et al.* (2010) showed the hierarchical roughness can be introduced in a one-step process. This was done by deposing a nickel film on a copper substrate through electrodeposition and the micro and nano structures were fabricated by controlling current density passing through the substrate. The resultant surface had water contact angles up to 154˚.

2.5 Reducing water ingress in cementitious materials

Deterioration of cementitious materials caused by water and water-borne ions is well-known, strategies have been employed to restrict the passage of liquid water through capillary pores. Providing a protective membrane or overlaying externally is effective in this regard through isolating the structure from water (Mindess, 2019). However, the membrane needs to be replaced as the membrane normally has a lifespan of 30 years versus 50 to 100 years for structures (The Concrete Society, 2013).

Capillary pores are the remain of original interparticle space that was occupied by mixing water. The greater the water/cement (w/c) ratio, the greater the remaining capillary water between hydration products and larger the capillary pores (Aitcin, 2019). Therefore, it is effective to decrease water penetration by reducing w/c ratio. Results from mass transport properties, carried out by Kim *et al.*, (2014) showed that by decreasing the w/c ratio of mortar from 0.6 to 0.45, the porosity of mortar at age of 91 days was decreased by 150%, and the sorptivity, moisture diffusivity, and air permeability correspondingly decreased by 259%, 266%, and 192% respectively. Increasing curing period to promote continuous hydration would also lead to a decrease in water absorption due to the refinement of pore structure as a result of the formation of continuous hydration products. Porosity distribution determined by mercury porosimetry showed that concrete moist cured for 28 days had a finer pore structure and lower total porosity compared to air cured concrete of the same age (Ramezanianpour & Malhotra, 1995). Concrete cured in water over 1 year yielded a total water absorption 45% lower than that cured under the same condition over 3 days (Pandey & Kumar, 2019).

Another method to reduce water ingress into hardened cementitious materials was achieved by replacing part of cement with pozzolanic materials, such as silica fume, slag, metakaolin, etc. These pozzolanic materials possess cementitious properties which produces C-S-H gel by reacting with calcium hydroxide that is a by-product formed by the hydration of C_2S and C_3S. This pozzolanic activity improves the microstructure of concrete by replacing low strength contribution calcium hydroxide with high strength C-S-H gel, resulting in a refined pore system (Massazza, 1998). Prolong curing for blended cement of these types is also necessary due to the slow rate of pozzolanic reaction, which is attributed to resistance to the movement of calcium ions to reaction sites in hardened cement matrix (McCarthy & Dyer, 2019). In addition, part of improvement in pore structure could be attributed to improved particle packing because most of pozzolanic materials are finer than Portland cement (Massazza, 1998). A consequence of this pore structure refinement is a greater resistance to water penetration. Dinakar, Sahoo & Sriram, (2013) examined concrete with a water/binder (w/b) ratio of 0.3 at

90 days. It was found that by replacing cement with 15% metakaolin powder the water permeability, penetration depth, and absorption were decreased by 78%, 60%, and 27% compared to the references, respectively. Sadrmomtazi *et al.,* (2018) conducted an extensive study to investigate the effect of silica fume on the porosity and water transport properties of concrete with a w/b of 0.45 at 28 days. Results showed the silica fume resulted in a reduction in pore size in cement mixture and a denser interfacial transition zone between paste and aggregates. At 10% silica fume replacement, the sorptivity of concrete was decreased by 43% and water penetration depth was reduced by 65% compared to controls.

2.6 Water resisting agents

The use of water resisting agents in cementitious materials has only become popular in recent decades as an alternative method to membrane water proofing system (The Concrete Society, 2013). Water resisting agents refer to materials that reduce the hydraulic permeability of concrete or impart water repellency to the exposed surfaces. Common water resisting agents can be broadly divided into two groups according to how they work with concrete (Dai *et al.*, 2010). The first group consists of those blocking the pore system and microcracks of concrete either by chemical reaction or adsorb suspension from solution to reduce its permeability. The second group consists of water-repellent materials, which serve as surface active agent by covering the surface of concrete and altering surface tension.

When consider the performance of these water resisting agents, they can also be subdivided into PRANs and PRAHs based on their ability of resisting hydrostatic pressure (PRANs refers to those can only be used in non-hydrostatic situation and PRAHs refers to those can withstand hydrostatic pressure) (Surahyo, 2019). PRAHs mostly comprise of very fine inert or reactive powders, such as fluorosilicates, calcium stearate power, powder forms of various resins and bitumen, etc (Hewlett, Justnes & Edmeades, 2019). This type of water resisting admixtures reduce water absorption of concrete mainly through capillary pores refinement. PRANs consist of organic materials, such as long chin fatty acid, vegetable and animal oil and petroleum-based products. This sort of material generates insoluble salt adhere to the wall of capillary pores when react with calcium in solution forming a water-repellent layer. Such hydrophobic walls lead to a large water contact angle that holds back water when they are trying to pass into concrete (McCarter, 1996). Concrete treated in this way exhibits reduced water permeability but its effect on vapor permeability is less significant. Table 2.1 presents the summary of selected studies on the influence of water resisting agents on the performance of concrete.

Table 2.1 Summary of selected studies on the effects of hydrophobic agents on concrete performance.

Study	Water resisting agent	Main results
Medeiros & Helene, (2008)	Silane/Siloxane	Water sorptivity of concrete coated with silane/siloxane was 2.1 to 7 times lower than the reference and the sorptivity further decreased as the number of treatments increased. However, the surface treatment was far less effective when the inlet water pressure was higher than 2450 Pa.
Dai *et al.*, (2010)	Silane-based water repellent agents and sodium silicate-based pore blockers	Concrete coated with pore blockers exhibited water absorption 30% lower than the reference, whereas the mass of concrete coated with water repellent agents barely increased after 30 wetting cycles. Pore blockers coating appeared less effective on chloride penetration compared to the water repellent agents. Repetitive treatment was required because the existence of cracks significantly increased the rate of chloride penetration as well as the corrosion of reinforcements even when the concrete was coated with water repellent agents.
Husni *et al.*, (2017)	Hydrophobic rice husk ash, which was achieved by dispersing rice husk ash into fluoroalkyl silane solution	Concrete coated with hydrophobic rice husk ash showed low contact angle hysteresis and a water contact angle of 152°. The water sorptivity and total water absorption of treated concrete was decreased by 44% and 40% respectively, and a certain degree of water pressure resistance was observed.
Wong *et al.*, (2015)	Hydrophobic PSA, which was achieved by dry ball milling PSA and stearic acid	Water absorption and sorptivity decreased when replacing part of cement with hydrophobic PSA. The hydrophobic PSA remained effective even when the samples were under a small water pressure and long-term immersion. The best performance was achieved in surface coated samples, where both absorption and sorptivity were reduced by up to 99% compared to the references.

		The study also observed higher air contents in samples containing hydrophobic PSA, the higher the amount of hydrophobic PSA used, the greater the amount of entrapped air voids.
Shahbazi *et al.*, (2020)	Amorphous carbon powder (ACP)	The presence of ACP led to a significant decrease in the workability of both paste and concrete, but no major detrimental effect on compressive strength was observed for replacement level up to 20%. Increased ACP content resulted in less surface wettability and lower water sorptivity. At ACP replacement level of 20%, sorptivity was decreased by 55% with little effect on total water absorption.
Malakopoulos *et al.*, (2021)	Butyl stearate and zinc stearate	Both butyl stearate- and zinc stearate- contained mortars were able to resist hydraulic pressure to a certain degree. However, Butyl stearate was superior to zinc stearate in terms of water repellency and chloride resistance because butyl stearate only slowly hydrolysed in alkaline environment of cement paste, which led to a more uniform distribution of admixture. Portland limestone cement mortars contained 5% wt. butyl stearate had water permeability and water absorption 98% and 74% lower than the reference, respectively.
Al-kheetan, Rahman & Chamberlain, (2019)	Sodium acetate, fluoropolymer, silane, and silicon resin	The bonding between hydrophobic coating and concrete was found to be dependent on the moisture content of concrete. Sodium acetate coating provided best protection against chloride transport at high moisture condition followed by silicon resin, whereas at fully dry condition, silane performed the best. Applying hydrophobic coatings onto wetted concretes showed decrease in chloride content of 35%, 41%, 65%, and 82% over controls for silane, fluoropolymer, silicon resin, and sodium acetate, respectively.

PRANs reduce water and ions transport through concrete which arises from capillary suction. Deteriorations related to water transport of this types, such as efflorescence and dampness, can also be effectively prevented by applying PRANs. However, materials in this group make minor contribution to resisting chloride transport in saturated concrete as it is governed by ion diffusion rather than capillary action (Dai *et al.*, 2010; Medeiros & Helene, 2008, 2009). For example, treatment of concrete coated with silane/siloxane resulted in a reduction in chloride diffusion coefficient of only 11% over controls under saturated condition (Medeiros & Helene, 2008). Penetration depth of hydrophobic agents appears to be another important factor in the performance of hydrophobic coating. Water repellents that have low viscosity, and therefore larger penetration depth achieving lower water sorptivity has been reported in several studies. For example, surface coating produced by using silane dispersed in solvent achieved water sorptivity 3.5 times lower than that using saline dispersed in water as coating agent (Medeiros & Helene, 2008). Cracks on concrete surface can be detrimental to the effect of hydrophobic coating on the prevention of corrosion (Tittarelli & Moriconi, 2011). However, Dai *et al.*, (2010) reported that if the hydrophobic coating was applied after the cracks were formed, no corrosion was observed after 1 year of cyclic wetting with sea water even when the width of cracks exceeded 0.2mm. These findings highlight the importance to consider the feasibility of hydrophobic coating in practice as concrete structures will crack under loading stress.

Hydrophobic admixtures, on the other hand, are more effective on resisting chloride migration through cracks as the newly exposed surfaces are also hydrophobic. However, the cracks on hydrophobic concrete resulted in a higher risk of corrosion because the water repellent nature of hydrophobic admixtures allowed oxygen diffused faster in unsaturated pores (Tittarelli, 2009; Tittarelli & Moriconi, 2011). In terms of durability, concrete containing hydrophobic admixtures were normally more durable than surface coatings as the performance of coatings showed deterioration when subjected to high temperature, ultraviolet radiation (UV), aging etc. For example, Jones, Dhir & GIll, (1995) found that temperature above 45°C significantly decrease the resistance of silane to chloride ion penetration due to the deterioration of hydrophobic nature of silane at high temperature. Fluorinated-based and siloxane-based hydrophobic coatings subjected to prolonged ultraviolet or damp heat exposure suffered from deteriorations and delamination due to the break of chemical bonds or solvolysis reaction (Lisco *et al.*, 2020).

However, some hydrophobic admixtures, such as soaps-based materials, entrain air due to their surfactant properties, which results in preventing high dosage to be used in order to avoid significant strength loss (Hewlett, Justnes & Edmeades, 2019). It is also noteworthy that some types of hydrophobic admixtures have similar function with water-reducer, therefore, the

contribution of water resisting ability are partly attributed to the less usage amount of water, which enhances the density of concrete.

There are at least seven brands of commercially available water resisting concrete admixture in existence today in British market: Caltite, Krystol, Xypex, Sika, Pudlo, Adprufe and Conplast. In the results reported, all these products decreased water penetration, and water permeability were reduced by 40% to 80% of the controls (The Concrete Society, 2008, 2013). However, it should be noted that the properties of control concrete used in these tests varied widely (The Concrete Society, 2013). For example, Caltitle used a control sample with a water permeability of $2.23*10^{-12}$ m/s, which is more permeable than structural concrete of which the permeability is typically $1*10^{-12}$ m/s at w/c ratio of 0.45 (Neville, 2011). The controls used by other products had water permeability range from $3.2*10^{-15}$ to $9.32*10^{-13}$ m/s, which are much lower than normal value. This cast doubt on the absolute values they reported, and assessing the relative performance of different admixtures should be treated with caution (The Concrete Society, 2013).

2.7 Hydrophobic calcium carbonate

Hydrophobic calcium carbonate powder (HPCC) was made by dry ball milling. Dry ball milling fractures calcium carbonate particles and thus, generate new surfaces (Figure 2.8). The organic substances act as coupling agents that cover the surface of calcium carbonate particles in the form of a self-assembled monolayer, giving the calcium carbonate particles hydrophobicity.

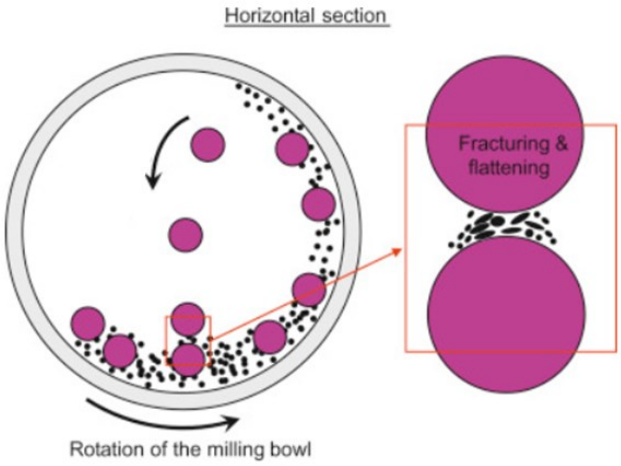


Figure 2.8 Schematic illustration of ball mill. Adapt from Faraji, Kim & Kashi, (2018).

The self-assembled monolayer is created by chemisorption of functional groups of organic molecules, the functional groups adsorb on substrates while leaving the tail groups facing

outward (Hu *et al.*, 2009). This process is known as “surface functionalization”. Kokkinis (2017) stated that the compounds used as coupling agents usually possess both hydrophilic and lipophile characteristics. The hydrophilic part adheres to the substrate leaving the lipophile part facing outward. Therefore, the surface characteristic changes due to the adsorption of the coupling agent. The surface functionalization also takes place on newly generated surfaces, but this process will cease when the ball milling reaches its operational limitation (Devarajan, Khadar & Chattopadhyay, 2007), at which substances cannot be broken up further.

Mihajlović *et al.*, (2013) proposed a detailed mechanism to illustrate the interaction between calcium carbonate filler and stearic acid during ball milling. The high temperature and pressure arising from the violent impact of grinding media provide appropriate conditions for the dissociation of stearic acid into [$RCOO^-$] and hydrogen ion (Hansen, Hamouda & Denoyel, 2000). [$RCOO^-$] stands for the stearic acid radicals, in which “R” refers to a 17-hydrocarbon chain. [$RCOO^-$], which carries a negative charged adsorb on the surface of calcium carbonate through a site-specific Ca-O bond. One carbonyl attaches to one calcium ion on the bulk surface forming calcium stearate. Alternatively, the dissolved hydrogen ion can be attracted to an exposed carbonate forming -CO_3H.

Fekete *et al.* (1990) and Shi, Rosa & Lazzeri (2010) analyzed the density of stearic acid on the surface of calcium carbonate. Based on crystallographic data, the surface density of calcium ion on calcium carbonate filler was 4.97 ions per nm^2. The density of which a stearic acid radical vertically adsorbed on a substance surface was 4.9 molecule per nm^2. Therefore, only one stearic acid can attach to one calcium ion on the surface of calcium carbonate filler.

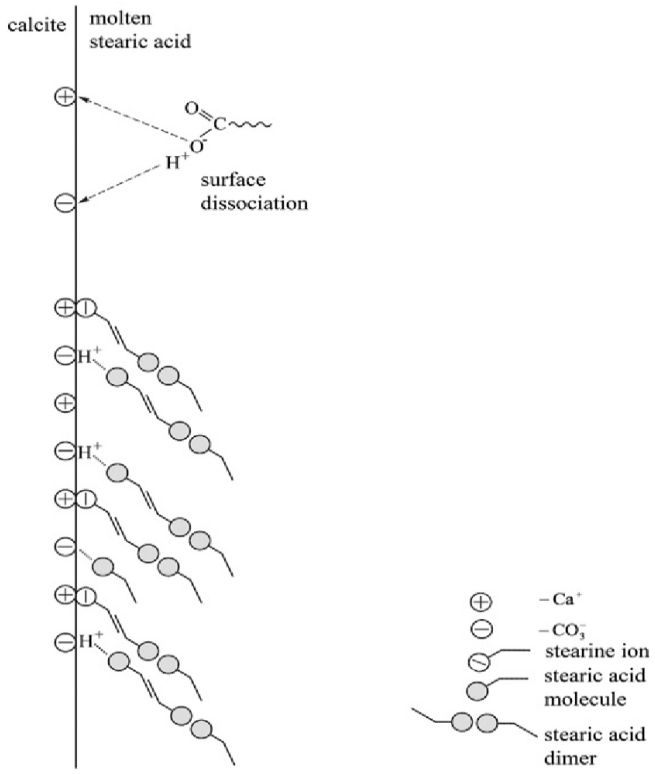


Figure 2.9 Adsorption of stearic acid molecules on the surface of calcium carbonate filler after dry milling (Mihajlović *et al.*, 2013).

However, the steric effect may cause some deficiencies on the chemisorbed monolayer. Instead of forming a vertically orientated monolayer, some hydrocarbon chains may be obliquely adsorbed on the surface of calcium carbonate (Mihajlović *et al.*, 2013) (Figure 2.9). Therefore, some calcium ions on the surface are blocked by earlier attached hydrocarbon chains, which interferes with the chemisorption of stearic acid on the blocked calcium ions. This aligns with the result of Rezaei Gomari, Denoyel & Hamouda, (2006) who calculated the average area occupied by single stearic ion after treating calcium carbonate filler by dry ball milling. They concluded that the orientations of tail groups are both perpendicular and horizontal to the surface.

Several layers of stearic acid may physically adsorb on the outer surface of the chemisorbed layer (Gilbert, Sutherland & Guest, 2000). The physisorption may start before the completion of the chemisorption of stearic acid. The local physisorption of adsorbates can be found on the surface close to the high concentration of stearic acid because of unevenly distributed stearic acid (Mihajlović *et al.*, 2013). Unlike chemisorption which usually involves chemical bond between adsorbed species and substrate, the physiosorbed molecules depend only on weak Van der Waals interaction. The interaction energy of chemisorption is of the order of 200 kJ mol^{-1}, which approximates ten times greater than that of physisorption (Micha, 2020).

Because of the weak binding between species, the electrons configuration of a combination can be viewed as a construction of the electron density of substrate and individual physiosorbed molecules. For this reason, the substrate surface may maintain its own properties instead of being modified by surfactant (Micha, 2020).

Jafari & Farzaneh (2013) applied infrared spectrometry to analyze the stearic acid cover on calcium carbonate fillers. They found peaks at around 2910 and 2850 cm^{-1}, which indicated the presence of asymmetric and symmetric methylene on the surface of fillers. Therefore, the hydrophobicity of treated calcium carbonate was mainly attributed to the nonpolar hydrophobic methylene coverage on its surface. Fekete *et al.* (1990) estimated the surface energy of calcium carbonate treated by stearic acid. They found that the higher the amount of stearic acid adsorbed on the surface of substrate, the lower the surface energy of treated calcium carbonate obtained. This complemented the findings from Jafari & Farzaneh (2013) that nonpolar methylene coverage on the surface of filler decreased its surface energy, which modified the wettability of substrate.

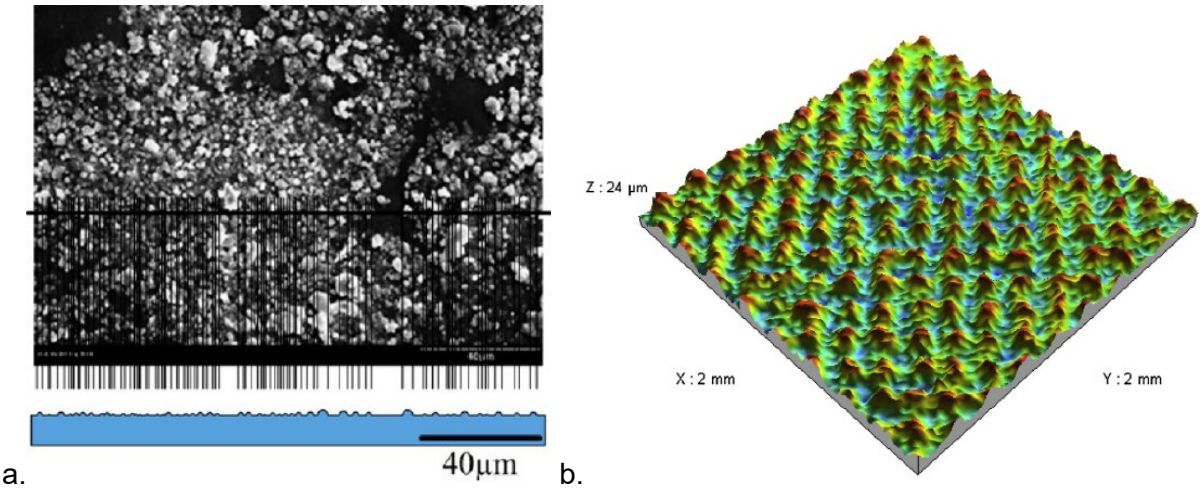
Compared to other fatty acids that are commonly used as coupling agent for surface modification, surfaces modified with stearic acid are found to possess the lowest wettability. Spathi *et al*, (2015) compared the effect of milling time, amounts, and the types of coupling agents on the hydrophobicity of treated paper sludge ash (PSA). Four types of coupling agents were tested in the experiment, which were capric acid (CH2(CH2)8COOH), myristic acid (CH3(CH2)12COOH), stearic acid (CH3(CH2)16COOH) and behenic acid (CH3(CH2)20COOH). It was concluded that the highest hydrophobicity was achieved by dry milling the PSA with 4 wt.% stearic acid for 8 hours. Similar results were found by Wang *et al.*, (2005), who used fatty acids with different chain lengths to modify the surface wettability of copper film. They observed that stearic acid achieved the best water repelling performance. In addition, Rezaei Gomari, Denoyel & Hamouda, (2006) adopted two types of 18 carbon atoms fatty acids, which are stearic acid and oleic acid, as coupling agents to change the surface wettability of mica and calcite. The results indicated that a fully saturated long chain (stearic acid) is more effective than an unsaturated long chain (oleic acid) on surface modification.

Kokkinis (2017) and Rabi'atu (2016) studied the residue hydrophobicity of hydrophobic calcium carbonate after being subjected to wetting-drying cycles. Glass slides coated with hydrophobic calcium carbonate powder were immersed in deionized water for 5 minutes and then dried in an oven at 50℃ for 5 mins. The results indicated a partial recovery of hydrophobicity after drying the samples, but the initial contact angle value was not achieved.

The water contact angle remained stable after several wetting-drying cycles. This effect was believed to be due to physical disruption of the surface roughness and the dissolution of loose packed coating that peels off during immersion.

2.8 Concrete with micro textured surfaces

Some recent studies have directed attention to potential application of micro textures on concrete structures in the light of its excellent water repelling property. Traditionally, roughness on concrete surfaces was produced through coating the surface with hydrophobic agent that mixes with mix-sized powder (Figure 2.10 a). The particles distributed across the surface form random roughness with a size range of nano to microns. For example, Muzenski, Flores-vivian & Sobolev, (2015) applied polymethyl hydrogen siloxane emulsion mixed with metakaolin micro particles on the surface of concrete. The treated surface had water contact angle of up to 123°, which was about 30% higher than references that only coated with polymethyl hydrogen siloxane. Gao *et al.*, (2018) tested asphalt concrete coated with a hydrophobic agent that was made by mixing saline emulsion with micro silica, showing improved droplets rolling behaviour and anti-icing property. Similar results were reported by She *et al.*, (2020) who found applying nano silica and n-Propyltriethoxysilane mixture on concrete gave a water contact angle of 155° compared to 128° on n-Propyltriethoxysilane coated flat surfaces, while applying nano silica alone decreased the water contact angle of concrete from 25 to 10°. They showed that droplets on this type of roughed surface were in the Wenzel state, rather than the Cassie-Baxter state. The low wettability of these particle coated surfaces arose from hydrophobic chemicals while the particles amplified the intrinsic hydrophobicity.



a. b.

Figure 2.10 Surface roughness produced through (a) applying micro particles on concrete surfaces (post-casting treatment) adapted from Flores-vivian et al., (2013) and (b) lithography (pre-treatment) adapt from Horgnies & Chen, (2014).

Another method that was used to fabricate surface textures is through pre-casting treatment such as lithography. Unlike the post-casting treatments described above, lithography is able to create surface structures of deliberately desired dimensions, as shown in Figure 2.10 b. Liu *et al.* (2017) carried out a series of experiments to transfer the micro texture of the lotus leaf to the surface of cement paste by soft lithography. Different amounts of polycarboxylate superplasticizer (0.2%, 0.4%, 0.8% and 1.5% weight of cement) were used to modify the viscosity of cement paste. They found that through visual inspection, the micro texture was successfully transferred with great fidelity when the superplasticizer dosage was 1.5 wt.%. The replicated lotus textured surface gave a water contact angle of ~140˚. At lower amounts of superplasticizer, the surface texture was uneven and ambiguous. Horgnies & Chen (2014) transferred a micro texture, which consisted of cones with a height of 30 μm and a spacing of 200 μm, onto the surface of concrete. They found PDMS residue left on the surface in the presence of silica fume. The resultant surface showed a water contact angle of 148˚ but was also sticky as water droplets were pinned on the surface. Coating the surface with siloxane-based film increased the water contact angle to 164° and made the surface slippery, with a contact angle hysteresis of 2.5°. They also found whether a surface texture can be produced through lithography relied on the material characteristic of the mold. Hydrophilic materials facilitated mixing water to move to the mould, which resulted in a weaker surface with open-pores (Malone, 1999), whereas hydrophobic materials prevented the formation of the water film which allowed a delicate micro texture to be created. The soft lithography has also been used to transfer the microstructure of sandpaper onto magnesium cement surfaces (Gao *et al.*, 2019). The cement was prepared by mixing MgO, $MgCl_2$ and water to a paste. Rheology of the paste has been found as a key factor responsible to the hydrophobicity of resultant surfaces as thick paste unable to fill in the cavities on PDMS mould leading to a defected surface. The greatest hydrophobicity was achieved on paste (w/b=0.87) embedded with structures transferred from sandpaper of 240 grits, with water contact angle up to 140°. Rolling motion of droplets was also observed on such a surface inclined at ~8° from a dropping height of ~5cm.

2.9 Summary

Surface hydrophobicity is achieved by low surface energy, roughness features, or a combination of both. Water droplets sit upon a heavily roughed surface may not enter the roughness features, with a layer of air trapped beneath it. As a result, the surface exhibited super hydrophobicity and low contact angle hysteresis due to small solid/water interface area. For concrete practice, water repellents that have low surface energy are commonly used as surface coating or admixture to decrease or inhibit the wetting capability of concrete. These

water repellents impart hydrophobicity to concrete through adsorbing on the wall of capillary pores, leading to an increase in water contact angle. However, very little attention has been devoted on exploring the use of surface roughness to introduce hydrophobicity onto the surface of concrete. Experimental investigation into the durability of cement-made surface texture and its influence on mass transport properties are lacking. This chapter highlights the need to systematically study the performance of micro textured cementitious materials and the feasibility of adopting surface structures to achieve a hydrophobic cementitious surface.

.

3 Methodology

This chapter describes materials and test methods used throughout this research. It includes information on material compositions, sample preparation, instrumentations, and detailed experimental procedures.

3.1 Sample preparation

3.1.1 Materials

The materials that were used in this study include Sylgard elastomer 184 (polydimethylsiloxane, PDMS), hydrophobic plant leaves (lotus and taro leaf), rosin meshes (25-micron), Portland cement (CEM I 52.5), silica fume (SF), sand, gravel, polycarboxylate superplasticizer (SP), calcium carbonate and stearic acid. From these materials, a range of samples with various micro textured surfaces were made. The textures were replicated from hydrophobic plant leaves or rosin meshes. Soft lithography was used in this research to produce negative templates of the original (master) textures.

Precipitated calcium carbonate and stearic acid were used to produce hydrophobic precipitate calcium carbonate (HPCC). The calcium carbonate was purchased from Fisher Scientific, with more than 99% purity and the stearic acid was purchased from Sigma-Aldrich, with more than 95% purity. Detailed description of the process to manufacture HPCC is given in Chapter 4.

The oxide compositions of the ordinary Portland cement (CEM I 52.5) and SF are presented in Table 3.1. The Portland cement was supplied by Breedon, which complied with BS EN 197 – 1. The calculated Bogue composition of the cement was 60.3% C_3S, 14.2% C_2S, 10.3% C_3A, and 7.3% C_4AF by mass. Silica fume was supplied by Elkem, which contained 98.8% SiO_2, and had a loss of ignition of 0.47%. The specific gravity of cement and SF were 3.1 and 2.9 respectively.

Table 3.1 Oxide composition and loss of ignition (LOI) for CEM I and SF.

	Oxide composition (%)								LOI (%)
	CaO	SiO_2	Al_2O_3	Fe_2O_3	MgO	Na_2O	K_2O	SO_3	
CEM I	63.4	20.8	5.4	2.4	1.5	0.3	0.7	2.7	2.1
SF	0.15	98.8	0.31	0.02	0.04	0.09	0.3		0.47

Thames valley sand was used as fine aggregate, with maximum particle size of 4.75 mm. The sand contained 23.5% particles <300 μm, 75.2% particles <1.18 mm, and 89.7% particles < 2.36 mm, which complied with BS 882 fine grading. The specific gravity at saturated and

surface dry condition (SSD) and water absorption of the sand were 2.6 and 1.7% respectively. Gravel was used as coarse aggregate that adhered to BS 882 coarse grading. The gravel contained 1.6% particles <2.36 mm, 7.2% particles < 4.75 mm, and 99.1% particles < 9.53 mm. The specific gravity at SSD and water absorption of the gravel were 2.5 and 2.2% respectively.

3.1.2 Preparation of master pattern mould

Sylgard elastomer 184 manufactured by Dow Corning was used for soft lithography. The Sylgard 184 consisted of two parts: silicone base and hardener. The two parts were mixed to produce a slurry that hardens to form a rubber-like solid mould. Two types of master pattern mould were prepared in this research. The first type was a negative structure transferred from plant leaves using soft lithography. The PDMS polymer (Sylgard 184) was cast onto the surface of the selected leaf and then cured at 60˚C for 12 hours. The leaf was then separated and removed from the solidified polymer. The polymer with negative imprint can then be used as a mould to replicate the leaf surface texture on cementitious materials. Another type of master pattern mould was prepared by immersing nylon microgrids with PDMS solution diluted with toluene at 1:1 ratio followed by oven curing at 120˚C until solidification. Note that a surface structure produced using the microgrid is not replication of an existed texture, the dimensions of structure depend on the size of mesh pore and wire diameter. Detailed description of the process to manufacture the master pattern moulds will be presented in Chapter 4. Cementitious samples with micro textured surfaces can then be prepared by casting them against the master pattern moulds.

3.1.3 Mix proportions

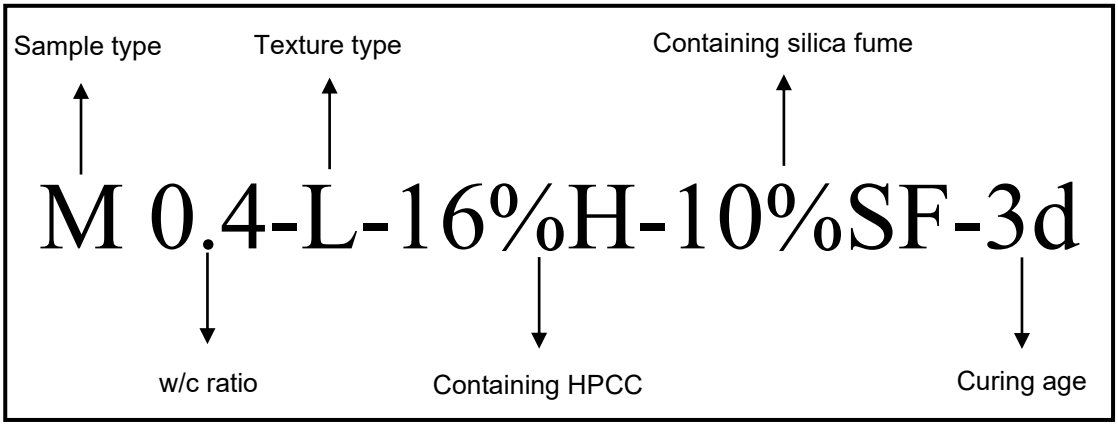
Cement paste, mortar and concrete mixes were designed based on absolute volume method, which assumes that the total volume of the sample equals the sum of volumes of its constituents (Neville, 1997). Aggregate volume ratio of 60% (pre-mixed state) was chosen, with a w/c ratio of 0.4. Since aggregate was stored in dry laboratory conditions, the batch water was adjusted to for the water absorption of the aggregate. In addition, batch water was corrected to account for the water content of the superplasticizer to ensure that the target water-to-cement (w/c) ratio was achieved. The mixes were assumed to be fully compacted and had negligible air content in the calculations. The samples prepared for this study were as follow:

1. CEM I pastes, mortars, and concrete (w/c: 0.4; curing age: 3 and 28 days; HPCC content: 0%, 4%, 8%, and 16%). For mortar and concrete, aggregate volume fraction

was 60% and sand-to-total aggregate ratio was 0.4. These were used to investigate the influence of HPCC on cement hydration and various properties of cementitious materials, including: workability, compressive strength, wettability, and mass transport properties [Chapters 4, 5].

2. CEM I pastes and mortars (w/c: 0.4; SP: 1.5%, sand volume fraction: 60%; HPCC content: 0%, 4%, 8%, and 16%; curing age: 3 days). These were used to investigate the fidelity of replicated micro texture, the feasibility of using a microgrid to produce hydrophobic textured surfaces, and the effect of the surface textures on wettability and water transport properties [Chapters 4, 5].
3. CEM I-silica fume blended mortars (w/c: 0.4; SP: 1.5%, sand volume fraction: 60%; HPCC contents: 0%, 4%, 8%, and 16%; curing age: 28 days). These were used to study the influence of PDMS coating on the wettability and water transport properties of surface textured samples (lotus, taro and microgrid) [Chapters 4, 5].
4. CEM I pastes and mortars (w/c: 0.4; SP: 1.5%; sand volume fraction: 60%; curing age: 3 days) and CEM I-silica fume blended mortar (w/b: 0.4; SP: 1.5%; sand volume fraction: 60%; curing age: 28 days). These were used to determine the durability of textured surfaces (lotus, taro and microgrid) exposed to harsh conditions [Chapter 6].
5. CEM I-silica fume blended concretes (w/b: 0.4; SP: 1.5%; aggregate volume fraction: 60%; sand to total aggregate ratio: 0.4; HPCC: 0%, 4%, 8%, and 16%; curing age: 28 days; microgrid texture) were used to demonstrate the surface texture is achievable at concrete scale [Chapters 4, 5].

The actual mix proportions will be given in the respective results chapter. Throughout the thesis, the following sample designation will be used (Figure 3.1):



Notation:

M =Mortar, P =Paste, C=Concrete

L = Lotus texture, T = Taro texture, MP =Microgrid pattern

H =HPCC, SF =Silica fume

Figure 3.1 Sample designation.

3.1.4 Sample batching, mixing and curing

Cement, aggregate, and HPCC were first batched and weighed to an accuracy of 0.1 g. Then the raw materials were dry mixed for 1 minute with mixer. Following dry mixing, the batch water was added and further mixed for another 1 minute. For micro textured samples, polycarboxylate superplasticizer was added during mixing to improve the rheological properties of the mixture so that the mixture was able to fill in the micro spaces on the PDMS mould. The mixture was compacted in two layers and vibrated on a vibrating table for 30 to 60 sec for each layer until no air bubbles escaped the surface. The compacted samples were then covered with wet hessian cloth and plastic sheeting at room temperature to prevent evaporation. The steel mould was demoulded 24 hours after casting and cured in a fog room at 20°C and 95%±5% relative humidity (RH) to the required curing age. Following curing, the samples were conditioned in an oven at 50°C, 8% RH until constant mass (assumed to be achieved when the rate of mass loss was less than 0.1% per day) for wettability and water absorption test. Soda lime was used to keep the oven free of CO_2 to prevent carbonation.

3.2 Workability, strength and hydration

3.2.1 Workability

The workability was determined using slump testing according to BS EN 12350-2. Fresh mortar or concrete were placed in a standard slump cone in three layers, each layer was rodded 25 times to compact the mix. Then, the cone was lifted carefully and the height different between the cone mould and slumped mix was measured. For paste mixes, a mini cone with a height of 75 mm and a diameter of 40 mm (top) and 90 mm (bottom) was used.

3.2.2 Compressive strength

Compressive strength of cementitious materials was measured at the age of 3 days and 28 days according to BS EN 12390-3. 100 mm mortar and concrete cubes were prepared for the strength test, while pastes were prepared as 50 mm cubes. Samples were placed at the centre of the platen on the universal testing machine and load was applied perpendicularly on the samples. Three replicate samples were prepared and measured for each mix and curing age, at a loading rate of 0.6 MPa/s.

3.2.3 Degree of hydration

The degree of hydration was determined to help reveal the influence of HPCC on the cement hydration process. The degree of hydration was estimated by measuring the amount of non-evaporable water in hydration products. Samples at age of 3 days and 28 days were dried at 105°C and subsequently heated to 1050°C for 3 hrs. The amount of non-evaporable water was taken as the mass loss between 105°C and 1050°C, corrected for the loss of ignition of cement and the decomposition of calcium carbonate. The degree of hydration was then determined as the ratio of the mass of non-evaporable water per gram of cement over that at complete hydration, 0.24 g/g (Berthier, 2013). Results were averaged from three replicate samples.

3.2.4 Isothermal calorimetry

Isothermal calorimetry analysis was used to measure the influence of HPCC on the rate of hydration of cement at early ages. The test was carried out on 3 g paste samples at w/c of 0.4 using a TAM air calorimeter at room temperature. The dry components were hand mixed for 1 minute before the addition of water. The paste was then mixed for another 2 minutes to achieve a homogeneous material and poured into test ampoules. There was an initial rapid change in recorded heat rate after lowering the ampoules into sample cells while the thermal equilibration was established. Data collection was therefore started 45 minutes after lowering the ampoules as from then the signal was considered correct. The measurement continued for 96 hours, and the results were normalized based on the mass of cement.

3.3 Mass transport properties

3.3.1 Water absorption

Sorptivity characterises one dimensional water uptake into a porous material by capillary suction, which is an important transport property for cementitious materials (Hall, 1989). Sorptivity was measured by sealing the side surfaces and leaving the bottom and top surface unsealed. For textured samples, the inflow surface would be the surface embedded with micro texture. The samples were put in water just reaching the bottom and supported by two plastic rods to ensure that the inflow surfaces were fully exposed to water (Figure 3.3). Sorptivity was obtained from the slope of the best-fit line of the cumulative absorption against the square root of elapsed time plot (Hall, 1989). This takes the form of

$$i = S\sqrt{t} + A_s \qquad \text{(eqn. 3.1)}$$

in which S denotes sorptivity (mm/min$^{0.5}$); i denotes cumulative absorption (mm); t denotes

elapsed time (min); and A_s denotes the y-intercept (mm) which relates to surface open porosity. McCarter & Watson (1997) interpreted A_s as the rate of water filling open pores, a larger A_s indicated a rapid filling and thus a higher open porosity. Each sorptivity value was determined using data obtained within the first hour of absorption (at least 5 data points). Samples were gently tamped surface dry with a cotton cloth to avoid damaging the micro texture, before each mass measurement. At the end of the water absorption test, samples were re-dried to constant weight in an oven at 50°C in preparation for the next cycle of wetting and sorptivity testing.

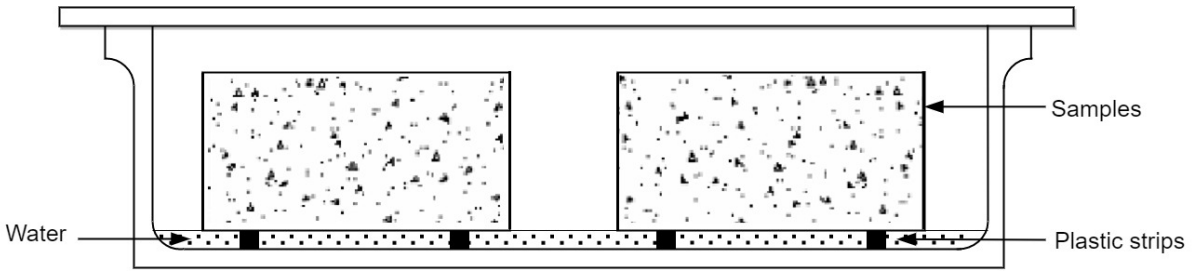


Figure 3.2 Experimental arrangement for water absorption. Adapted from Wong (2006).

3.3.2 Water vapour absorption

In an environment of high humidity, water vapor ingress is the dominant mechanism of water transport. Water absorption is also involved but this is more subtle in comparison with vapor ingress. The ability of a sample to resist moisture sorption was evaluated by comparing the rate of weight gain through one-dimensional water vapor absorption when exposed to high humidity.

The samples were cut into 25 mm by 25 mm small squares with a thickness of 10 mm using a diamond bladed saw and then dried in an oven at 50°C until constant mass. For micro textured samples, the surface areas on which embedded with the micro textures were extracted since only the influence of surface textures on moisture resistance is of interest. Waterproof tape was used to seal the sides and bottom of the samples to ensure that the moisture can only enter the samples through the textured surface. The samples were then exposed to 98% RH at 25°C over 5 months. Weight gain of each sample was measured every day for the first two weeks and every 7 days thereafter. The effect of HPCC and surface textures on water vapor absorption was determined based on the rate of mass gain and the cumulative mass gain at the end of experiments.

3.3.3 Oxygen diffusivity

For corrosion of reinforcement embedded in concrete, oxygen must be available at the reaction sites where water is reduced by oxygen to produce hydroxyl ions (Mindess, 2019).

Therefore, the rate of corrosion is closely related to the availability of oxygen and capacity of cementitious materials to transmit oxygen. Diffusion of gas through a cementitious sample is mainly governed by ordinary diffusion and Knudsen diffusion. The Fick's law ($J = -D\frac{\partial C}{\partial x}$) can serve as a good approximation to describe the flux *J* as a function of effective diffusivity *D* and concentration gradient.

Oxygen diffusivity was determined by measuring the flow of oxygen gas through a sample subjected to an oxygen concentration gradient. Cylindrical samples of 100 mm in diameter and 50 mm thick were prepared for the testing. Figure 3.4 shows the illustration of the device used for measuring the diffusivity. The sample was placed in a ring test cell, in which gasses diffused through. One side of the sample was exposed to oxygen while the opposite side was exposed to nitrogen at the same pressure so that the movement of gas was driven by random molecular motion. Prior to the test, the oxygen concentration in nitrogen stream was measured. To ensure leakage does not occur through the edge, the sample was placed inside a rubber ring and sealed by applying a 1.5 tonne compression onto the rubber ring. The oxygen concentration in the outflow gas was monitored and measured at steady state with a zirconia oxygen analyser. Then, the oxygen diffusivity can be determined based on the following equation given by Lawrence (1984):

$$D = \frac{Q \times t_h}{A \times (C_2 - C_1)} \qquad \text{(eqn. 3.2)}$$

Where: Q is oxygen diffusion rate at a pressure of 1 bar (m^3/s)

$$Q = \frac{R_1}{60 \times 10^6} \times (G_1 - G_0) \times \frac{P_1^* - \Delta P}{100} \qquad \text{(eqn. 3.3)}$$

t_h is the thickness of the sample (m)

A is the cross-section area of the sample (m^2)

R_1 is flow rate of nitrogen stream (mL/min)

R_2 is flow rate of oxygen stream (mL/min)

G_1 is percentage of oxygen in outflow stream

G_0 is percentage of oxygen in initial nitrogen stream

P_1^* is pressure of oxygen stream (bar)

ΔP is pressure difference between oxygen and nitrogen stream (bar)

C_2 is concentration of oxygen in the oxygen stream at 1 bar (m^3/m^3) in steady state

$$C_2 = \left[100 - \left(\frac{R_1}{R_2} \times \frac{(G_1 - G_0)}{2} \times \frac{\sqrt{32}}{\sqrt{28}}\right)\right] \frac{P_1^*}{100} \qquad \text{(eqn. 3.4)}$$

C_1 is mean concentration of oxygen in the nitrogen stream at 1 bar (m^3/m^3) in the stable state

$$C_1 = \frac{(G_1 + G_0)}{2} \times \frac{(P_1^* - \Delta P)}{100} \qquad \text{(eqn. 3.5)}$$

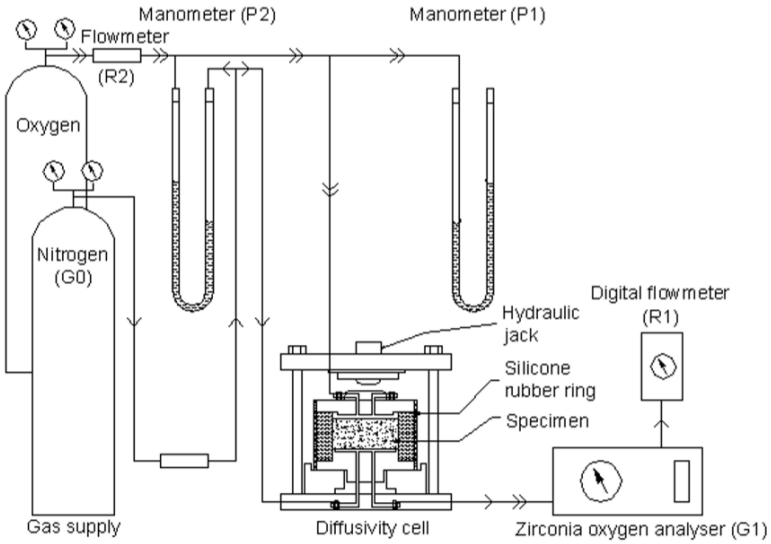


Figure 3.3 Schematic diagram of the diffusion test set up adapted from Wong (2006).

3.3.4 Oxygen permeability

Unlike gas diffusion that is entirely driven by concentration gradient, gas permeation occurs when a pressure difference exists across a sample. Although gas permeation is not of major relevance to most degradation mechanisms of concrete, it has been commonly used as a performance indicator of concrete quality. Gas permeability is a measure of the ability of a sample to pass gas under pressure difference. Normally, a highly porous sample is considered to have a high permeability coefficient. According to Darcy's law, flux through a sample is proportional to the pressure gradient and permeability coefficient:

$$q = -\frac{k}{\mu} \nabla P \qquad \text{(eqn. 3.6)}$$

Where: q is the flux (m/s)

k is the permeability coefficient (m^2)

μ is the viscosity of fluid (Pa*s)

∇P is the pressure gradient (Pa/m)

However, this expression is only strictly applicable to saturated incompressible flow, such as water. In order to yield a representative value of permeability coefficient for gas, Carman (1956) extended the original Darcy's law to compressible fluids with provisions that the mass flux (ρ*q) in the sample is a constant in steady state and the gas in the sample can be considered as an "ideal gas". By multiplying both sides of the Darcy's equation by density ρ and substituting ρ with pressure P and integrating both sides:

$$q = \frac{k}{2\mu t_h}\frac{(P_1^2 - P_2^2)}{P_2} \qquad \text{(eqn. 3.7)}$$

Where: t_h is the thickness of sample (m)

P_1 and P_2 are pressures on the inflow and outflow faces respectively (Pa)

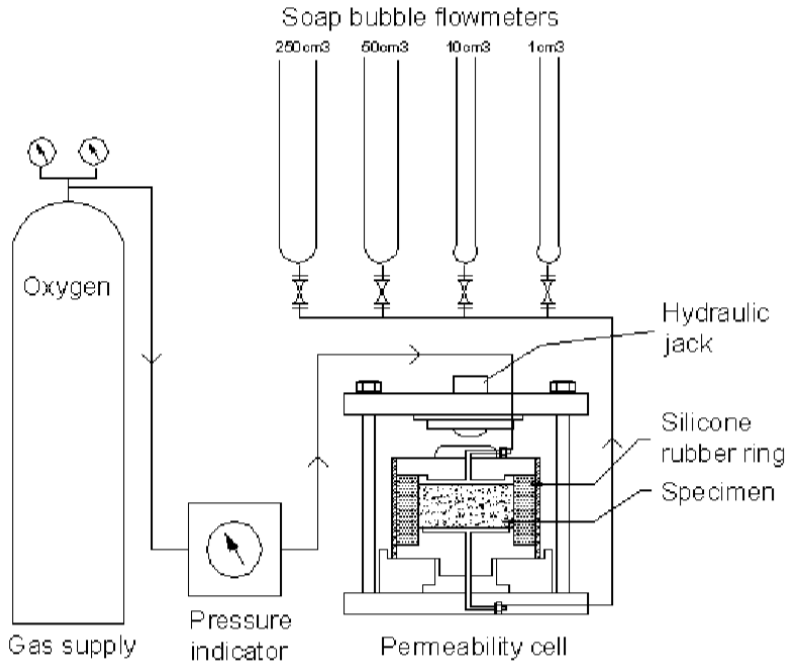


Figure 3.4 Schematic diagram of the permeability test set up adapted from Wong (2006).

Figure 3.4 shows the experimental set up. The cylindrical sample was placed in a ring test cell and the curved surface was sealed by compressing the elastic rubber ring using a hydraulic jack at 1.5 kN to prevent leakage. The top of the sample was exposed to pressurised oxygen so that flow occurred through the sample under a pressure gradient, instead of by diffusion. The outflow flux at steady state was determined by calculating the velocity of a soap bubble passing through a glass tube of a given volume. At least four readings were recorded for each test and a max to min ratio of less than 1.02 was deemed to reach steady state.

However, the permeability coefficient obtained from Darcy's law will be overestimated due to slippage of gas molecules at pore walls, especially at low gas pressures. The effect of gas slippage is significant in micropores with sizes that are of similar magnitude to the mean free path of gas molecules, where Knudsen diffusion is the dominant mechanism. Gas flow through pores governed by Knudsen diffusion will lead to a large error in the calculated permeability coefficient using Darcy's equation, which was derived for slow viscous flow e.g. water. For compressible fluids such as gasses, the calculated permeability coefficient will vary depending on the applied pressure gradient.

Klinkenberg (1941) proposed a simple correction method by modifying the Poiseuille's equation using slip boundary conditions given by Kundt & Warburg (1875) and thereby introduced the concept of intrinsic permeability. The intrinsic permeability depends only on the characteristics of the sample and is independent of the applied pressure. The expression for intrinsic permeability coefficient given by Klinkenberg (1941) is:

$$k_m = k_{int}\left(1 + \frac{b}{P_m}\right) \qquad \text{(eqn. 3.8)}$$

Where: P_m is the average pressure at inflow and outflow faces ($P_m = \frac{P+P_2}{2}$).

k_m is the measured permeability coefficient at a given pressure P.

k_{int} is the intrinsic permeability coefficient.

b is a constant related to the gas and the temperature.

From this expression, the physical meaning of k_{int} is the permeability coefficient at infinite pressure. In this case, the gas behaves like a liquid with a very small mean free path to pore size ratio, where the gas transport is entirely governed by viscous flow. It should be noted that due to the sensitivity of cement-based materials to water, the intrinsic permeability that is based on Klinkenberg correction and water permeability is not always in good agreement. However, liquid permeability determined using nonpolar liquids, such as ethanol, has been reported to have a close agreement with gas intrinsic permeability (Hall & Hoff, 2012a).

In this study, three gas pressures of 0.5, 1.5 and 2.5 bars above atmospheric pressure were used, and their corresponding measured permeability coefficients were plotted against the inverse of mean pressure. An example of this can be seen in Figure 3.5. The intrinsic permeability coefficient was then obtained from the y-axis intercept of the best-fit line.

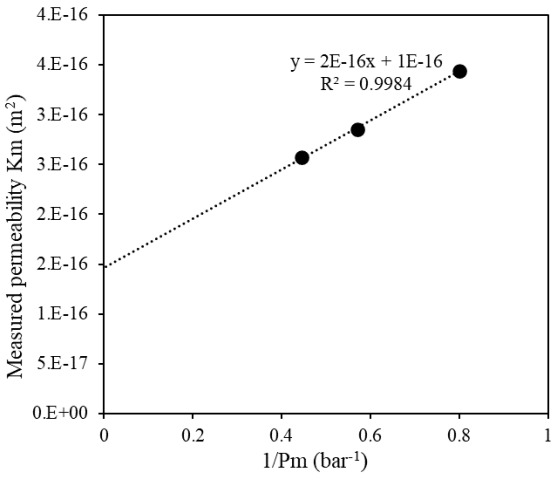


Figure 3.5 An example of applying Klinkenberg correction for gas slippage to determine the intrinsic permeability coefficient.

3.4 Surface properties

3.4.1 PDMS residue

A potential factor that may influence the measured properties of the hydrophobic cementitious materials developed in this study is the presence of residual PDMS due to the use of PDMS mould to create micro textures. Since PDMS is an inert material and insoluble in water, the presence of residual PDMS may influence the hydraulic properties and surface wettability of the samples. For this reason, it is crucial to determine if there is any PDMS remaining on the surface of sample after demolding.

A Nicolet Fourier-transform infrared spectroscopy (FTIR) was used to identify specific chemical bonds that would imply the existence of trace PDMS on the surface of cementitious samples. The FTIR was equipped with built-in Attenuated Total Reflection (ATR) crystal and had spectral range between 15-27000 cm^{-1}. The ATR uses the property of internal reflection resulting in an evanescent wave which is very suitable for examining surface composition since it only interacts with substances very close to the tested surface.

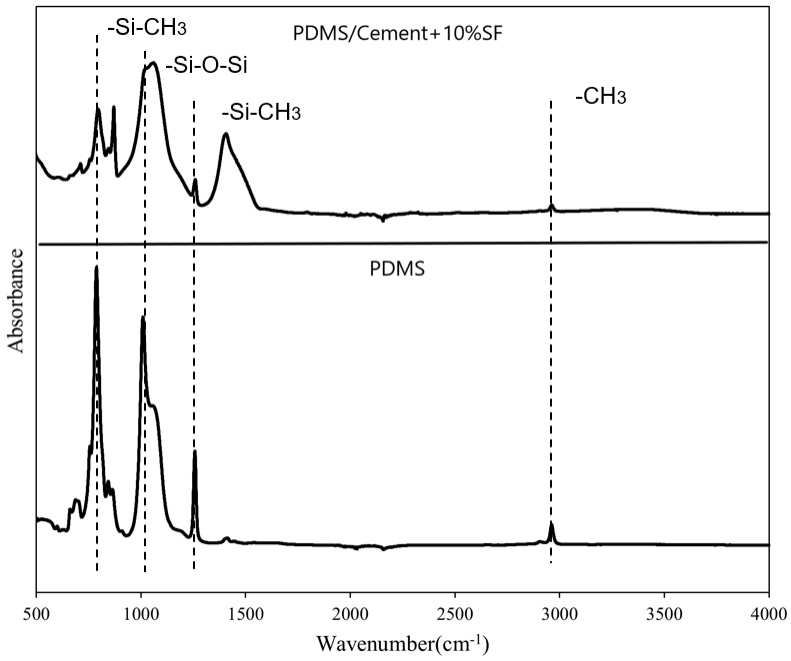


Figure 3.6 An example of FTIR spectrum showing PDMS grafted on paste containing 10%SF.

Cement pastes were made for this experiment because the sample had to be small and held in place by a clamp to maintain good contact with the ATR crystal during scanning. The samples were made by casting a thin layer of cement paste on a PDMS mould. As the cement paste was very brittle, it cracked when pressure was applied, producing smaller fragments that can thus be pressed against the ATR crystal to achieve good evanescent wave and sample interaction. An example FTIR spectrum of PDMS left on the surface of a paste sample is shown in Figure 3.6. To reduce random noise, each sample was scanned for 32 times to yield a final spectrum.

3.4.2 Static water contact angle

The wettability of samples was quantified by using a drop shape analyzer (Krüss DSA-100), which equipped with a high speed camera shoot at 2300 frames per second. The sample was exposed to a uniform LED illumination and a deionized water drop was placed on its surface using software-controlled single-dosing unit. The projection of the drop was captured by a camera placed on the opposite side of the LED and the static water contact angle was then measured automatically using Laplace-Young fitting (Figure 3.7). In most case, the software can precisely distinguish the liquid phase from substrate. But for reproduced leaf surfaces, the solid-liquid interface sometimes cannot be identified due to local roughness. Therefore, a manual baseline was used in this situation by fitting points manually picked along the solid-

liquid interface. The size of the droplet used for static contact angle measurement was less than the capillary length of water.

$$L_c = \sqrt{\frac{\gamma_w}{\rho_w g}} \qquad \text{(eqn. 3.9)}$$

In which γ_w represents the surface tension of water, ρ_w represents the density of water and g represents gravitational acceleration. For ambient temperature of 20°C, the capillary length of water is 2.71 mm, which corresponds to a volume of 10.4 µl. The influence of gravity on the shape of a water droplet can be neglected if its diameter is less than the capillary length (Berthier, 2013). Therefore, the volume of 4 µl was selected for static contact angle measurements. Sample surfaces were cleaned using dust remover before measurement. Average of repeated measurements with low standard deviation was used as representative. To determine the minimum number of repeats required, 5, 10, 15, 20, 25 measurements were tested on a lotus textured surface, with average contact angle of 123.8° (11.4), 119.2° (10.8), 120.1° (9.3), 119.5° (8.6), and 120.4° (8.2), respectively (standard deviation given in brackets). This indicates that fifteen measurements were satisfactory and therefore, the average of fifteen measurements at random places was taken for each reported contact angle in this research.



Figure 3.7 Left: Photograph shows a water droplet sitting on a lotus textured surface (P-L-0%H-0%SF). Right: The droplet was analysed using Laplace-Young fitting to obtain the contact angle.

3.4.3 Contact angle hysteresis

Contact angle hysteresis, which is an important parameter characterizing adhesion and wetting of surface, is defined as the difference between advancing angle and receding angle. These are the contact angles at the leading edge and trailing edge respectively, just before a

droplet starts to roll off a surface when tilted. Measuring the tilting angle when a drop starts to roll off is also a key factor since it corresponds self-cleaning ability. A water droplet was gently placed on the surface of the sample, which was fixed to the tilt table of the drop shape analyzer. Both advancing and receding angles were measured by the analyzer and the angle of the tilt table was recorded when the water droplet started to roll off.

Apart from contact angle hysteresis, droplets were released from certain heights onto textured surfaces inclined at different angles to see under what conditions the lotus effect (rolling and bouncing motion of droplet) can take place on a textured surface. The surface was inclined at 2° intervals from 0° to 30° and the drop height was increased at 2 cm intervals from 0 cm to 30 cm. Note here that several mechanisms of water travelling on the surface are involved such as rolling, bouncing, sliding, and pinning. However, it is relatively easy to distinguish rolling and bouncing behaviour from sliding and pinning as the latter would leave water traces on the surface.

3.5 Scanning electron microscopy

3.5.1 Observations of surface textures

A Hitachi TM4000 plus scanning electron microscope was used to observe the surface textures. It is equipped with a high sensitivity 4-segments backscattered electron (BSE) detector and a low vacuum secondary electron (SE) detector with magnifying power of up to 10,000x, which is high enough to observe the delicate surface roughness embedded on the surface of cementitious samples. Secondary electron observation mode at low accelerating voltage of 5 kV was used to observe the topography of surface texture.

A horizontal profile of surface textures can be obtained from 3D reconstruction using the Hitachi 3D map software. The 3D morphology was reconstructed from 4 images taken in different directions by the BSE detector. The ring four-quadrant detector surrounds electron beam path, each part of detector can receive backscattered electrons from different directions. Four detectors were located in two orthogonal directions. A pair of opposite detectors was used to assess the slope in that direction to distinguish shadow regions from pores. Pores would appear the same in all directions while shadow regions would appear lighter in colour when the slope is inclined towards the detector. The local slope was assessed by the intensity of reflected electrons from the surface. Once the slope is determined in both directions, the topography map can be automatically generated by software. Therefore, the dimension of surface textures can be measured directly on the topography map.

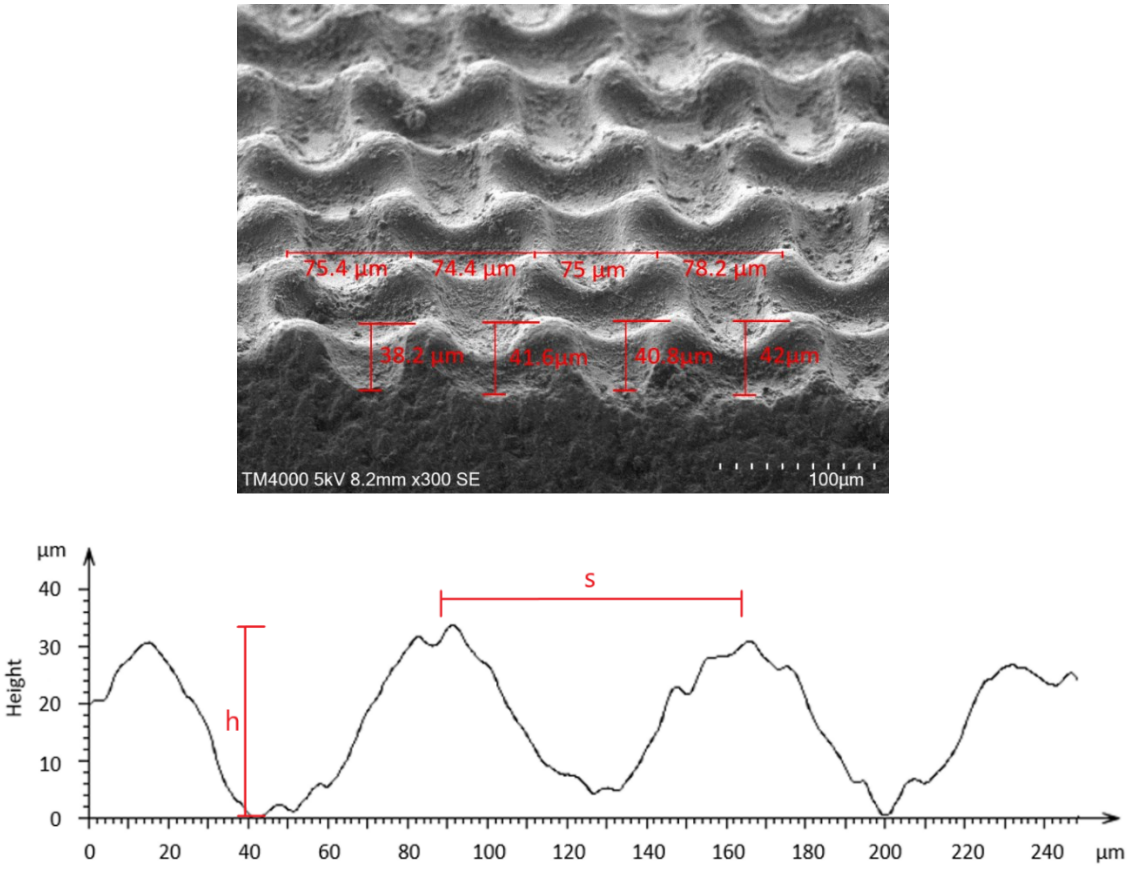


Figure 3.8 Top: SEM image of a cement paste sample cast against a PDMS coated nylon microgrid; Bottom: Cross section profile of fabricated texture reconstructed by 3D map software.

Figure 3.8 shows an example of the cross-section profile of microgrid pattern reconstructed using 3D map software. Note that the profile cannot provide the exact details of surface structure, but it is useful for determining the dimensions of large-scale texture. For example, it can be seen in Figure 3.7 that the peak-to-peak distance of micro textures, s, given by reconstructed profile is ~ 78 µm, which is consistent with that directly measured from the SEM image. The height of micro textures, h, given by the software seems to constantly slightly lower than the height measured from images. However, the height determined from images is over estimated due to projection angle. It can be said that topography reconstruction provides an effective and simple method to capture the main features of a micro texture.

3.5.2 Sample preparation for BSE imaging

Samples for BSE imaging were encased and impregnated with epoxy resin to preserve the microstructure and to facilitate the discrimination of pores, hydration products and unreacted phases. For encasing, the sample observation surface was adhered to the bottom of a rubber

mold which was then filled with epoxy resin, thereby sealing all surfaces except for the observation plane in epoxy resin. After hardening, the remaining adhesive on the observation plane was removed using a 220-grit SiC paper and then polished using a 1200-grit SiC paper. Epoxy impregnation was then undertaken in vacuum to expel air originally present in pores which may hinder the penetration of the resin. After vacuuming of 4 hours, a low viscosity epoxy resin mixture of 44: 6: 3 epoxy: hardener: toluene was pumped into the vacuum chamber, covering the sample surface (Wong & Buenfeld, 2006). The impregnated samples were then placed in a pressure chamber at an air pressure of 2.5 bar for 24 hours. Excess epoxy on the observation surfaces was removed by dry grinding at successively finer grit size down to 1200. Finally, the surfaces were polished using diamond abrasives of size 6, 3, 1, and 0.25 μm. Periodic checks were made to ensure that the well-prepared sample is scratch free when viewed at 500 times magnification.

3.5.3 BSE imaging

BSE imaging was used to characterize the microstructure of cementitious materials. Based on the stereology (Russ & Dehoff, 1999), the volume fraction of a phase is equal to the area fraction in a 2D random section measured through image analysis. Therefore, quantitative measurement on 2D images can be related to the actual 3D structure.

The area of hydration product, anhydrous cement, and pore can be easily segmented using BSE imaging mode on the basis of average atomic number contrast and appropriate thresholding (Wong, 2006). For mortar and concrete samples, the aggregates were segmented manually since it is relatively easy to determine the position of cement matrix-to-aggregate boundary. Pores filled with epoxy resin appear very dark in BSE images, which enables them to be distinguished from other phases. To segment resin filled pores, a pore binary mask was created according to the overflow pore segmentation method (Wong, Head & Buenfeld, 2006). Here, the upper threshold for pores was defined as the inflection point of the cumulative brightness histogram (Figure 3.9 a, b). Anhydrous cement is usually the brightest phase due to its high average atomic number. In a typical brightness histogram of the BSE image of hardened cementitious material, the anhydrous cement gives a distinct peak at the region of high brightness, which makes it easy to be distinguished from other phases. Therefore, anhydrous cement can be segmented by selecting the minima gray value between the peaks representing the hydration products and the anhydrous cement as the lower threshold (Figure 3.9 c, d).

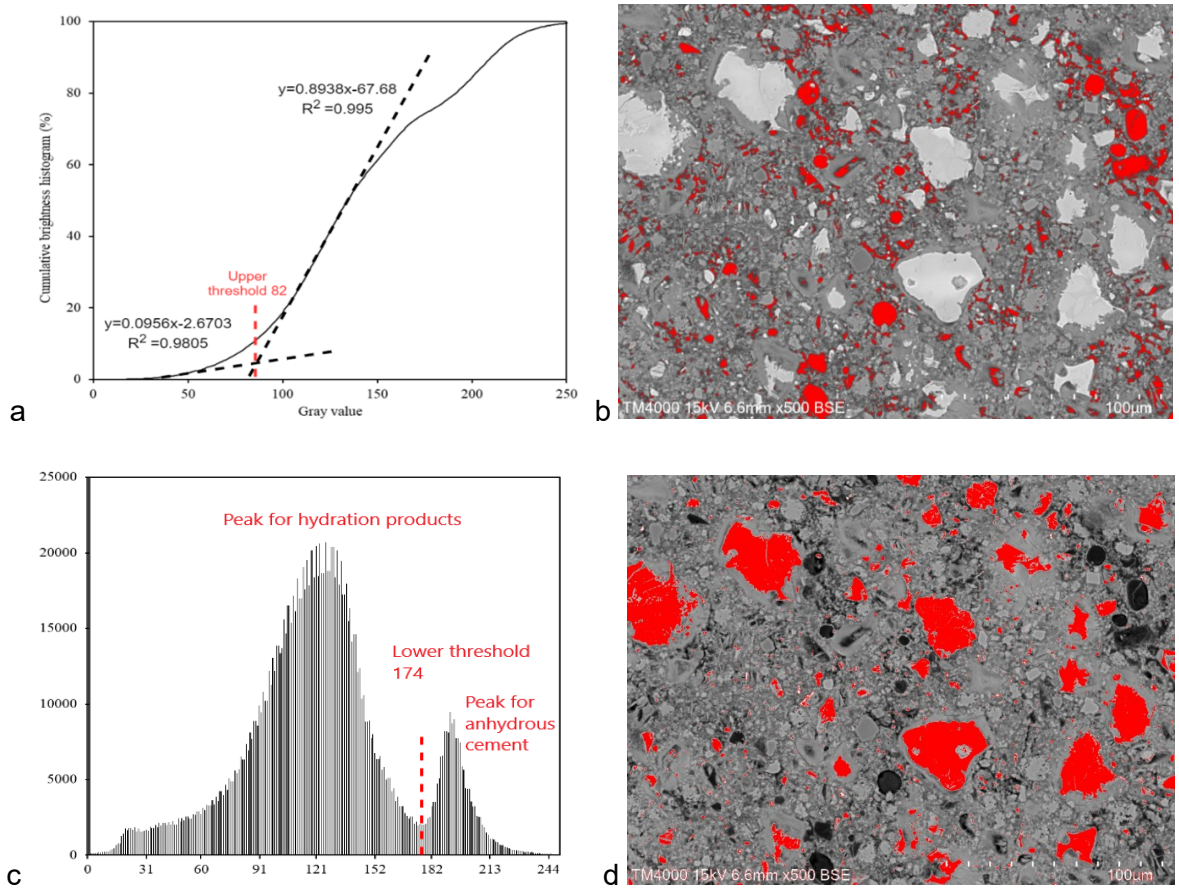


Figure 3.9 (a) Cumulative brightness histogram versus grey value. The red dash line indicates inflection point determined by overflow method. (b) Segmented pores. (c) Brightness histogram for cement paste showing a distinct peak for anhydrous cement. (d) Segmented anhydrous cement.

3.6 Durability of micro textures

3.6.1 Abrasion resistance

Abrasion resistance is of vital importance to the durability of micro textured surfaces. In general, hardened cement pastes tend to have good resistance to moderate abrasion. One of the factors governing abrasion resistance is surface finish. For example, a smooth surface provides a uniform-force bearing surface (Mindess, 2019). Therefore, repeated friction may cause a roughened surface to deteriorate faster than a smooth one.

Figure 3.10 shows the apparatus used for abrasion resistance measurement of micro textured surfaces. A string was tied around the middle of sample (50 mm cube) and this was used to pull the sample back and forth in a horizontal movement. The sample, with textured surface downward, was placed on a 1200-grit SiC paper and the surface was subjected to abrasion

due to the gravitational force acting on it. To minimize the influence of pressure variation on the determination of abrasion resistance, the mass of the samples was controlled such that they differed by no more than 5 g. The mass of the samples ranged from 179.26 g to 183.79 g, therefore, the pressure exerted on the bottom surface was about 720 Pa.

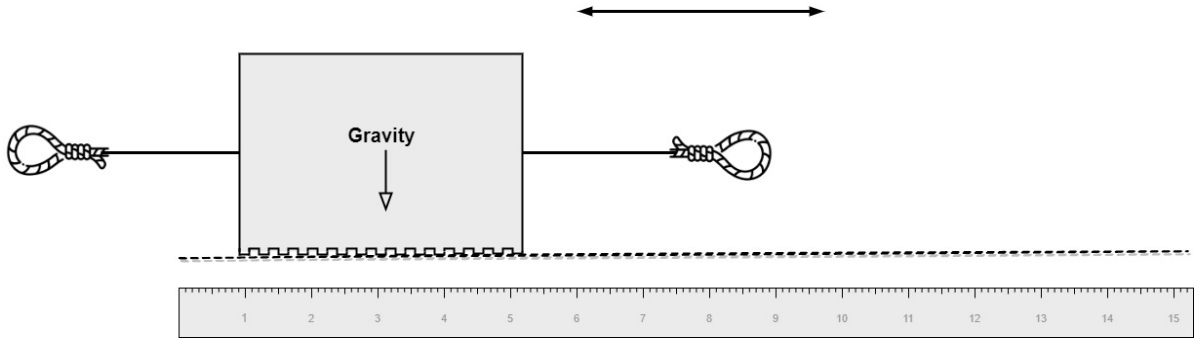


Figure 3.10 Schematic diagram of test arrangement for determining abrasion resistance.

The hydrophobicity of micro textured surfaces subjected to abrasion was determined by measuring water contact angles. The water contact angles were measured before and after every cycle of pulling (a cycle is once back and forth on the SiC paper, with pulling distance of 20 cm) until the measured contact angle approached that of the control sample. Compressed air was used to remove debris produced during the abrasion experiment on the SiC paper and cementitious samples before every contact angle measurement. This test was performed on three replicate samples.

3.6.2 Exposure to humid environment

Micro-textured cementitious samples were cast as 25 mm * 25 mm square with a thickness of 10 mm. Three replicates were prepared for each type of samples. The initial topography of the textured surfaces was observed using SEM to provide a benchmark for comparison. Then, the samples were stored in an environmental chamber at room temperature and 98% RH. Each type of textured samples was divided into two groups for two different exposure periods, one month and three months. After exposure, the changes in surface topography and microstructure was examined with the SEM. In addition, the wettability of the evolved surface textures was assessed by measuring changes in the water contact angle.

3.6.3 Carbonation

Micro textured and non-textured mortars with various amount of HPCC (three replicates) were prepared as standard 50 mm cubes and conditioned in an environmental chamber at room

temperature and 60% relative humidity. Soda lime was used to prevent carbonation during conditioning. The PDMS moulds were removed before placing the samples into the incubator to avoid other types of deterioration. Following conditioning, the samples were placed in a carbonation chamber at 3% CO_2 and 68% RH for 1 month. This exposure condition would be adequate to carbonate the entire surface since the results of Zhang (2022) showed that the surface of cementitious materials can be fully carbonated within several days of accelerated carbonation (4% CO_2; 65%RH).

The carbonated samples were then sectioned in half and sprayed with phenolphthalein solution to determine the carbonation depth. SEM was used to observe the change in surface topography and Raman spectroscopy was used to determine the chemical composition of carbonated cementitious surface, to detect the presence of calcium carbonate. Water contact angle was tested before and after carbonation to evaluate the influence of carbonation on wettability.

After spraying with the phenolphthalein indicator, three identifiable regions can normally be visually defined across the surface. These are a completely carbonated layer below the exposed surface, a transitional / partially carbonated region that shows gradual increase in purplish-pink colour intensity with increasing depth, and an uncarbonated core. The passage of CO_2 into the bulk of cement paste is controlled by diffusion, in which the diffusing CO_2 molecules are gradually immobilized as they react with cement matrix. Therefore, there is a sharp reaction front at which the concentration of CO_2 is zero. In this work, the carbonation depth is defined as the distance between the exposed surface and the sharp reaction front. For each type of sample, fifteen measurements were made at random locations using a digital calliper and the average was taken.

3.7 Summary

The experimental method and material compositions are presented in this chapter. Different types of samples and the process of sample preparation are given. The actual mix proportion will be given at the experimental section of each subsequent results chapter. The methods to produce hydrophobic powder and micro textures on the surface of cementitious materials will also be described in the next chapter. The performance of hydrophobic cementitious materials is evaluated via static contact angle measurement and contact angle hysteresis. Wetting behaviour of droplets on such a surface is determined via releasing water droplets on the surface inclined at different angles and from different heights. Mass transport tests and image analysis of microstructure are based on well-established methods. It is noted that moisture content of samples strongly affects mass transport properties. Therefore, the samples must

be properly conditioned to a standard moisture state before testing to allow meaningful comparison between samples. The durability of cementitious micro textures can be determined from the change in surface morphology and wettability after exposure to harsh conditions including abrasion, high CO_2 level (3% CO_2), and long-term exposure to humid environment.

4 Development of hydrophobic cement-based materials

Hydrophobic cementitious surfaces are achievable by lowering the surface energy and introducing surface roughness. In this chapter, novel routes to achieve this were explored. A hydrophobic powder was produced by dry milling calcium carbonate and stearic acid, and the feasibility of using it as a hydrophobic concrete additive was evaluated. The powder was essentially inert in cement matrix as it had no influence on cement hydration. Compressive strength and microstructure of mortar and concrete remained largely unaffected by HPCC content of up to 16 wt.%. However, flat cementitious samples containing 16 wt.% HPCC achieved a water contact angle of only 53°, which is insignificant. Therefore, methods for surface roughness fabrication were investigated. Micro textures transferred from hydrophobic plant leaves (lotus and taro) using lithography showed high fidelity with the originals. Surfaces constructed to mimic natural hydrophobic surfaces using nylon microgrids exhibited a water contact angle of 112°, which was similar to that of lotus textured surfaces. The wettability of micro textured cementitious surfaces decreased further when the surfaces were PDMS coated. However, none of the micro textured cementitious surfaces exhibited self-cleaning behaviour as droplets pinned at where they were placed. Exploration of the motion of droplets on the hydrophobic cementitious surfaces was also reported. Droplets were released from a height to the surface inclined at different angles. The results showed that at certain combinations of inclined angle and drop height, rolling action was observed as the inertia of falling droplets overcame the adhesion between the droplets and the surface, while higher drop heights caused the droplets to penetrate the micro textures and wet the surface.

4.1 Introduction

The ease of water penetration into cementitious materials is directly linked to the long-term durability of structures. Water and water-borne ions may attack concrete and cause degradation both physically and chemically. Therefore, the wettability and mass transport property of the concrete cover is of considerable importance to the durability of reinforced concrete. Recent developments in the area of water-resisting cementitious materials include incorporating hydrophobic agents for surface modification. One of the most commonly used approach is integral waterproofing, that is by using hydrophobic agents as partial replacement of the cement or as an addition. The hydrophobic agents are expected to uniformly distribute over the bulk of the concrete, as well as surfaces, and therefore altering the properties of the surface.

Other methods to achieve water resistance is by surface treatment, for example by brushing or spraying hydrophobic or pore blocking agents onto the surface of cementitious materials (Moon, Shin & Choi, 2007; Dai *et al.*, 2010; Medeiros & Helene, 2008; Al-kheetan, Rahman & Chamberlain, 2019). Some recent studies have also suggested the potential application of micro textures on concrete structures, in the light of the excellent water repelling property that can be achieved with certain textures (Facio & Mosquera, 2013; Lu *et al.*, 2019; Subbiah *et al.*, 2018; Liu *et al.*, 2017; Horgnies & Chen, 2014). The approach to achieve micro textured surfaces can be grouped into two categories: post-treatment and pre-treatment.

Post-treatment involves coating the surface with a hydrophobic agent that contains a mix-sized powder. The powder itself is not hydrophobic but forms random roughness in the size of nano to micrometres, which amplifies the intrinsic hydrophobicity of the coating (section 2.1.3). For example, asphalt concrete coated with a mixture of saline emulsion and micro silica brought about anti-icing property and super hydrophobicity, with water contact angle of 150.7° (Gao *et al.*, 2018). Spray-coating of concrete with polymethyl hydrogen siloxane emulsion mixed with metakaolin micro particles resulted in a surface texture that gave water contact angles up to 123°, while a flat polymethyl hydrogen siloxane coating showed a contact angle of 88° (Muzenski, Flores-vivian & Sobolev, 2015).

Another technique for the fabrication of textured cementitious materials is lithography. Unlike post-treatments, the roughness is created by casting wet concrete against a mould or template on which is embedded with a negative texture (Xia & Whitesides, 1998; Geissler, 2011; Zhao, Xia & Whitesides, 1997; Hu *et al.*, 1999). Such a method has been used to transfer lotus and sandpaper structures onto cementitious surfaces. Water droplets sat on these surfaces were reported to be in the Cassie-Baxter state, with water contact angles higher than 120°. Surface textures consisted of conical shape have also been created on concrete using lithography. Surface coating of the textured surface with siloxane resulted in a water contact angle up to 160° and a low water tilted angle. To the best of our knowledge, there are only three research studies available in the public domain on the formation of micro textures on cementitious materials. These studies have reported the effect of micro textures on water contact angle, but not on other properties. Therefore, a thorough study on micro textured cementitious surfaces is still very much needed.

In this chapter, a new type of hydrophobic powder (HPCC) made by dry milling calcium carbonate and stearic acid is evaluated. This type of hydrophobic addition has several advantages such as low-cost, low-toxicity, and ease of manufacture. Lotus and taro leaf structures are transferred onto cementitious surface using lithography. A novel approach to

fabricate surface structures that mimic hydrophobic plant leaves (lotus and taro) by using microgrids is presented. In addition, the micro textured surfaces are modified by coating with low-energy polymer through a one-step process (to create a rough and low-energy surface). The overall aim of this chapter is to study the feasibility of these hydrophobic treatments systematically, and to examine their effect on surface wettability including water contact angle, contact angle hysteresis, and rolling behaviour of water droplets.

4.2 Experimental

Cementitious samples with a w/c ratio of 0.4 were prepared according to the mix proportion shown in Table 4.1. Total aggregate volume for mortar and concrete was set at 60%. Properties of materials were given in Section 3.1.1 and the procedures for mixing and curing were presented in Section 3.1.4. The main variables in mix design were HPCC content, the type of surface textures and surface coating. This research was mainly carried out at paste and mortar scale as we are more interested in surface properties. Among the three types of surface texture, only microgrid patterned concretes were prepared to determine the feasibility of creating micro textures at concrete scale.

Table 4.1 Summary of mix proportions.

	Cement (kg/m^3)	Silica fume (kg/m^3)	Water (kg/m^3)	HPCC		Plasticizer (kg/m^3)	Sand (kg/m^3)	Coarse aggregate (kg/m^3)	Curing (days)
				%	kg/m^3				
Non-textured									
P-Non-0%H	1383.9	-	553.6	0	-				3 and 28
P-Non-4%H	1351.7	-	540.7	4	54.1				3 and 28
P-Non-8%H	1320.9	-	528.4	8	105.7				3 and 28
P-Non-16%H	1263.4	-	505.3	16	202.1				3 and 28
M-Non-0%H	532.9	-	213.2	0			1598.8		3 and 28
M-Non-4%H	528.1	-	211.2	4	21.1		1584.2		3 and 28
M-Non-8%H	523.3	-	209.3	8	41.9		1569.9		3 and 28
M-Non-16%H	514	-	205.6	16	82.2		1542.1		3 and 28
C-Non-0%H	533.6	-	213.4	0	-	-	624	900	3 and 28
C-Non-4%H	528.3	-	211.4	4	21.1	-	618.1	891.5	3 and 28
C-Non-8%H	523.2	-	209.3	8	41.9	-	612.3	883.1	3 and 28
C-Non-16%H	513.2	-	205.3	16	82.2	-	601	866.9	3 and 28
Micro textured (Lotus/Taro/Microgrid patterned)									
P-L-0%H P-T-0%H P-MP-0%H	1360.4	-	544.2	0	-	20.4	-	-	3
P-L-4%H P-T-4%H P-MP-4%H	1329.2	-	531.7	4	53.2	19.9	-	-	3

P-L-8%H P-T-8%H P-MP-8%H	1299.4	-	519.8	8	104	19.5	-	-	3
P-L-16%H P-T-16%H P-MP-16%H	1243.7	-	497.5	16	199	18.7	-	-	3
M-L-0%H M-T-0%H M-MP-0%H	529.4	-	211.7	0	-	7.9	1588.2	-	3
M-L-4%H M-T-4%H M-MP-4%H	524.6	-	209.8	4	21	7.9	1573.8	-	3
M-L-8%H M-T-8%H M-MP-8%H	519.9	-	208	8	41.6	7.8	1559.7	-	3
M-L-16%H M-T-16%H M-MP-16%H	510.8	-	204.3	16	81.7	7.7	1532.3	-	3
Micro textured and coating (Lotus/Taro/Microgrid patterned)									
M-L-0%H-10%SF M-T-0%H-10%SF M-MP-0%H-10%SF	475.9	52.9	211.5	0	-	7.9	1586.3	-	28
M-L-4%H-10%SF M-T-4%H-10%SF M-MP-4%H-10%SF	471.6	52.4	209.6	4	21	7.9	1572	-	28
M-L-8%H-10%SF M-T-8%H-10%SF M-MP-8%H-10%SF	467.4	51.9	207.7	8	41.5	7.8	1557.9	-	28
M-L-16%H-10%SF M-T-16%H-10%SF M-MP-16%H-10%SF	459.2	51	204.1	16	81.6	7.7	1530.5	-	28
C-MP-0%H-10%SF	476.1	52.9	211.6	0	-	7.9	634.4	915	28
C-MP-4%H-10%SF	471.8	52.4	209.7	4	21	7.9	628.7	906.7	28
C-MP-8%H-10%SF	467.5	51.9	207.8	8	41.6	7.8	623	898.6	28
C-MP-16%H-10%SF	459.3	51	204.1	16	81.7	7.7	612	882.8	28

Two techniques were used to determine the particle size of HPCC: Mastersizer 3000 laser diffraction system and SEM. For the laser diffraction method, an Aero S dry powder disperser was used instead of a wet dispersion unit because the HPCC particles would float on water leading to huge errors in the measurement. For the SEM method, the HPCC particles were spread directly onto an adhesive film on the sample holder stub, and the loosely attached HPCC were removed by compressed air. When using these techniques together we hope that a clear understanding of both particle size distribution and particle shape can be obtained. Contact angle of the liquids was measured on a flat and even HPCC surface made by taping a glass slide on the top of a steel plate with a circle cutout in the middle and fill the cutout with HPCC powder. Then taped another slide on the bottom, turned it over and removed the top slide, which created a flat HPCC surface. A total of 15 measurements were made at different locations and averaged.

The influence of HPCC on compressive strength was tested on paste, mortar, and concrete containing various amounts of HPCC (0%, 4%, 8%, and 16%) at ages of 3 and 28 days based on BS EN 12390-3 (Section 3.2.2). Degree of hydration was tested on paste only as cement hydration would not be affected by aggregates. The pastes were heated up to 1050°C using a furnace and the degree of hydration was determined through the loss of non-evaporable water (Section 3.2.3). Isothermal calorimetry analysis was also carried out on pastes (3 g) using TAM Air calorimeter and equal mass of dry sand as reference, as described in Section 3.2.4. All tests were conducted in three replicates and the data was collected over 96 hours. Porosity of HPCC containing cementitious materials was determined by BSE imaging analysis (Section 3.5.3). Samples were sectioned, impregnated with epoxy resin and polished to a flat surface. Pores and micro cracks in the cement paste matrix can be easily segmented in BSE-SEM as these appear darker than other phases. Images were taken at different locations, with 20 measurements made on each sample.

Methods used to fabricate hydrophobic cementitious materials will be detailed in later sections. The fidelity of reproduced surface texture using soft lithography was determined by comparing the dimension distribution of original surface texture with that of reproduced surface texture. Distance between adjacent papillae *s*, height *h* and diameter *d* of papillae were directly measured from the SEM images using ImageJ. The distance s was measured from the top view while height *h* and diameter *d* were measured from the side view. An example of how these dimensions were measured is shown in Figure 4.1. The distribution of height, diameter, and distance between adjacent papillae were plotted with over 500 individual measurements.

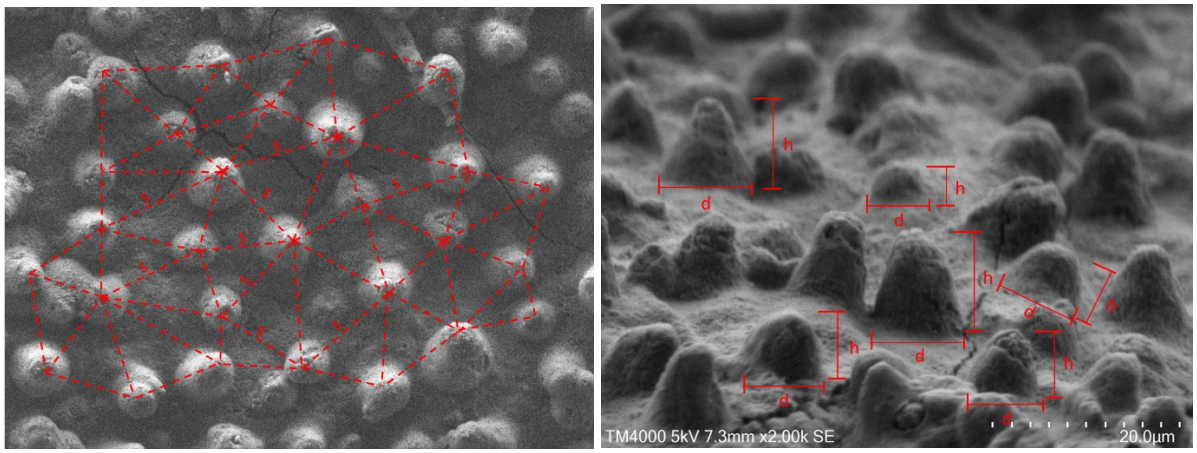


Figure 4.1 Illustration of how the distance between adjacent textures, and height and diameter of individual texture (papillae) are measured.

Thin paste samples (P-0%H-0%SF, P-0%H-10%SF) with w/c ratio of 0.4 and curing age of 3-day were prepared for FTIR ATR analysis to examine PDMS residue on cementitious surface

as described in Section 3.4.1. The analysis was carried out at 10 randomly selected areas to yield representative data and to avoid bias. Wettability of hydrophobic surfaces was determined by measuring the water contact angle, contact angle hysteresis, and droplet rolling motion as described in Sections 3.4.2 and 3.4.3. For non-textured non-hydrophobic samples, contact angles were recorded immediately after placing the droplet since the angle would decrease over time due to capillary absorption. Droplets on textured surfaces were more stable and less affected by absorption. Each reported contact angle was an average of 15 replicate measurements unless stated otherwise.

4.3 Hydrophobic precipitated calcium carbonate

The hydrophobic powder was made by dry ball milling precipitated calcium carbonate and stearic acid using the procedures described in Chan (2018) and Khoo & Lim (2017). Figure 4.2 shows the experimental setup. Raw materials were scooped into a beaker and weighed. The ratio of stearic acid to precipitated calcium carbonate was 0.02 by weight, based on the work of Ng & Shah (2016) who found that the highest hydrophobicity was obtained by dry milling 2 wt.% stearic acid with calcium carbonate for 2 hours. The batched calcium carbonate (100g) and stearic acid (2g) was then poured into a 1-litre porcelain ball milling shell with 500 g milling media. The milling media was spherical high-density alumina with an average radius of 15 mm. A rubber ring was placed between the lid and the ball milling shell and then firmly clamped. The shell was slowly inverted to make sure that it is completely sealed before placing into the ball mill. Then, the ball mill was set to rotate at a speed of 78 rpm for two hours. Water droplets placed on the resultant HPCC surface showed water contact angle of 159.7°, indicating super hydrophobicity.

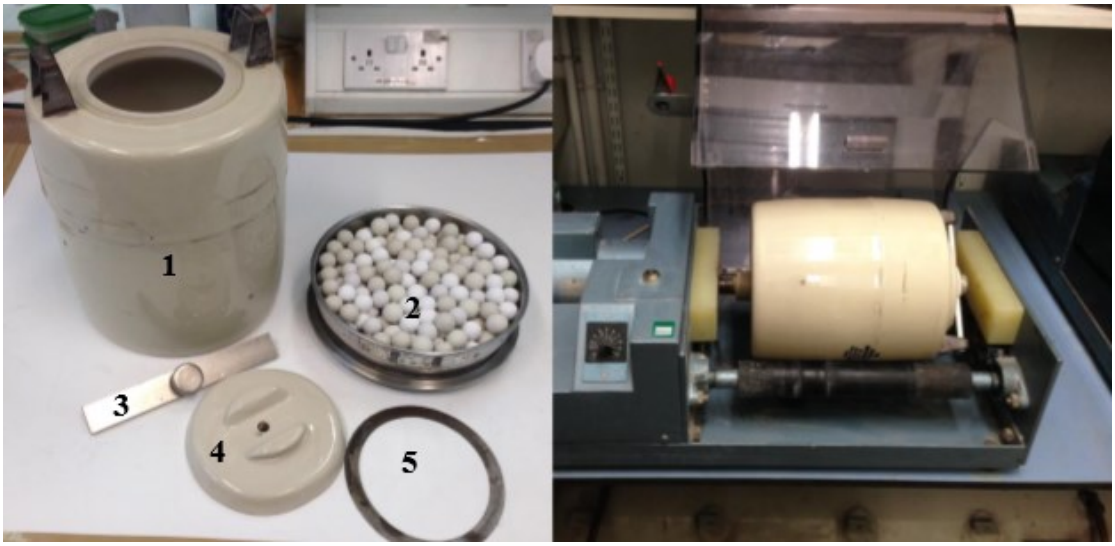


Figure 4.2 Ball mill equipment. Left: (1) porcelain ball milling shell (2) milling media (3) clamp (4) milling shell lid (5) rubber ring. Right: ball mill roller.

4.3.1 Particle size

The particle size distribution of HPCC was measured using Mastersizer 3000. Samples of newly made HPCC were dispersed by air for laser diffraction analysis. The produced HPCC was a white powder, with an average density of 2.53 g/cm^3. Particle properties of HPCC measured by Mastersizer 3000 showed that the HPCC ranged in size from 0.1 to 21.2 μm and had a surface area of 6.38 m^2/g. Figure 4.3 shows the average distribution of five measurements. The results showed good repeatability and consistency, with the difference between cumulative volumes of 10%, 50%, 90% for each measurement being less than 4%. The cumulative volume against particle size plot shows that the HPCC contained 10% of particles smaller than 0.323 μm, 50% smaller than 2.94 μm and 90% smaller than 12.3 μm.

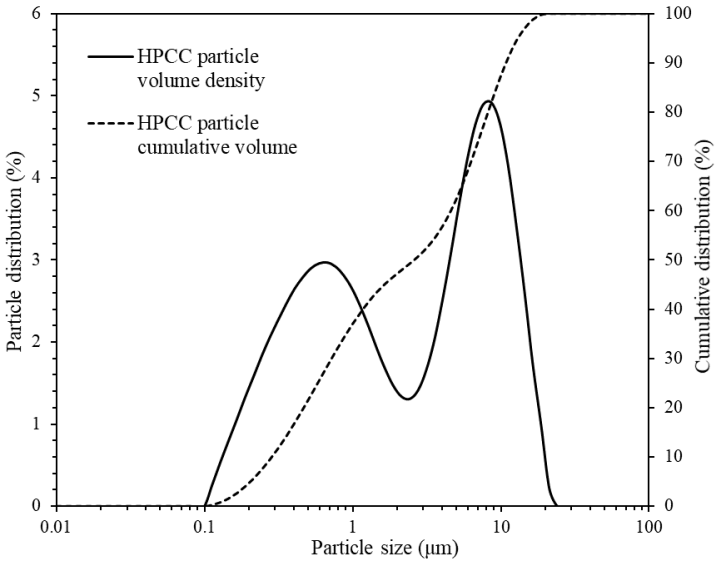


Figure 4.3 Particle size distribution and cumulative volume of HPCC determined using laser diffraction granulometry.

It is worth noting that the result given by the Mastersizer 3000 is an equivalent spherical diameter calculated from the area in relation to laser scattering properties. Care must be taken with this assumption of spherical shape since the actual particle geometry may influence its performance in cement paste, such as bond strength. Therefore, the HPCC was also observed using SEM. The image in Figure 4.4 a clearly shows large HPCC agglomerates with diameters between ~3 µm and ~ 14 µm. Scanning the HPCC agglomerates under a field emission SEM (Zeiss Sigma 500VP) at 10,000x magnification showed that some HPCC particles have prismatic morphology with a height of approximate 1.5 µm, while other particles appear to have an irregular granular morphology with diameters below 0.5 µm (Figure 4.4 b).

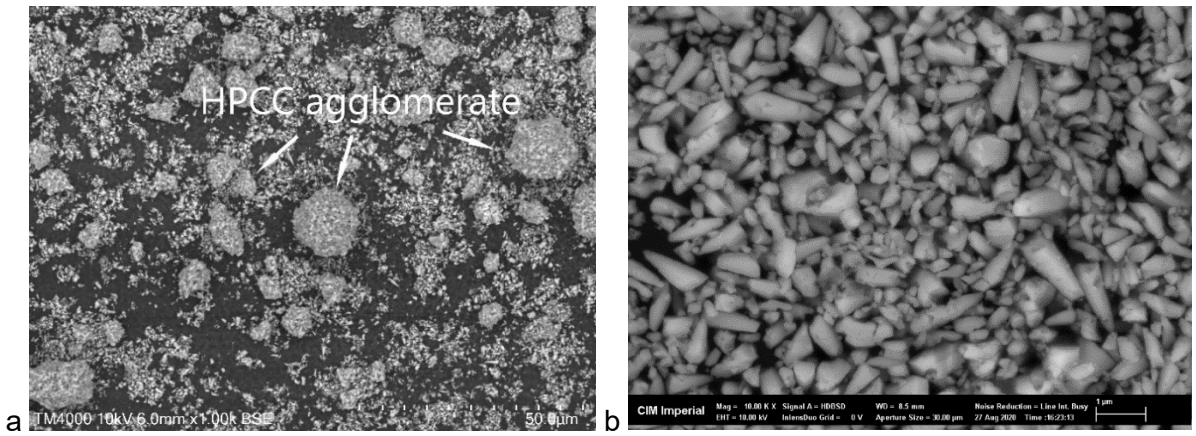


Figure 4.4 SEM image of HPCC taken at (a) 1000x and (b) 10,000x magnification.

Laser diffraction and photomicrography indicate that agglomeration of some particles have occurred during ball milling. An agglomerated clump of particles can be mistaken for a single large particle by the particle size analyzer when it passes through the optical bench and therefore introduces errors in the measured size distribution. In thermodynamics, agglomeration of fine particles is a spontaneous process in which the particles tend to group together in the form of large clumps to minimize their excess surface energy. To prevent agglomeration of particles, dispersants or process control agents are commonly used during ball milling. The dispersants that act as surfactants absorbed on the particles can neutralize surface charges arisen from broken chemical bonds and provide a steric barrier keeping powder particles from agglomeration. Interestingly, stearic acid is a commonly used dispersant (Shaw *et al.,* 2003; Zhang & Guo, 2018; Lemoisson & Froyen, 2005). Increasing the content of stearic acid during milling of HPCC may reduce the degree of agglomeration, but, from the result of Ng & Shah (2016), a higher amount of stearic acid will lead to a decrease in the hydrophobicity of the product.

HPCC agglomerates that persist in cementitious materials is undesirable since particles inside the agglomerate have little or no role in impeding water ingress. Therefore, this reduces the effectiveness of HPCC as a water-resisting agent especially at high contents. Although it seems unavoidable for the agglomeration to take place during HPCC milling, the shear force imparted during casting and mixing of the cementitious materials is expected to break-up the agglomerates and disperse the HPCC particles. To verify this, EDX mapping was used to identify HPCC agglomerates in cement matrix. Slices of mortar sample containing 16% HPCC were impregnated and polished via the procedure described in section 3.5.2 and observed at 1000x magnification using BSE imaging. If the large agglomerates persist, element maps would show large areas where are deficient in silicon/aluminium/iron but are rich in calcium. In addition, the HPCC agglomerates may be easily distinguished from other cementitious phases due to its distinct morphology. A total of 50 randomly selected areas were scanned, none of these areas showed the sign of HPCC agglomerate. It can be said that the HPCC particles were well-dispersed in cement matrix and the agglomerates did not persist.

4.3.2 Workability

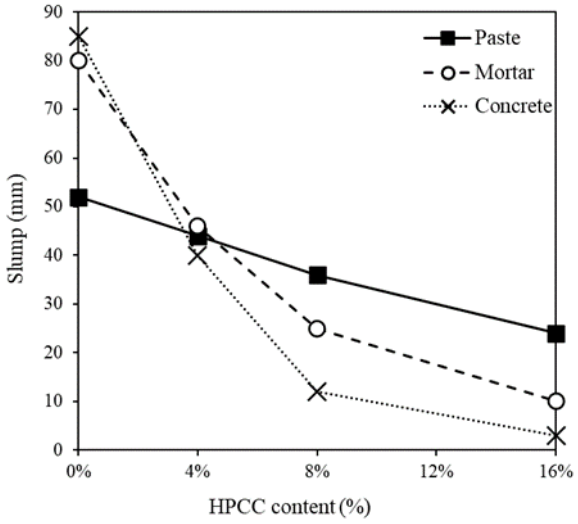


Figure 4.5 Effect of HPCC content on slump

The influence of HPCC on the slump of paste, mortar, and concrete is shown in Figure 4.5. The workability of cementitious materials decreased with increasing amount of HPCC. 16% HPCC decreased slump by 53.8% on paste compared to that of 0% HPCC. The slump of concrete appears to be slightly more sensitive to HPCC than mortar. At all HPCC content, concrete has a lower slump than the mortar. It is noted that the batch water has been adjusted to correct for the absorption of aggregates, so the decrease in slump cannot be attributed to a decrease in effective water content due to coarse aggregate absorbing more water than sand.

The rheology of mixture relates to the interparticle friction between aggregates (Sims, Lay & Ferrari, 2019). The rougher the aggregate, the greater the friction. Cement paste acts as lubricant which releases part of the interparticle friction. A ‘dryer’ cement paste is not only less workable but also less effective to release friction, as well as to facilitate movements between aggregate. In this study, the mix design of concrete was made by replacing 60% of sand in mortar with coarse aggregate while the total aggregate volume remained the same. Coarse aggregate particles however are relatively more angular and rougher compared to sand particles, which makes the slump of concrete lower than that of mortar.

4.3.3 Strength and cement hydration

The influence of HPCC on compressive strength of paste, mortar and concrete is shown in Table 4.2. For all mixtures, the compressive strength increased at longer curing time, as expected. No significant difference in strength of mortar and concrete made with 0%, 4%, 8%,

and 16% HPCC was observed at ages of 3 days and 28 days. However, the HPCC decreased the compressive strength of paste by up to 38.5% at 16% addition. For the reason that the decrease in compressive strength was only observed on paste samples will be explained in later section.

Table 4.2 Compressive strength (MPa) of cementitious materials containing various amounts of HPCC. Standard errors are showed in brackets.

HPCC content	Paste		Mortar		Concrete	
	3 days	28days	3 days	28 days	3 days	28 days
0%H-3d	33.9(0.32)	48(1.15)	22.1(0.09)	31.5(1.12)	29.3(0.69)	38(0.23)
4%H-3d	30.3(0.64)	44.3(0.77)	21.9(0.1)	32.2(0.9)	31.3(0.74)	38.1(0.75)
8%H-3d	25.9(0.38)	35.5(0.38)	22.5(0.37)	31(0.74)	28.8(1.3)	37.1(0.89)
16%H-3d	23.2(1.5)	29.5(1.06)	22.9(0.14)	31.1(1.15)	27.7(0.98)	35.2(1.33)

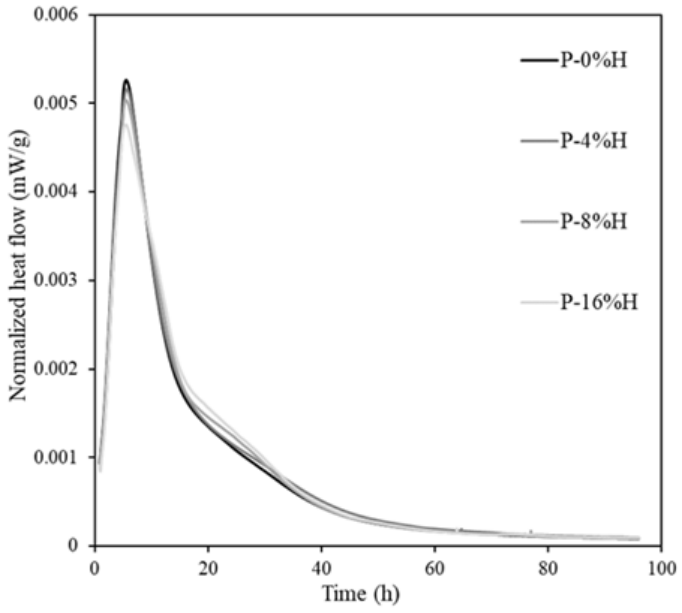


Figure 4.6 Isothermal calorimetry curves for pastes containing 0%, 4%, 8%, and 16% HPCC.

The isothermal data for paste containing HPCC shows that the rate of cement hydration was unaffected by 4% of HPCC (Figure 4.6). At 8% addition, the peak of heat flow was 4.3% lower than the reference and it was further decreased at 16% addition. This agrees with the results of the degree of hydration estimated by determining the non-evaporable water content of paste (Table 4.3), which shows that pastes containing HPCC had slightly lower degree of hydration

at the ages of 3 days since the hydration was slightly delayed in the presence of high level of HPCC (>8%).

Table 4.3 Influence of HPCC on degree of cement hydration.

		3 days	28days
HPCC content	P-0%H	0.61	0.67
	P-4%H	0.62	0.68
	P-8%H	0.59	0.67
	P-16%H	0.6	0.66

These results indicated that HPCC is an inert fine powder to cement which can be used as an addition without significant influence on cement hydration.

4.3.4 Microstructure

Figure 4.7 shows porosity of cementitious materials determined by Image analysis on SEM-BSE micrographs. Note that the porosity of cement matrix is defined as the volume fraction of air voids, micropores in C-S-H gel and interconnected capillary pores for cementitious materials. However, SEM images were taken at 100x magnification, with a pixel spacing of 0.96 μm. This means pores with radius smaller than 0.48 μm may be unable to be detected using SEM due to the limit of resolution, which leads to an underestimation of porosity. However, it would be effective to detect large air voids that may arise from the use of HPCC. The porosity reported in Figure 4.7 were the average of 20 measurements taken at different locations. The small variation of porosity means the values are representative. It was found that the porosity of pastes increased with increasing HPCC content, while the porosity of cement matrix in mortar and concrete was largely unaffected by HPCC addition. For example, a 16% HPCC paste had 249% greater porosity than that of the cement paste matrix in concrete containing the same HPCC content. Note that the area occupied by aggregates were manually selected along its boundary and were not included in the calculation of porosity. It should be stressed that a porosity of ~2% is rather low for cement matrix at 3 days age with a w/c of 0.4. This is because the porosity reported in Figure 4.7 is air content rather than total porosity.

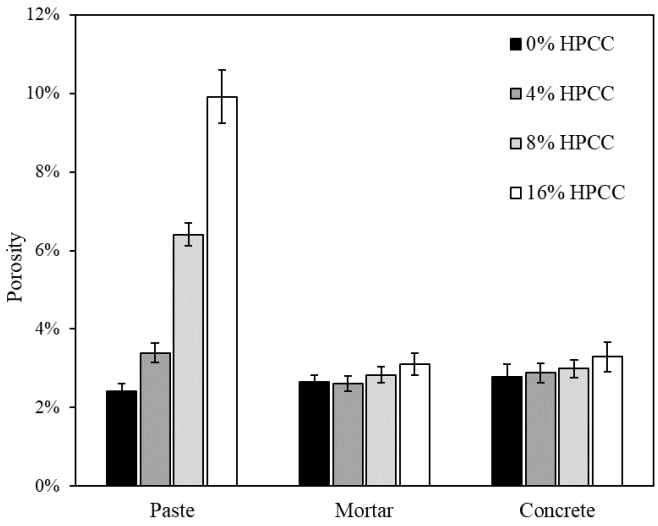


Figure 4.7 The porosity of cementitious samples with various amount of HPCC.

The SEM-BSE images taken from the samples showed that large air voids with diameter up to ~400 μm can be observed in the paste samples, especially in those containing high dosages of HPCC (>8%). However, air voids in the mortar and concrete samples were much less than that of pastes and smaller in size as well, regardless of the HPCC content in the samples.

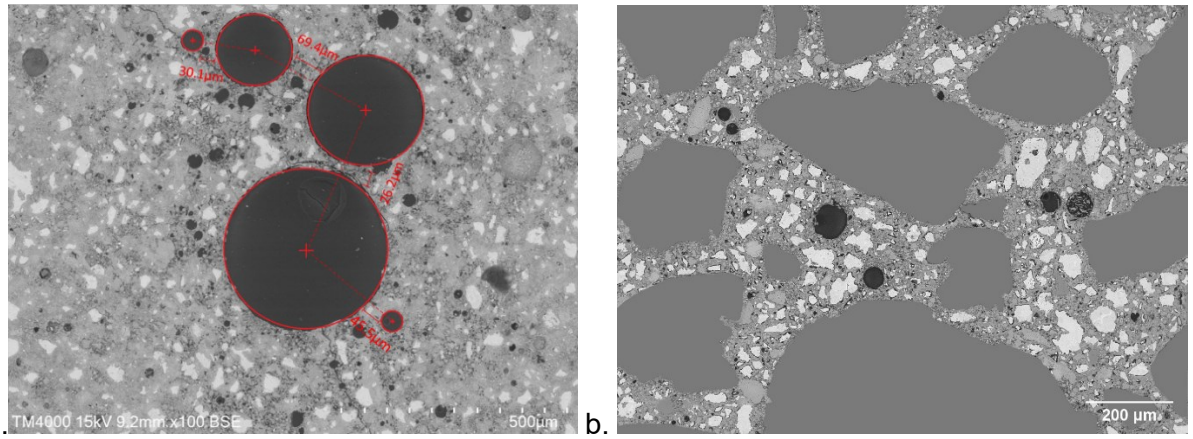


Figure 4.8 BSE scanning electron micrographs of impregnated paste (a) and mortars (b) with 16% HPCC (3 days, w/c 0.4), at 100x magnification.

Figure 4.8 (a) shows a typical example of air voids in the paste sample containing 16% HPCC. The distance between adjacent air voids were measured using Image J and shown in the figure. The air voids were approximately circular and thus their separation distance can be estimated as the distance between their centres minus the sum of radii. These air voids stay very close to each other, with the smallest measured separation distance of ~26 μm in this example. Such characteristics are unlike entrapped air voids normally observed in plain

cement pastes sample, which tend to be well-dispersed and far apart. Having such short separation implies that the air voids seen in HPCC pastes are not trapped air pockets, since if it was the case, the voids would merge during vibration.

Instead, it is believed that these voids formed from pockets of mix water that have been trapped/encased in a sheath of HPCC particles during mixing. To illustrate this, Figure 4.9 shows a layer of HPCC particles attaching onto a water droplet forming a barrier when the droplet was rolled across the HPCC. Droplets placed on a glass would fully wet the surface to form a flat puddle while a HPCC encased droplet was able to stand on the glass surface without spreading since the water molecules were separated from the glass by HPCC. It is expected that this phenomenon can also happen during the preparation of cement paste mixtures, causing the voids seen in Figure 4.8 (a) to form.

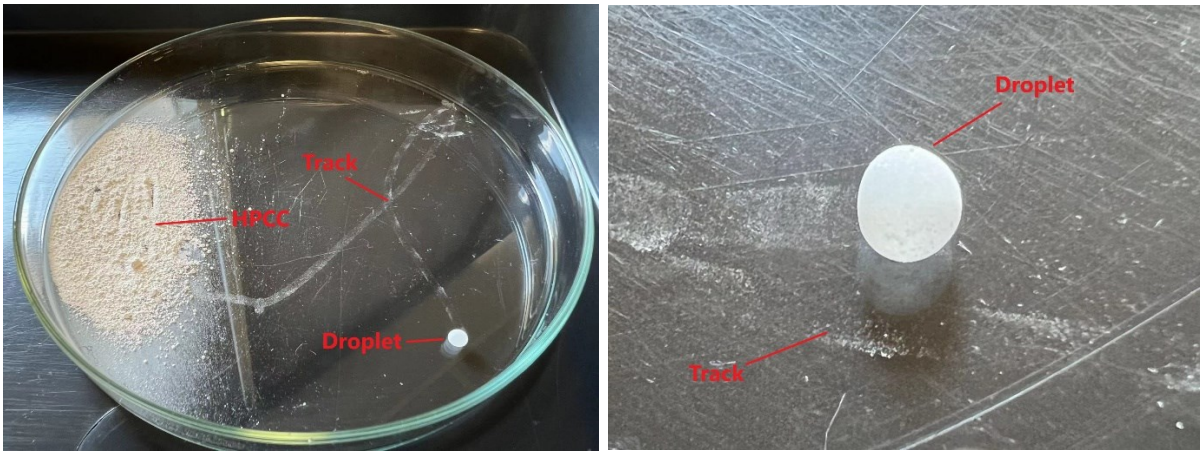


Figure 4.9 A water droplet is encased in a sheath of HPCC as it rolls over a glass surface.

The mechanism of water encasement with HPCC is explained as follows. The hydrophobicity of HPCC arises from the attachment of stearic acid on the surface of calcium carbonate filler during dry ball milling. Stearic acid molecules attaches to filler either by chemisorption or physisorption (Gilbert, Sutherland & Guest, 2000), in which physisorption leads to a weak bonding between stearic acid and filler (Section 2.7). When the HPCC is in contact with water, loosely packed physisorbed stearic acids detach from the substrate and gather in the form of micelles, with hydrophilic carboxyl face outside in contact with water while the hydrophobic hydrocarbon tails are grouped together in the center of micelles. The portion of surface not covered with stearic acid tends to face towards water molecules due to the intrinsic hydrophilic nature of calcium carbonate filler, while the portion still covered with stearic acid tends to orientate away from water molecules. As a result, these partially covered HPCC particles attach to the water droplet forming a sheath. In cement mixture, the sheath of HPCC prevents

the encased water droplet from reacting with the cement, as well as from merging with adjacent droplets.

This water encasing mechanism is supported by the fact that clusters of air voids were not observed in the control paste samples without HPCC. In mortars and concretes however, the presence of aggregate particles produces physical impact during mixing that breaks up the water droplets encased with HPCC. Therefore, the number and size of air voids are much lower in the mortar and concrete samples. The excess air voids in HPCC paste samples is a factor that contributes to significant strength loss as shown in Section 4.3.3. Generally, compressive strength decreases with increasing air content at equal w/c ratio. In contrast, the compressive strength of mortar and concrete samples were less affected by HPCC due to the absence of these voids. The mix water encased in HPCC sheath cannot immediately participate in the hydration reaction with cement, which leads to a lower peak of heat flow than the reference (0%HPCC) as detected by calorimetry (Section 4.3.3). This water encasing mechanism is possibly another factor that contributes to the decrease in slump as seen in Figure 4.5.

4.4 Hydrophobic micro textured surfaces transferred from plants

Soft lithography was used to transfer the micro textures from natural hydrophobic leaves onto cementitious materials. To perform soft lithography, a PDMS mold was created by lining a plant leaf on the bottom of steel mold and firmly clamping the mold to prevent leakage of PDMS liquid. The hydrophobic plant leaves used in this research were lotus and taro leaves. Lotus leaves were obtained from a local Chinese grocery. The leaves were dried and preserved in good condition. Water contact angle measurement showed that the lotus leaf had an average water contact angle of 158.5° and a contact angle hysteresis of 6°. Taro leaves were picked and sun-dried before they were used as a master for soft lithography. The microstructure of dried taro leaf comprised of deformed bumps about 15-30 μm in diameter due to the loss of water (Figure 4.10 b). Super hydrophobicity can still be observed on dried taro leaves, which showed a water contact angle of 163.2°, and self-cleaning property.

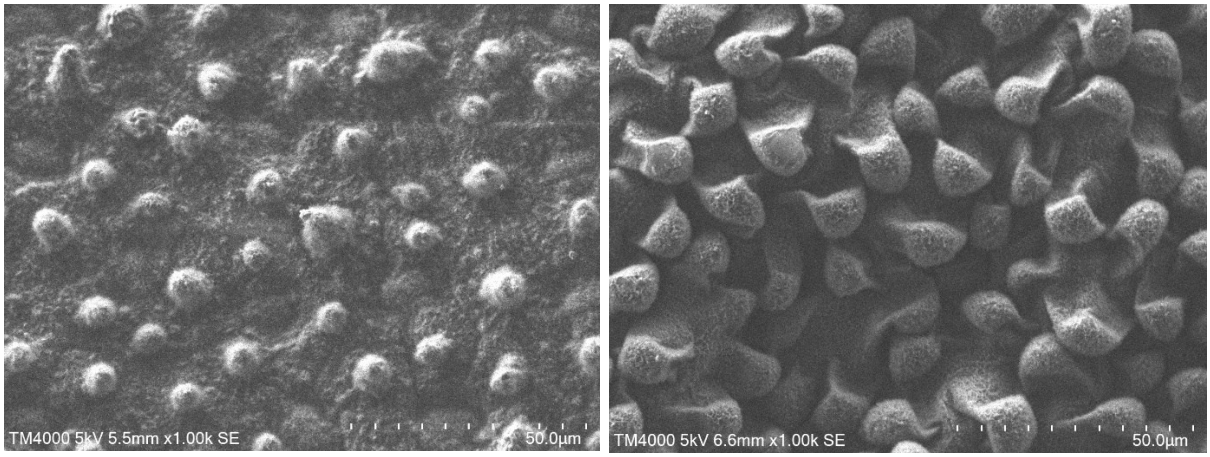


Figure 4.10: SEM image of surface texture on lotus leaf (left) and taro leaf (right).

To prepare a master mold, a small piece (50mm*50mm) of the plant leaf was cut and extracted (Figure 4.11). The main veins were avoided while cutting because the veins will make an uneven surface on the PDMS negative replica. If the surface of the negative replica was uneven, the surface of cementitious sample would also be uneven. An uneven sample surface would make it difficult to define a baseline when using a drop shape analyzer for measuring water contact angle.

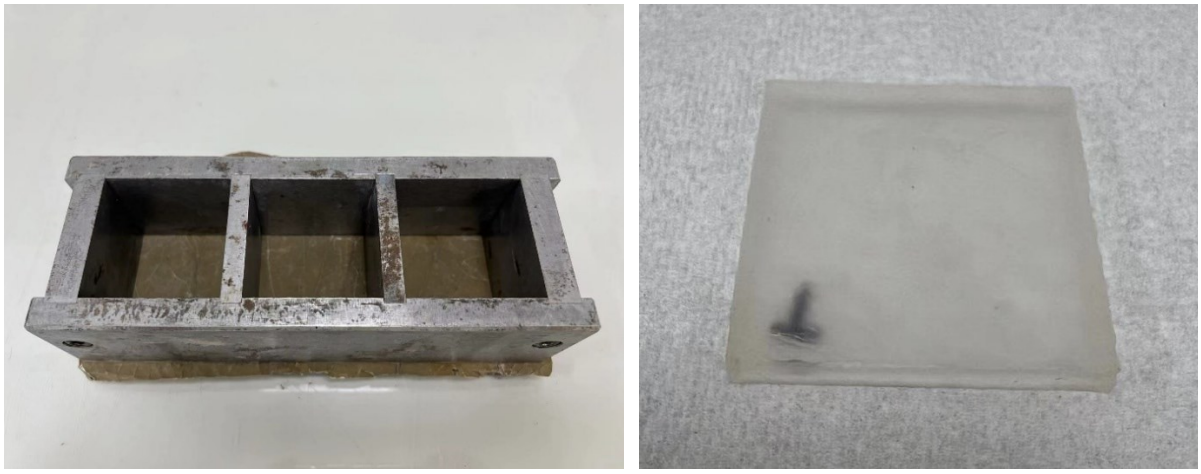


Figure 4.11 Preparation of mould for soft lithography and the produced PDMS mould.

Figure 4.12 is an illustration of the procedures used for replicating the micro texture on a plant leaf and transferring the texture to the surface of cementitious material. The PDMS mold was manufactured using Sylgard 184 silicone elastomer. The PDMS pre-polymer base was mixed with the curing agent at a ratio of 10:1 by weight as recommended by the manufacturer. Then, the mixture was put in a vacuum desiccator to remove air bubbles that are entrapped during mixing. The degassing procedure lasted for 20-30 minutes until no more air bubbles escaped from the mixture.

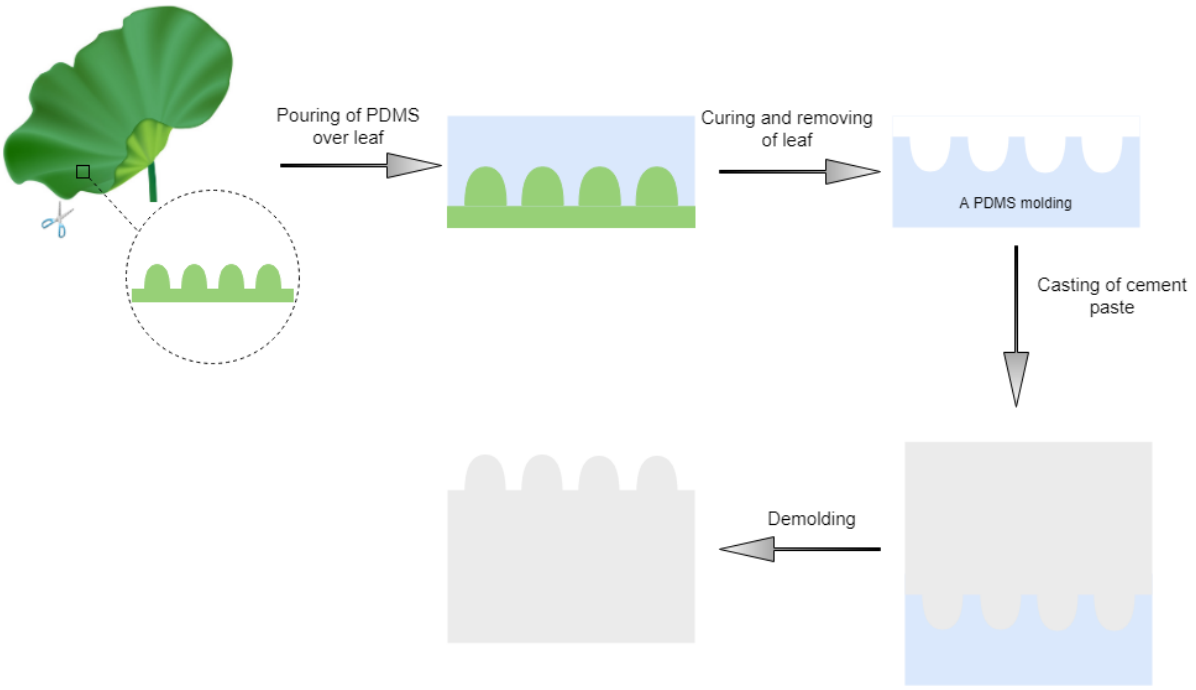


Figure 4.12 Formation of a PDMS mould from a plant leaf and reproducing the texture onto a cementitious material sample.

The degassed PDMS was then poured evenly on to the master pattern and cured in an oven to expedite the cross-linking of the polymer. The temperature of the oven was set at 60 degrees Celsius and the PDMS mould was cured for 12 hours until solidification. The fully cured PDMS mould was allowed to cool to room temperature, and then slowly and carefully peeled off from the master. After that, a scanning electronic microscope was used to observe the surface of the PDMS negative replica to examine whether the microstructure of plant leaf was replicated from the master. Figure 4.13 shows the negative pattern of lotus and taro texture on PDMS master moulds.

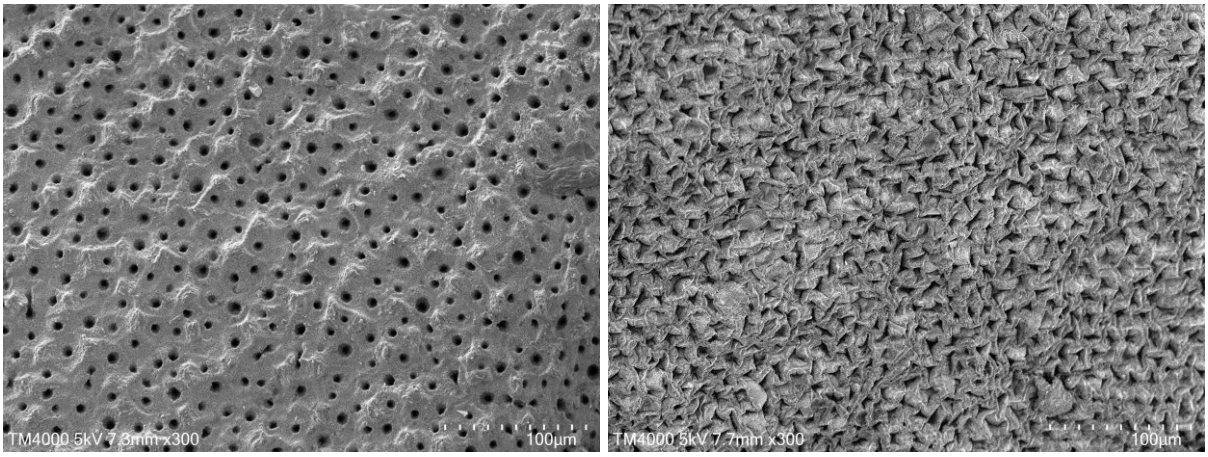


Figure 4.13 SEM image of PDMS master mould showing a negative template of lotus (left) and taro (right) leaf texture.



Figure 4.14 Left: lining the PDMS master on the bottom of steel mould. Right: The appearance of sample surface (M-L-0%H-0%SF) cast against the PDMS mould.

The PDMS negative replica was trimmed to 50*50 mm in order to fit and line the bottom of the steel mould used for casting cementitious samples (Figure 4.14). Demolding oil was carefully applied on the sides of steel mould to avoid dripping down onto the lining. The process for casting and curing samples in a fog room were described in Section 3.1.4. Note that the PDMS mould was removed after curing to avoid potential degradation during the curing period. Examples of the replicated micro textures on the surface of mortar samples are shown in Figure. 4.15.

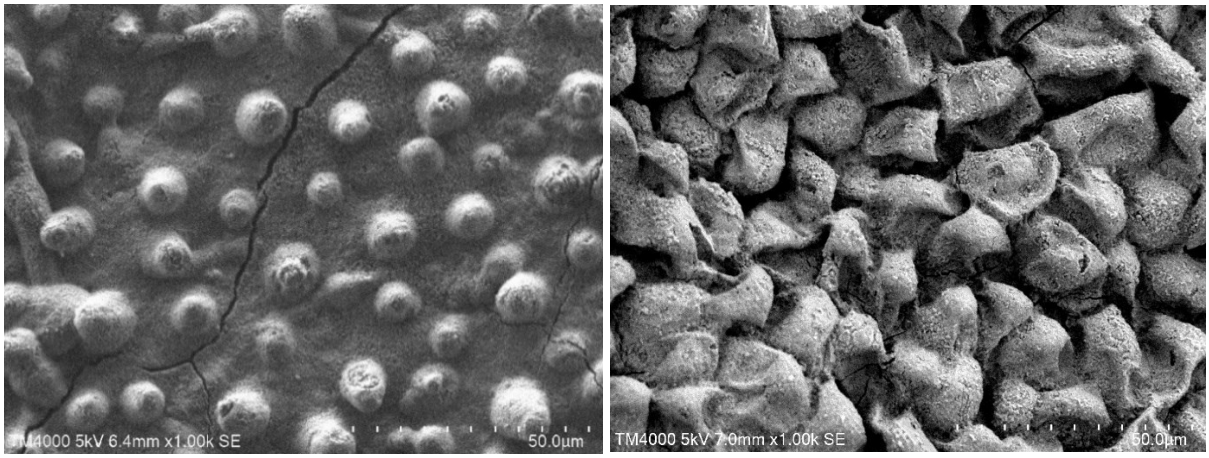


Figure 4.15 SEM images of the replicated surface textures on mortar samples. (Left) Lotus textured surface (Right) Taro textured surface.

The soft lithography approach was generally very successful in transferring micro textures from natural hydrophobic leaves onto cementitious materials. However, it is not perfect and occasional damages can be seen. Figure 4.16 shows examples of damaged lotus and taro textures observed on 3-day old mortar samples with w/c of 0.4 that reveal the presence of hollow shells. This type of damage was rare but was found on mortar and paste samples. A tentative explanation is that the presence of some large cement grains or aggregate particles have partially blocked the pores on PDMS mold during casting, causing an incomplete filling as illustrated in Figure 4.17. Size distribution of cement particle determined using wet dispersion analysis (dispersant: isopropyl alcohol) showed that the cement particles were ranging from 0.5 µm to 127 µm in diameter with 50% of particles larger than 17 µm. The pits on the PDMS mould have a narrow entrance of approximately 12 µm in width, hence the scenario illustrated in Figure 4.17 can happen considering the geometric restriction and wide range of particle size distribution of the cement used. The hollow texture formed will be weak and prone to damage when the sample is de-molded.

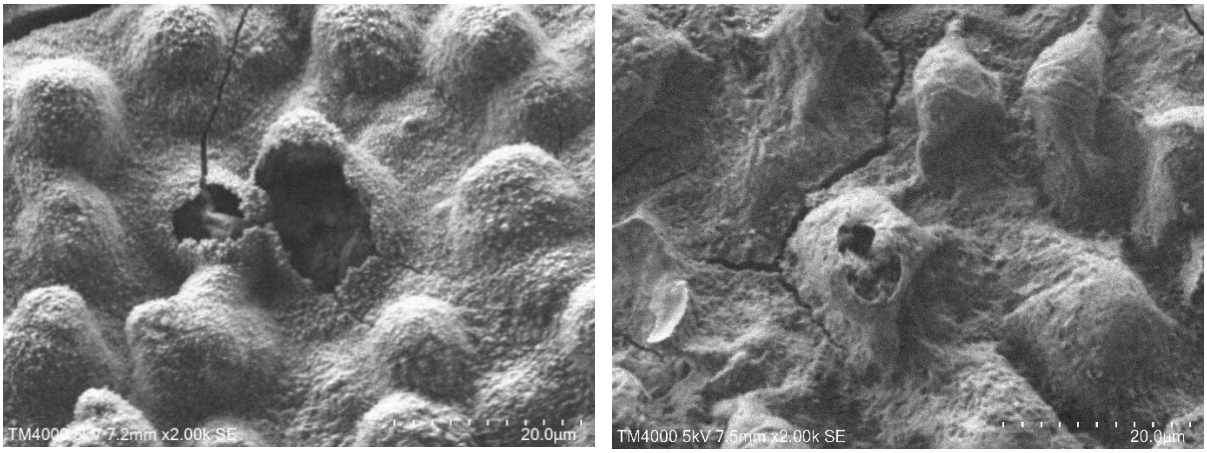


Figure 4.16 Void space within the microstructure of lotus textured mortar (left) and taro textured mortar (right).

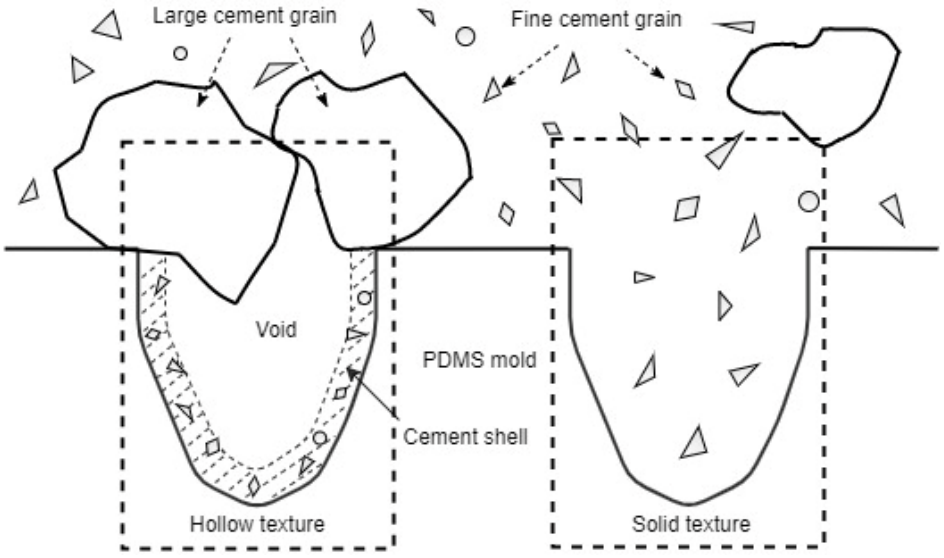


Figure 4.17 Schematic showing blockage of the PDMS mould by large cement grains forming a hollow texture (left) rather than a solid texture (right). The hollow texture is prone to damage as shown in Figure 4.16.

4.4.1 Fidelity of reproduced surface structure using soft lithography

The fidelity of reproduced surface structure was studied using lotus texture because its regular shape lends itself to easy quantitative evaluation with the use of SEM and image analysis. This research was carried out on a M-L-0%H-0%SF sample. Cross section profiles reveal that the asperities on the surface of lotus leaf consist of sinusoidal grooves, which are similar with that observed on the surface of the mortar sample (Figure. 4.18). The statistical distributions of the measured dimensions (separation distance, diameter, and height) of intact lotus texture papillae are shown in Figure. 4.19. Note that the leaf sample. Used to measure the dimensions

of original papillae was extracted from an area close to where the leaf was used for soft lithography to minimize variation and ensure representativeness. Results are expressed as percentage. The distribution for both the original and reproduced lotus texture can be fitted to a typical bell curve with coefficient of determination (R^2) larger than 0.9. Peak fitting shows the average distance between adjacent papillae on a lotus leaf is 22.9 μm, which is close to the average distance of reproduced papillae of 22.7 μm. Measurement of the height and diameter of papillae on a lotus leaf demonstrates similar distribution. Both original and reproduced textures show height in the range of 5.5 to 15.5 μm, with a diameter to height ratio ~1. Hellinger distance between the height and diameter of original and reproduced papillae is 0.0867 and 0.0571, respectively, which shows high similarity between the probability distributions.

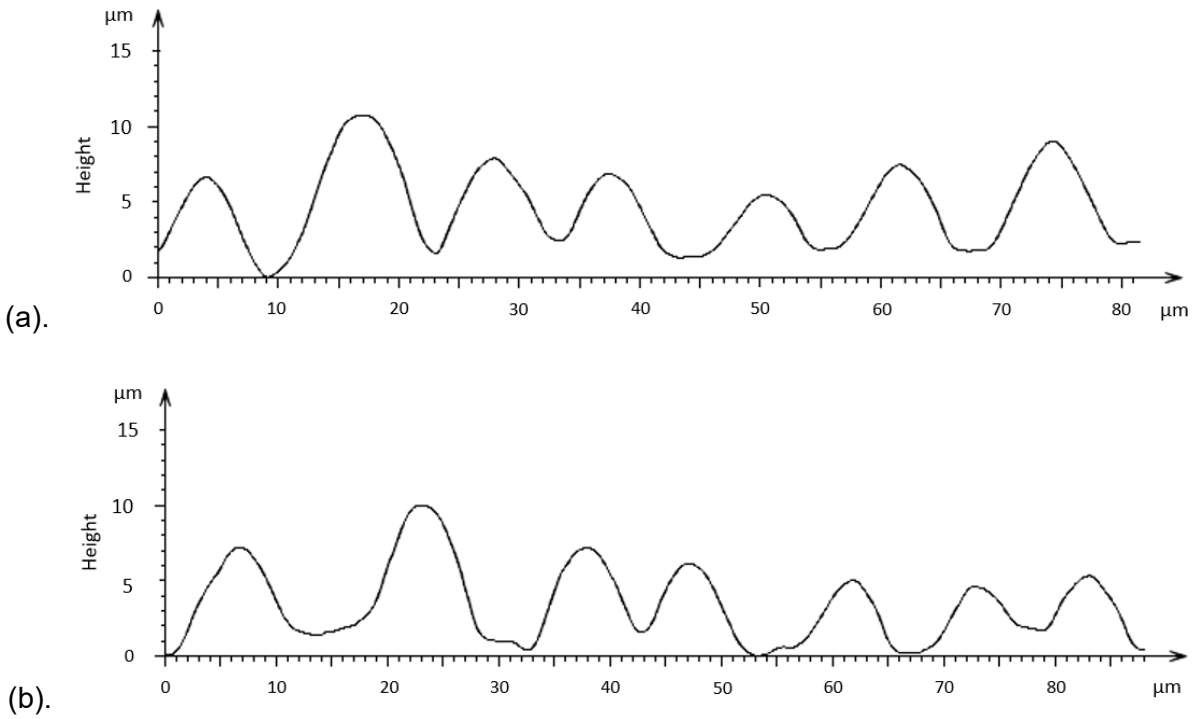
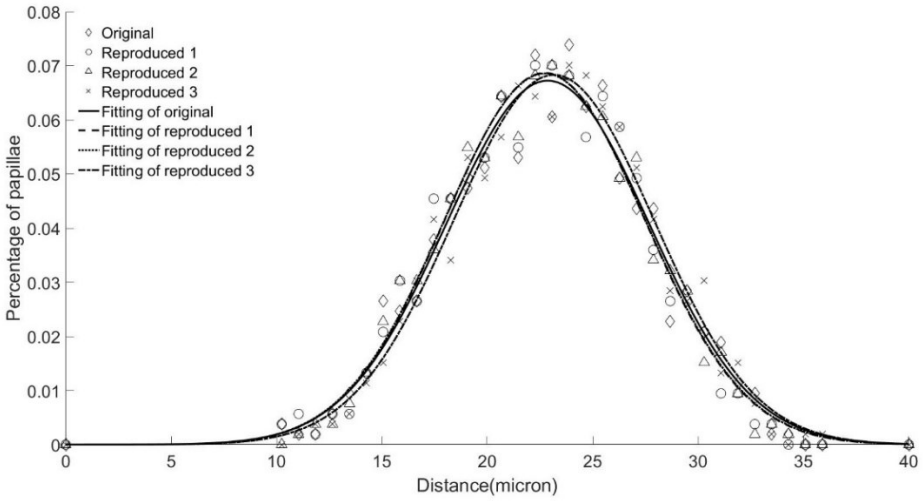
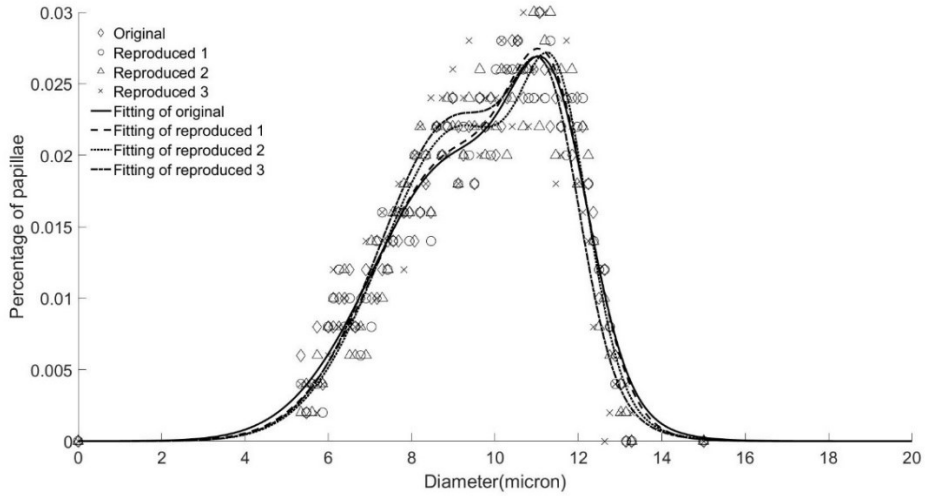


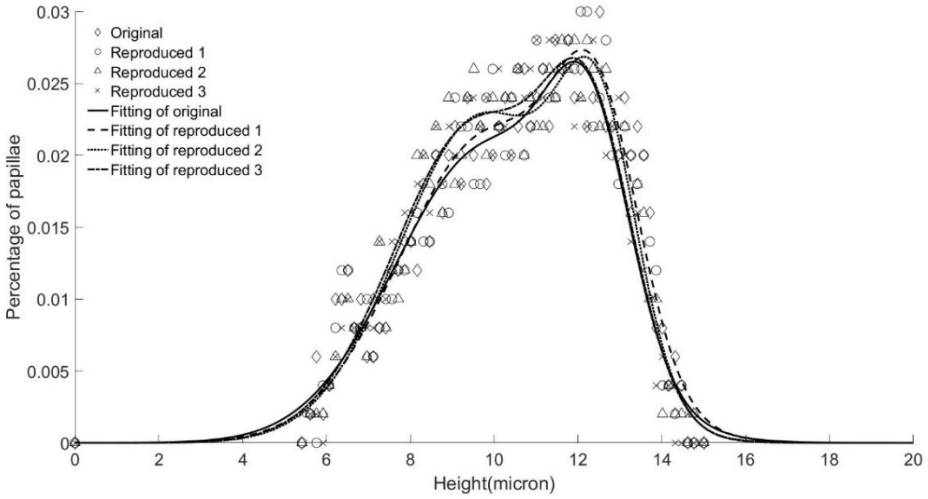
Figure 4.18 Cross section profiles of lotus papillae: (a) original lotus leaf, and (b) reproduced on a mortar sample using soft lithography.



(a).



(b).



(c).

Figure 4.19 Distribution of original and reproduced papillae dimensions: (a) separation distance, (b) diameter, (c) height.

The PDMS mould can be used for repeated casting after cleaning in water. Dimensions of the reproduced textures made with the same mould repeatedly can exhibit satisfactory fidelity to the original texture (Figure 4.19). Hellinger distance between the original and reproduced texture made with the same mould after 3 cycles is 0.069, 0.1305, and 0.1151 for distance, diameter, and height respectively. However, further cycles of casting and de-moulding using the same mould are likely to degrade the fidelity and lead to flawed textures as shown in Figure 4.20, with increasing frequency on subsequent casting. These imperfect surface textures are mainly due to blockage of the PDMS mould caused by attached debris or remnants from the previous cast. These debris or remnants are difficult to remove completely, and the cumulative effect of pore blockage would lead to large-scale flawed structure. In this study, the PDMS mould was only used up to 3 times before replacement to ensure the highest fidelity between the original and reproduced texture.

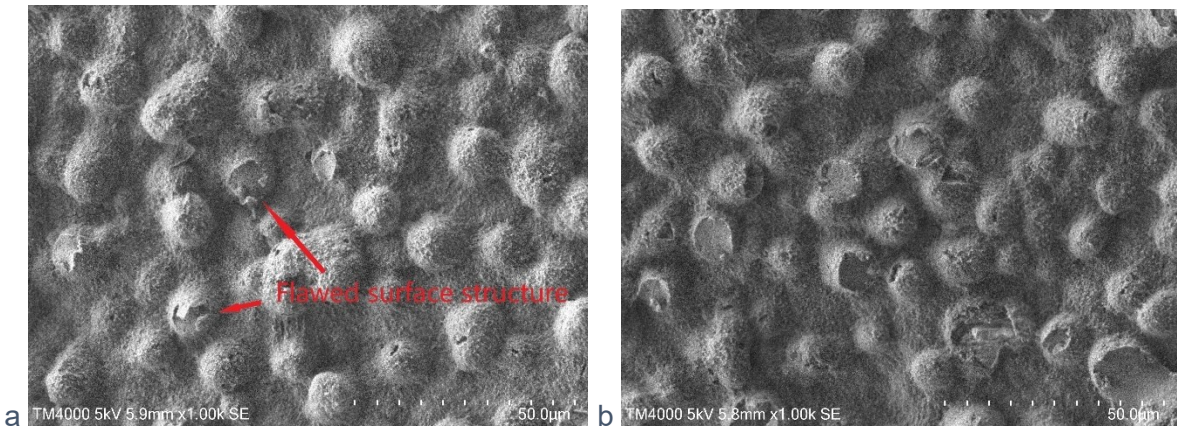


Figure 4.20 Examples of flawed surface textures made using the same PDMS mould after 3 cycles of casting (left) and after 5 cycles (right).

4.4.2 PDMS residue

Figure 4.21 displays examples of FTIR spectrum of PDMS and of the paste sample which was cast on a PDMS mold. PDMS shows absorption peaks at 787.63 cm^{-1}, 1257.74 cm^{-1}, and 1009.56 cm^{-1} which represent the deformation of methyl groups and Si-O-Si chemical bonds (Johnson *et al.*, 2013). The cement paste sample was examined at 10 different locations and all the 10 spectrums did not show the characteristic absorption peaks of PDMS. This indicates that very little or no PDMS residue remained on the sample surface.

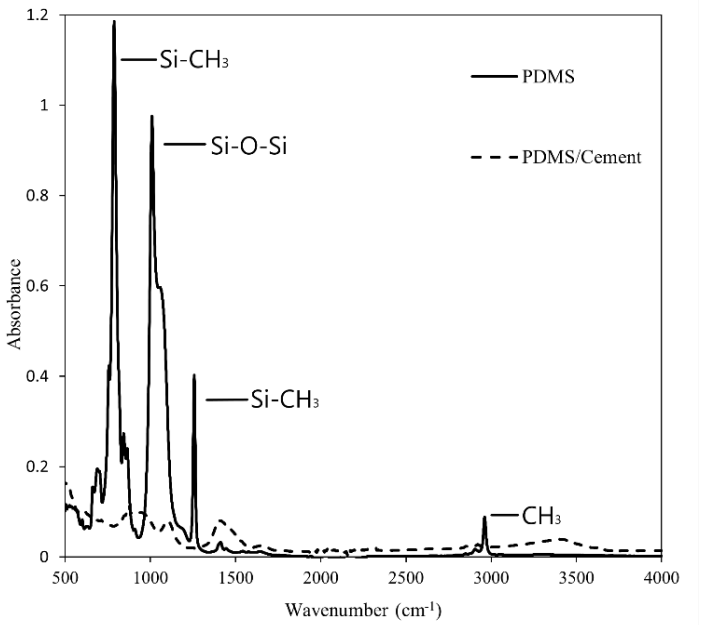


Figure 4.21 FTIR spectrum of PDMS and of cement paste interface. The spectra were taken from 500 cm^{-1} to 4000 cm^{-1} at a resolution of 4 cm^{-1}.

4.5 Coating micro textured surfaces

Surface wettability relates not only to surface roughness but also surface energy. It is expected that combining micro textures and a hydrophobic coating may lead to a superhydrophobic cementitious surface. However, conventional paints or spray applied hydrophobic coatings, such as polymer composites, form a dense coating with thickness ranging from 0.1 to 1 mm (Pan *et al.*, 2017), which fully covers and obscures the surface micro texture. In this section, a new method to coat micro textured cementitious material was investigated. Inspired by the work of Horgnies & Chen (2014), the addition of silica fume (SF) was found to result in PDMS residue on cementitious surface. It is therefore possible to create a thin PDMS coating that covers the entire micro textured surface without changing the designed surface topography.

Coating the cementitious surface with PDMS was achieved by replacing part of cement with SF, so that the PDMS molecules react with SF and transfer onto the textured surface through a grafting reaction. The SF will also react with CH generated from the hydration of cement and as a result, the PDMS molecules are bonded onto the cementitious sample. Figure 4.22. shows a schematic diagram of PDMS coating on a micro textured cementitious sample. This reaction is demonstrated in Figure 4.23. In the presence of water, siloxane groups (Si-O) in SF are hydrolyzed to form reactive hydroxyl groups (Si-OH). This hydrolysis also happens to PDMS molecules, in which water molecules break the Si-O-Si backbone chain to form hydroxyl-terminated PDMS. As a result, these PDMS molecules are able to form covalent

bond with hydroxyl group on SF and therefore grafting on its surface (Marinova *et al.*, 2005; Teisala *et al.*, 2020).

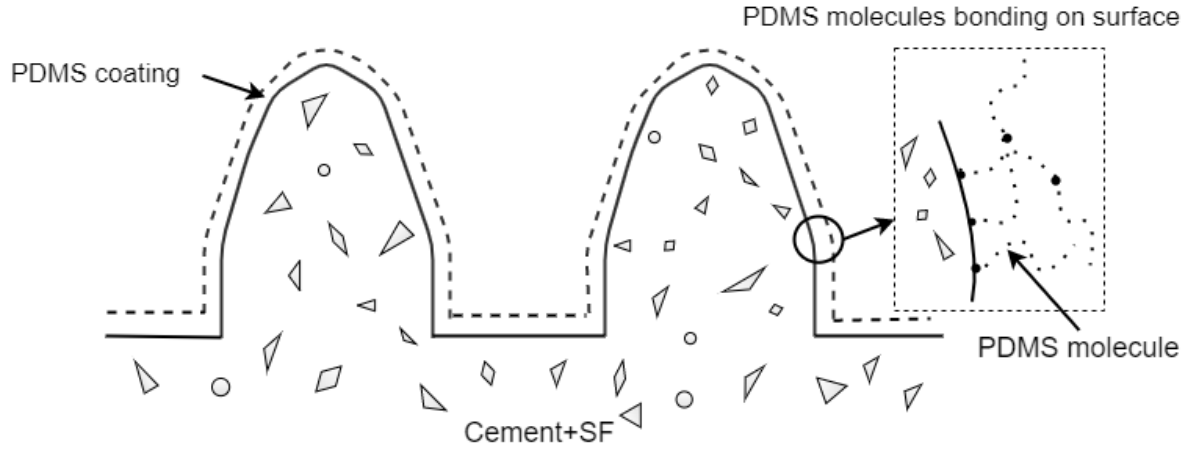


Figure 4.22 PDMS molecules coating the surface of SF mortar through grafting reaction.

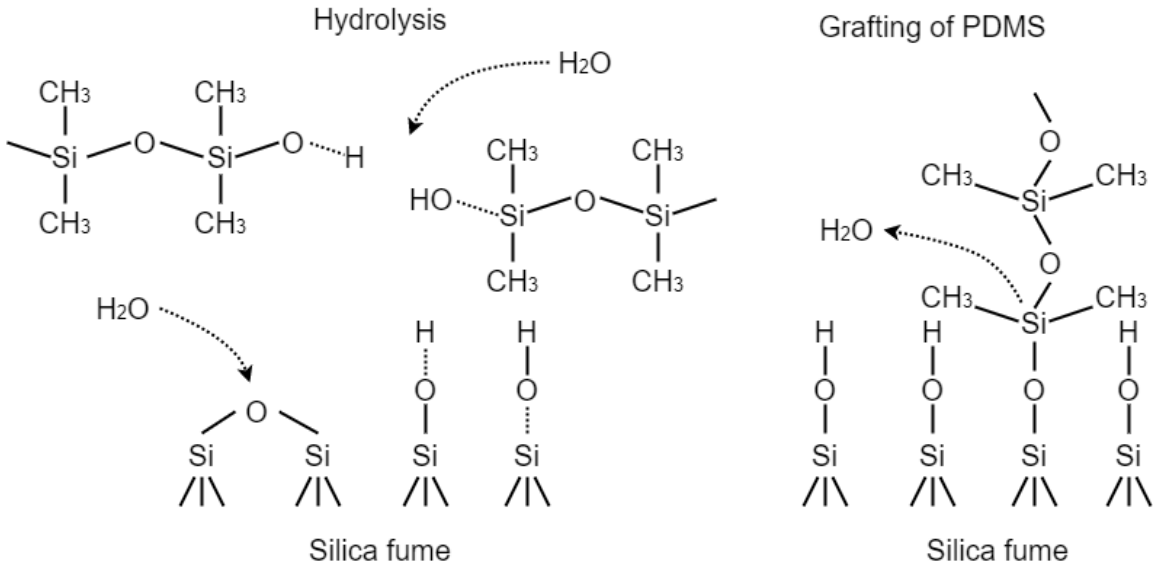


Figure 4.23 The transfer of PDMS molecules on to the surface of SF.

Trials were made on lotus textured paste samples (w/c 0.4) to determine the SF content and curing time required to achieve adequate bonding between SF and PDMS and therefore, forming a surface coating. SF replacement levels of 10 wt.% and 20 wt.% and curing time of 28 days and 91 days were tested. Note that the PDMS moulds were removed after curing for the grafting reaction to happen. It was found that at 20% replacement level, after 28 days of curing, the PDMS mould was difficult to remove from the cementitious sample. SEM imaging showed that part of cementitious material on the surface was missing, probably because the material was tightly bonded with the PDMS mould and was peeled off when demolding (Figure

4.24 a). A similar appearance was also observed on samples containing 10% SF and cured for 91 days. At 20% replacement level and curing time of 91 days, the bonding between the PDMS mold and samples was so extreme that using a knife to remove the PDMS mold was necessary. The 10% replacement level and 28 days of curing is shown to be the optimum with surface appearance (Figure 4.24 b). The surface appeared very similar to the original texture and patches of material removed during demolding were very occasionally observed. Therefore, experiments in this chapter were conducted on samples with 10% SF at 28 days of age.

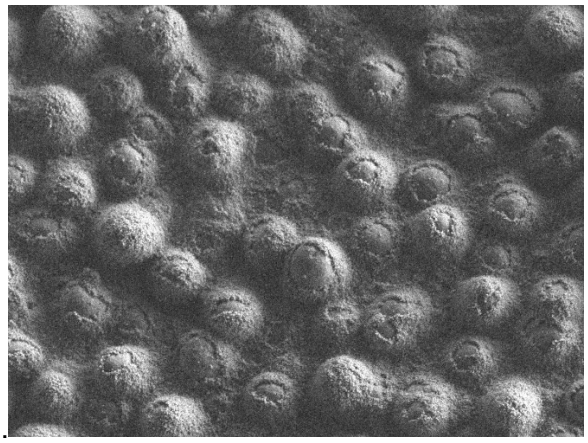
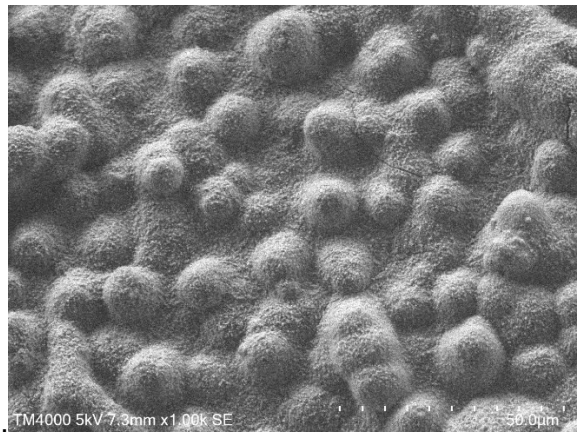
a.  b. 

Figure 4.24 SEM images of lotus textured mortars (a) 20% SF, 28 days; (b) 10% SF, 28 days.

4.5.1 PDMS residue

FT-IR spectrums of PDMS and paste samples (with and without SF) casted against a PDMS mold are shown in Figure 4.25. Peak at 1020 cm^{-1} represents the stretching of Si-O-Si which exists in both SF and PDMS (Johnson *et al.*, 2013). However, peak overlaps were observed at 2960 cm^{-1}, 1260 cm^{-1}, and 790 cm^{-1}, which represent the deformation of Si-CH_3 bond. This indicates that PDMS molecules have bonded on to the surface of the cementitious sample containing SF. All 10 spectrums obtained from different locations of the paste sample exhibited peaks representing the existence of PDMS, which means the PDMS coating has a good surface coverage.

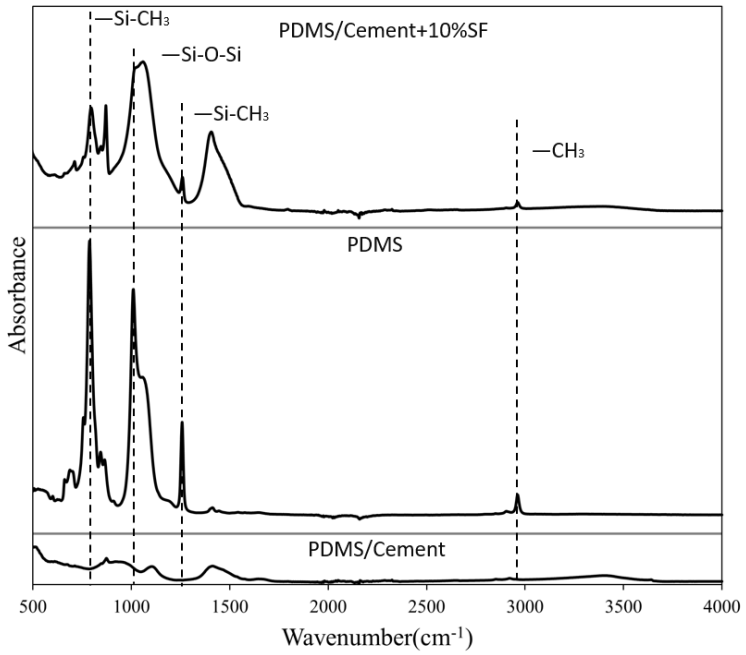


Figure 4.25 Comparison of FTIR spectrums obtained from PDMS and paste samples with or without 10% SF cast against PDMS mould.

The PDMS coating was too thin to be observed with SEM, but its thickness can be estimated by analogy with that measured on PDMS coated glass slides in the work of Teisala et al. (2020), since both the surface of glass slide and SF particles contain hydroxyl groups (Si-OH) that are sites where the grafting reaction happens. Teisala *et al.*, (2020) measured the thickness of PDMS film bonded on a glass slide at room temperature by ellipsometry and atomic force microscope (AFM). It was found that the thickness was 2.8 nm after 1 day of curing and increased to 5.1 nm after 10 days of curing as PDMS molecules 'grow' in the presence of water through hydrolysis. However, the PDMS film grows at a decreasing rate due to the decreased water diffusion through the film. Therefore, it is estimated that the thickness of PDMS coating on the textured cementitious samples was of the order of ~10 nm.

4.6 Hydrophobic microgrid patterned surface

Fabricating a PDMS mold and using this mold for reproducing surface texture is an easy way to create hydrophobic surface structures on cementitious samples in a laboratory, but this method is unlikely to be practical on site as soft lithography is probably not suitable for the creation of surface texture on a large scale. Therefore, an easy and relatively inexpensive approach to create a micro textured cement surface over a large area is required to replace soft lithography. This problem can be viewed as somewhat of a problem for mold design. A possible method is to replace the PDMS mold by a synthetic material with suitable pattern that

mimics (rather than recreates) natural hydrophobic surfaces (such as lotus or taro leaf). In this section, the formation of a micro texture using a microgrid (mesh) was attempted. The resultant surface texture would consist of repeating structural units.

Figure 4.26 shows a schematic cross section of a cementitious material that contains surface indentations made by using a microgrid. Theoretically, the hydration products will fill the microgrid pores thereby creating a connected network of open channels with semi-circular cross section which was originally occupied by the microgrid wires. The surface texture composes of a periodic array of square micropillars on a square grid, whereby the separation distance between the micropillars depends on the diameter of the microgrid wire.

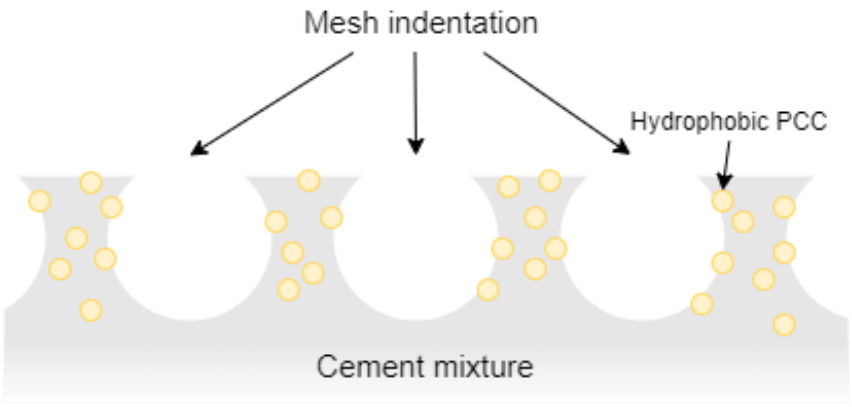


Figure 4.26 A schematic illustration of a textured surface created by casting cementitious material in a mould embossed with a microgrid.

The microgrid was obtained by dismantling a nylon mesh bag into a single layer of microgrid. SEM image showed that the microgrid was woven from wires ~50 μm in diameter and have ~178 holes/cm^2 with an aperture width of ~28 μm (Figure 4.27). Therefore, the generated micropillar array on a textured cementitious sample was theoretically have approximate ~178 pillars/mm^2 with ~50 μm in height. To prepare microgrid patterned samples with a PDMS coating, the nylon mesh needs to be modified with PDMS first before being used as a mould to generate surface structure. The surface modification was done by dip-coating the microgrid in diluted PDMS solution to create a thin film coating of PDMS. Toluene, which is primarily used as a solvent in the preparation of PDMS solution, was used in this study. The diluted PDMS have lower surface tension, forming liquid films on microgrid apertures that can easily stretch and collapse as the solvent dissipates before the PDMS solidifies. The viscosity of the coating solution is a key factor affecting the quality of the end product. If the solution is too thick, it will be difficult for excess liquid to drain off, which may result in complete blockage of the microgrid apertures once the PDMS solidifies. In contrast, a very dilute solution will lead to greatly delayed solidification.

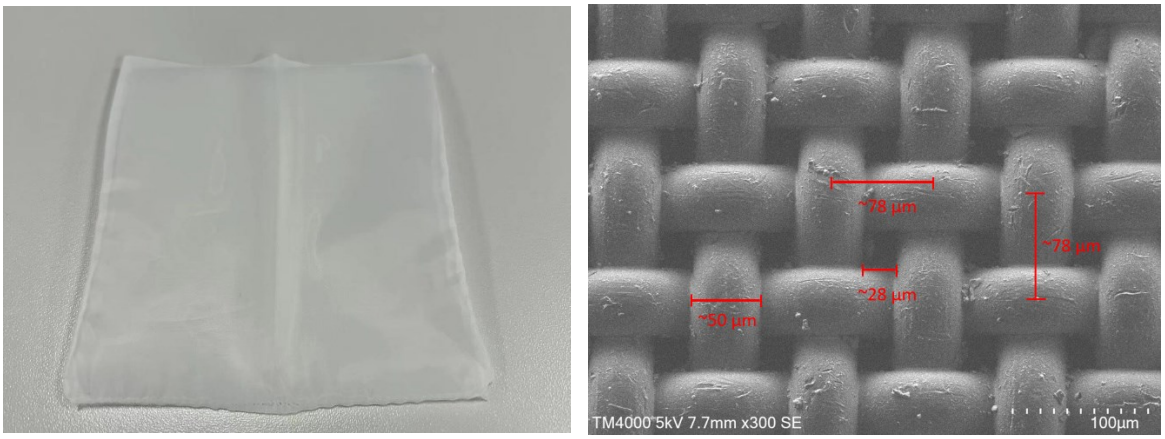


Figure 4.27 Left: microgrid obtained by dismantling nylon bag. Right: SEM showing the texture and dimensions of the microgrid.

The microgrid was immersed in a 1:1 PDMS: toluene solution for half a minute and withdrawn. The coated microgrid was hung in lab air for 24 hours to let the excess liquid drip off and then cured in an oven at 120°C for at least 48 hours until the PDMS solidified. This treatment can be repeated if desired. The chemical composition of the modified microgrid surface was analyzed by FTIR-ATR at five randomly chosen positions, with the aim of detecting the presence of PDMS on the nylon substrate. The data was recorded with a resolution of 4 cm^{-1} over the range of 500 to 4000 cm^{-1}. The spectrum of coated microgrid in Figure 4.28 shows strong absorption peaks from methyl and Si-O-Si bonds near 1260 cm^{-1}, 1010 cm^{-1}, 790 cm^{-1}. However, the FTIR spectroscopy did not detect absorption peaks at 3300 cm^{-1}, 1630 cm^{-1}, 1530 cm^{-1}, which correspond to the presence of nylon. The lack of these characteristic peaks for nylon indicate that the substrate was completely covered with PDMS.

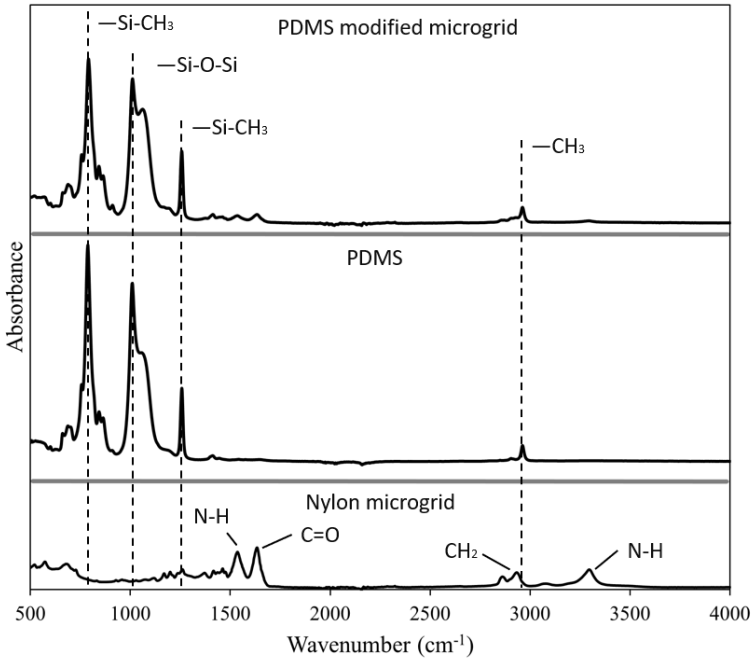


Figure 4.28 A comparison of the FTIR spectrums from nylon microgrid, PDMS and PDMS coated nylon microgrid.

Microgrids dipped into 1: 2 and 1: 5 PDMS: toluene solutions were also tested. Small peaks associated with trace nylon can occasionally be found in the spectrum of microgrid dipped in the 1:2 solution, which indicates the presence of defects on the coating (not shown here). Lee and Lee (2008) showed that the shrinkage of PDMS cured at 100°C was 1.94%, and this increased at higher dilutions. Therefore, the defective coating may arise from the shrinkage of PDMS during curing since the coating is too thin to withstand stresses induced by shrinkage. The exposed substrate can be completely covered by repeating the dip-coating process 2 to 3 times. For a microgrid dipped in the 1:5 solution, the very dilute PDMS barely solidified even after curing at 120° for 5 days. Therefore, in this study, the 1: 1 solution was not used in repeated dip-coating.

Figure 4.29 shows example surfaces of cement paste samples produced by casting against a layer of nylon microgrid in a steel mold. Interestingly, samples cast against uncoated nylon microgrids showed indentations from microgrid wires and excessive microscopic bug holes, but not the designated micro pillars. Since the microgrid can be easily peeled off after casting, these defects are unlikely to be attributed to the grid removal process. Trial experiments were carried out in an attempt to reduce the number of defects, for example by replacing 20% of cement with SF of equal mass. Since SF has particle size 100 times smaller than cement particles, it would fill up the apertures more easily. The sample was de-molded 7 days after casting so that the SF would have enough time to react with hydration products (calcium

hydroxide). However, this did not lead to significant improvements in the surface texture (Figure 4.29 b), which meant that the occurrence of bug holes was irrelevant to the cement particle size. Water droplets placed on these surfaces were absorbed immediately into the sample indicating strong wettability.

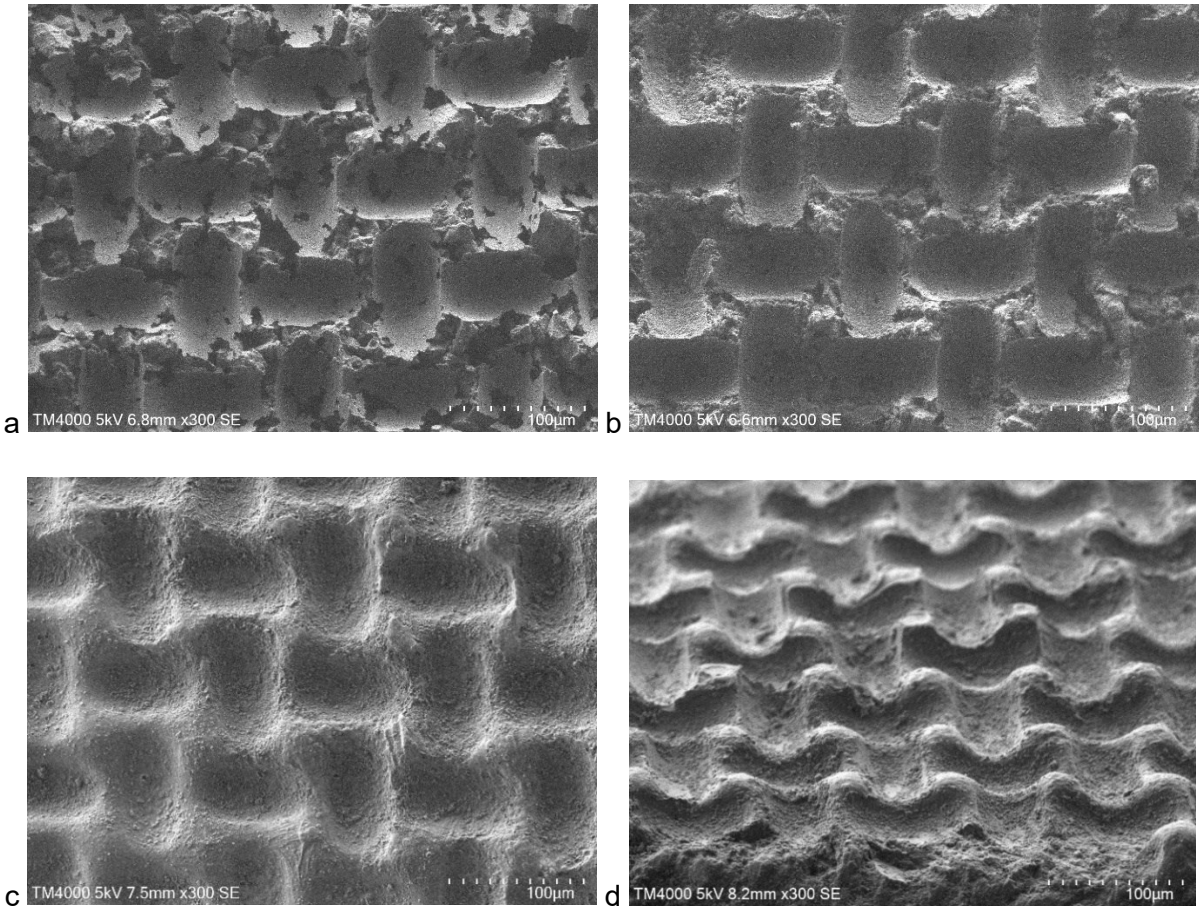


Figure 4.29 The surface appearance of samples cast against nylon microgrid. (a) P-0%H-0%SF and (b) P-0%H-20%SF, cast against uncoated nylon microgrid. (c) and (d): top view and side view of P-0%H-0%SF cast against a PDMS coated nylon microgrid.

In contrast, cementitious samples cast against a PDMS coated nylon microgrid show significant improvements in the surface texture (Figure 4.29 c, d) compared to those cast against uncoated nylon microgrid. The samples are virtually defect free and exhibit the desired surface topography. Furthermore, the new samples did not show the hollow texture that affected the earlier samples (as shown in Figure 4.16 for example). This observation further validates the geometric restriction hypothesis since the microgrid pattern has a width of ~30 µm at its narrowest point and an average width of entrance of ~80 µm. The larger size effectively mitigates the entrance blocking effect, resulting in a solid surface texture with side length of ~25 µm, a height of about ~40 µm, and a top-to-top distance of ~80 µm (Figure 4.29).

These dimensions are consistent to those of the original nylon mesh (Figure 4.27). FTIR spectrums of the microgrid patterned surface show that PDMS is successfully transferred onto the cementitious sample containing 10% cement replacement with SF, while no PDMS residue is detected on samples that did not contain SF (Figure 4.30).

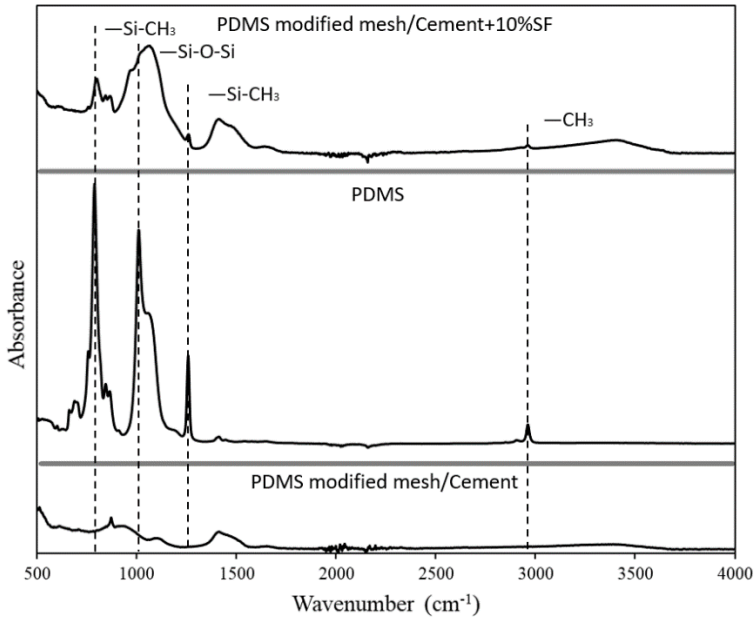


Figure 4.30 Comparison of FTIR spectrums obtained from PDMS and paste samples with or without 10% SF cast against PDMS modified microgrid.

Observations made during sample preparation suggest that the surface structure is also dependent on the hydrophobicity of the material used in the mold. For example, the nylon microgrid maintains a water-rich region at the cement/mold interface. During compaction and prior to setting, the mix water tended to migrate towards the mold thereby increasing the local w/c ratio. Because nylon microgrid is a hydrophilic material, the bleed water is maintained at the cement/mold interface. Note that nylon is hydroscopic, its moisture content at relative humidity in the range of 35% to 65% is 1.5% to 2% wt., and it is capable of absorbing 5% to 8% wt. at saturation (Sepe, 2013). However, this may not be enough to eliminate the accumulated bleed water. Furthermore, the absorbed water will be released from nylon back to the cementitious material as hydration proceeds. As a result, the saturated nylon microgrid would maintain a water-rich region that produced a weak surface. A similar result was found by Horgnies & Chen (2014), who reported that their attempt to produce a textured cementitious surface by using a master mold made with a hydrophilic material (PVA) ended in failure, whereas another attempt succeeded using a mold made with a hydrophobic material (PDMS). They attributed this difference to the formation of a water film at the cement/PVA interface due to the wettability of PVA. In contrast, the hydrophobic nature of PDMS was able to repel excess

bleed water while allowing cement particles to settle on its surface and form the desired surface texture.

4.7 Wettability of hydrophobic cementitious materials

4.7.1 Water contact angle

The water contact angle of cementitious samples was tested by static water drop measurements (Section 3.4.2). Results are summarized in Table 4.4. For non-textured samples, no significant difference was observed in the water contact angles measured on paste, mortar, or concrete, indicating that the presence of aggregate has no influence on surface wettability. However, the addition of HPCC caused an increase in the water contact angle. A higher content of HPCC added into the mix leads to a higher water contact angle. The water contact angle ranged from 24.9° for the control samples (0% HPCC) to 55.5° for the sample with 16% HPCC. Nevertheless, the results indicate a hydrophilic surface property for all non-textured samples irrespective of the content of HPCC.

Table 4.4 Water contact angles measured on the prepared cementitious samples. The numbers in brackets indicate standard error.

		HPCC content			
		0%	4%	8%	16%
Nontextured/ uncoated	P-Non-0%SF-3d	24.9 (2)	39.3 (3.87)	43.1 (4.7)	55.5 (5.5)
	M-Non-0%SF-3d	24.9 (2.1)	35.4 (3.96)	46.5 (3.66)	51.6 (2.14)
	C-Non-0%SF-3d	25.2 (2.05)	33.5 (2.53)	42.8 (2.51)	52.2 (3.54)
Textured/ uncoated	P-L-0%SF-3d	120.1 (2.4)	126.2 (2.79)	126.8 (2.49)	135.6 (2.42)
	P-T-0%SF-3d	123.3 (2.96)	127.2 (2.79)	127.1 (2.64)	142.9 (2.6)
	P-MP-0%SF-3d	113 (2.53)	112.9 (2.84)	117.8 (3.46)	134 (3.42)
	M-L-0%SF-3d	117.3 (2.51)	123.4 (2.57)	124.9 (2.58)	133.6 (2.14)
	M-T-0%SF-3d	122.4 (2.04)	125.7 (2.41)	128.3 (2.39)	140.4 (2.24)
	M-MP-0%SF-3d	111.9 (2.67)	113.8 (2.62)	118.7 (3.49)	130.5 (2.95)
Textured/ PDMS coated	M-L-10%SF-28d	138.5 (1.23)	137.7 (1.17)	137.9 (1.17)	139.5 (0.98)
	M-T-10%SF-28d	138.1 (0.98)	141.3 (1.1)	138.8 (1.26)	137.7 (0.91)
	M-MP-10%SF-28d	132.7 (0.93)	134.2 (0.84)	133.9 (0.92)	134.8 (0.98)
	C-MP-10%SF-28d	131.3 (0.97)	133.8 (1.31)	132.9 (0.9)	135.5 (1.11)

Samples with micro textured surfaces were superior compared to non-textured samples in terms of hydrophobicity. Droplets on the micro textured surfaces were stable, with less than 5° change in water contact angle over 15 seconds. Again, there is no significant difference in water contact angle between mortar, concrete, and paste. Adding HPCC into micro textured samples resulted in a lower surface wettability. For example, the taro-textured surface with 16% HPCC had water contact angle of ~140°, which is higher than the taro-textured surface without HPCC (~123°) and much higher than that of non-textured surface containing 16% HPCC (~50°). Microgrid patterned surfaces achieved contact angles of ~112°, which are comparable to those found on lotus and taro textured surfaces. This implies that the microgrid pattern is roughly as effective as lotus and taro textures in terms of reducing surface wettability. By adding 16% HPCC, the water contact angle on microgrid patterned surface further increased to around 130°.

PDMS coated textured samples showed lower wettability compared to un-coated samples. Flat PDMS surface showed a water contact angle of 105°,which is consistent with the contact angle reported in literatures (Alvaro, Mata; Aaron J, Fleischman; Shuvo, 2005; Khorasani, Mirzadeh & Kermani, 2005). The PDMS coated textured samples showed water contact angles in the range of 133° to 138°, indicating that hydrophobicity was enhanced by surface textures. However, the HPCC content in mixture had little/no influence on water contact angle since in this case, the textured surfaces were already coated with PDMS. It is also interesting to note that the data obtained from PDMS coated samples had much smaller standard errors than the uncoated samples. This may be attributed to the fact that PDMS transferred through grafting reaction formed a thin uniform coating, whereas the HPCC were randomly scattered over the surface. As a result, the obtained water contact angle was influenced by non-uniform distribution of local HPCC concentration.

4.7.2 Contact angle hysteresis

The contact angle hysteresis was characterized by measuring contact angles on an inclined micro textured surface (Section 3.4.3). The water droplets on the micro textured samples created contact angles larger than 90°, as presented in Table 4.4, in which some measurements on PDMS coated surfaces and those containing 16% HPCC showed water contact angles approaching or exceeding 150°. However, none of these water droplets rolled off the surface. Instead, all droplets pinned on the surface when the surface is titled vertically or fully inverted. An example of this is given in Figure 4.31. Therefore, it was not possible to measure the contact angle hysteresis in the conventional manner.

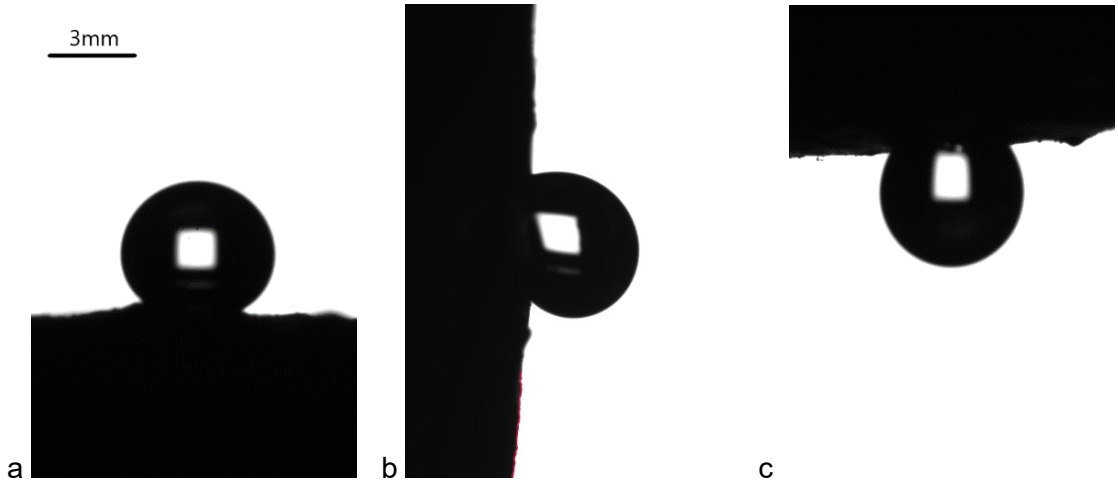


Figure 4.31 Water droplet pinned on M-L-0%H-10%SF when the sample was rotated by 90° (b) and 180° (c).

4.7.3 Motion of water droplets

The behaviour of water droplets was found to be different when they were dropped on an inclined micro textured surface. Rolling or bouncing of droplet can be achieved at certain combination of releasing height and angle of inclination. The motion space is shown in Figure 4.32 where solid (black) markers indicate the combinations where rolling or bouncing motion were observed. Generally, at a given height, if the motion of droplets was observed at a certain angle of inclination, it will also be observed at larger angles. Figure. 4.33 shows an example of the movement of droplets on a M-L-0%H-0%SF surface inclined at an angle of 30°. When a droplet was released from 4 cm above the surface, the droplet rolled off the surface leaving no trace of water (Figure 4.33 a). However, when the releasing height was increased to 30 cm, the droplet became pinned to the location where it hit the surface. The micro textured surfaces exhibited no hydrophobicity in this case since the water contact angle was less than 90° as shown in Figure. 4.33 b. The droplet then spread out and was gradually absorbed into the sample. However, droplets rolling across the surface were observed again if the surface was dried and the releasing height was reduced back to 4 cm.

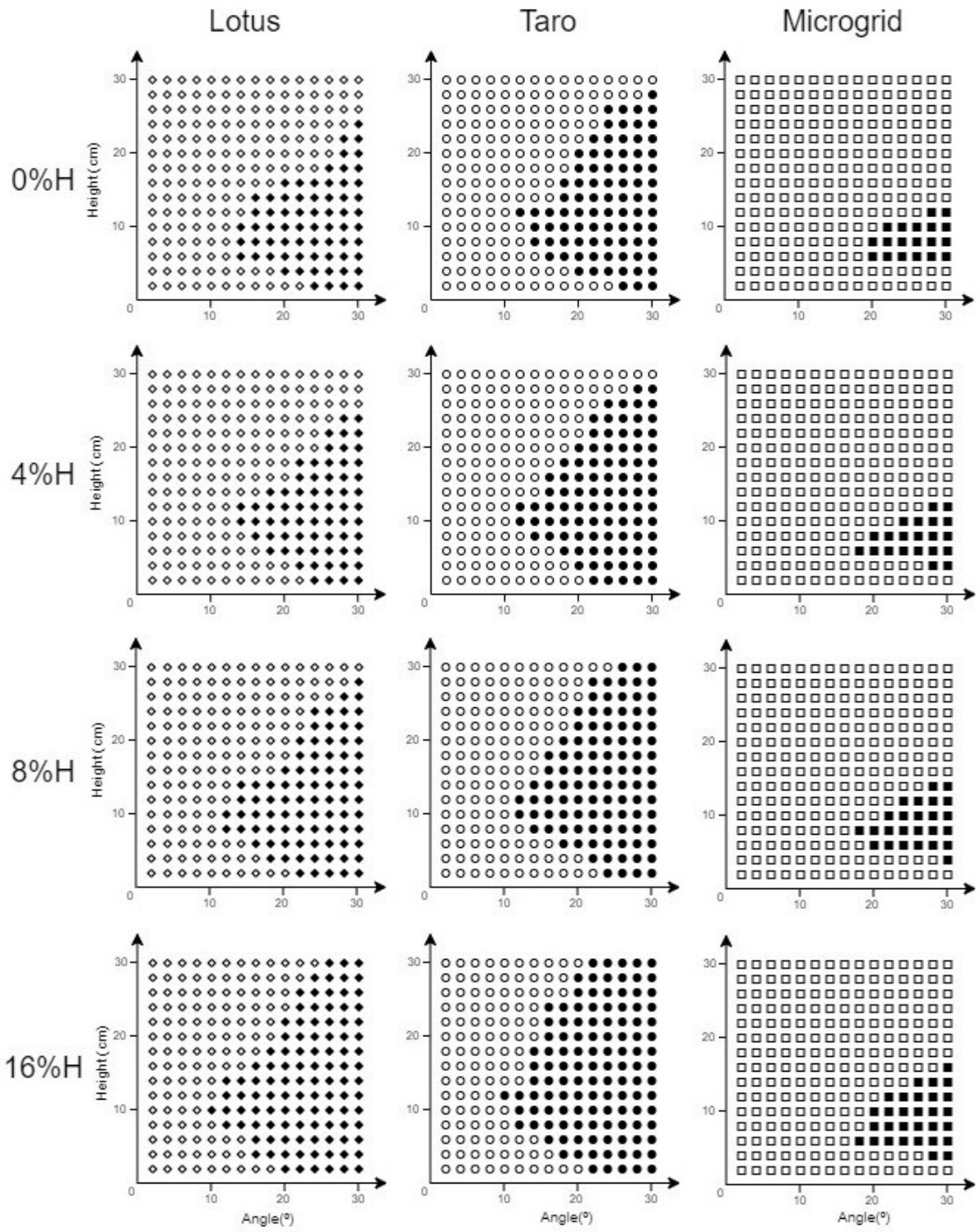


Figure 4.32 Motion space of falling droplets for micro textured mortars (0%SF, 3 days old) with various amounts of HPCC.

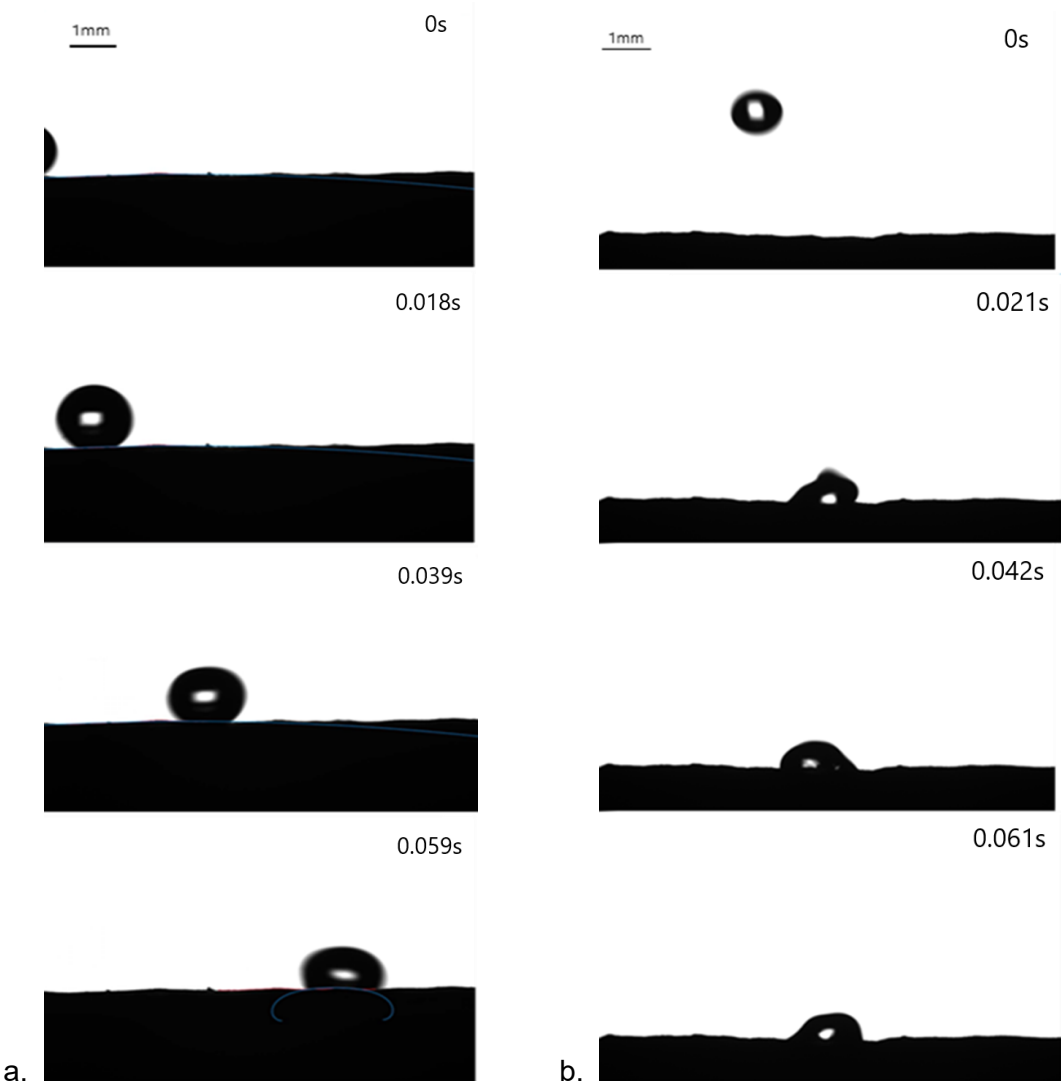


Figure 4.33 Examples of wetting behavior of water droplets dropped from (a) 4 cm and (b) 30 cm above a M-L-0%H-0%SF surface inclined at 30°.

The results show that microgrid patterned surfaces are more susceptible to the impact of falling droplets than lotus and taro textured surfaces, since droplet motion was not observed when the releasing height was greater than 12 cm. However, droplet movement was promoted by textured surface with HPCC. The higher the HPCC content, the lower the inclination angle and releasing height needed for droplets to roll off the surface. When droplets were dropped about 4 cm above a MP-0%H-0%SF surface inclined at 30º, the droplets moved over a short distance and then became pinned on the surface (Figure 4.34 a). The same pinning behaviour was also observed on MP-4%H-0%SF. At 16% HPCC, the droplets rolled off the surface leaving no traces of water on the surface (Figure 4.34 b).

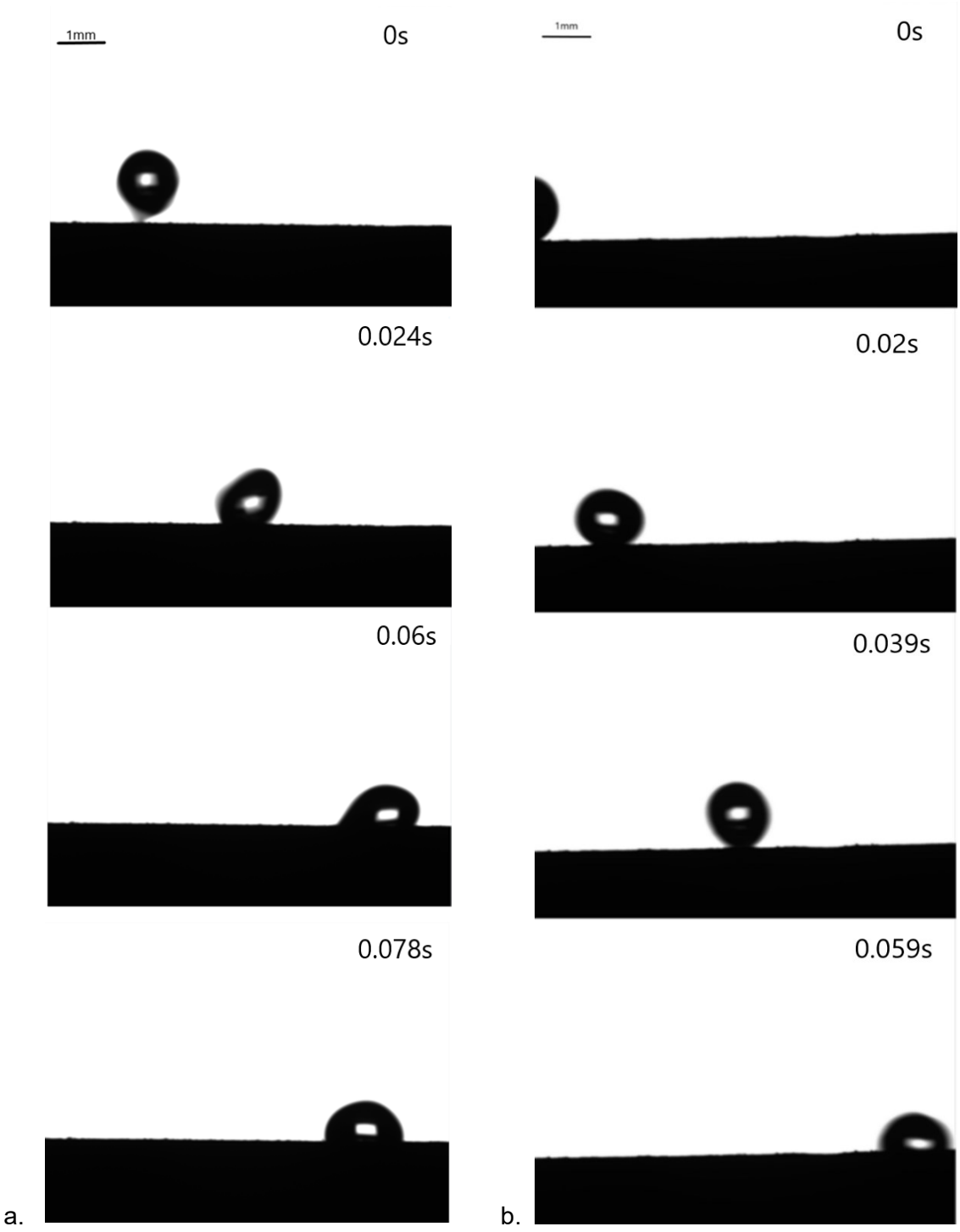


Figure 4.34 (a) A water droplet dropped from a height of 4 cm became pinned on M-MP-0%H-0%SF inclined at 30° after rolling over a short distance. (b) A water droplet dropped from the same height rolled across M-MP-16%H-0%SF surface inclined at 30°.

PDMS coating on cementitious surface greatly improved the mobility of water droplets. It can be seen from Figure 4.35 that rolling droplets were observed on the coated lotus and taro

textured surface inclined at 10° and on the coated MP surface inclined at 12°. The coating also improves the ability of texture to withstand impact from falling droplets.

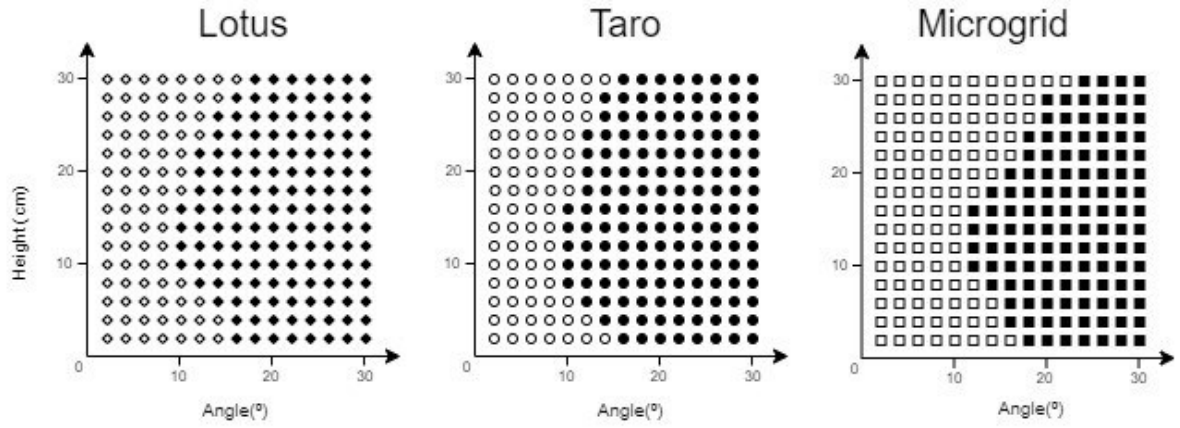


Figure 4.35 Motion space of falling droplets for PDMS coated micro textured mortars (0%HPCC, 10%SF, 28 days old).

4.7.4 Discussion

The results showed that micro textured surfaces have lower surface wettability than nontextured ones. Note that FTIR spectrums (Figure 4.21 and 4.30) showed no PDMS residue was detected on surface of sample cast against a PDMS mould. Therefore, the increase in water contact angle can be completely attributed to the effect of micro textures. The movement of droplets across the surface is a good indication of wetting mechanism. Bouncing or rolling off an inclined surface suggests a Cassie-Baxter state since repulsion from air trapped under the droplets makes the surface slippery. However, it is well-established that wetting of inherently hydrophilic material is always energetically favorable (Liu *et al.*, 2007; Nosonovsky & Bhushan, 2007; Whyman & Bormashenko, 2011). Droplets placed on a hydrophilic surface would be expected to penetrate the surface texture and spread over as roughness brings about enhanced hydrophilicity. Hence, it is interesting to observe that water droplets placed on the micro textured surfaces stabilized at high contact angles since cementitious materials exhibit hydrophilic properties.

The reason for this can be attributed to the pinning of contact line on the side wall of the surface textures, preventing water to penetrate into the space between them. As discussed in Section 2.1.5, water pinning is promoted by roughness such as sharp edges, defects, and cavities. Cementitious surface textures generally include additional smaller scale roughness on microstructure, which increases the likelihood of contact line pinning. In the presence of HPCC, the pinning would also happen at the boundary between cement matrix and HPCC

particles (Section 2.1.5). The contact angle must be augmented by at least 135°, which is the difference between the contact angle of cement paste and HPCC, in order to pass through the HPCC particle. It should be stressed that even though the pinning effect leads to water droplets exhibiting high contact angle, the droplets are in a metastable state (Bormashenko, 2015; Ishino, Okumura & Quéré, 2004). As shown in Section 2.1.7, an input pressure would cause the penetration of water into surface textures. For micro textured surface coated with PDMS, the air trapped by surface structure under water droplets is energetically flavored as the surface material (PDMS) exhibits hydrophobicity.

Despite having a high contact angle, the pinning behavior of water droplets was observed in all cases. An explanation is that the textured surfaces display “petal effect” in which the gravity of droplets is largely offset by adhesion (Liu & Jiang, 2010; Dawood, Zheng & Liew, 2011; Lai *et al.*, 2009). Pores in the range of 2 nm to hundreds of microns exist in the cement paste matrix as it is a porous material by nature (Hewlett, Justnes & Edmeades, 2019). When a droplet is placed on the surface of cementitious materials, water would be absorbed into these capillary pores. This leads to an adhesive force caused by meniscus, which prevents the movement of droplets. PDMS coating created by grafting reaction is probably too thin to avoid some level of infiltration of the coating by water, thus the petal effect was also observed on coated samples. Micropores of the order of 2 to 8 nm have little contribution to the percolation of water flow in cement paste (Hewlett, Justnes & Edmeades, 2019), but they may act as sealed pockets which generate negative pressure upon droplets (Dawood, Zheng & Liew, 2011; Lai *et al.*, 2009).

When a droplet is released from a certain height above an inclined surface, inertia combined with gravity, can overcome the adhesive force while the force component perpendicular to the surface is not sufficiently large to de-pin the contact line. This allows the droplet to remain in the Cassie-Baxter state and move across the surface. Low energy materials (HPCC and PDMS coating) not only contribute to the pinning of contact line on the wall of micro textures, but also decrease the attraction between surface and droplets, making the droplets easier to move. However, the transition from the Cassie-Baxter state to the Wenzel state would happen when a droplet is released from a height that is large enough for the force perpendicular to the surface to drive the droplet downward (depinning the contact line). This explains why the rolling behaviour of a droplet is related to its release height. The Cassie-Baxter state does not recover once the droplet touches the bottom of surface texture (Whyman & Bormashenko, 2012).

The ability of a micro textured surface to hold a droplet against its own weight and body forces is related to surface structure density (Extrand, 2004; Zheng, Yu & Zhao, 2005). A denser surface structure allows for a greater resistance to water penetration. Given this, the large surface structure of microgrid pattern make it less effective to withstand droplet impact as it has a surface structure density of 178 per mm^2, while lotus and taro textures have density of ~3500 and ~3900 per mm^2 respectively (section 4.4 and 4.6). It is also interesting to notice that lotus and taro textures have similar structure density, but the taro textured surface allowed for a higher drop height without pinning on the surface at a given inclination angle. This observation can be attributed to an "energy-stable configuration" of the taro texture. This refers to protruding features on micro textures, such as mushroom-like or nail-like textures as illustrated in Figure 4.36. These protruding features create a high energy barrier to pin the contact line, as a result, the air cushion beneath the droplets becomes more stable. This finding agrees in principle with the results obtained by Bormashenko (2015) and Whyman & Bormashenko (2011), who reported that protruding features that favour contact line pinning can be manipulated to create super hydrophobicity from a hydrophilic material.

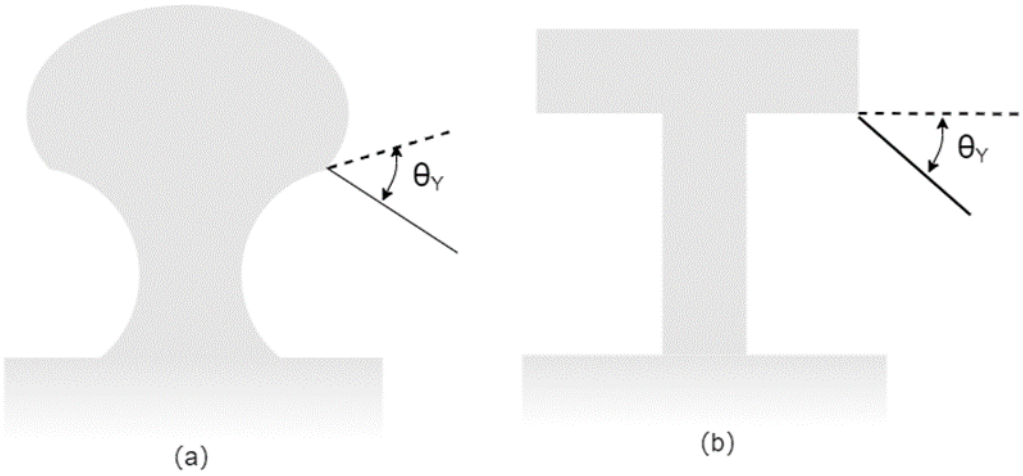


Figure 4.36 Two examples of "energy-stable configuration" to maintain the Cassie-Baxter wetting state on a roughened hydrophilic surface: (a) mushroom-shaped element. (b) nail-head-shaped element.

The energy-stable features on taro texture were formed during drying of the leaves when exposed to sun. The wall of epidermal cells of taro is very thin, so that the deformation can take place easily. When a fresh leaf is exposed to strong sunlight, cells become dehydrated and drying shrinkage occurs and, in consequence, the resultant cell walls exhibit distortion and irregular shape. The deformed area provides the energy-stabled topographic feature (arcs concave inward as pointed out by red arrow in Figure 4.37) for pinning the contact line.

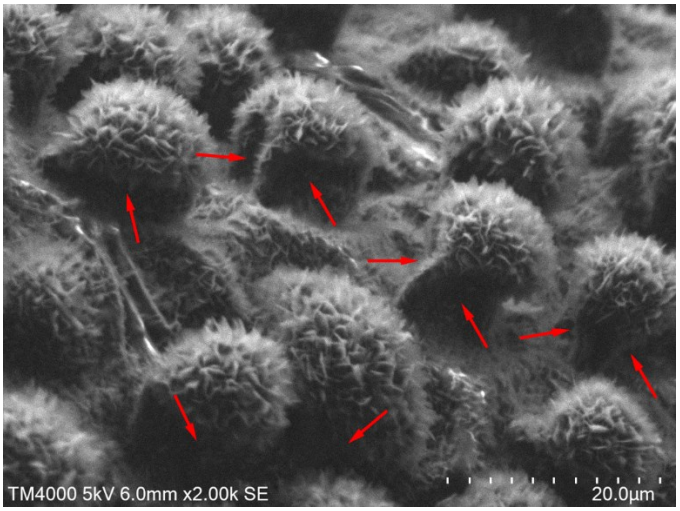


Figure 4.37 SEM image of deformed cell walls of a dried taro leaf. Red arrows show the energy-stable features for contact line pinning.

When compared to real hydrophobic leaves, the contact angles on reproduced surfaces were reduced by approximate 20° to 40° (Table 4.4). Adding HPCC or coating with PDMS narrowed the difference, but the contact angles were still lower than that of real leaves. The main reason for the lower contact angle is because the nano tubules on the surface of real leaves are not reproduced on cementitious materials. As discussed in Section 2.1.7, hierarchical structures result in a lower water solid interface area than single-scale structures, leading to higher water contact angles. Soft lithography has a limited resolution and it is unable to replicate the nano tubules on plant leaves that are typically in the size 100 to 200 nm (Ensikat *et al.*, 2011). Cheng *et al.* (2006) removed the nano tubules by annealing lotus leaves at 150°C for 1 hours. The resultant surface had a water contact angle of 126°, which is like the contact angles obtained on the reproduced lotus textured cementitious materials in this study.

The findings in this chapter indicate that a micro textured hydrophobic surface can be constructed from cement mixture. Treatment of the surface with lower energy materials modifies surface properties and further increases hydrophobicity. Comparing these results with existing studies suggests that the created surfaces are on par with most hydrophobic treated cementitious materials reported in the literature. All the micro textures created in this chapter give water contact angles comparable to concretes coated with commercial silicate and fluoropolymer paints, which gave contact angles of 116° and 111°, respectively (Al-kheetan, Rahman & Chamberlain, 2020). Siloxane is another commonly used hydrophobic treatment and this gave water contact angle of ~108°, and the addition of nano particles to induce surface roughness resulted in a further increase to 123° (Muzenski, Flores-vivian & Sobolev, 2015). However, the surface structures produced with soft lithography achieved a

greater increase in hydrophobicity than roughness created through incorporating nano particles, as PDMS coated textured surfaces had contact angles ~138°. It should be noted that the contact angle of PDMS alone is 105° and therefore the observed increase in hydrophobicity is attributable to the induced surface textures. Research on motion of droplets on a micro textured cementitious surface is very limited. Horgnies & Chen (2014) reported water droplets with a contact angle of 140° pinned on a horizontal micro textured surface consisted of repeated conical units. Gao *et al.* (2019) reported rolling motion of droplets on a magnesium cement surface tiled at a small angle that was embedded with random roughness transferred from a sandpaper using soft lithography, but did not report on the influence of release height.

4.8 Conclusion

Ball milling of calcium carbonate with stearic acid resulted in a super hydrophobic powder, HPCC, with water contact angle of 160°. Particle sizing analysis revealed that the dispersed HPCC particles had a size range between 0.05 to 1.5 μm, with prismatic and granular morphologies. However, the HPCC particles tend to agglomerate and form clumps of larger particles. Cement hydration was unaffected by HPCC, but showed a water encasing effect that influences workability, compressive strength, and microstructure of the resulting cementitious materials, especially for neat cement pastes. However, this effect was less severe in mortars and concretes because the presence of aggregate particles and their impact during mixing breaks down HPCC agglomerates and releases the trapped mix water.

Soft lithography was found to be a very effective method for transferring the micro texture of plant leaves onto cementitious samples. Both qualitative SEM and quantitative image analysis showed high similarity between the original and reproduced surface structures. However, the PDMS mould used for transferring surface textures should be applied no more than three times because the cumulative effect of pore blockage due to adhered debris and remnants in the mould would affect the fidelity of the cast texture. The research also showed that casting SF-containing cementitious mixtures on a PDMS mould resulted in the transfer of PDMS onto textured samples through grafting reaction between SF particles and PDMS. The grafted PDMS molecules formed a thin layer (approximately 10 nm) on the surface of samples. Optimum level of replacement of cement by SF and curing time were found to be 10% and 28 days respectively because a higher replacement level or longer curing time resulted in excessive bonding between the cementitious material and PDMS mold, leading to surface damages during demolding.

A microgrid pattern, which consists of repeating structure units, can be created on

cementitious materials using nylon mesh. However, cementitious mixtures directly cast against a nylon microgrid yielded a surface that is full of bug holes due to the presence of a water-rich layer at the microgrid-paste interface. The use of PDMS coating changes the wetting tendency of nylon and eliminates this water-rich layer. Pre-coating the nylon mesh with PDMS prior to casting has been shown to be a successful strategy for producing microgrid textures on cementitious materials with high fidelity.

The results from this chapter also showed that the surface structure and contact angle of textured samples were not affected by the presence of fine or coarse aggregate particles in mortar or concrete scale samples. This is because of the relatively large size of aggregate particles meant that they were not involved in the creation of micro textures. Therefore, it can be said that the wettability of micro textured cementitious materials is mainly governed by surface geometry and the properties of the cement paste mixture.

Wetting behaviour of micro textured surfaces was related to how a droplet reaches the surfaces. A rolling or bouncing motion of droplets were observed when they were released onto tilted surfaces, indicating the Cassie-Baxter wetting state. However, the transition from Cassie-Baxter state to the Wenzel state can occur if the impact forces water droplets to penetrate the surface structure. Results from observing the motion of droplets at various release heights and inclination angles showed that taro-textured surfaces possessed the greatest resistance to droplet impact while microgrid-textured surfaces had the lowest resistance. Adding HPCC and/or PDMS coating was able to modify the surface properties, resulting in a more slippery surface and a greater droplet impact resistance.

Droplets resting on horizontal textured surfaces showed contact angles in the hydrophobic to superhydrophobic regimes, such as on PDMS coated samples. However, these droplets remain pinned on the surface even when the surfaces were fully inverted. This is because adhesion forces, which mainly arise from capillary suction, significantly restricted the movement of droplets. It can also be concluded that gravity and the inertia of falling droplets can overcome the adhesive forces to allow the droplets to move along tilted surfaces.

5 Mass transport properties of hydrophobic cementitious materials

This chapter looks at the effect of hydrophobic treatments (surface microstructures and HPCC) on mass transport properties of cementitious materials. Images of micro textured surfaces submerged in water revealed the presence of air cushion between the micro textures. The air cushion was initially stable and resisted coalescence on micro textured samples containing high HPCC content (16%) or PDMS coated surfaces. However, the air cushion shrank over time and eventually disappeared (within 15 minutes) as it gradually dissolved in water. Furthermore, the effects of HPCC and micro textured surfaces on mass transport properties were studied. This showed that HPCC was effective in hindering water ingress, but not water vapour transport. Concrete samples containing 16% HPCC by the weight of cement showed on average 65% lower water sorptivity than concrete samples without HPCC. Similarly, surface micro textures hindered water absorption, but had no influence on water vapour transport. The resistance against water absorption was related to the formation and stability of air cushion between the micro textures. The influence of water pressure on the performance of hydrophobic cementitious materials was determined by measuring water absorption at 25 cm water depth. For the first time, a modified Sharp Front model of water absorption was established to describe the imbibition behaviour of the porous materials in the presence of external water pressure in sealed condition. It was found that the water pressure resulted in an increase in water sorptivity suggesting the surface microstructure and HPCC are less effective under pressurized conditions.

5.1 Introduction

Concrete structures in contact with water over time can suffer from various types of deterioration, many of which are related to the ingress of aggressive species through water absorption. The gradual deterioration of concrete structures may lead to leakage and loss of load-bearing capacity. To enhance the long-term durability of cementitious materials in aggressive environments, conventional methods include using low water/cement (w/c) ratio and pozzolanic supplementary cementitious materials to substitute a portion of cement to refine its porosity (Kim *et al.*, 2014; Massazza, 1998) or adopting membranes as a physical barrier to prevent water ingress (The Concrete Society, 2013). However, the use of low w/c ratio and/or blended cements are limited to some extent by practical requirements (e.g. workability) and these approaches do not eliminate porosity or mass transport entirely. Furthermore, certain blended cements have lower reactivity and strength gain or impact other

properties, for example a lower resistance to carbonation compared to Portland cement (McCarthy & Dyer, 2019). Waterproofing membranes may fail over time and require regular monitoring and maintenance. Therefore, developing concretes with water-resisting property is of great importance for the durability of concrete structures.

A potentially effective strategy used in practice is through addition of water resistance admixtures in concrete. These admixtures may contain pore blockers or form a water repellent coating on the capillary pore walls, thereby increasing the water contact angle and impeding water ingress (Hewlett, Justnes & Edmeades, 2019). The most common water-resisting admixtures can be divided into two groups: water repellents and crystalline products. Water repellents contain mainly oily or waxy compounds, such as long-chain fatty acids, stearate, and mineral oils. Products in this group are thought to disperse in water and react with calcium ions to form insoluble calcium salt, which precipitates as the concrete hardens. It is this precipitate that modifies the surface wettability of capillary pores and results in hydrophobicity (Medeiros & Helene, 2008; Al-kheetan, Rahman & Chamberlain, 2019; Nunes & Slízkova, 2014). The hydrophobic action of crystalline waterproofing products is different from that of water repellents. This type of admixture can slowly react with hydration products and moisture to form crystalline products that block pores (Li *et al.*, 2019). Compared to conventional methods, water resistance admixtures can be used at high dosages without significant strength loss and can be applied on existing structures.

It is well-established that air can trap within submerged micro textured surfaces (Domingues *et al.*, 2018; Arunachalam *et al.*, 2020; Domingues, Arunachalam & Mishra, 2017). This can occur even for textured surfaces made of hydrophilic materials due to chemical heterogeneity or additional smaller scale roughness on the textured surfaces (Kaufman *et al.*, 2017). However, to the best of our knowledge, there are no existing studies on the phenomena of air trapping and its effects on mass transport properties of micro textured cementitious materials. Therefore, it would be interesting to determine if air trapping occurs on the micro textured cementitious materials developed in Chapter 4 and establish its potential to reduce water ingress.

In this chapter, an optical microscopy technique was used to detect and study the air cushion trapped between microgrid textured cementitious materials. Furthermore, mass transport properties of hydrophobic cementitious samples were measured and the effect of PDMS coating on enhancing the stability of trapped air was highlighted. Water absorption testing was carried out to determine the effect of HPCC and micro textures on sorptivity. Textured and nontextured samples were tested for water imbibition under a hydrostatic pressure which is

sufficiently high to cause the collapse of trapped air. These results would help determine the significance of trapped air cushion on reducing water absorption. Finally, water vapour absorption was tested to understand the effects of the developed surfaces on gas transport.

5.2 Experimental

Cementitious samples tested in this chapter were prepared at w/c ratio of 0.4 according to the mix design given in Table 4.1. PDMS moulds for producing surface textures were used no more than 3 times to ensure a high fidelity of the cast textures as discussed in Section 4.4.1. Then, the samples were cured according to Section 3.1.4. Following curing, the samples were oven dried at 50°C until constant weight, defined as a mass change of less than 0.1% per day, to achieve a uniform and constant moisture state prior to the mass transport tests.

It is certainly useful to determine if a textured cementitious surface is able to maintain the Cassie-Baxter state when submerged underwater. Therefore, an experiment was designed to observe the development of trapped air between surface textures. Optical imaging is commonly used for studying the wetting state of submerged surfaces (Domingues *et al.*, 2018; Domingues *et al.*, 2017; Arunachalam *et al.*, 2020). However, the method has a finite resolution and is only suitable for monitoring trapped air on textured surfaces that have a regular pattern composed of large features such as posts and gratings (Lloyd, 2015). Visual assessment of the wetting state of irregular random textures and uneven surfaces with optical microscopy is difficult. Therefore, in this study, optical microscopy was used for observing the wetting states of microgrid textured samples only since these consist of large repeating structural units.

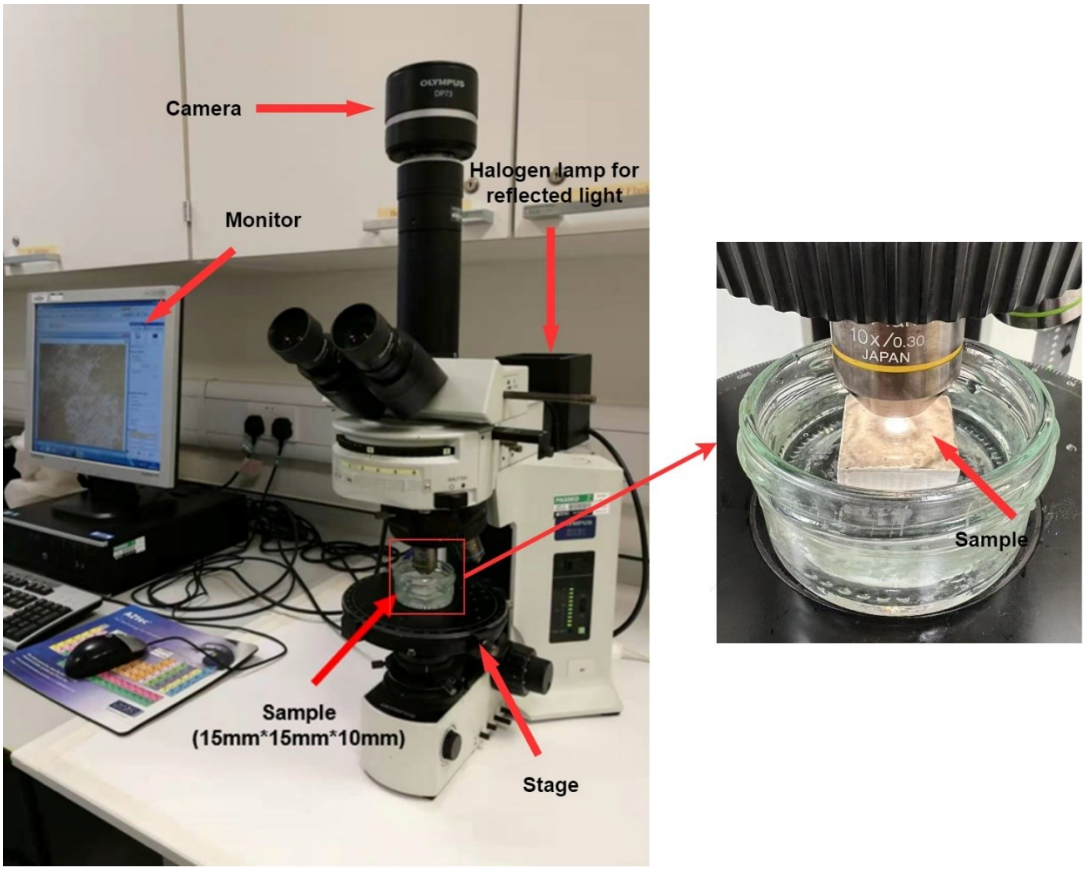


Figure 5.1 Experimental arrangement using an optical microscope and digital image processing to study the air cushion trapped between surface textures of cementitious materials.

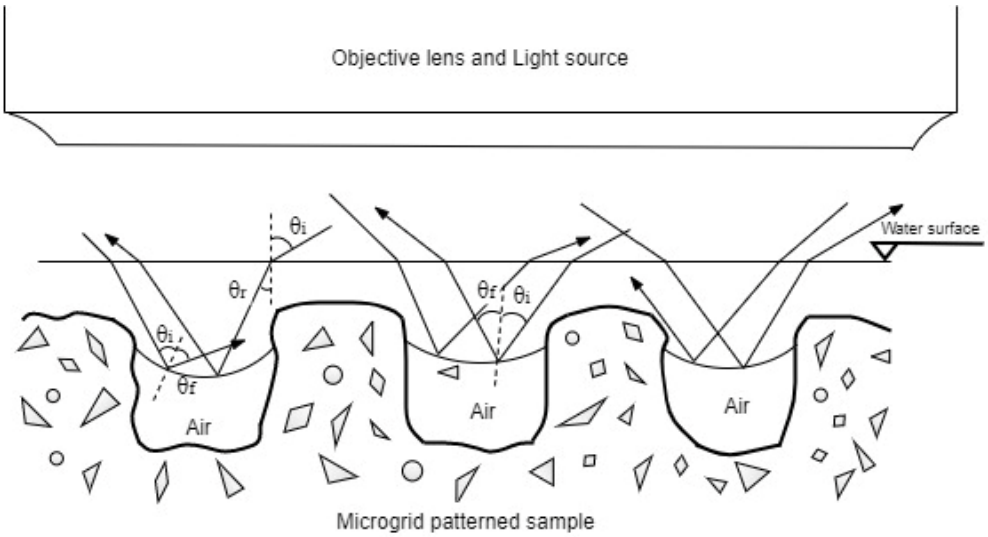


Figure 5.2 Schematic diagram showing the light propagating paths through water and reflected at the trapped air/water interface.

Figures 5.1 and 5.2 show the actual test arrangement and a schematic of the optical imaging method to detect trapped air. The sample was sectioned into small pieces, about 15 mm in

both length and width, using a precision diamond saw. The bottom and sides of sample were sealed with waterproof tapes leaving the textured surface exposed to air. The sealed sample was then placed in a container with the textured surface facing upward. Water was then syringed into the container slowly until the textured surface was entirely submerged.

Reflection occurs when the microscope light beam passes through water and hits the water-air cushion interface between pillars. This is schematically shown in Figure 5.2. Therefore, the air cushion will appear brighter and can be distinguished from the darker wetted area. In some cases, the detection of air cushion was facilitated by processing the raw (colour) images using ImageJ to give binary images to highlight the trapped air. This allows the area fraction of air cushion to be approximated and plotted as a function of immersion time.

Gas transport (oxygen diffusion and permeation) tests were carried out on cylindrical samples 50 mm in height and 100 mm in diameter, following the procedures described in Section 3.3.3 and 3.3.4. Since the micro textures were considered a surface treatment and had no influence on bulk gaseous transport properties, these tests were only carried out on non-textured samples to determine the influence of HPCC. The same samples were used for oxygen diffusion followed by oxygen permeation since the tests were non-destructive. It is recognized that the difference in mass before and after the test was less than 0.5 g and regression coefficients of linear fit used to determine the intrinsic permeabilities were greater than 0.98 that allow for their values to be considered valid. The results are reported as averages obtained from three replicate samples.

Water vapour absorption data was obtained on mortars of 25 cm by 25 cm by 10 cm. The samples were covered with waterproof tape with only the textured surfaces exposed to moisture (98% RH, 25°C), as described in Section 3.3.2. The increase in mass of samples due to vapour absorption was measured every day for the first two weeks and every week thereafter. If vapour condensates into liquid on surface, the surface was dried with a tissue first before weighing.

Water sorptivity was measured according to Section 3.3.1 on at least three replicates. The sides of each sample were covered with waterproof tape and the bottom face was then exposed to water to ensure one dimensional water uptake. Mass recordings of non-textured sample were performed at 20 mins interval for 4 hours, while textured samples were measured at 10 mins interval due to air trapped at the surface dissolving in water over time. After that, the samples were oven dried again at 50°C to constant mass for cyclic wet-dry testing.

Lotus textured mortars with PDMS coating were used to measure the influence of hydraulic pressure on their water sorptivity. Theoretical maximum hydraulic pressure that the surface

can withstand was estimated using a model proposed by Zheng, *et al.,* (2005), which assumed the work done by external pressure was totally transformed into the increase of interfacial energy (Appendix I). Results from water contact angle measurement and observation of trapped air cushion indicated that the performance of PDMS coated surface texture under water is independent of HPCC content in cement matrix. Therefore, HPCC should not be considered in the calculation. The estimated maximum water pressure is 2133 Pa (relative to atmospheric pressure). This means the trapped air cushion can survive a water pressure up to 2133 Pa, which corresponds to a water depth of 22 cm, without collapsing to the Wenzel state.

Based on the above calculation, submerging samples in water of 25 cm depth would eliminate the effect of texture. In this study, new samples were made and tested to avoid the potential influence of aging and deterioration. The experimental procedures were similar to those described in Section 3.3.1. The only difference was that these samples were tested in a bucket filled with water to a depth of 25 cm, instead of in a shallow tray (Figure 5.3).

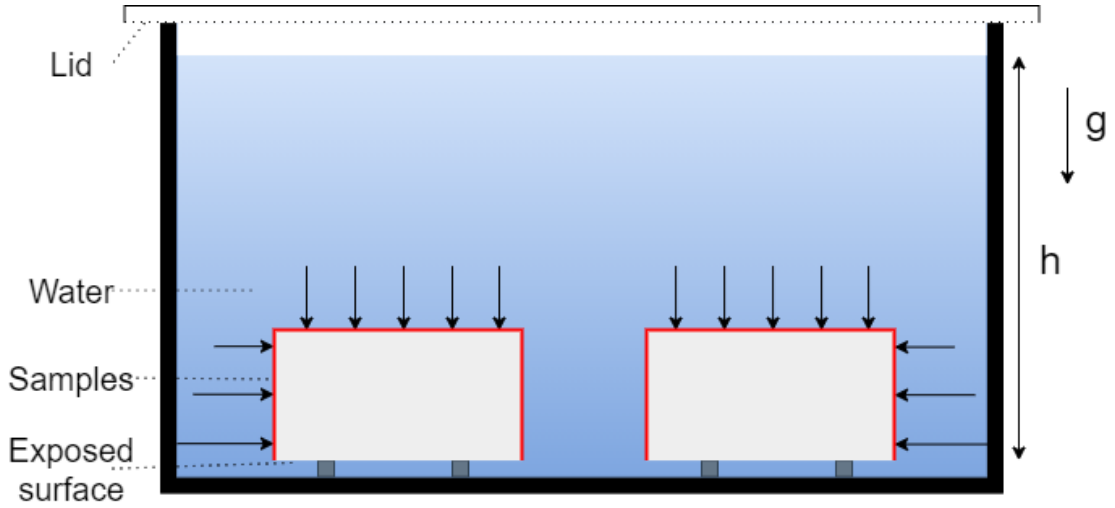


Figure 5.3 Low pressure water absorption apparatus. The exposed surfaces are placed face downward on plastic strips. Red lines represent the surfaces sealed with waterproof tape.

Total water absorption data was obtained on standard 50 mm cubes. Samples were first submerged into water and the absorption was carried out in vacuum for 4 hours. The samples were then removed from the vacuum chamber and left in water for a further 43 days until saturation. Total absorption can be calculated as the difference between the mass of saturated and dried samples. Porosity can be estimated from the absorption data, which was given by equation:

$$\varphi = \frac{(m_s - m_d)}{\rho V_{cm}} * 100\%$$

Where m_s and m_d are the mass of saturated and dried samples respectively, ρ is water density and V_{cm} is the volume of cement matrix.

This test was carried out on non-textured samples only as the amount of water can be absorbed at saturation is related to the porosity of the bulk sample, which is not affected by surface micro textures.

5.3 Trapped air cushion

Figure. 5.4 shows the development of air cushion on a MP-8%H sample. These images were taken at 100x magnification. An air cushion (Figure. 5.4 a), which covered a large fraction of surface, can be observed immediately after the textured sample was immersed in water. This happens when the air originally present in the texture cannot escape. The air film then dissolves into the surrounding water or coalesces to form air bubbles (Figure. 5.4 b and c). The bubbles grow continuously to form larger bubbles, while the air cushion decreases simultaneously (Figure. 5.4 d). Typically, it takes less than 180 seconds for the air cushion to disappear. For samples containing low amounts of HPCC (MP-0%H and MP-4%H), the lifetime of air cushion is even shorter. In these samples, the air cushion either quickly coalesces into air bubbles or does not form throughout the observation.

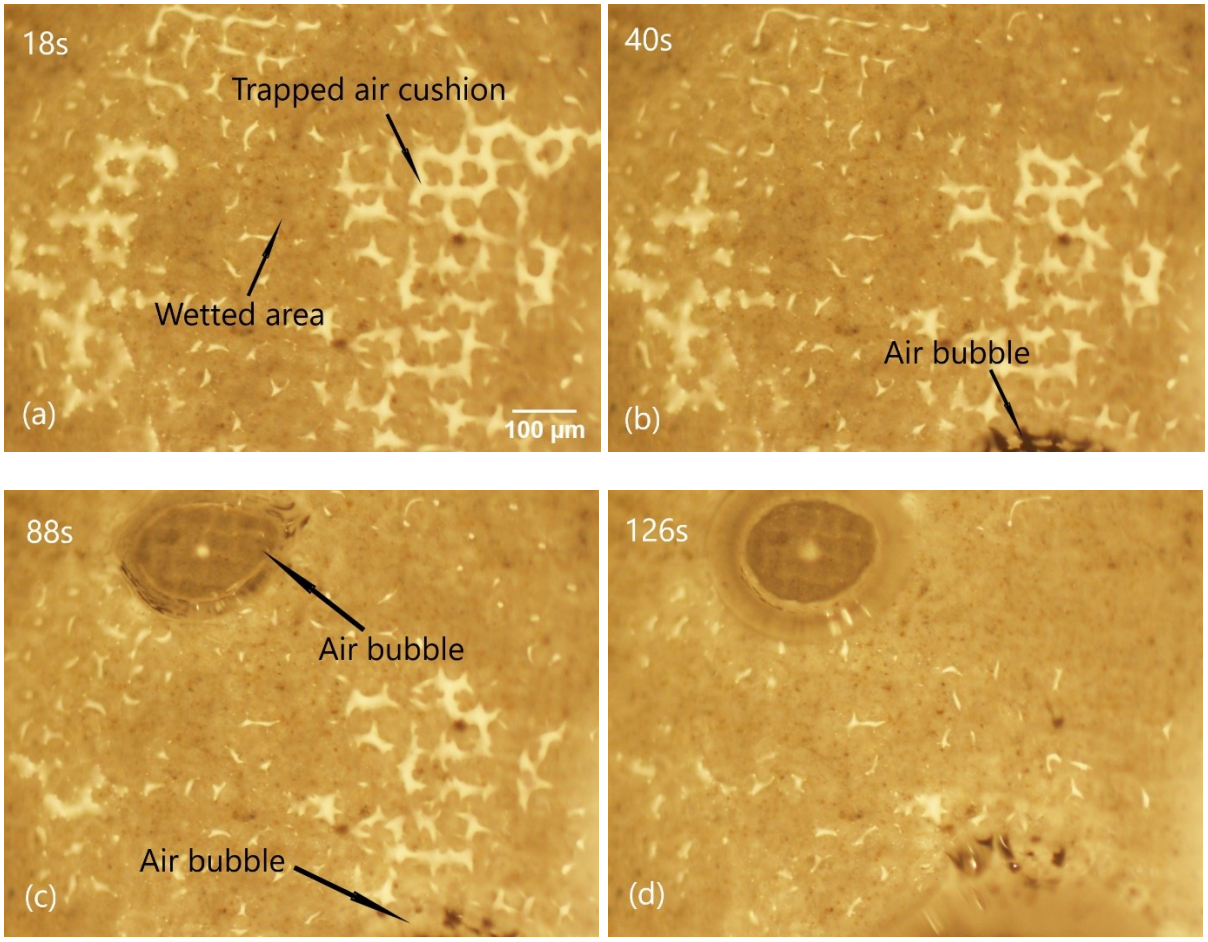
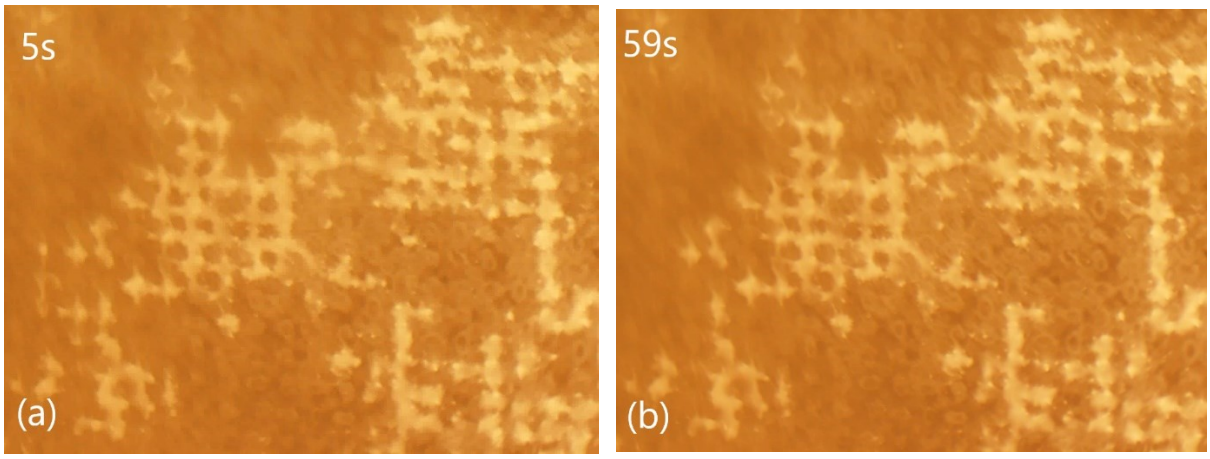


Figure 5.4 Optical microscope images of the evolution of air cushion on a MP-8%H sample at the same location. Time counting began when the surface was immersed in water.



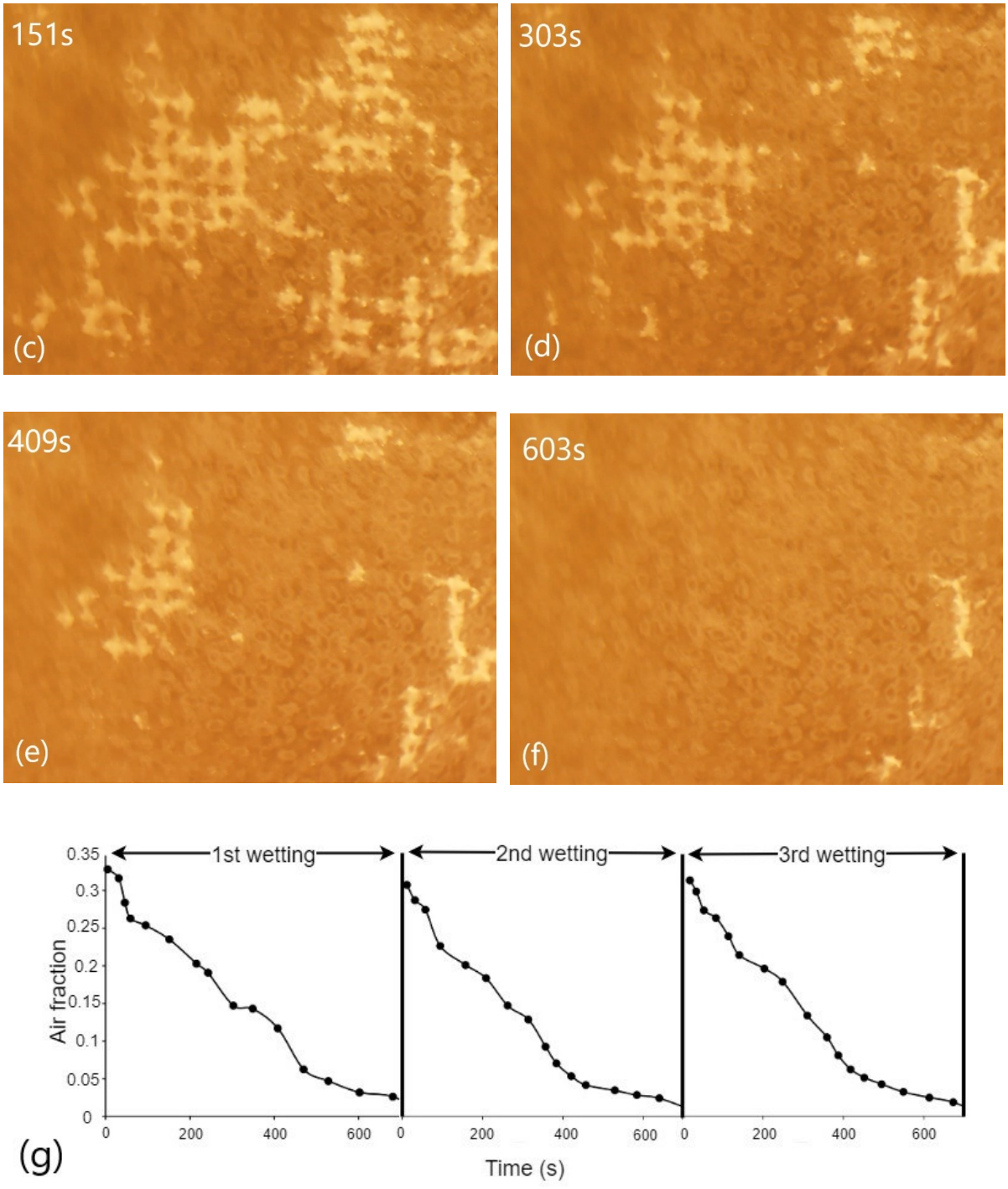


Figure 5.5 (a-f) Sequence of images showing the air cushion on a MP-16%H sample slowly disappearing through dissolution. (g) Graph shows the fractional area of air cushion decreases with time. Multiple wetting experiments show repeatable behavior.

The time sequence optical micrographs in Figure 5.5 show the evolution of air cushion on a MP-16%H sample. The presence of a continuous air cushion can be observed immediately after the textured surface was immersed in water and this existed throughout the observation.

The coalescence of the air cushion to form air bubbles was also observed, but this occurred with much lower frequency. When considering these results in comparison with the results from MP-0%H, MP-4%H, and MP-8%H, the content of HPCC influences the stability of air cushion. The higher the HPCC content, the greater the stability of the air cushion. This can be attributed to the chemical heterogeneity introduced by HPCC causing pinning of the three-phase contact line and a higher amount of HPCC would be more effective in water pinning (Kaufman *et al.*, 2017). This increases the lifetime of air cushion by preventing the transition to fully wetted state. The colour micrographs were converted into binary images to highlight the air cushion and segmented to produce a plot of the area fraction of air cushion against elapsed time. It shows a slow progressive decrease in the air cushion which continues for approximately 10 minutes. It is noted that although air trapped within the internal capillary pore system can diffuse out and escape the external surface (Hall & Hoff, 2012a), this is not sufficient to maintain the air cushion. The air cushion cannot be restored once it is completely dissolved. However, the air cushion can be restored if the sample is dried and re-immersed in water, as seen in Figure 5.5 g.

The possibility that the collapse of air cushion is triggered by microscopic condensed water droplet as described by Seo *et al.* (2018) needs to be considered. Water vapour condenses into water droplets on the base of the surface texture pillars and keeps expanding until the condensate reaches the suspended water-air interface. Since the air pocket is encircled by invading water, it is no longer separating the solid from water. The formation of microscopic droplets in cavities was observed by Lv *et al.* (2015) in their study of asymmetric meniscus collapse. They found that micro droplets formed immediately after a textured surface is immersed in water and that the presence of condensed water droplets significantly shortens the lifetime of the Cassie-Baxter state. By comparing cavities of different compositions, they concluded that the base of cavities made of hydrophilic materials would facilitate the formation of condensed droplets. A similar conclusion was obtained by Duan (2017). Data from Seo *et al.* (2018) show that the condensed droplets are the primary cause of transition from the Cassie state to the Wenzel state on a hydrophilic surface when the lifespan of air pockets is longer than 10 mins since this duration is long enough for the condensed droplets to grow. Therefore, it is the physics of condensation that usually controls the lifetime of the air cushion on a textured surface made of hydrophilic materials. However, in this study, the disappearance of air cushion cannot be attributed to condensation triggered collapse because the cement paste is by nature a porous material. If microscopic droplets are formed due to condensation, they would be absorbed into capillary pores immediately rather than remain on the base of micro pillars.

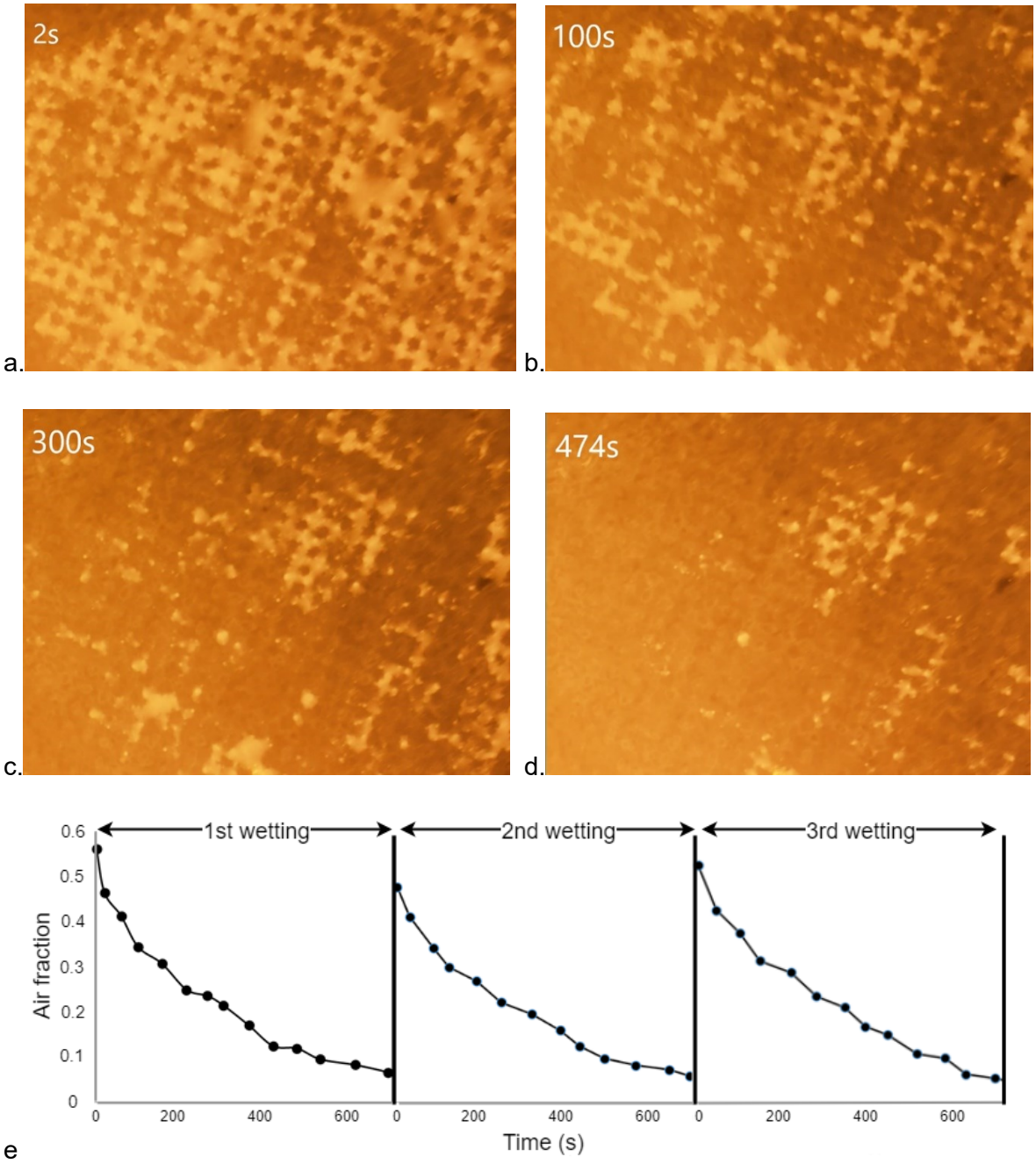


Figure 5.6 (a-d) Optical microscope images of trapped air cushion on a PDMS coated microgrid patterned mortar (M-MP-0%H-10%SF). (e) Graph shows the area fraction of air cushion decreases with time. Cyclic wetting and drying experiments show similar behaviour.

Figure 5.6 shows the development of air cushion trapped between water and a M-MP-0%H-10%SF sample. Similarly, a continuous air cushion can be observed immediately in all microgrid patterned samples that were PDMS coated (MP-0%H-10%SF, 4%H-10%SF,8%H-10%SF and 16%H-10%SF), when immersed in water, indicating that the formation of air cushion was not related to HPCC content in these samples. This is consistent with the results

of water contact angle, which showed that the wettability of PDMS coated surfaces was independent of HPCC content (Section 4.7.1). The area of air cushion gradually decreased over time as air dissolved in water. About 10 to 15 mins was required for the trapped air to be completely dissolved. Furthermore, coalescence of the air cushion into bubbles was very rare on the submerged PDMS coated samples (only 1 in 15 observations), compared to uncoated samples containing 4% and 8% HPCC. Therefore, it is clear from these results that the PDMS coating significantly enhances the stability of trapped air and enables the air cushion to be maintained for a longer period. Figure 5.6 (e) shows the area of air cushion against time. Again, the air cushion was fully restored when the sample was surface dried and re-wetted.

The air cushion was occasionally disrupted by gas out-fluxing from capillary pores. This phenomenon can be observed on both PDMS coated and uncoated samples due to the porous nature of cementitious materials. Figure 5.7 shows the sequence of air cushion development on a microgrid patterned surface. An air bubble can be seen forming at the upper right corner of each image, due to air that was continuously expelled from capillary pores. The air bubble grew rapidly and engulfed the surrounding air cushion as it spreads outward.

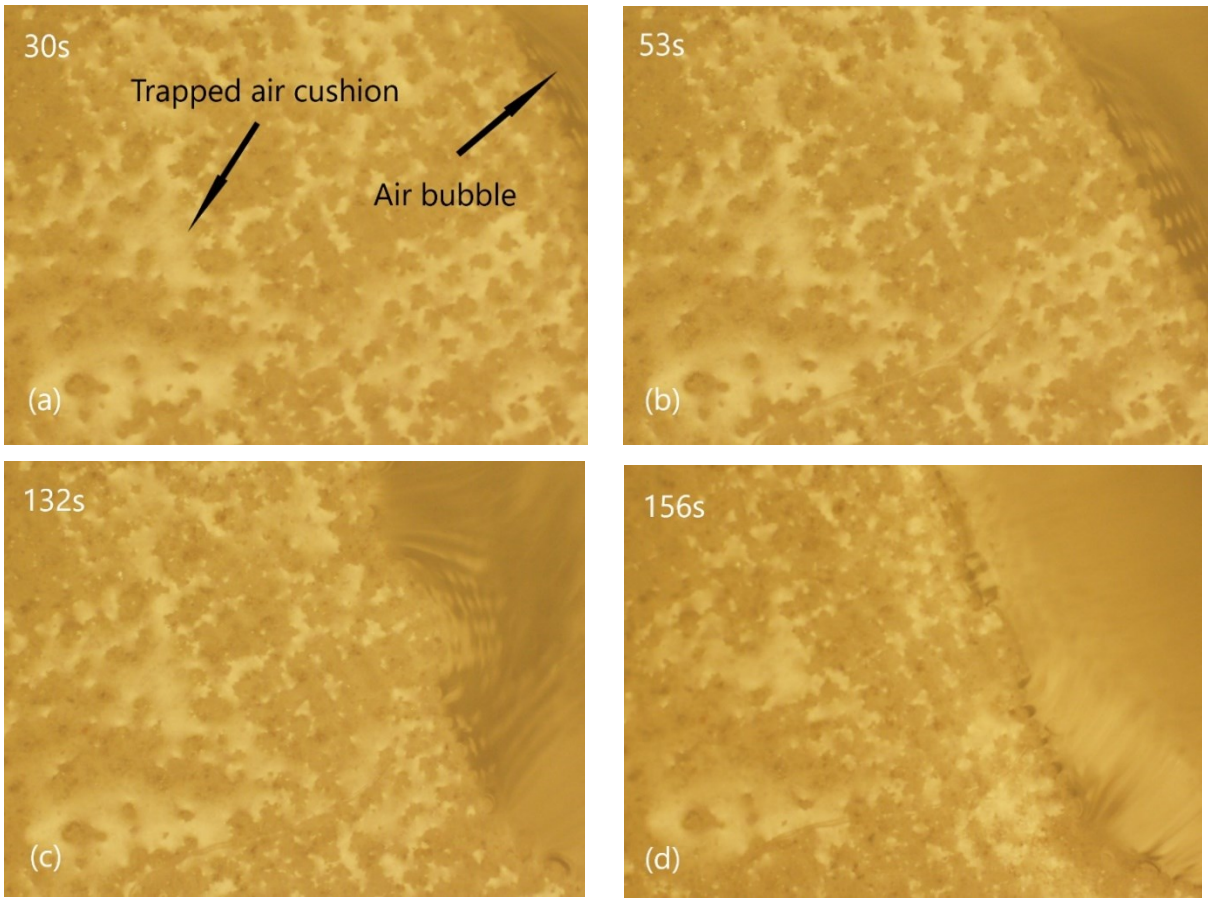


Figure 5.7 Optical microscope images of an air bubble (top right corner) growing rapidly on a

PDMS coated microgrid patterned mortar (MP-0%H-10%SF) sample, engulfing the surrounding air cushion.

This observation continued until the bubble grew to the size of the entire microscope viewing window, or until the bubble left the surface due to buoyancy. The whole process of bubble formation takes approximately 2 to 8 minutes, and the textured surface is left with no trapped air cushion once the bubble has floated away. Therefore, bubbles released from the textured surface can disrupt the integrity and longevity of the trapped air cushion.

5.4 Water sorptivity

The sorptivity values of hydrophobic cementitious samples are listed in Table 5.1. Water absorption showed a strong linear relationship to $t^{1/2}$ as evidenced by the high coefficient of determination R^2 for all samples.

Table 5.1 Summary of water sorptivity ($\times 10^{-2}$ mm/min$^{0.5}$).

		HPCC content			
		0%	4%	8%	16%
Nontextured/ uncoated	P-Non-3d	84.2(6.03)	32.7(2.99)	26.1(1.16)	15.1(0.5)
	M-Non-3d	16.6(0.58)	10.9(0.47)	7.6(0.08)	6.5(0.32)
	M-Non-10%SF-28d	4.9(0.28)	4.2(0.89)	3.5(0.18)	3.1(0.61)
	C-Non-3d	16(1.26)	11.3(1.75)	6.9(1.48)	5.6(1.4)
Textured/ uncoated	P-L-3d	63(3.35)	22.3(4.67)	17.8(3.29)	9(1.85)
	P-T-3d	66.6(1.53)	22.2(3.45)	16.4(4.31)	8.2(2.53)
	P-MP-3d	64.1(2.2)	26(3.06)	19.8(2.57)	9.8(2.75)
	M-L-3d	13.9(1.51)	9.3(0.71)	6.2(0.93)	4.3(0.6)
	M-T-3d	13.7(0.78)	9(0.26)	5.7(0.73)	4(0.45)
	M-MP-3d	13.9(0.39)	9(0.43)	6.1(0.51)	4.2(0.39)
Textured/ PDMS coated	M-L-10%SF-28d	1.5(0.25)	1.3(0.44)	1.1(0.23)	0.8(0.26)
	M-T-10%SF-28d	1.2(0.12)	1.3(0.34)	0.9(0.09)	0.7(0.26)
	M-MP-10%SF-28d	1.6(0.27)	1.4(0.46)	1(0.06)	0.9(0.25)
	C-MP-10%SF-28d	1.7(0.25)	1.5(0.09)	1.1(0.15)	1(0.2)

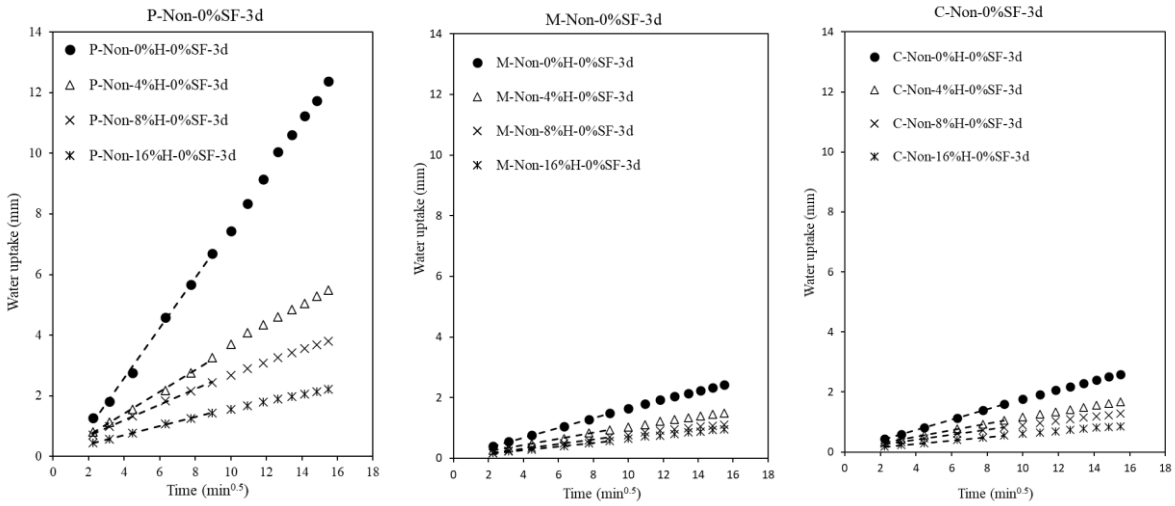


Figure 5.8 Water absorption curves for uncoated non-textured samples with different HPCC contents. Left: paste; Middle: mortar; Right: concrete.

It can be seen that addition of HPCC powder has a clear effect on decreasing absorption and the water sorptivity coefficient. Both properties decreased with increase in HPCC content. The sorptivity of P-Non-16%H was 0.15 mm/min$^{0.5}$ compared to approximately 0.84 mm/min$^{0.5}$ for control samples (P-Non-0%H). Non-textured mortars and concrete displayed lower sorptivity values compared to the pastes since ~60% vol. of cement matrix was replaced by dense aggregate, and aggregate absorption had little effect on the sorptivity of cementitious materials. M-Non-4%H showed a 34.3% lower water sorptivity compared to M-Non-0%H. Further increase of HPCC content to 8% produced a water sorptivity 54.2% lower than the control, and the difference between 8% and 16% HPCC was negligible. Non-textured concrete samples followed a broadly similar trend to the mortars: sorptivity decreased by up to 56.9% at 8% HPCC addition, but a minor difference was observed between 8% and 16% HPCC. Silica fume replacement resulted in a large reduction in sorptivity due to its filler effect and pozzolanic reactivity, which refine the capillary pore structure, leading to a decrease in water absorption. For the detailed mechanism of HPCC action, we have reasons to believe that the reduction in sorptivity is mainly associated with the hydrophobicity of the inner wall of capillary pores as HPCC particles fixed within cement matrix. When water front moves along the capillary pore and reaches fixed HPCC particles, convex meniscus would form that holds back the movement of water front (Lam & Lutsko, 2017). In addition, the physical blocking effect of the HPCC powder may also contribute to part of reduction in water absorption.

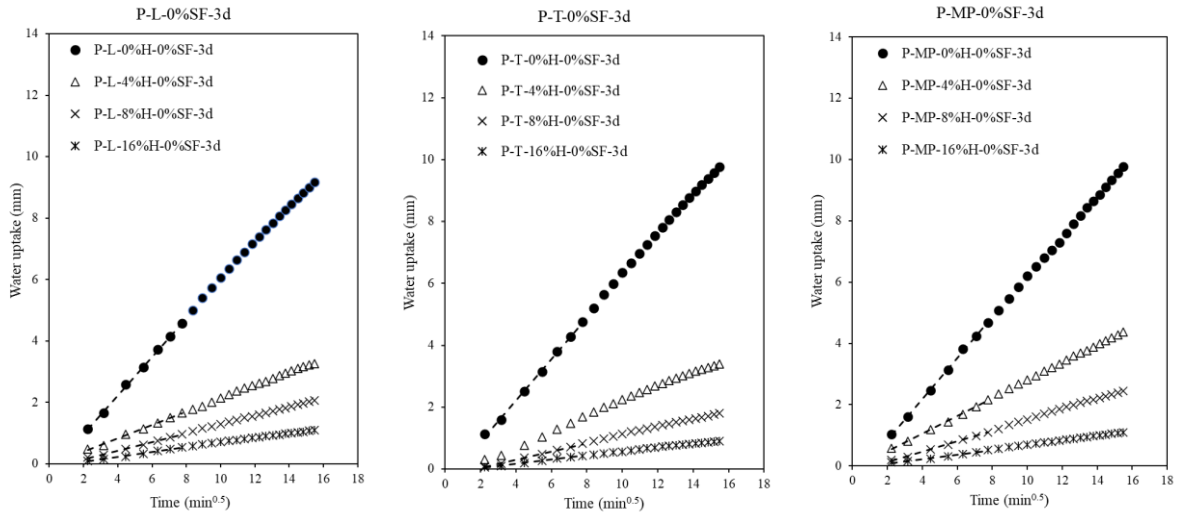


Figure 5.9 Water absorption curves for micro textured pastes with different HPCC contents. Left: Lotus; Middle: Taro; Right: microgrid pattern.

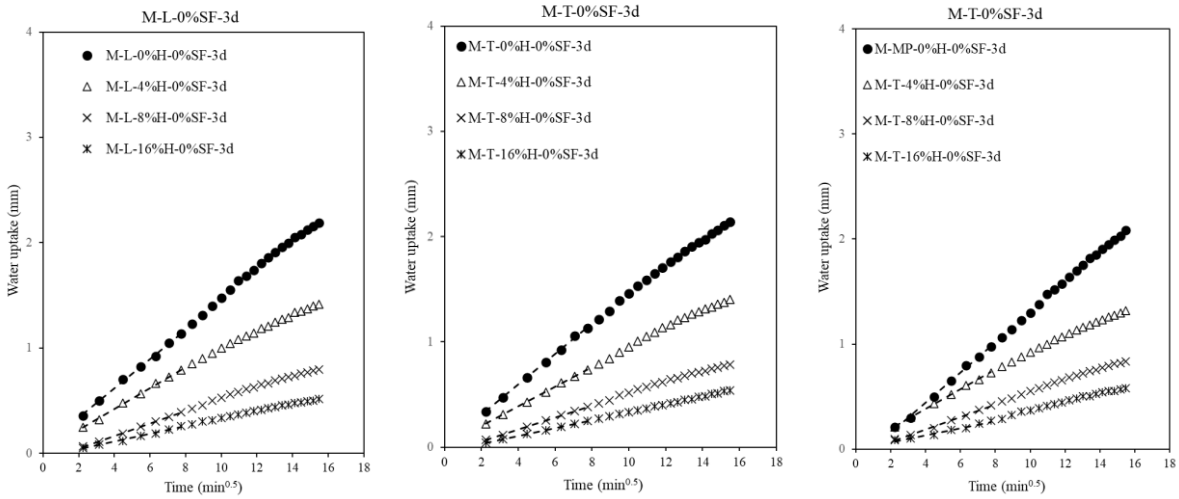


Figure 5.10 Absorption curves for uncoated micro textured mortars with different HPCC contents. Left: Lotus; Middle: Taro; Right: Microgrid pattern.

For uncoated micro textured samples, pastes with 0% and 4% HPCC showed about 20% to 30% lower water sorptivity than their non-textured controls. Marked differences in the sorptivity between textured and non-textured pastes were noticed at higher HPCC contents (>8%). For example, the sorptivity of lotus, taro, and microgrid textured pastes containing 16% HPCC were 40%, 45%, and 35% lower than the 16% HPCC non-textured pastes respectively. The sorptivity of micro textured mortars showed a similar trend to that of micro textured pastes. Water sorptivity of micro textured mortars containing 0%, 4%, and 8% HPCC was about 10-25% lower than M-Non-0%H. Again, a prominent decrease in sorptivity was observed on micro

textured mortars containing 16% HPCC. The sorptivity was decreased by 34%, 38%, and 35% for M-L-16%H, M-T-16%H, and M-MP-16%H, respectively, compared to M-Non-16%H.

It is worthwhile to note that superplasticizer itself is able to decrease sorptivity to some extent because superplasticizer leads to a high degree of dispersion of cement grains, which results in an improved hydration degree and therefore denser capillary pore structure (Hewlett, Justnes & Edmeades, 2019). Therefore, part of reduction in sorptivity observed on micro textured samples could be attributed to the effect of superplasticizer.

The reduction in water uptake and sorptivity coefficient is likely to be linked to the reduction in water-solid interface caused by the trapped air cushion as observed in Section 5.3. The stability of air cushion is crucial to the effect of micro texture on reducing water uptake. For example, textured samples containing 16% HPCC showed sorptivity values about 40% lower than the non-textured 16% HPCC samples because the continuous air cushion between micro textures isolated a part of the sample surface from wetting. The air cushion was restored at every mass measurement since the sample surface was dried before each weighing. For textured samples containing less than 16% HPCC, insufficient amount of HPCC leads to the air cushion quickly coalesces into air bubbles due to weak pinning effect and therefore, was less effective for blocking water ingress. This explains the large reduction in sorptivity observed only at 16% HPCC.

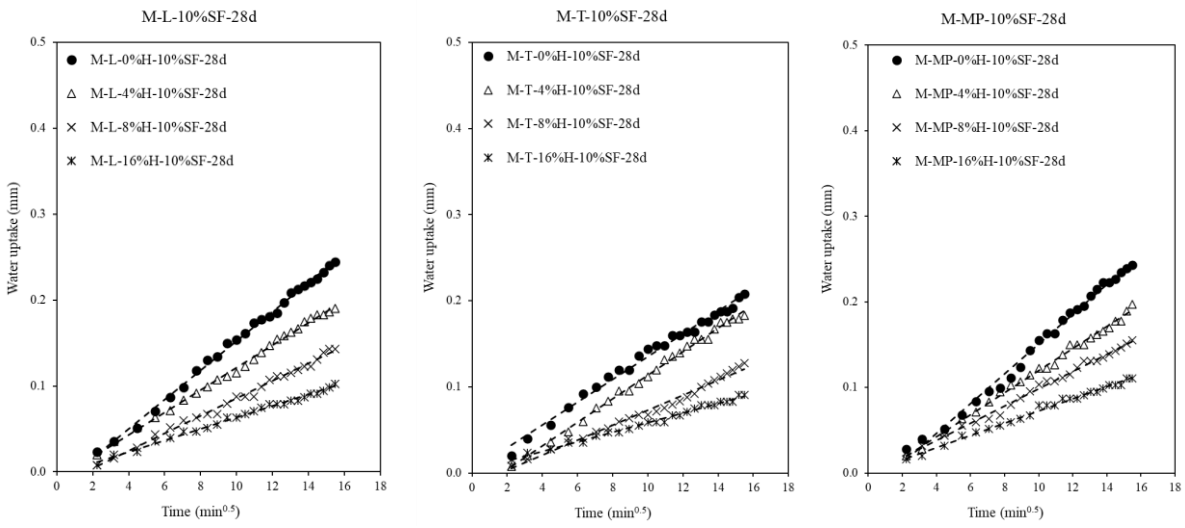


Figure 5.11 Water absorption curves for PDMS coated micro textured mortar with different HPCC contents. Left: Lotus; Middle: Taro; Right: Microgrid pattern.

PDMS coating has been shown to significantly reduce the water sorptivity of textured samples. As seen from Table 5.1, PDMS coated textured mortars (0% HPCC) showed water sorptivity ranging from 0.012-0.016 mm/min$^{0.5}$, which is much lower than M-Non-0%H-10%SF. A similar

result was found on concrete samples. This shows a significant improvement over the uncoated micro textured samples. This improvement is mainly attributed to the air cushion forming on coated surfaces, which was not observed on surface without coating or HPCC, as shown in Section 5.3. In addition, the coating itself may also serve as a physical barrier that isolates the sample from water. Adding HPCC further decreased sorptivity. For example, PDMS coated mortars with 4%, 8%, and 16% HPCC had sorptivity around 12%, 27%, and 42% lower than their HPCC-free controls, exhibiting a similar trend to that of non-textured samples. This shows that the effect of PDMS coating on reducing water absorption is independent of HPCC content in the sample. The trapped air cushion only plays the role of hindering water contact with sample surface. However, once water has been absorbed into the sample, it is the HPCC that hinders water transport within the bulk capillary pore system.

The ability of HPCC on decreasing water absorption is roughly on par with other hydrophobic powder additives. Wong *et al.*, (2015) developed a hydrophobic powder that was made by dry milling paper sludge ash and 4% wt. stearic acid. They found that 3-days-old concrete at w/c of 0.38 containing 12% hydrophobic powder shows water sorptivity 86% lower than controls. Qu & Yu, (2018) tested 28-days-old mortar at w/c of 0.5 containing a hydrophobic powder that was made by dry ball milling bottom ash and 4%wt. stearic acid. They observed that the water sorptivity was reduced by about 57% for samples containing 20% hydrophobic bottom ash. Shahbazi *et al.* (2020) applied amorphous carbon powder as hydrophobic additive into 3-days-old concrete with w/c of 0.4. They found that 20% addition of carbon powder led to a 55% reduction in water sorptivity.

A lower sorptivity can be achieved by combining HPCC with surface textures to limit the contact of water with the sample. The lowest sorptivity achieved in this study was 0.0074 $mm/min^{0.5}$, on SF-containing samples at 28 days age (Table 5.1). Normally, cementitious materials containing pozzolanic materials (10-20%), with w/b ratio of 0.4-0.5 achieve water sorptivity in the range of 0.053-0.083 $mm/min^{0.5}$ at 28 days age (Turk, Karatas & Gonen, 2013; Leung *et al.*, 2016; Sahoo, Parhi & Panda, 2021; Razak, Chai & Wong, 2004). Water curing decreases water sorptivity of blended concrete by around 40 to 60% relative to air-cured concrete at the same age (28 days) as adequate supply of water facilitate pozzolanic reaction (McCarthy & Dyer, 2019; Razak, Chai & Wong, 2004). High-performance concrete using low w/b ratio of around 0.35-0.5 had water sorptivity 0.023 to 0.036 $mm/min^{0.5}$ after 180 days of water curing (Olufemi Samuel, 2012). Comparing these to our data, the combination of HPCC, PDMS coating, and surface textures was able to decrease water sorptivity beyond the level that can be achieved by prolonged water curing, low w/b ratio or addition of pozzolanic materials.

5.5 Influence of hydrostatic pressure

5.5.1 Hydraulic pressure to break down metastable Cassie-Baxter state

The previous sections showed that micro textures on the surface of cementitious samples had a beneficial effect on sorptivity due to air trapped between surface textures blocking water penetration. However, this air cushion may be destabilized or eliminated when exposed to a sufficiently large hydraulic pressure. This could force the water-gas interface to penetrate into the microstructure. The air is pushed into the cementitious sample though open pores on its surface and, to a lesser extent, dissolved in water (Singh *et al.*, 2006). Without the trapped air cushion, water sorptivity values for textured samples may be similar to those of non-textured samples. Therefore, an attempt was made on PDMS-coated lotus textured mortars to study their water absorption behavior under pressurized condition. In addition, a modified sharp front model was applied to aid the understanding of the imbibition behavior in such case.

5.5.2 Imbibition with air trapping under hydrostatic pressure

The simplicity of sharp front model (Section 2.2) renders it a valuable aid for the analysis of complicated situations. To study the imbibition of water using the experimental arrangement shown in Figure 5.3, the positive hydrostatic water pressure on the inflow surface and the effect of trapped air in capillary pores on the water-front must be considered. The modeling was carried out using the sharp front model since it can give satisfactory accuracy for porous materials such as limestone (Ioannou *et al.*, 2009), brick (Hall, 1981), and autoclaved aerated concrete (Ioannou, Hamilton & Hall, 2008). The purpose of this modeling is to find out if the absorption behavior still follows the square-root time relationship when subjected to these conditions, and to determine if sorptivity can still be used to measure the rate of water uptake. The imbibition with air trapping was studied by Hall & Hoff (2012) and Ioannou *et al.* (2003). Building on their study, modeling involving the effect of static water pressure for samples immersed underwater was completed.

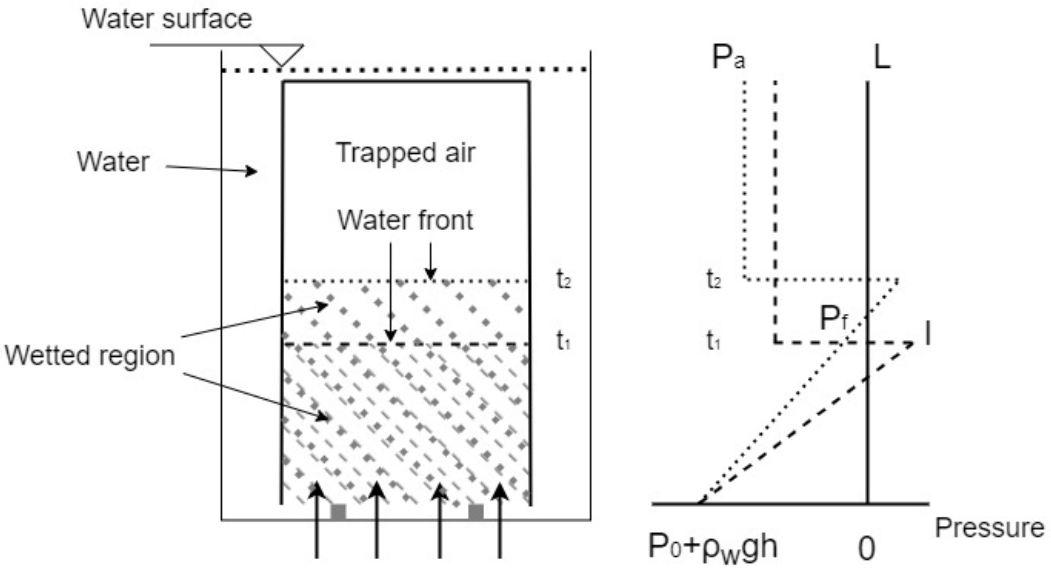


Figure 5.12 Progressive development of build-up air pressure P_a in a bulk sample of length L ($t_2 > t_1$). $P_0+\rho_w gh$ is pressure on the inflow surface and P_f is capillary pressure.

Different from the situation analyzed before in which air is free to leave the bulk of samples, here the trapped air will generate a resistance against the movement of water-front. Capillary pressure P_f and external pressure $P_0+\rho_w gh$ (absolute pressure) at inflow surface remain constant throughout the entire process while air pressure against the water-front increases as water imbibition occur, as shown in dashed line (Figure 5.12). Based on Boyle's law, the air pressure ahead of water, P_a, is

$$P_a = P_0 L/(L - l)$$

In which P_0 is atmospheric pressure; L is the sample length; and l is the length of wetted area. At equilibrium, the air resistance equals to inward forces exerted on the water-front.

$$P_a - P_0 - \rho_w gh = -P_f$$

In which $\rho_w gh$ is the water pressure; P_f is the capillary pressure (the value of P_f is negative because it is a pull). Therefore, the length of wetting area at equilibrium, x_e, is

$$x_e = \frac{-P_f+\rho_w gh}{P_0+\rho_w gh-P_f} L \qquad \text{(eqn. 5.1)}$$

In this case, the water movement in capillary pores is driven by a net force acting on the water-front. From Darcy's law, the capillary flow can be expressed as

$$u = \frac{di}{dt} = -K\frac{P_f+P_a-P_0-\rho_w gh}{l} \qquad \text{(eqn. 5.2)}$$

by substituting i=ΦI into equation 5.2

$$\frac{di}{dt} = -K\Phi\frac{P_f}{i} + K\Phi\frac{\rho_w gh}{i} - K\Phi\frac{P_0}{\Phi L - i} \qquad \text{(eqn. 5.3)}$$

In which ΦL represents the amount of water absorbed when saturation has been reached. In order to solve this differential equation, it would require simplification. Hall & Hoff (2012) proposed two dimensionless variables, $X=i/i_e$ and $T=S^2t/i_e^2$ in their solution, in which i_e is the amount of water absorbed at equilibrium and S is the intrinsic sorptivity. Here a new parameter, S', which is the sorptivity under water pressure, is introduced to replace the parameter S, by which the simplified form of differential equation 5.3 can be expressed in terms of $\lambda=i_e/\Phi L$. The detailed deduction of equation is listed as follows.

Since $dX=di/i_e$ and $dT'=S'^2dt/i_e^2$, by replacing di and dT with dX and dT respectively, and eliminating P_a by the Boyle's law, the equation 5.3 can be written as:

$$\frac{dX}{dT'} = -K\Phi\frac{\left(P_f - \rho_w gh\right)}{S'^2 X} - K\Phi\frac{P_0}{S'^2\left(\frac{1}{\lambda} - X\right)}$$

Hall & Hoff (2012) gave the sorptivity under pressure as $S'^2 = 2K\Phi\left(\rho_w gh - P_f\right)$. Therefore, this differential equation can be further reduced to:

$$\frac{dT'}{dX} = \frac{2X(1-\lambda X)}{1-X}$$

Integrating this equation with respect to X gives

$$T' = \lambda X^2 - 2(1-\lambda)[X + \ln(1-X)] \qquad \text{(eqn. 5.4)}$$

Where λ is a constant which lies in the range of [0, 1]. This function satisfies the boundary condition T'(X=0) = 0. For most building materials, the capillary pressure is of the same order of magnitude as the atmospheric pressure. For example, the capillary pressure of clay brick is approximately 0.11 MPa, which corresponds to an average pore radius of 1.3 μm determined by the Laplace equation (Ioannou *et al.*, 2003). Since the average capillary pore radius of cement paste is typically less than 1 μm (Beaudoin & Odler, 2019), it is reasonable to deduce that the capillary pressure of capillary pores in cement paste is equal to or even greater than that of clay brick. Given the water pressure applied to a textured surface is only 2452 Pa, which is much less than either the capillary pressure or atmospheric pressure, the contribution of water pressure to the value of λ can be neglected in this case. Therefore, the range of λ can be narrowed down to [0.5, 1].

Figure 5.13 shows plots of the inverse function of equation 5.4 against $T^{1/2}$ for all values of λ

ranging from 0.5 to 1. It can be seen from Figure 5.13 that, as expected, there is only a minor effect of air pressure ahead of water-front on the sorptivity at the early stage. Therefore, the water absorption curve at the early stage can be expressed in a simplified form $X=T^{1/2}$ without introducing too much error. Rearranging this equation, we can get $i=S't^{1/2}$. This analysis means that sorptivity can still be used as a meaningful parameter to compare the hydraulic properties of samples when they are tested under water pressure with trapped air.

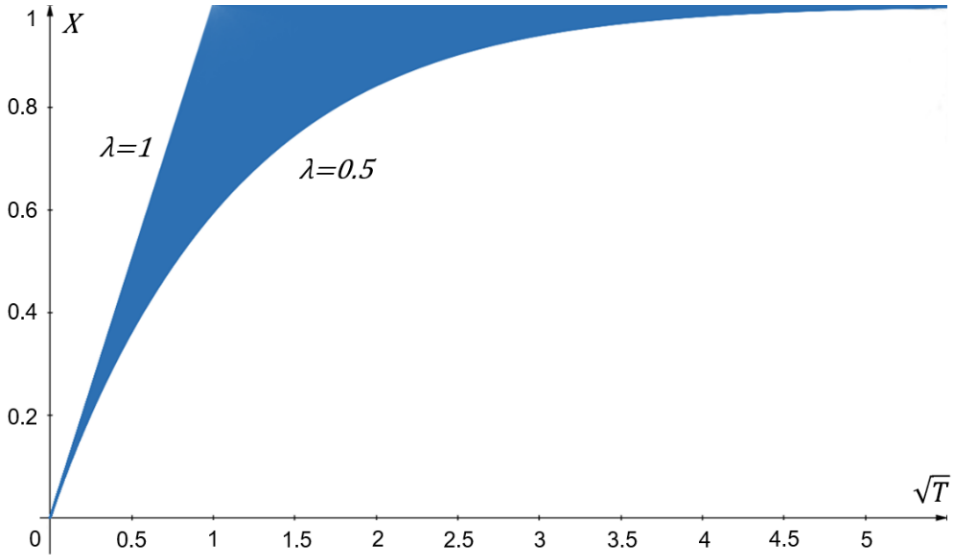


Figure 5.13. The family of curves of equation 5.4 with different values of λ in the range of 0.5 to 1. The results are insensitive to the value of λ for small $\sqrt{T}$, whereas it will cause great difference at longer times.

5.5.3 Water absorption under hydraulic pressure

The sorptivity was measured at water depth of 25 cm (2452 Pa) as it was estimated that the PDMS coated lotus texture had the ability to withstand a maximum pressure of 2133 Pa (Appendix I). The results shown in Figure 5.14 were plotted following the sorptivity law based on unsaturated flow in porous material. As shown in Section 5.5.2, the opposite reaction force acting on the water-front as it advances along the capillary pore and the compressed air ahead of it has negligible effects on water sorptivity curve at early stages. The measured sorptivity was therefore determined using data collected within the first 2 hours since the accuracy of measurements made with it would not be excessively degraded.

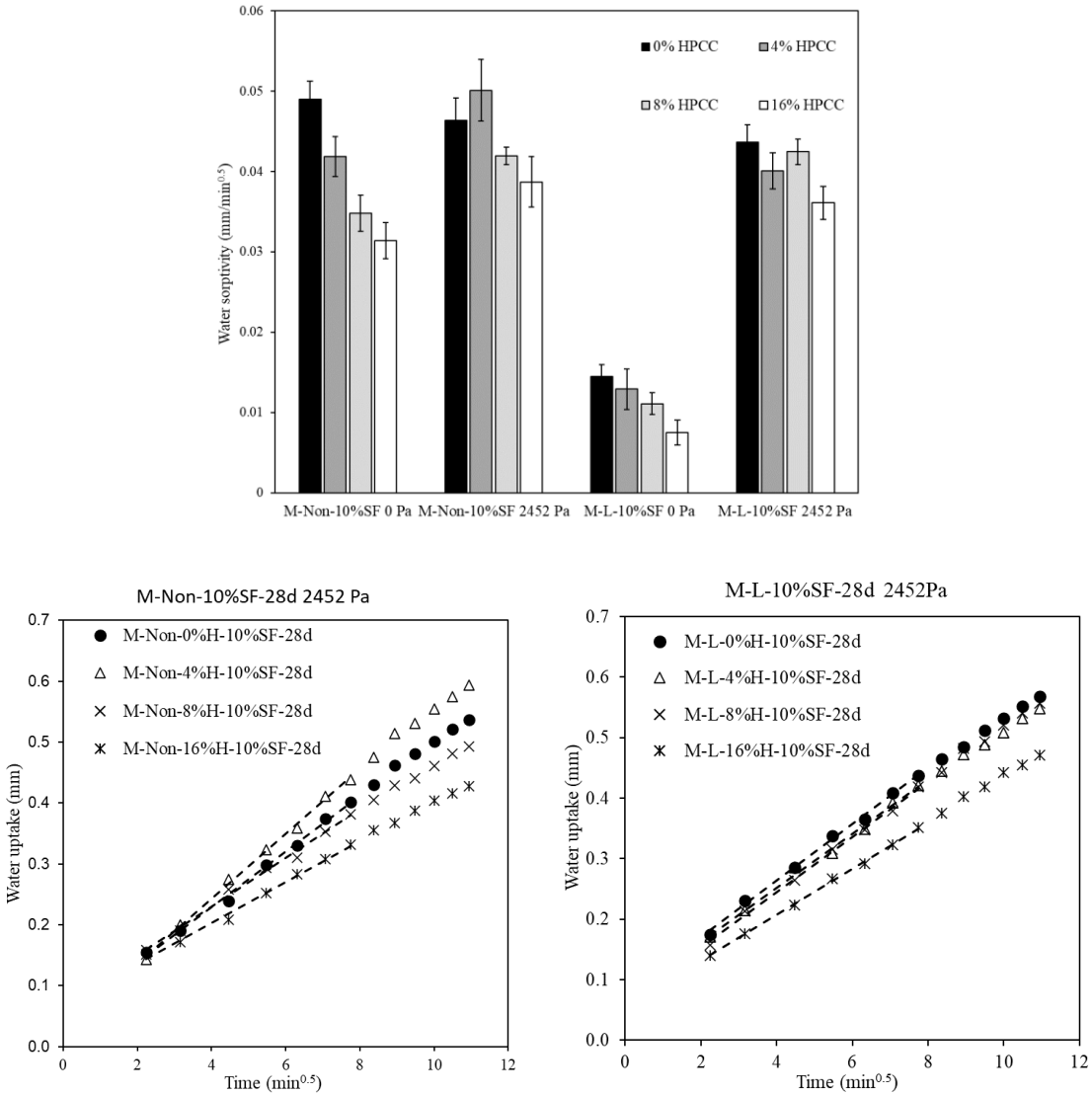


Figure 5.14 Sorptivity values and water absorption curves for samples tested under 2452 Pa water pressure.

As shown in Figure 5.14, water absorption for samples measured under a water pressure exhibited a linear relationship with $t^{0.5}$, and the sorptivity values of M-Non-0%H-10%SF were generally unchanged compared to that measured under unpressurized condition. This confirms the calculation shown in Section 5.5.2. Sorptivity for M-Non-4%H-10%SF and M-Non-8%H-10%SF were similar to that of the control sample. M-Non-16%H-10%SF had the lowest sorptivity of 0.0413 mm/min$^{0.5}$, but this is around 23% greater compared to the sorptivity when it is not subjected to water pressure. Both observations indicate that water pressure (2452 Pa) reduces the effect of HPCC on the resistance of water ingress. Comparison of PDMS coated lotus textured samples showed a significant increase in sorptivity when tested under pressure. M-L-16%H-10%SF again showed the lowest rate of absorption but was about

4 times higher compared to the sorptivity tested under unpressurized condition.

In general, there is no clear trend in the water resistance with respect to the content of HPCC, and the embedded surface texture did not give added benefit to water resistance under such conditions. The similarity between the sorptivity values for the non-textured and of textured samples indicate a similar absorption behavior during the entire test period. This supports the previous statement that the surface texture traps a layer of air cushion at the water-solid interface, and therefore hinders water imbibition.

5.6 Total water absorption

Table 5.2 Total water absorption of cementitious samples containing different amounts of HPCC.

	HPCC content			
	0%	4%	8%	16%
P-Non-3d	40.99(1.39)	42.4(1.25)	45.33(1.89)	46.16(1.43)
M-Non-3d	19.45(0.96)	20.25(1.98)	16.72(0.86)	15.09(1.05)
C-Non-3d	20.37(0.87)	18.81(0.92)	16.44(0.98)	14.62(1.24)

Paste controls have a lower porosity compared to both mortar and concrete controls because sample compaction by vibration is easier and more complete in the absence of aggregates particles (Figure 5.15). HPCC incorporation generally increased the amount of water absorbed at saturation for paste samples, while mortars and concretes showed about 25% lower absorption at 16% HPCC addition relative to their 0% HPCC controls (Table 5.2). If we take into account of the dilution effect of HPCC since it does not absorb water, water absorption per unit volume of cement matrix would be around 4, 3.9, 3.4, 3.2 ($*10^{-4}$ g/mm^3) for mortars or concretes with 0%, 4%, 8%, 16% HPCC respectively (Figure 5.15). This finding suggests that HPCC acts not only as a surface-active agent, but also as a pore blocking material. However, this seems contradictory to the data from pastes showing that total water absorption increased with HPCC content. This can be explained by recalling the finding from image analysis in Section 4.3.4 where it was observed that the incorporation of HPCC resulted in large, entrapped air voids in pastes due to the water encasing effect of HPCC. This had a far less significant influence in mortars and concretes due to the presence of aggregate particles. These entrapped air voids have a minor role on water sorptivity due to the low capillary suction (Wong *et al.*, 2015), but they significantly contribute to the total water absorbed at saturation.

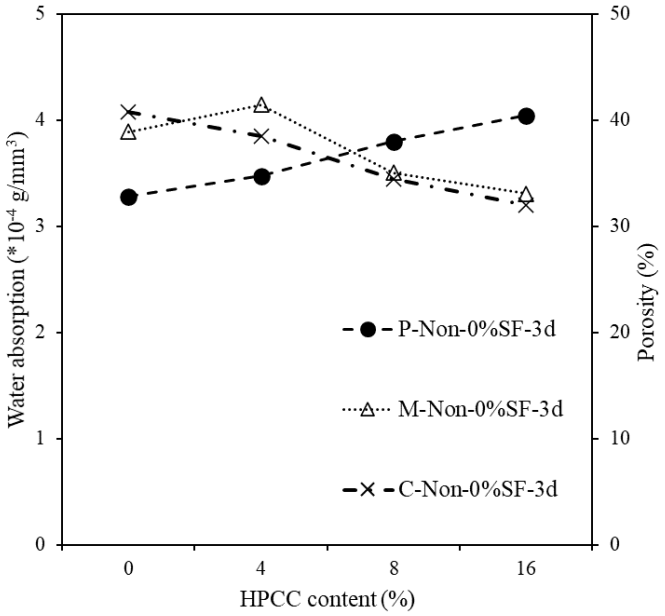


Figure 5.15 Water absorption and porosity of cement matrix. The results have been corrected for aggregate and HPCC content to account for the dilution effect.

It is noted that the porosity calculated by water absorption is much larger than that determined by image analysis (Section 4.3.5). This is because cementitious materials, with w/c ratio of 0.4, generally includes pores with radii between 2 nm to 5 μm, but determination of pores with radii smaller than 0.4 μm is difficult using image analysis due to the limit of resolution (Bye, 1999). These pores are accessible by water, yet undetected by image analysis, hence a large difference between the two methods is observed.

5.7 Gas transport properties

Oxygen diffusion and permeation were measured on non-textured pastes, mortars and concretes (w/c 0.4; 3 days) to determine the effect of HPCC on gas transport properties. For pastes, both gas permeability and diffusivity coefficients were found to increase in the presence of HPCC (Figure 5.16). Compared to diffusivity, permeability appeared more susceptible to HPCC and showed a greater extent of increase. The rate of increase in diffusivity and permeability reached a maximum at 4% HPCC addition and then reduced thereafter. In samples with 16% HPCC, the diffusivity and permeability increased by 30.6% and 92.9% over the controls, respectively. In contrast, gas transport properties of mortars and concretes were less affected by HPCC addition (Figure 5.16). Diffusivity of mortar and concretes remained constant, while permeability increased by around 37% over the controls. Compared to the results of water sorptivity, it can be said that the main effect of HPCC is

decreasing water absorption, as 16% addition of HPCC caused more than 60% reduction in sorptivity over plain mortar or concrete.

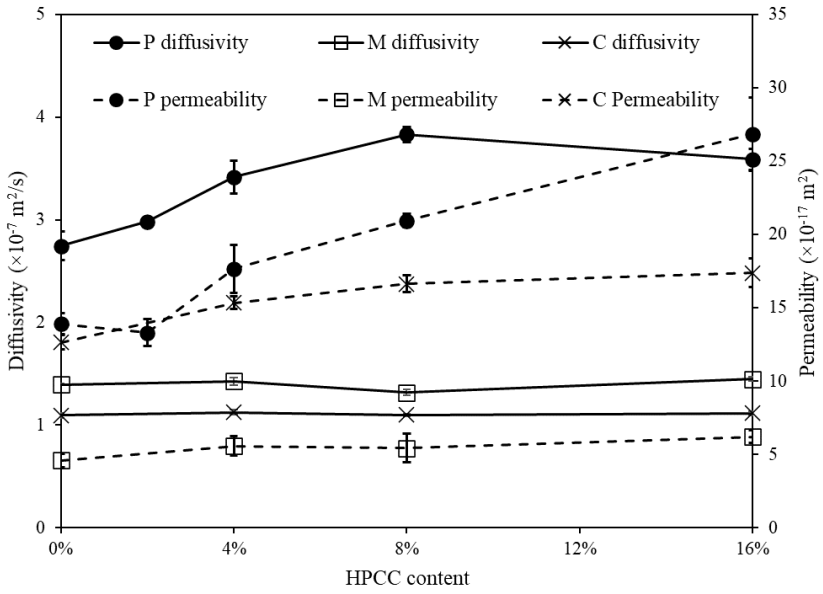


Figure 5.16 Effect of HPCC on gas diffusivity and gas permeability of non-textured cementitious samples at 3 days.

These results give an indication that adding HPCC facilitates gas transport within cement paste. This is probably because the HPCC induces some entrapped air voids in the bulk sample as discussed in Section 4.3.5. This is analogous to the effect of air entrainment on concrete, which has been shown to increase the coefficients of diffusivity and permeability by a factor of up to 3 (Wong *et al.*, 2011). The presence of large air voids could also explain why permeability increased to a greater extent than diffusivity since pressure-induced gas flow is strongly size dependent. For mortars, the influence of interfacial transition zone (ITZ) on gas transport is relatively insignificant when aggregate volume fraction is less than 70% and sample thickness to the maximum aggregate size is less than 10 (Wong *et al.*, 2009). Therefore, the mortar samples showed a less prominent increase in gas transport properties and this is consistent with the microstructure study which indicated the porosity of mortar remained more or less constant with increasing HPCC content. In addition to air voids, shrinkage-induced microcracks that occur during drying prior to testing may also play an important role in the high gas transport coefficients in pastes containing high dosage of HPCC. Microcracks may initiate at numerous air void interfaces, which increases connectivity of pore structure and facilitates gas transport (Wong *et al.*, 2011). In pastes, the microcracks tend to extend and to link together due to the lack of aggregate (Wu *et al.*, 2021; Wong *et al.*, 2009).

However, the propagation of cracks is more likely to be constrained in mortars and therefore, prevents the formation of macrocracks (Wu *et al.*, 2021).

Concretes had diffusivity values close to the mortars, but their permeability was up to 3 times higher. This indicates that pressurized gas flow is more severe in concretes, which is consistent with findings from previous studies. Possible reasons for this are greater micro bleeding within concrete that caused the formation of a wider ITZ, allowing gas to quickly pass through. Furthermore, presence of coarse aggregates in concrete increases the likelihood of bleed water trapping under the aggregate particles, causing an increase in porosity at the ITZ and initiation of drying-induced microcracking (Wong *et al.*, 2009). Such phenomenon is well reported in the literature to exacerbate pressure-induced gas flow in concrete samples subjected to drying conditions (Wong *et al.*, 2009; Wu, Wong & Buenfeld, 2015).

5.8 Water vapour absorption

Figure 5.17 show the vapour absorption curves of micro textured mortars containing 0% and 16% HPCC. In general, the absorption curves of the textured samples almost mirror the curves of non-textured samples. This indicates that surface textures do not affect the vapour absorption of cementitious samples. It is also clear from the results that the HPCC has no effect on hindering water vapour sorption into a cementitious material. This is because HPCC impart hydrophobicity to the cementitious material through modifying the wettability of wall of capillary pore, but the transport of vapour is dependent on gas diffusion (Section 5.7).

When compared to the samples made of plain mortar, SF resulted in a lower cumulative mass gain and a lower rate of vapour sorption (Figure 5.18). This difference in vapour sorption behavior is attributed to the filler and pozzolanic effects of SF on the refinement of the pore structure. Large interconnected capillary pores will be de-percolated and subdivided into smaller pores in the presence of SF (Lewis & Fidjestol, 2019). The reduction in pore volume and connectivity, and the increase in tortuosity will lead to lower moisture transport and therefore total water gain.

From the mass measurements of SF-containing textured and non-textured mortars, the PDMS coating did not hinder the passage of water vapour into the samples. This suggests that the accessible pores on the surface of cementitious materials are not blocked by the PDMS molecules grafted on the surface. There is a benefit to be gained in creating grafted PDMS coating on cementitious materials. Unlike water proofing admixtures that provide an impermeable seal against the transport of moisture, the grafted PDMS coating is permeable to water vapour while restricting the ingress of liquid water. This allows continuous hydration

and pozzolanic reaction to happen after the treatment as they both relies on the passage of moisture from the external environment.

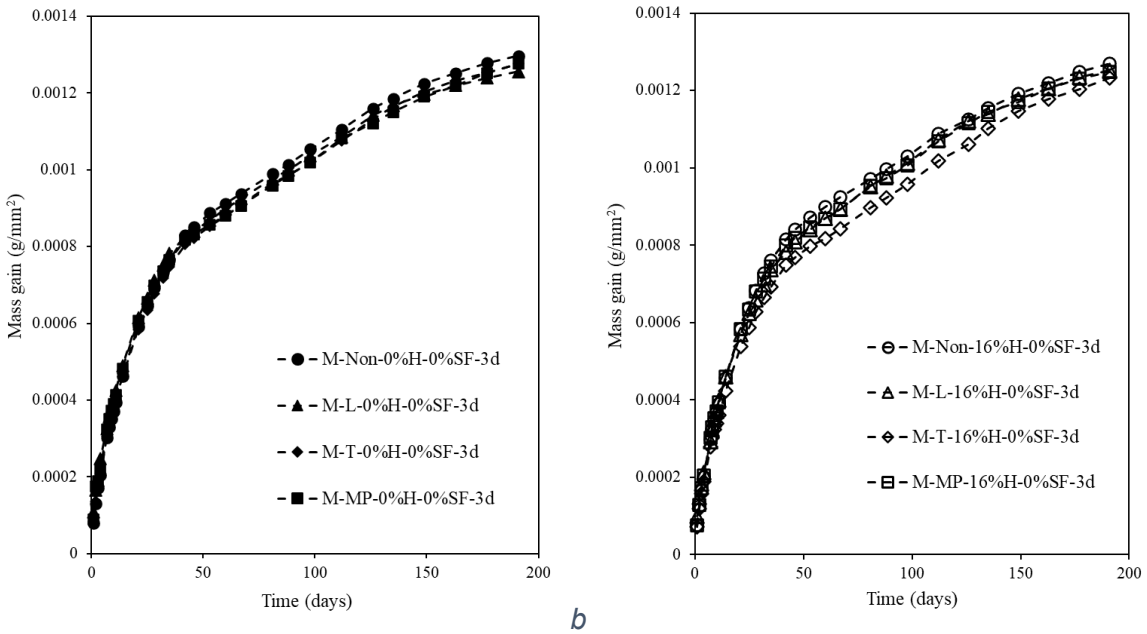


Figure 5.17 Mass gain of mortar samples containing (a) 0% HPCC and (b) 16% HPCC exposed to 98% RH.

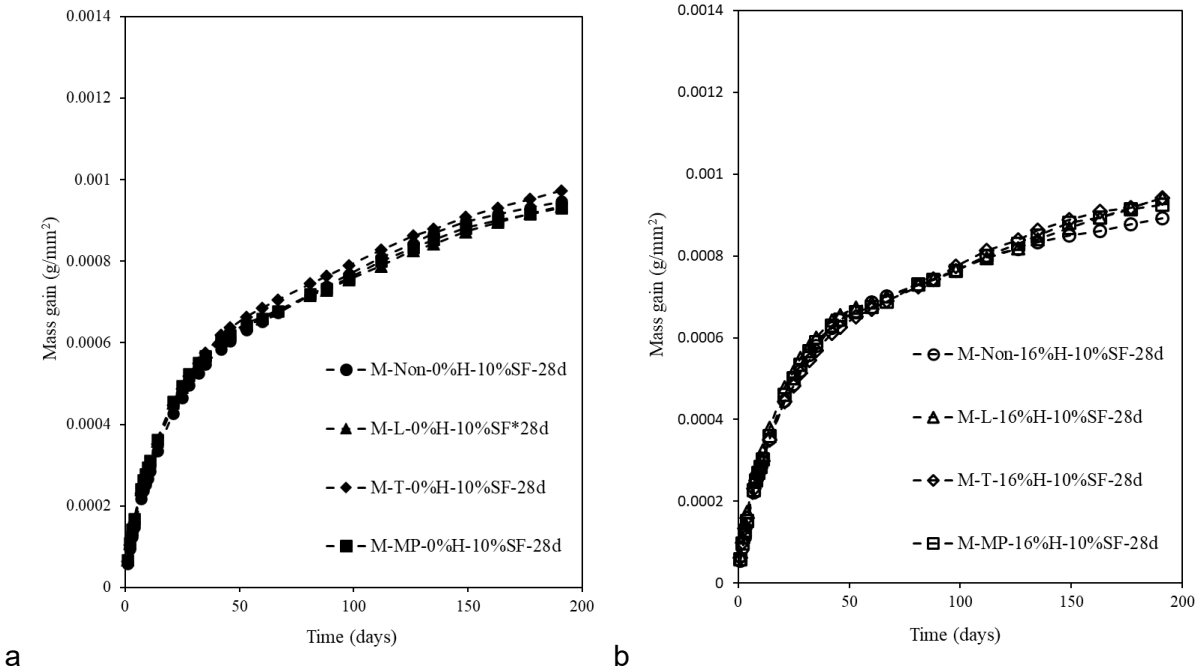


Figure 5.18 Mass gain of SF-containing mortar samples containing (a) 0% HPCC and (b)16% HPCC exposed to 98% RH.

As moisture uptake proceeds, condensed droplets with a contact angle of 17° to 22° were observed after ~112 days of exposure to 98%RH on textured samples irrespective of HPCC content. Such a low contact angle indicates the failure to establish an air cushion at the water-solid interface from which the droplet and the sample can be separated.

The surface texture loses its ability to trap air in high humidity environment since the mechanism for wetting by condensation is different from that for wetting by contacting water. Droplets condensing in the Wenzel state was also reported by Cheng *et al.* (2005), who placed dry lotus leaves in an environment of saturated water vapour. Similarly for fresh lotus leaves, the condensed droplets lose part of mobility (high contact angle hysteresis) due to wetting between papillae (Liu & Choi, 2013). Similar experiments conducted by Wier & Mccarthy (2006) on surfaces made of array of dimethyldichlorosilane modified posts with various dimensions led to the same result. Microscopic imaging of the developing condensed droplets revealed that the failure to form an air cushion was because the vapour phase tends to first nucleate at the base of the texture and subsequently grow to fill the gaps. For textured cementitious samples, the condensed micro droplets will be absorbed into the bulk material. Therefore, surface texture plays no role in impeding the ingress of moisture from condensation.

It is interesting to note that the condensed droplets occur before the samples reach saturation. This seems contradictory to the above discussion that the condensed droplet will be immediately absorbed into capillary pores since the pores network is not filled. To explain this phenomenon, it is necessary to consider the moisture uptake process more fully. In a humid environment, water molecules traverse a certain distance along connected pores and adsorb on to the pore wall due to strong attractive interaction. This adsorbed film of water becomes thicker as water molecules build up, with the film close to the exposed surface growing faster than the film deeper inside the sample (Künzel, 1995). Since the attraction acting on water molecules decreases with increasing distance from the pore wall, the multilayer adsorption is always accompanied by surface diffusion which is thermally promoted (Xi, Bazan & Jennings, 1994). This means that the adsorbed water molecules with high potential energy (far away from the surface) will spontaneously jump between adsorption sites with a tendency to “flow” inward as the adsorbed layer is thinner on the inside of sample (Künzel, 1995). HPCC molecules on the pore wall will affect the formation of adsorbed water layers, as well as surface diffusion, due to its hydrophobicity. However, the effect of surface diffusion is negligible in high humid conditions (Xi, Bazan & Jennings, 1994).

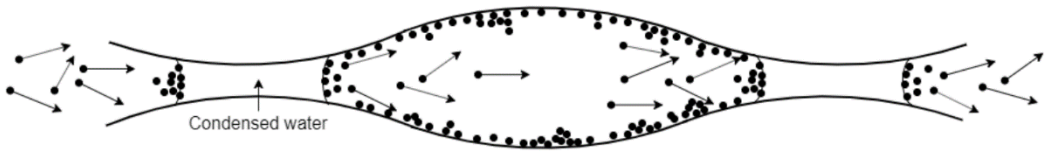


Figure 5.19 Moisture transport in a capillary pore with two narrow constrictions. Black solid circles represent water molecules.

As sorption proceeds toward saturation, water meniscus will first form at pore constrictions ("ink bottle necks") and thereafter, the water transport mechanism will be a combination of capillary suction and water vapour diffusion. In reality, a capillary pore includes multiple narrow constrictions along its length, therefore, the pore will be separated into several disconnected sections by condensed water. Water vapour is now transported by a mechanism in which the vapour is condensed at one end of a water pocket and evaporated at the other end of the water pocket, as shown in Figure 5.19. Pockets of condensed water redistribute themselves driven by capillary action due to differences in radius of curvature of water meniscus. For most building materials, the moisture transport coefficient of the redistribution of capillary water is ten times less than the coefficient for capillary suction (Künzel, 1995). At equilibrium, small pores will fill with water while the large pores remain empty. These large pores will eventually be filled but it is a slow process which is governed by the diffusion of trapped air (Hall & Hoff, 2012b).From the above discussion, it is reasonable to suggest that the condensed droplets will start to grow on the external surface of sample at the point when air diffusion dominates the moisture uptake process, rather than at the saturation point.

5.9 Conclusion

Optical microscopy was used to view the development of trapped air between micro textures when submerged in water. It was found that air cushion does not exist on textured samples with HPCC content less than 4%. At 8% HPCC, air cushion was observed immediately after immersion in water. However, the air cushion layer lasted for less than 3 mins before coalescing into air bubbles. Stability of the trapped air cushion increased with HPCC content. At 16% HPCC, the area of air cushion slowly shrank as air dissolved into surrounding water. This whole process took ~10 mins. These observations were consistent with the water absorption data, which showed that the effect of micro textures on decreasing water imbibition is related to HPCC content. Micro textured samples with less than 4% HPCC gave sorptivity values roughly 20% lower than their non-textured references, while samples containing 16%

HPCC had sorptivity values more than 35% lower than those of non-textured reference samples at similar HPCC content.

Stability of air cushion to coalescence increased when the textured surfaces were PDMS coated. The air cushion on PDMS coated textured surfaces had higher surface coverage and survived a longer time than those of HPCC-containing samples. When combined, the water sorptivity of PDMS coated textured samples containing 16% HPCC decreased by a further 40%. However, in the presence of external hydraulic pressure, the performance of submerged micro textured samples degraded due to the transition from Cassie-Baxter to Wenzel state. As a result, micro textured samples gave similar sorptivity values to non-textured samples.

The application of micro textures, HPCC, and PDMS coating had little or no effect on gas transport properties and water vapour absorption of mortars and concretes. Condensates on textured surfaces do not form a layer of air cushion. Instead, they showed water contact angles in the Wenzel state because the droplets nucleate at the base of the texture and subsequently spread to fill gaps as more water condensed. HPCC-containing pastes showed a slightly different gaseous transport behaviour due to air voids that form in the bulk of material caused by the water encasing effect of HPCC. The presence of these entrapped air voids resulted in a significant increase in gas permeability and total water absorption, which increased with HPCC content. However, this had little effects on water sorptivity due to the low capillary suction of air voids.

6 Durability of hydrophobic cement-based materials

Small changes in the physical characteristics of surface micro textures may cause a large reduction in hydrophobicity. This chapter investigated the durability of cementitious micro textures when exposed to several aggressive environments, including high humidity (98% RH), high concentration of CO_2 (3%), acidic environment, abrasion and cyclic wetting and drying. It was found that no significant differences in surface morphology and hydrophobicity occurred after exposure to 3% CO_2 (at 68% RH) for a month. Micro textures were damaged after being pulled on a 1200-grit SiC abrasive paper and the hydrophobicity was lost. Paste samples experienced significant efflorescence after 3 months of exposure to 98%RH. However, this can be alleviated by reducing the cement content to limit the amount of calcium hydroxide produced. Partial replacement of cement with supplementary cementitious materials such as silica fume would also alleviate efflorescence by consuming the calcium hydroxide in addition to increasing the abrasion resistance of micro textures. The hydrophobicity of deteriorated surface was related to the dimension of micro textures. In general, larger micro textures appeared to be less affected by small changes in morphology. Results from cyclic wetting and drying showed no marked degradation in the hydrophobic properties of HPCC treatment, whereas micro textures were affected by drying-induced cracking. Micro textured samples containing silica fume were more durable than those made with plain CEM I systems under cyclic wetting and drying, showing less than 20% increase in water sorptivity after five cycles of wetting and drying. However, exposure to acidic environment was detrimental to surface micro textures as severe drying-induced cracking appeared on the surface after 7 days of leaching in nitic acid solution at a pH of 2.

6.1 Introduction

Previous chapters have shown micro textures provided a significant benefit by decreasing wettability and water transport properties of cementitious materials. However, a key aspect of cement-made micro textured surfaces is its durability. Hardened cementitious materials generally contains anhydrous cement, calcium hydroxide and other components that will continue to react albeit at a slower rate, causing changes to the porosity and microstructure over time. The presence of these phases is unavoidable. For example, concrete with a w/c ratio of 0.49 contains around 12% vol. of anhydrous cement at age of 7 days and reduces to around 5% vol. after 1 year of curing (Horne, Richardson & Brydson, 2007). The data reported in previous chapters were obtained on relatively young samples. Furthermore, these samples were stored in a dry environment (an oven) after demolding and curing, so that the delicate surface structures would be preserved since most deterioration mechanisms affecting

cementitious materials involve moisture (Section 2.3). Even through the samples were removed from the oven and allowed to cool to room temperature before testing, during which reactions may resume, the influence on surface structures is expected to be negligible.

Since the contribution of roughness on hydrophobicity is only effective within the scale of microns to sub-microns (Zheng & Lü, 2013), small changes to the dimensions of micro textures may lead to deterioration of performance. For example, the height of the micro textures must be sufficiently large to satisfy the requirement that the base is prevented from direct contact with water (Extrand, 2004). This is confirmed by He *et al.* (2013), who showed that water droplets on a silicon surface consisted of micro pillars over 40 μm in height were in the Cassie-Baxter state, with a contact angle of ~150°, whereas the hydrophobicity was lost when the micro pillars were reduced by half in height. Zhang *et al.* (2017) and Patankar (2010) came to a similar conclusion that sagging liquid air interface or small external forces, such as vibration and collision, can easily trigger the transition between two wetting states on a textured surface with short structures. Physical damage of local surface structures may also lead to the failure of establishing or maintaining the air cushion (Domingues, Arunachalam & Mishra, 2017; Hensel *et al.*, 2014).

Given the above and the slow reaction of cementitious phases during long service life may raise concerns about changes to the topography of textured surface and as a result, its wettability. The fragile nature of micro textures also makes it vulnerable to physical damage. In this chapter, the longevity of cement-made micro textures was studied. Samples were exposed to various conditions including abrasion, acid leaching, cyclic wetting/drying, high humidity and high CO_2 environment. The aim was to investigate how such aggressive environments would affect the performance of micro textured surfaces. The work covered in this chapter was the first reported study on the durability of micro textured cementitious surfaces.

6.2 Experimental

Mix proportions of samples tested in this chapter are given in Table 6.1. All samples were prepared at water/binder ratio of 0.4. Silica fume (SF) was used as partial replacement for cement, and HPCC was used as an addition in some mixes. Mortars were produced with a sand volume fraction of 60%. Tests in this chapter were carried out on pastes and mortars as the previous chapters have showed that the presence of large aggregate particles (gravel) had no influence on the performance of micro textures.

Table 6.1 Summary of mix proportions.

	Cement (kg/m^3)	Silica fume (kg/m^3)	Water (kg/m^3)	HPCC		Plasticizer (kg/m^3)	Sand (kg/m^3)	Coarse aggregate (kg/m^3)	Curing (days)
				%	kg/m^3				
Non-textured									
P-Non-0%H	1383.9	-	553.6	0	-				3
P-Non-4%H	1351.7	-	540.7	4	54.1				3
P-Non-8%H	1320.9	-	528.4	8	105.7				3
P-Non-16%H	1263.4	-	505.3	16	202.1				3
M-Non-0%H	532.9	-	213.2	0			1598.8		3
M-Non-4%H	528.1	-	211.2	4	21.1		1584.2		3
M-Non-8%H	523.3	-	209.3	8	41.9		1569.9		3
M-Non-16%H	514	-	205.6	16	82.2		1542.1		3
Micro textured (Lotus/Taro/Microgrid patterned)									
P-L-0%H P-T-0%H P-MP-0%H	1360.4	-	544.2	0	-	20.4	-	-	3
P-L-4%H P-T-4%H P-MP-4%H	1329.2	-	531.7	4	53.2	19.9	-	-	3
P-L-8%H P-T-8%H P-MP-8%H	1299.4	-	519.8	8	104	19.5	-	-	3
P-L-16%H P-T-16%H P-MP-16%H	1243.7	-	497.5	16	199	18.7	-	-	3
M-L-0%H M-T-0%H M-MP-0%H	529.4	-	211.7	0	-	7.9	1588.2	-	3
M-L-4%H M-T-4%H M-MP-4%H	524.6	-	209.8	4	21	7.9	1573.8	-	3
M-L-8%H M-T-8%H M-MP-8%H	519.9	-	208	8	41.6	7.8	1559.7	-	3
M-L-16%H M-T-16%H M-MP-16%H	510.8	-	204.3	16	81.7	7.7	1532.3	-	3
Micro textured and coating (Lotus/Taro/Microgrid patterned)									
M-L-0%H-10%SF M-T-0%H-10%SF M-MP-0%H-10%SF	475.9	52.9	211.5	0	-	7.9	1586.3	-	28
M-L-4%H-10%SF M-T-4%H-10%SF M-MP-4%H-10%SF	471.6	52.4	209.6	4	21	7.9	1572	-	28
M-L-8%H-10%SF M-T-8%H-10%SF M-MP-8%H-10%SF	467.4	51.9	207.7	8	41.5	7.8	1557.9	-	28
M-L-16%H-10%SF M-T-16%H-10%SF M-MP-16%H-10%SF	459.2	51	204.1	16	81.6	7.7	1530.5	-	28

Samples for carbonation were first conditioned in an environmental chamber where the RH was controlled at ~60% and soda lime was used to absorb CO_2, prior to exposure to carbonation. Samples for other tests were conditioned in an oven at 50°C and around 8% RH after demolding to achieve constant mass prior to testing. Abrasion resistance of surface structures were tested on textured samples without HPCC using the experimental setup described in section 3.6.1. Contact angles were determined by averaging 15 measurements across the surface. Acid leaching was carried out on samples without HPCC using diluted nitric acid with a PH value of 2. Samples were sealed with epoxy resin except the surface to be exposed to acid leaching. To maintain the pH value, the acid leachant was changed every 1 to 2 days. After 7 days of exposure, the samples were sliced and dried to determine the depth of leaching front using EDX mapping.

Cyclic wetting and drying was carried out on samples used for water sorptivity testing (section 5.4). The saturated samples were returned to the oven after sorptivity testing and dried to constant mass. These samples experienced a total of 5 cycles of wetting and drying and subjected to the same procedure as described in section 3.3.1. The change in the topography of surface structures after experiencing long-term exposure to 98% RH was examined using a SEM (section 3.6.2). Paste and mortar samples without HPCC addition were used for this test. The deteriorated surfaces were then analysed by XRD and EDX to check for changes in composition. Influence of HPCC on carbonation depth was examined on mortars. The samples were cut and sprayed with phenolphthalein indicator to determine the depth of carbonated area that was delineated by the reaction front of calcium hydroxide (section 3.6.3). SEM was used to observe the surface topography of carbonated textured surfaces followed by contact angle measurement. Raman spectroscopy was used to determine whether the surfaces were fully carbonated.

6.3 Abrasion resistance

Figure 6.1 shows the measured water contact angles plotted as a function of pulling distance. The wettability of flat surface appear unaffected by abrasion as the water contact angle was generally unchanged after pulling the sample through 100 cm. However, the wettability of textured samples is susceptible to abrasion. For lotus and taro textured surfaces, pulling the samples through 20 cm resulted in only a small reduction in water contact angle. A significant decrease in water contact angle was observed for both types of surfaces after pulling through 40 cm, and the textured surfaces began to show signs of deterioration such as scratches. Abrasion causes a transition from hydrophobic regime to hydrophilic regime. After 80 cm, the majority of papillae was destroyed, and the surface was covered in deep scratches.

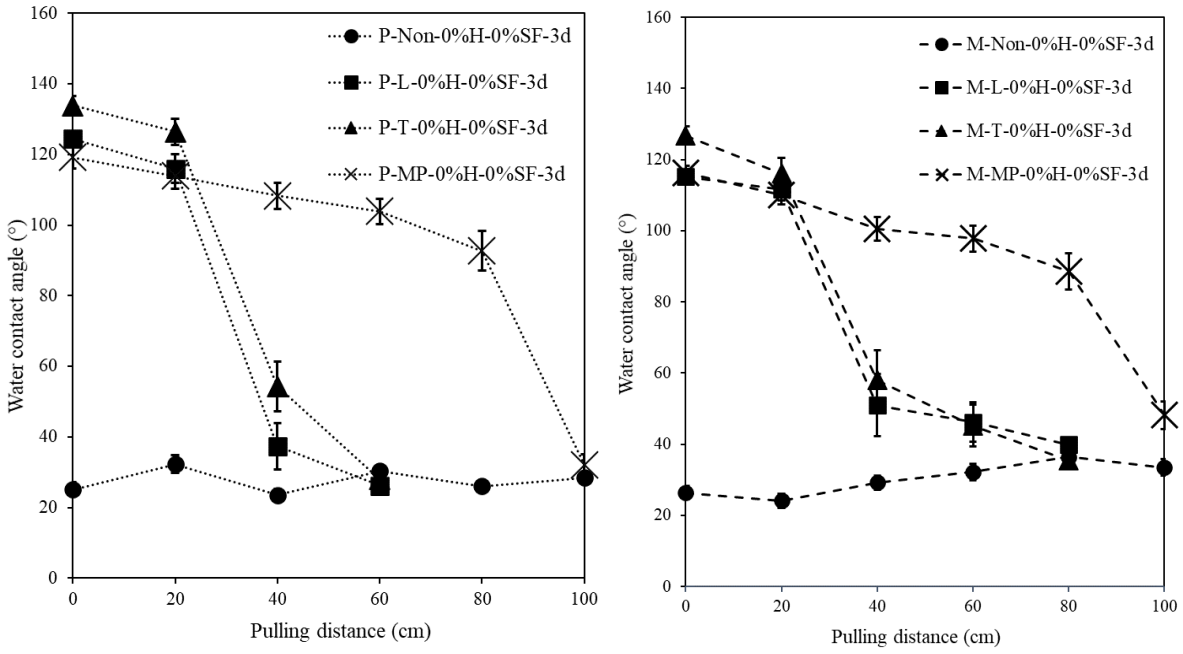


Figure 6.1 Water contact angle versus pulling distance for textured pastes and mortars. Error bars represent standard error.

The microgrid patterned surface exhibited a different trend to the lotus and taro textured surfaces. The water contact angle for microgrid patterned sample barely changed after pulling through 20 cm. After pulling for 60 cm, the microgrid patterned surface experienced a decrease of about 14% in water contact angle. A substantial decrease in the hydrophobicity of microgrid patterned surface occurred between pulling distance of 80 cm and 100 cm.

As expected, damage to the surface textures leads to a loss of hydrophobicity. When comparing the results of L-0%H-0%SF-3d and T-0%H-0%SF-3d with MP-0%H-0%SF-3d (Figure 6.1), it is found that the microgrid pattern has better anti-abrasion quality than the plant textures. Since the microgrid pattern has dimension ~2 times and height ~4 times larger than that of plant textures (section 4.6), it is reasonable to deduce that the abrasion resistance is related to the size of the surface texture. The larger the surface texture, the greater the abrasion resistance.

It can be seen from Figure 6.1 that the presence of fine aggregate had virtually no effect on the abrasion resistance of micro textured surfaces. This is because the surface textures typically consist of features much smaller than the size of aggregate. Therefore, the micro textures are only made of cement paste, and the abrasion resistance of micro textured surfaces made of mortar are similar to that of paste.

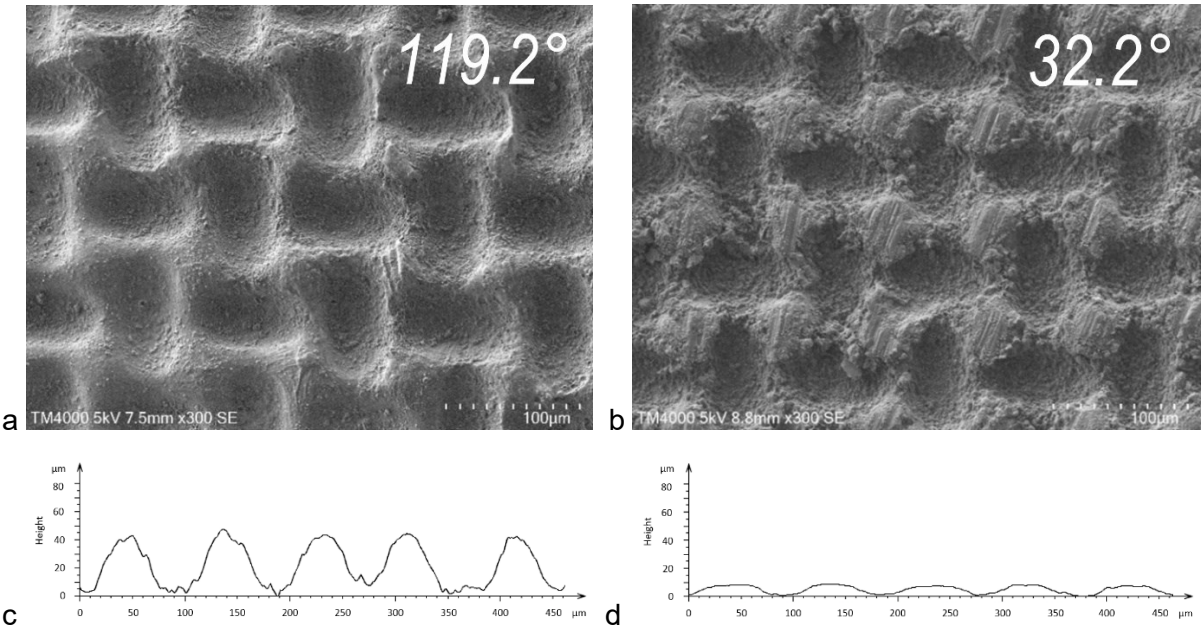


Figure 6.2 (a) and (c). Surface topography and profile of a P-MP-0%H-0%SF-3d sample. (b) and (d) Surface topography and profile after pulling through 100 cm on a 1200-grit SiC paper.

SEM images taken at the end of the experiment showed that the texture has not been completely destroyed when the microgrid pattern lost its hydrophobicity, as shown in Figure 6.2. The remaining surface texture has a height of less than 10 µm, about a quarter of the original height prior to abrasion. This shows that a shortened surface texture loses its hydrophobicity because it is no longer able to suspend the water-air interfaces. As a result, the water droplet comes into contact with the base of texture, leading to the transition from the Cassie-Baxter state to the Wenzel state.

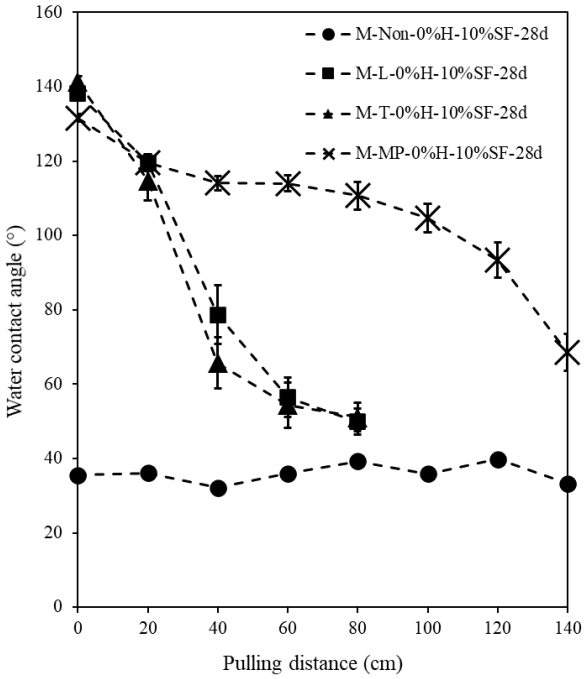


Figure 6.3 Water contact angle versus pulling distance for textured samples made of SF-containing mortar. Error bars represent standard error.

Figure 6.3 shows the contact angle of abraded SF-containing micro textured surfaces. There was a clear reduction in water contact angle in all cases after pulling over 20 cm. Compared to Figure 6.1 in which water contact angles of uncoated samples decreased by less than 20° after pulling through the same distance, this is probably mainly due to the removal of PDMS coating during abrasion. After pulling over 40 cm, SF-containing lotus and taro textures showed resultant contact angles ~70°, which are larger than those made of plain cement (~55°), indicating a greater resistance to abrasion. Moreover, the microgrid patterned surfaces made of SF-containing mortar remained in hydrophobic regime (>90°) after pulling through 120 cm while their plain cement counterpart has lost its hydrophobicity after 100 cm.

The greater abrasion resistance comes from an increased in the strength of SF-containing mortar. It has been demonstrated that the abrasion resistance of concrete is primarily a function of concrete strength (Thomas, 2007). Normally, a higher concrete strength would lead to a greater abrasion resistance. However, it is worth noting that brittleness can increase when the content of micro silica in a mix is higher than 10% (Levy, 2012). As a result, a micro texture may be fractured rather than wear out when subjected to abrasion. This may explain why the lotus and taro texture with SF showed minor improvement in abrasion resistance than microgrid pattern, since their size is smaller, which makes them easier to fracture.

6.4 Acid leaching

After 7 days of leaching, the surfaces of all samples turned yellow due to the loss of calcium. The EDX maps of the cross-section of leached paste showed a silica-rich surface zone with only a small amount of calcium, which indicates that most of calcium was removed from the cement matrix (Figure 6.4). Decalcification proceeded from the surface via the propagation of reactive front, which resulted in a clear leaching boundary with core. The decalcified area was porous, with a depth of about 90 μm.

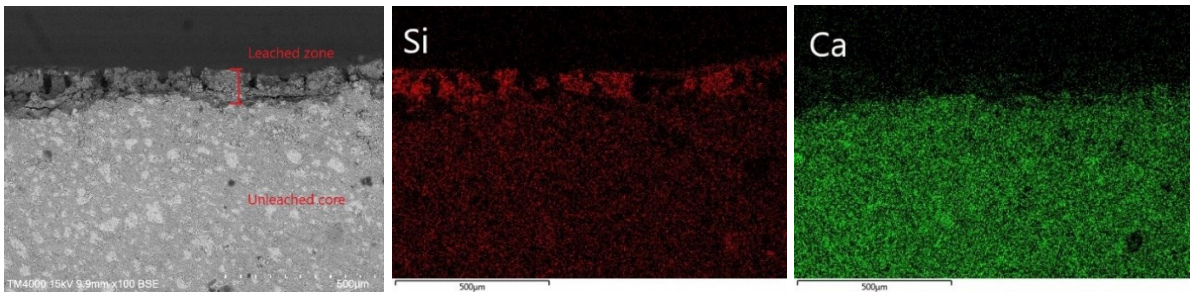


Figure 6.4 Silicon and calcium maps of a textured paste (P-L-0%H-0%SF) after acid leaching.

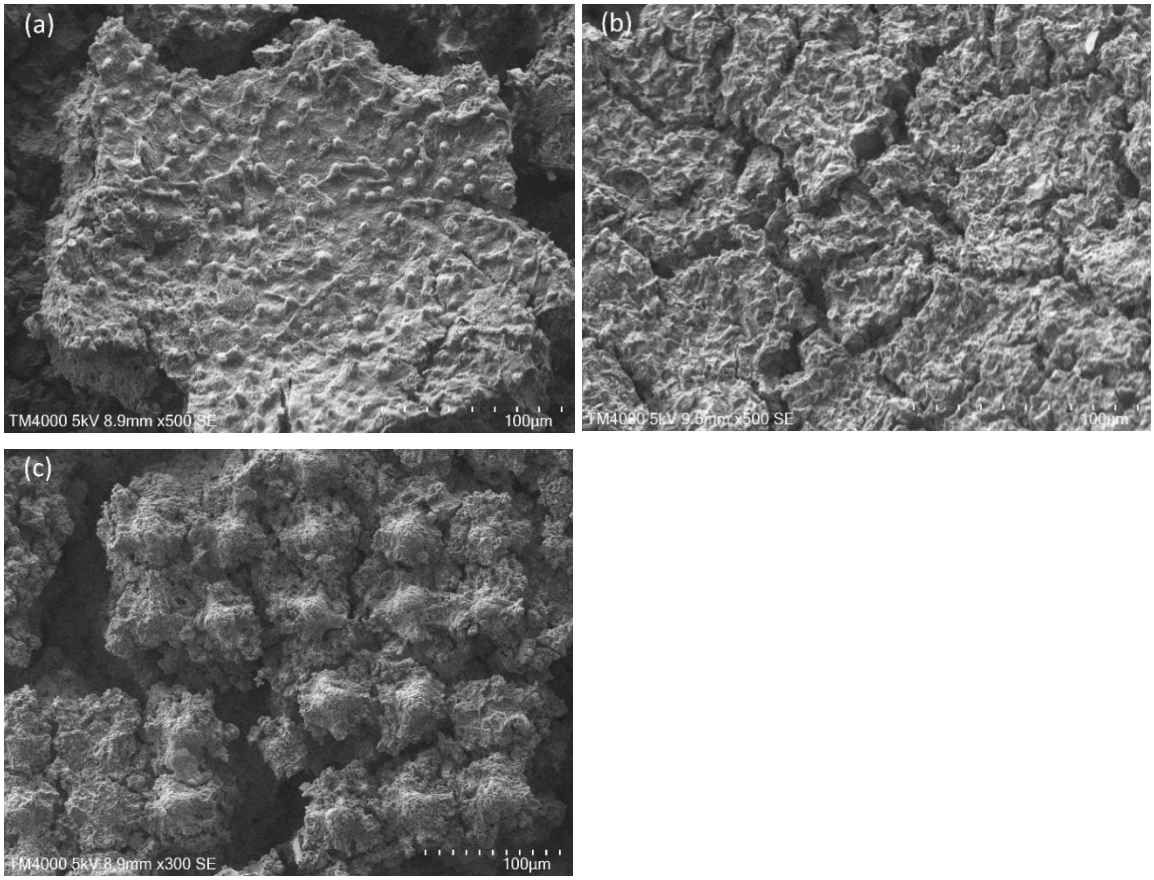


Figure 6.5 Scanning electron micrographs of textured pastes leached at a pH of 2 for 7 days. (a) P-L-0%H-0%SF, (b) P-T-0%H-0%SF, (c) P-MP-0%H-0%SF.

Although the surface structures can still be seen on the leached surfaces, the textured surfaces have completely lost its hydrophobicity due to the formation of a “map-pattern” cracking in the base (Figure 6.5). Water droplets placed on the sample spread across the surface and were absorbed into the bulk of sample immediately. The presence of aggregate in the samples appeared to have virtually no effect on restraining the cracking as both pastes and mortars exhibited the same type of deterioration. The cracks initiated during the process of drying. A similar phenomenon has been observed on cement pastes stored in distilled water for 12 months, after which microstructure examination showed a gel-like surface due to leaching with small cracks (Margi, 1998). It was reported that the cracks formed as a result of gel drying. Drying in stepwise decrease of RH did not prevent the cracking from happening. The weak mechanical properties of the leached layer contributed to the surface cracking, where they can easily deform under the tensile force produced by the liquid meniscus (Scherer, 1990). Baker & Bishop (1997) found that the acid leached cement samples possessed a porosity of 80%, which was much higher than pre-leaching. As the liquid evaporated, the meniscus attached to the pore walls pull the walls together while the remaining silica gel structure is liable to this shrinking force exerted on them. Cracks eventually develop through weak paths when the tensile stress exceed the strength limit of the material.

6.5 Cyclic wetting and drying

As shown in Figure 6.6, all pastes exhibited various degrees of deterioration in sorptivity after having been subjected to five cycles of wetting and drying. For non-textured pastes, P-Non-0%H-0%SF have split or crumbled, while the sorptivity of P-Non-4%H-0%SF, P-Non-8%H-0%SF, and P-Non-16%H-0%SF have increased by ~169%, 92%, 52% compared to their initial sorptivity, respectively. The standard deviation in the data, as shown by the error bars, have also increased after the samples have experienced several cycles of wetting and drying. This indicates the variability in water absorption behavior and sorptivity values of individual samples have increased. Furthermore, deviation from square root-time behavior was found on some samples containing low amounts of HPCC (<8%) at the end of the third wetting cycle, where the cumulative absorption was less well fitted by linear regression (Figure 6.7). These samples exhibited an S-shaped absorption curve during cyclic wettings and this phenomenon exacerbated with each subsequent cycle. This is another indication that some samples have deteriorated because the square root-time behavior is only valid when the sample is homogeneous (Hall & Hoff, 2012c; Wu *et al.*, 2019). In this experiment, sorptivity values determined by linear regression with R^2<0.95 were not included in the calculation of the average of sorptivity.

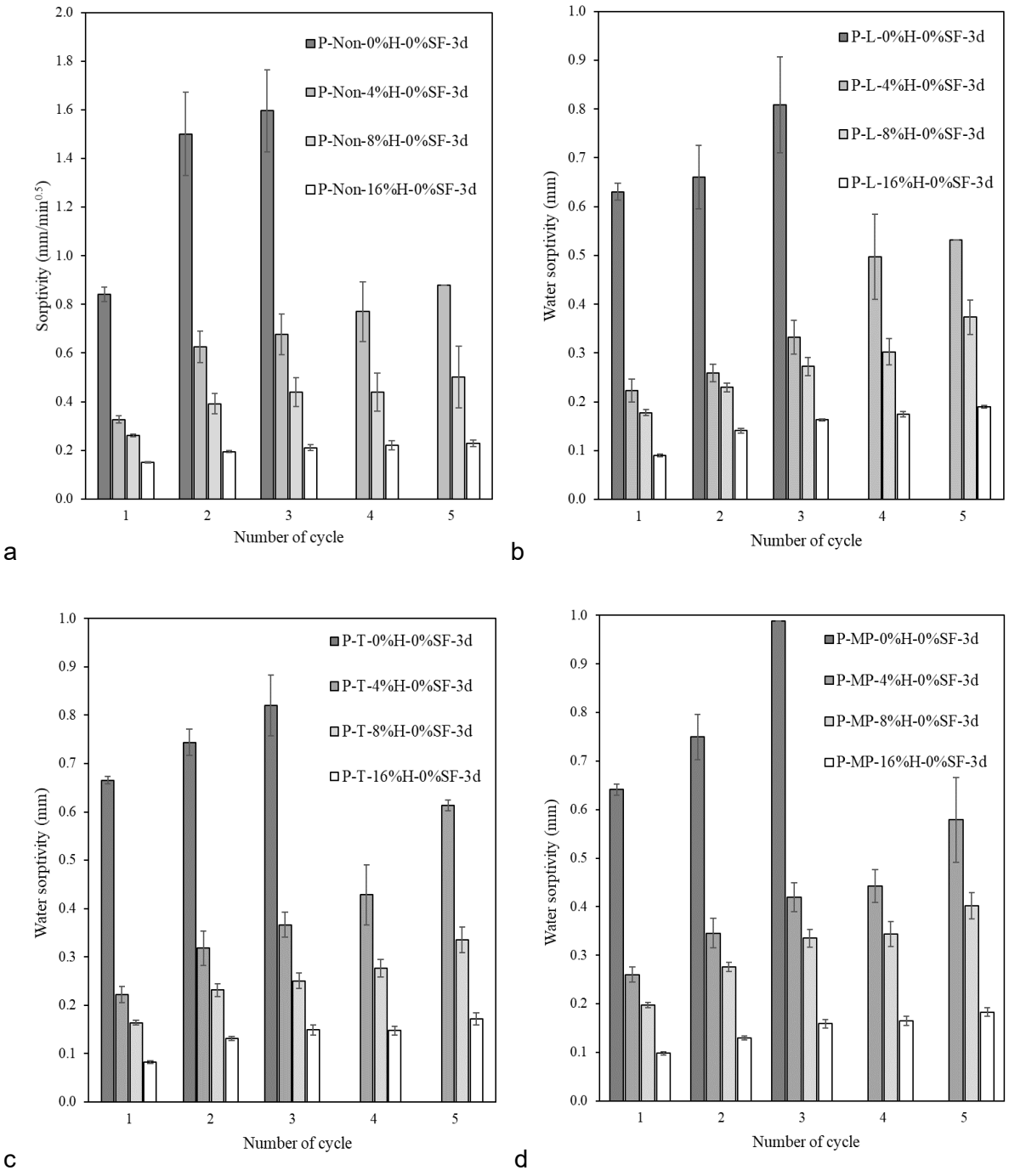
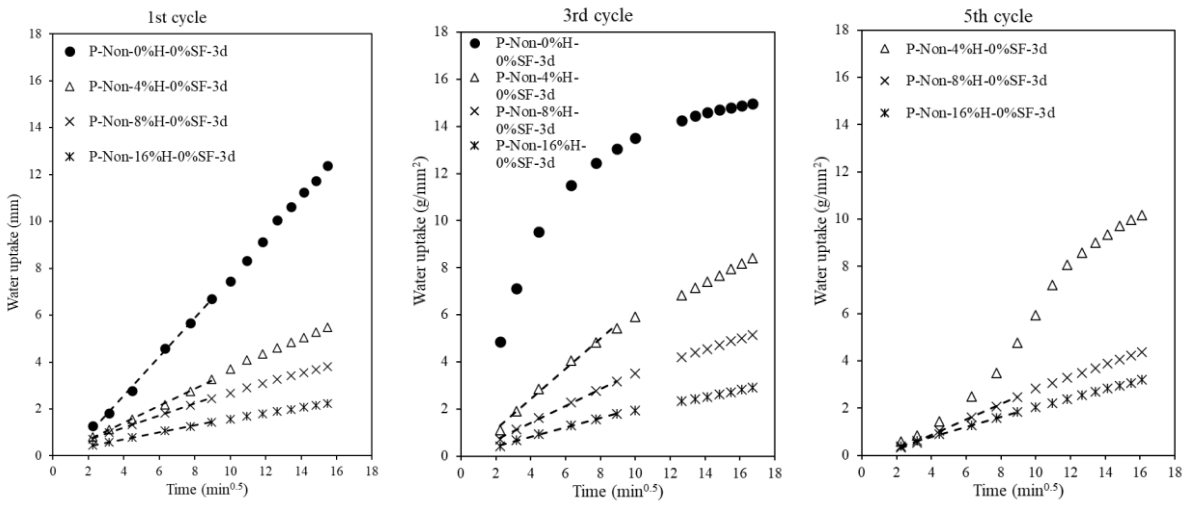
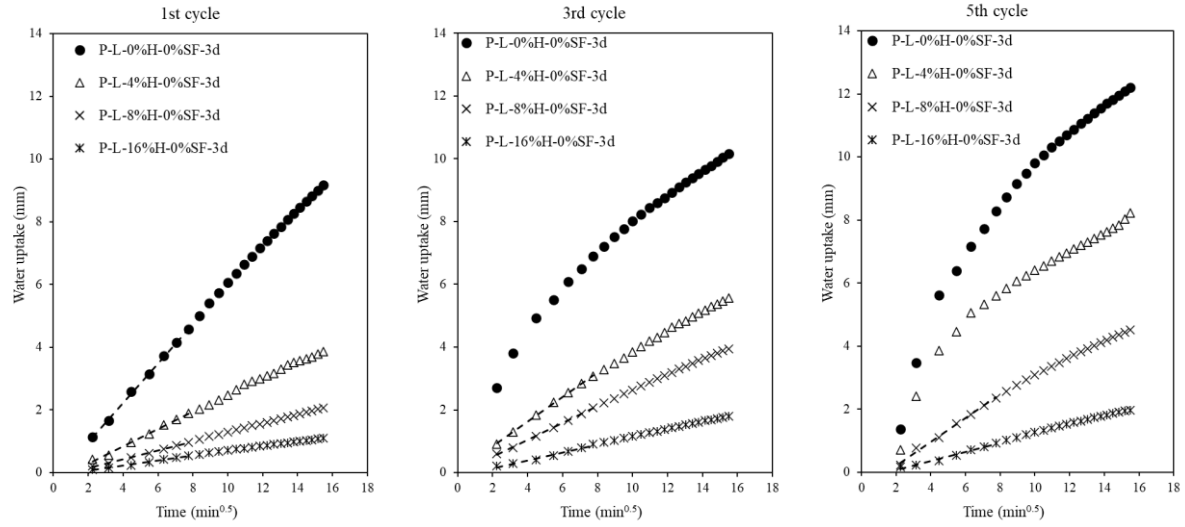


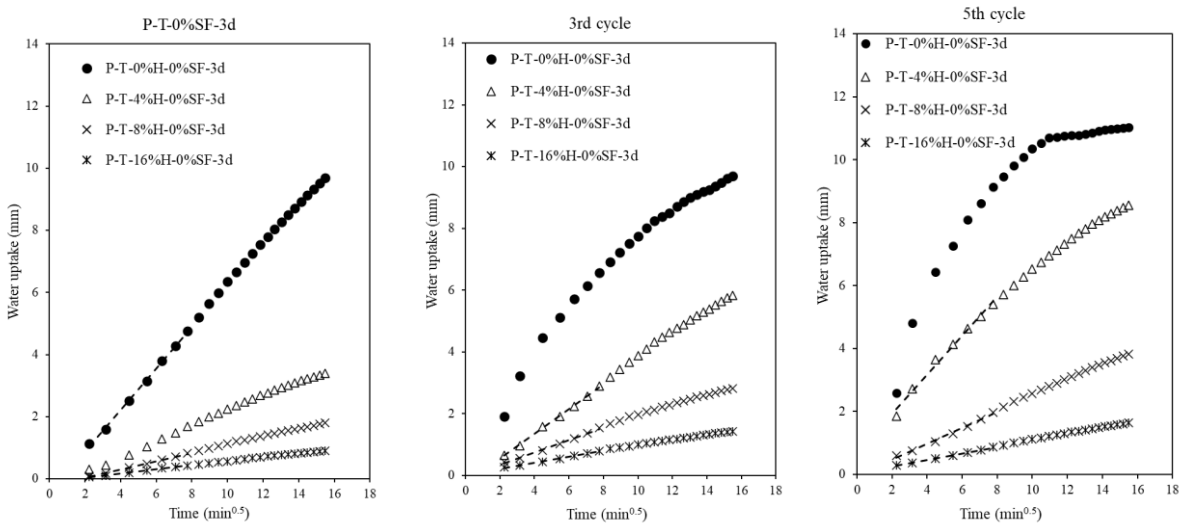
Figure 6.6 Sorptivity of paste samples subjected to cyclic wetting and drying (a) Non-textured, (b) Lotus textured, (c) Taro textured, (d) Microgrid patterned. Error bars represent standard deviation.



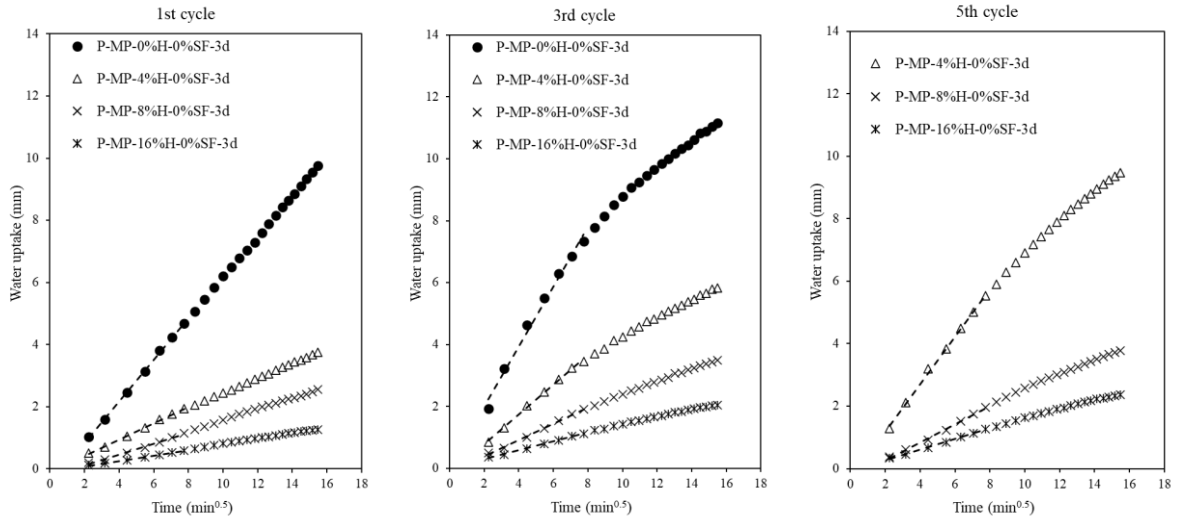
(a) Nontexture



(b) Lotus texture



(c) Taro texture



(d) Microgrid pattern

Figure 6.7 Example of cumulative water uptake plots for paste samples containing various amount of HPCC at the 1st, 3rd, and 5th wetting cycle.

Micro textured pastes with 16% HPCC had their sorptivity values almost doubled at the end of 5th wetting cycle. This indicates a more sever deterioration compared to the P-Non-16%H, as the latter increased by only ~52%. If we compare the sorptivity at each cycle, taking lotus textured pastes as an example, P-L-16%H showed sorptivity 40.1%, 27.8%, 22.9%, 21.1%, and 16.8% lower relative to P-Non-16% at the end of 1st, 2nd, 3rd, 4th, and 5th wetting cycles, respectively. The textured samples showed a large increase in sorptivity after three wetting cycles, indicating deterioration of the surface texture. The surface suffered cracking and some of the large cracks can be seen by the naked eye, as showed in Figure 6.8. Micro cracking

was also of significance to structural integrity of micro texture as the cracks have split surface structures, as shown in Figure 6.8. It is likely that the cracks have led to the failure of establishing an air cushion. Domingues, Arunachalam & Mishra (2017) and Hensel *et al.* (2014) reported that local damage of surface structures would lead to wetting transition from the Cassie to the Wenzel state and trigger the collapse of air cushion at surrounding area. Such damages would cause the textured cementitious materials to behave as non-textured ones. In addition, the cracks may act as convenient paths for water to bypass the air cushion covered area, which downplays the effect hydrophobicity on hindering water imbibition.

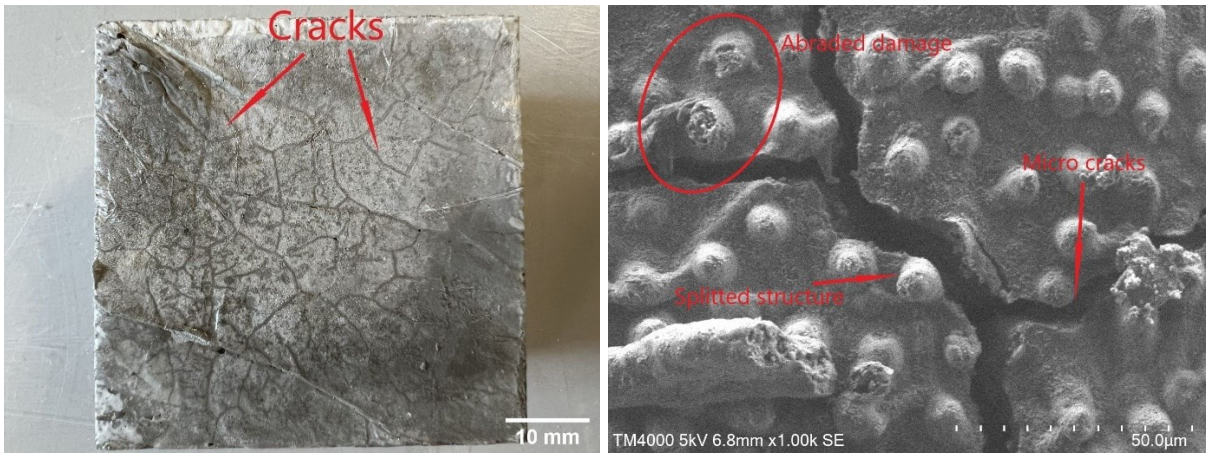


Figure 6.8 Cracks on a P-L-16%H-0%SF-3d after subjected to cyclic wetting. Left: large cracks seen by the naked eye. Right: micro cracks seen under a SEM.

The microcracking and increase in the sorptivity of pastes were so extreme that these are most likely the result of oven-drying. Wong *et al.* (2009) reported that oven-drying at 105° increase the sorptivity of mortar (w/c: 0.55, 3 years old, 55% vol. sand) than oven dried at 50° by 100% at most. The deterioration is mainly resulted from microcracking and the collapse of C-S-H gel structure when water is removed from the layered structure. Slow diffusion of interlayer water was found to begin from C-S-H layer of ≈2 nm below 25% RH (Baroghel-Bouny, 2007; Beaudoin & Odler, 2019). Meniscus that forms between C-S-H sheets during the exit of interlayer water pulls adjacent sheets into close proximity, and as a consequence produces denser local C-S-H packings (Beaudoin & Odler, 2019). This assertion was confirmed by Gajewicz *et al.* (2016), who verified the rearrangement of C-S-H globules after drying paste samples at various conditions. They found that newly formed coarse pores (>20 nm) were created at the expense of finer pores (<10 nm). This was evidenced by the fact that the amount of water absorbed in newly formed coarse pores during re-wetting was almost equal to the decrease in water absorbed into fine pores. Therefore, it can be expected that the rearrangement of aggregates of C-S-H sheets due to the action of meniscus effect happened

during oven drying at 50°C and 10% RH.

Water re-entering layered structure during the subsequent wetting stage causes swelling of C-S-H gel but without an equivalent re-expansion due to some irreversible deformation. Gajewicz *et al.* (2016) concluded that up to 80% of fine gel pores recovered after 12 days of re-wetting (porosity of samples consisted of 96% of fine pores and 4% coarser pores (>10 nm) before drying) while coarse pores caused by irreversible C-S-H sheets collapse accounted for 80% of the coarser pores after drying. One explanation is that the local irreversible deformation of C-S-H layers is linked with compressive stress exerted by absorbed water through capillary suction (Beaudoin & Odler, 2019). As water re-enters layered structure, absorption region subjects to a complex stress field which can basically be classified as a spreading stress tangential to the C-S-H sheets and a shear stress normal to the C-S-H sheets. The collapse of C-S-H layered structure may begin by initial rupture at the point where fault existed due to a delay in response to the expansion of interlayer rehydration. Although it was observed that the deformation of C-S-H layered structure took place on first drying and, to a lesser degree, in subsequent wetting-drying cycles(Jennings, Kumar & Sant, 2015), the general picture is that repeat wetting and drying increase the number of ruptures as well as cause a rapid increase in size, which eventually leads to the damage of samples.

In the presence of HPCC, the hydrophobic particles embedded in the wall of capillary pores, which inhibit its wetting capacity. This means less water would be absorbed into the bulk of sample during wetting cycles and therefore, the paste samples suffer less severe deformation of C-S-H structure in the following drying cycles. However, protection from HPCC against the deterioration related cyclic wetting may not be sufficient at low HPCC content (<4%) since the S-shaped absorption curves started to be observed at the end of 5^{th} wetting cycle (Figure 6.7).

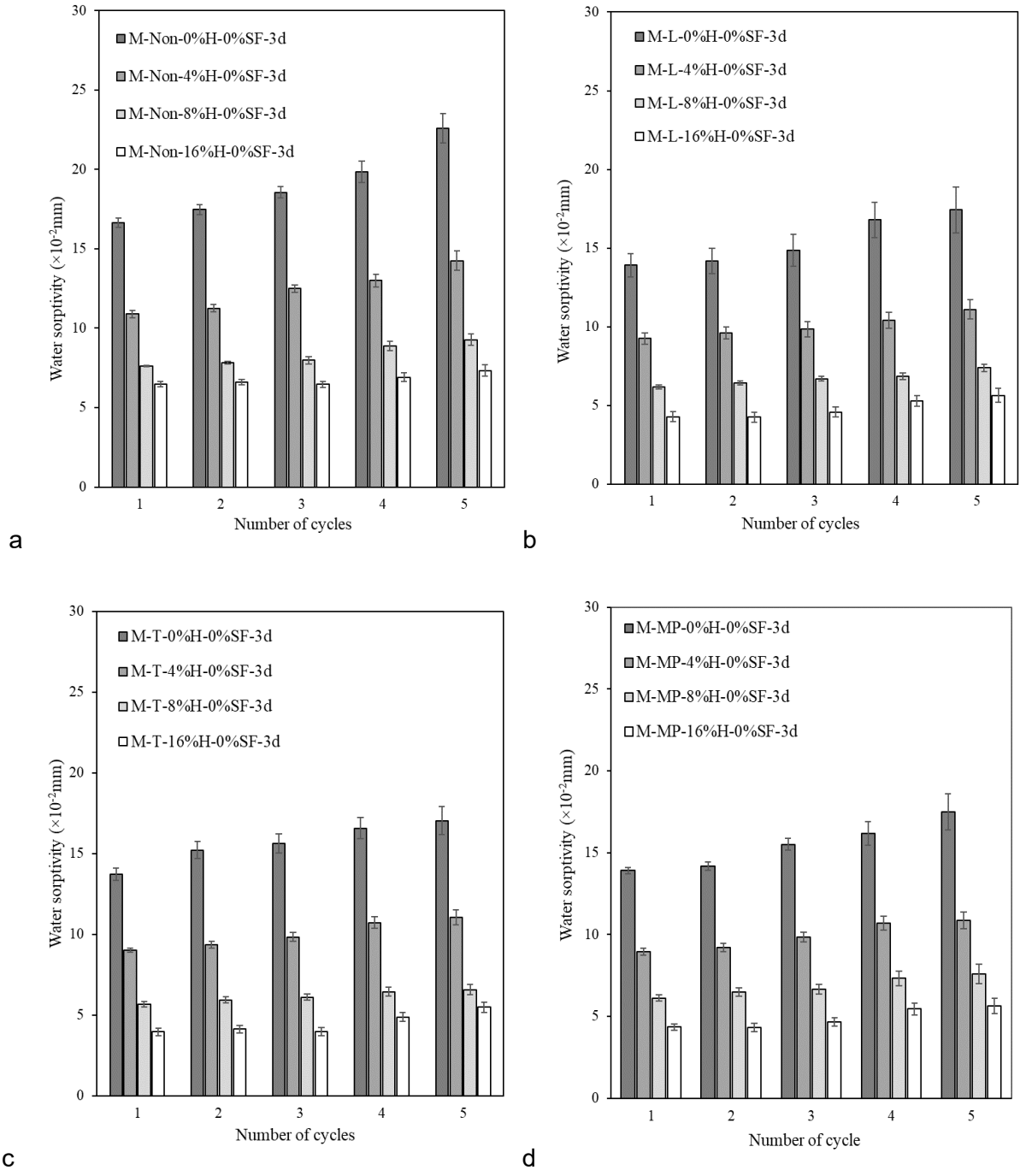


Figure 6.9 Sorptivity of uncoated mortar samples subjected to cyclic wetting and drying (a) Nontextured, (b) Lotus textured, (c) Taro textured, (d) Microgrid patterned. Error bars represent standard deviation.

When compared to the non-textured pastes, mortar samples showed a moderate variation in sorptivity between wetting cycles (Figure 6.9). No deviation from the i-$t^{0.5}$ relationship was observed for all measurements indicating the samples experienced only minor deterioration. Sorptivity of M-Non-0%SF-3d at the end of the fifth cycle showed increase range from 13.3-

35.8% compared to the first cycle, while pastes have displayed significantly higher deterioration. This is expected considering that mortars contain lower volume fraction of cement paste. As analyzed earlier, deterioration process is driven by water and vapor movement between C-S-H sheets. Aggregate decreases total paste content and itself has insignificant water absorption. Therefore, mortar samples will deteriorate much slower than paste samples because of lower water uptake and loss during each wetting-drying cycle. The deformation of cement matrix was also restrained by aggregate, which mitigate deterioration.

Surface textures on mortars appear to have more consistent contribution to decreasing water sorptivity than the pastes when subjected to cyclic wetting. For example, when compared to water sorptivity of M-Non-16%H-0%SF, the M-L-16%H-0%SF sample showed average reduction in sorptivity of 33.8%, 35.6%, 29.2%, 23.6%, and 23.2% at the end of 1^{st}, 2^{nd}, 3^{rd}, 4^{th}, and 5^{th} wetting cycles, respectively. These improvements could be attributed to aggregate restraining the deformation of cement matrix, so that the textured surfaces were less affected by cracking.

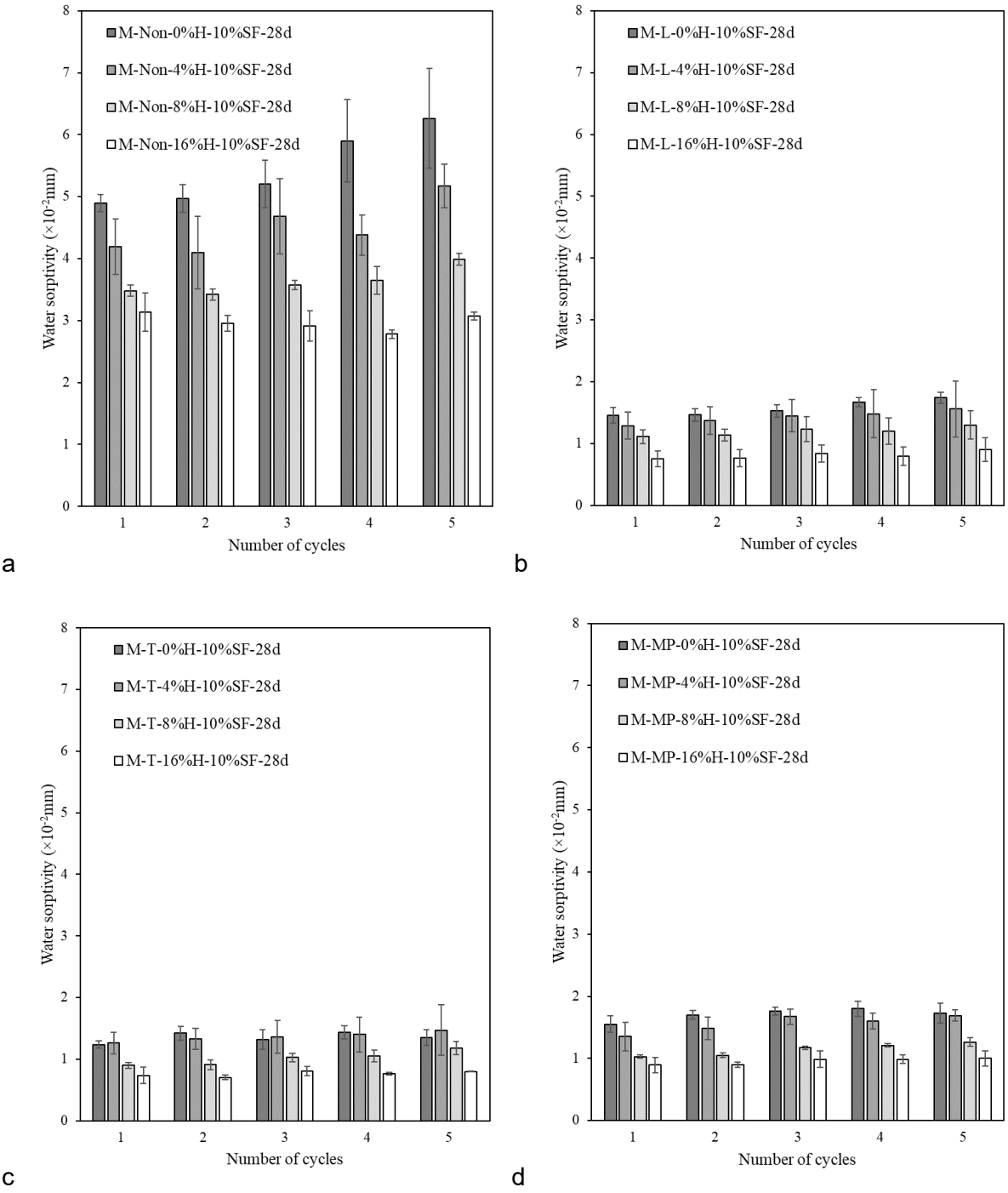


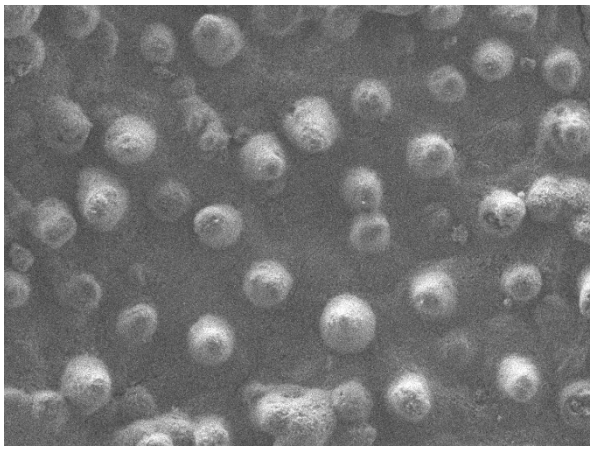
Figure 6.10 Sorptivity of PDMS coated mortar samples subjected to cyclic wetting and drying (a) Nontextured, (b) Lotus textured, (c) Taro textured, (d) Microgrid patterned. Error bars represent standard deviation.

Textured surfaces covered with PDMS coating yielded the best performance on hindering water imbibition under cyclic wetting. The sorptivity values for all types of coated textured samples displayed only a minor variation between wetting cycles (Figure 6.10). The SF played an important role in pore structure refinement, leading to a lower water sorptivity of the bulk of

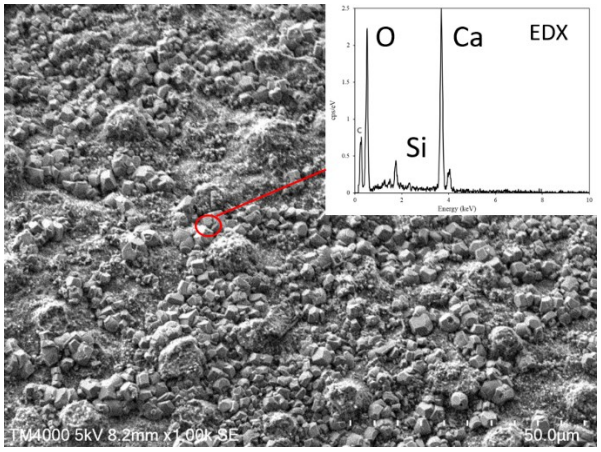
material and reduced risk of cracking under cyclic wetting. The PDMS coating remained effective in reducing water absorption at the end of the fifth cycle as the sorptivity was increased by only 20% at most when compared to the first cycle. The samples were oven dried at 50°C for over 1 week between each wetting cycle and submerged in water for 20 hours in total, and it can be seen that the PDMS coating is quite durable even when exposed to extreme conditions. Normally, degradation of PDMS film in water was found to be very slow through hydrolysis (Teisala *et al.*, 2020), approximately several months to dissolve a few nanometers of PDMS film in water at room temperature. They also reported that the PDMS film grafted on a glass slide showed no sign of deterioration after subjected to UV radiation, mild abrasion, high temperature, and rinsed with water under sonication. Rapid deterioration of the PDMS film was observed in high acidic (PH ≤ 1) and high alkalinity (PH ≥ 13) solutions or high temperatures of about 300°C (Teisala *et al.*, 2020; Camino, Lomakin & Lazzari, 2001; Thomas & Kendrick, 1969). The environmental conditions to which a concrete structure is subjected are varied, but normally below these limits. It is therefore reasonable to postulate that the PDMS coating grafted on cementitious samples will be able to provide a relatively long-term protection against water transport.

6.6 Influence of humid environment

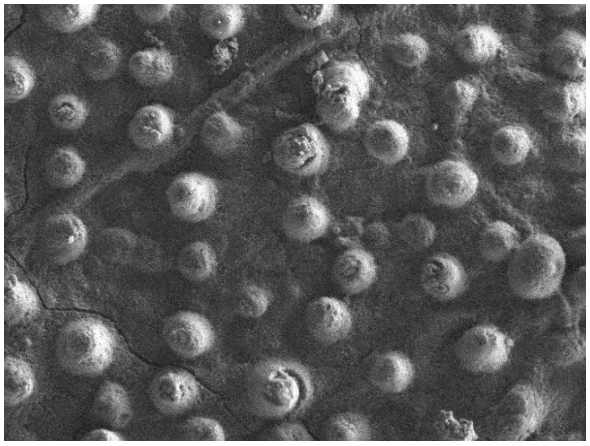
Before the textured samples were subjected to 98% RH exposure, reproduced surface textures exhibited great similarity to the original textures on plant leaves. After 1 month of exposure to 98% RH, upon visual examination the textured surfaces remained roughly the same as that before exposure. Anhydrous cement may continue to react in this condition as hydration would only suspend at RH lower than 80% (Snyder & Bentz, 2004; Flatt, Scherer & Bullard, 2011). Anhydrous cement normally appears in cement matrix as unreacted cores with build-up of hydration products (outer products), mainly C-S-H gel around the hydrating particles forming a barrier to further reaction. The hydration of anhydrous cores would continue at a slower rate as moisture diffuse through the outer product layer. C-S-H gel generated from continuous hydration (inner products) has a compact homogeneous morphology whereas the outer products are fibrillar (Richardson, 2004). However, the inner products are surrounded by the outer products and therefore, had no or little effect on altering surface properties. XRD analysis showed mainly hydration products present on the surface, indicating other types of deterioration may be of less significance during the first month of exposure (Figure 6.11 (m)).



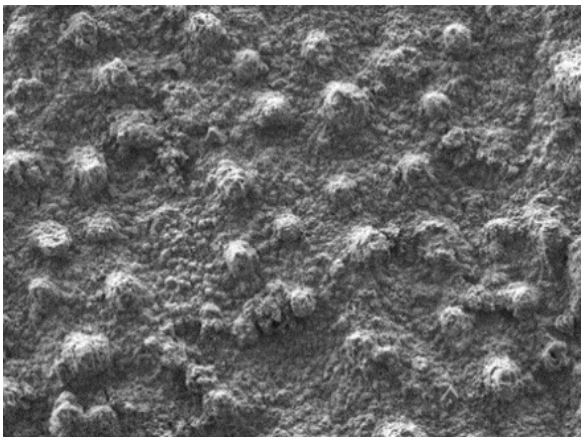
(a) P-L-0%H-0%SF-3d 1 month



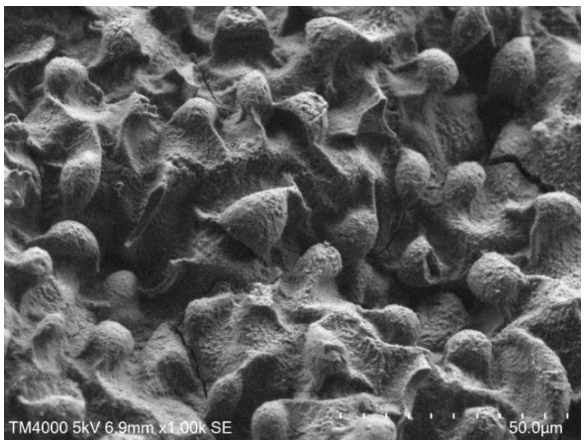
(b) P-L-0%H-0%SF-3d 3 month



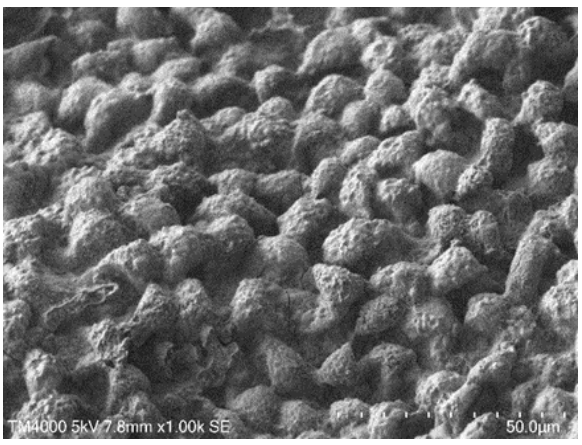
(c) M-L-0%H-0%SF-3d 1 month



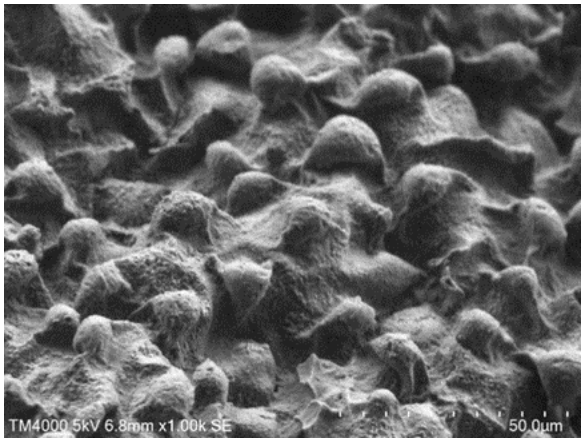
(d) M-L-0%H-0%SF-3d 3 month



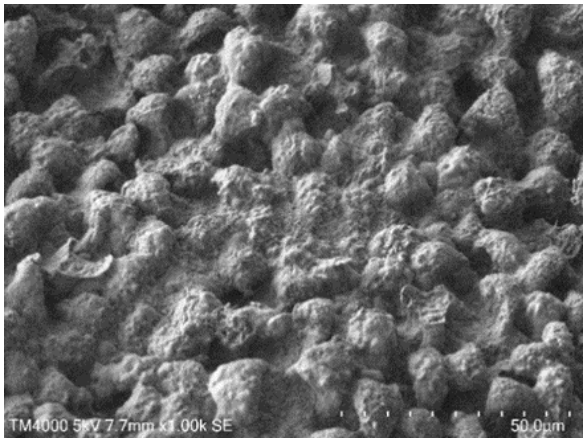
(e) P-T-0%H-0%SF-3d 1 month



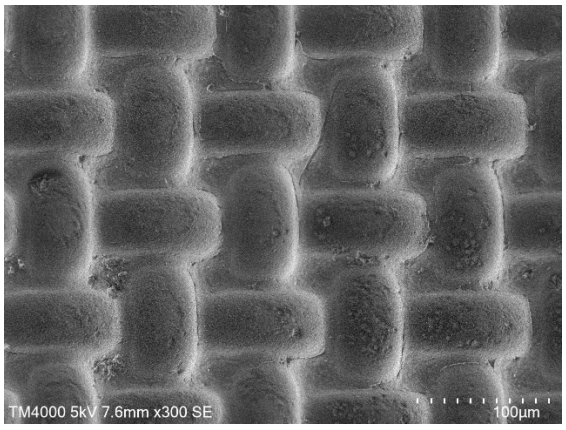
(f) P-T-0%H-0%SF-3d 3 month



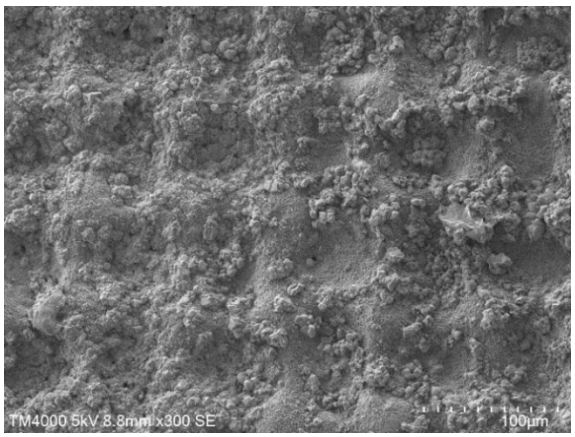
(g) M-T-0%H-0%SF-3d 1 month



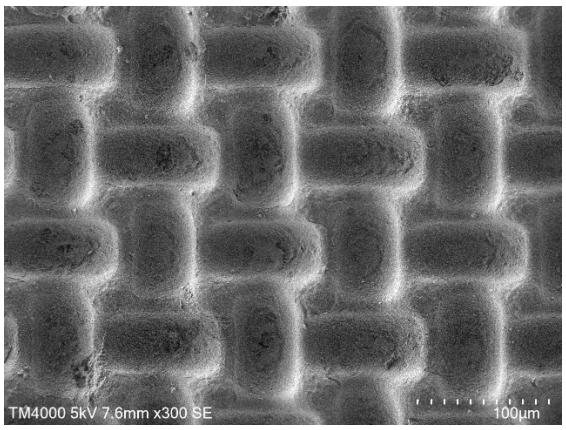
(h) M-T-0%H-0%SF-3d 3 month



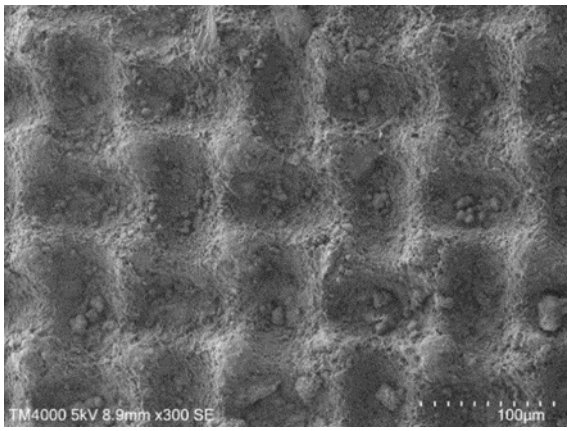
(i) P-MP-0%H-0%SF-3d 1 month



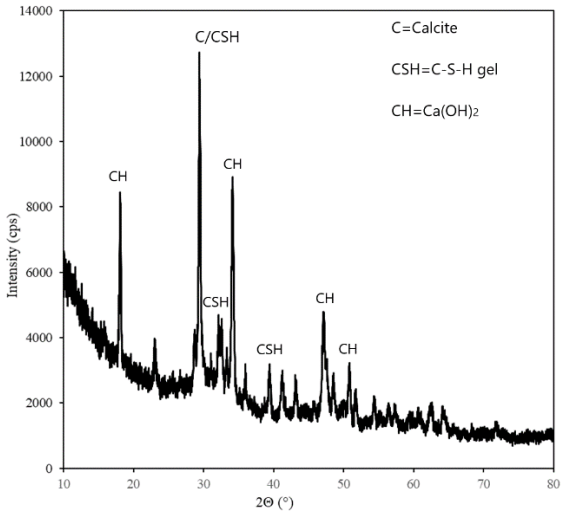
(j) P-MP-0%H-0%SF-3d 3 month



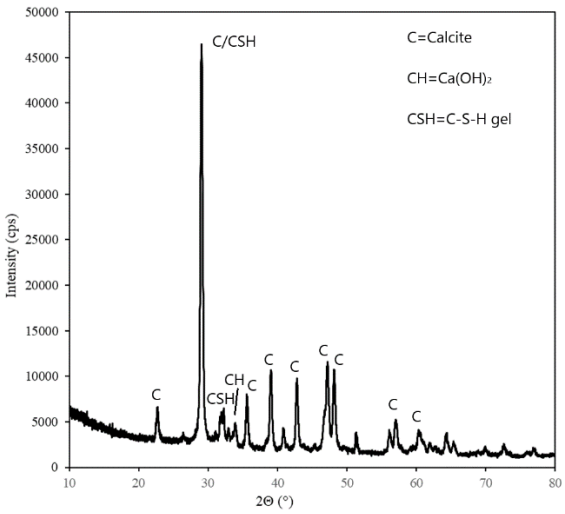
(k) M-MP-0%H-0%SF-3d 1 month



(l) M-MP-0%H-0%SF-3d 3 month



(m) M-MP-0%H-0%SF-3d 1 month



(n) M-MP-0%H-0%SF-3d 3 month

Figure 6.11 (a)-(l) Micro textured pastes and mortars subjected exposure to 98% RH for 1 and 3 months. (m) XRD analysis of surface exposed for 1 month. (n) XRD analysis of surface exposed for 3 months.

For samples exposed to 98% RH for 3 months, the geometry of surface textures was largely altered. Figure 6.11 (b) shows that newly formed phases, with a similar size to lotus papilla, have developed on the textured surface. These phases presented a polyhedral appearance and most of them are found on the base of textures. EDX analysis showed these phases have high calcium and carbon content but deficient in silicon (Figure 6.11 (b)). XRD showed that the major mineral phases present on the textured surface after 3 months exposure were calcite (Figure 6.11 (n)). These results indicate that these phases are most likely calcium hydroxide leached out from the bulk of sample and may have subsequently carbonated. This type of deterioration should be attributed to the efflorescence of cement.

The reason that efflorescence was a dominant deterioration mechanism is probably due to the fact that the samples were saturated with water through water vapour sorption. Normally, a layer of water film on the surface of sample is essential to the occurrence of efflorescence, as suggested by Dow & Glasser (2003). They explained that the presence of a water layer on the surface of cement facilitated efflorescence and resulted in rapid CO_2 absorption. Alkaline environment within the concrete can increase the solubility of CO_2 by two to three orders of magnitude compared to in pure water because the presence of hydroxide prevents the CO_2 from dissolving in water in the form of carbonic acid (Dow & Glasser, 2003). As calcium hydroxide continuously leach out, calcium ions are transported into the carbonate-rich water film and precipitate as calcium carbonate by “through-solution mechanism”. The precipitated calcium carbonate quickly builds up on the surface as the alkaline environment accelerates

the absorption of CO_2, which in turn removes the calcium ions and hydroxyl from solution and forces more calcium hydroxide to dissolve to maintain pH.

When compared to micro textured pastes, the textured mortars suffered from relatively moderate level of surface deterioration after 3 months of exposure to 98% RH. This is because the mortars had 60% vol. cement paste replaced by aggregate particles, which reduced the amount of leachable calcium in the cement matrix. In addition, the presence of aggregate increased the tortuosity of capillary pore network and hence impeded the transport of calcium ions.

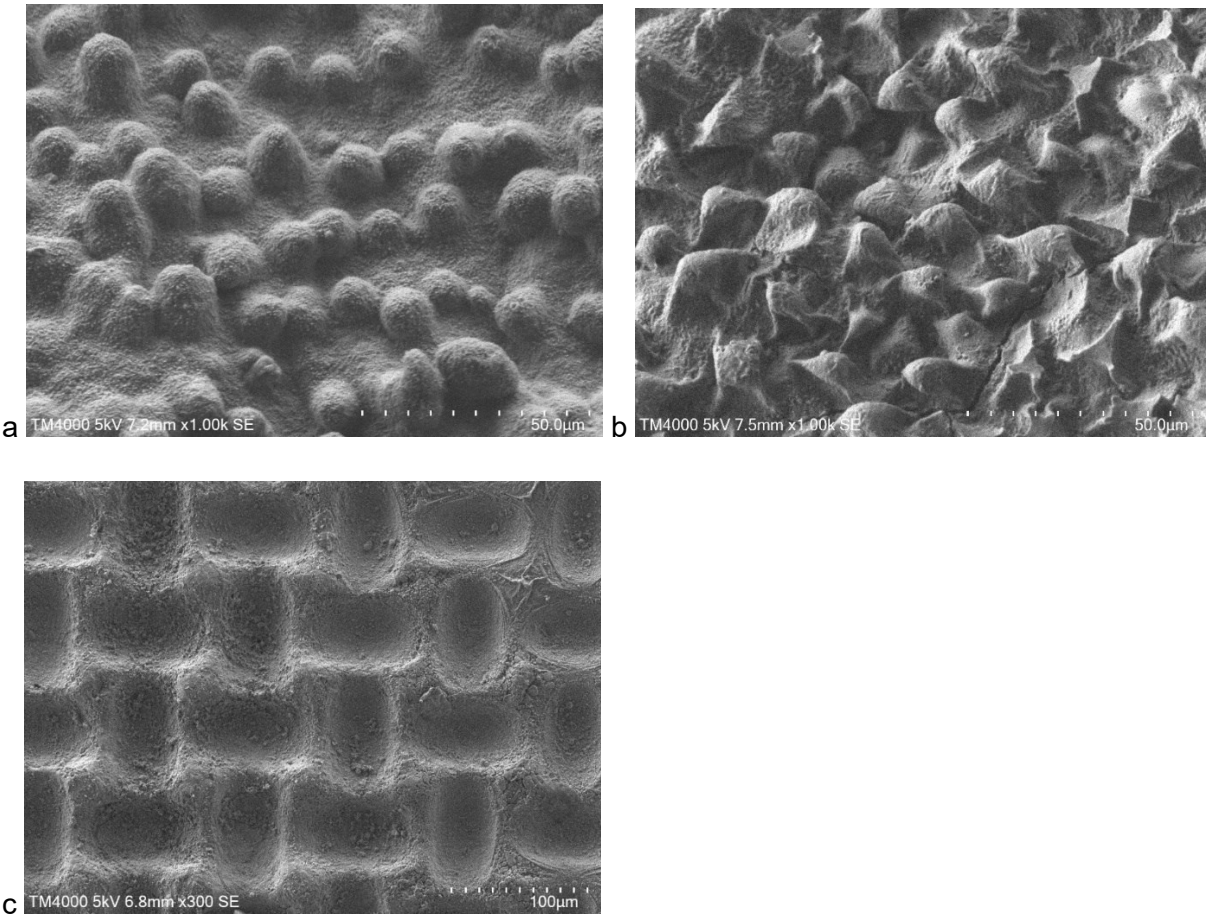


Figure 6.12 SEM images of (a) M-L-0%H-10%SF-28d (b) M-T-0%H-10%SF-28d (c) M-MP-0%H-10%SF-28d exposed to 98% RH for 3 months.

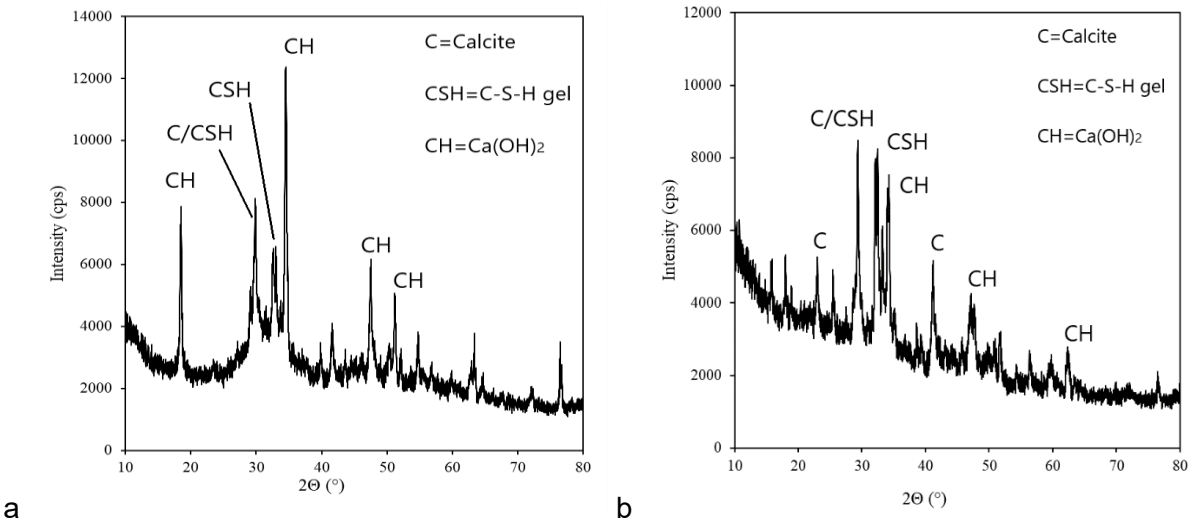


Figure 6.13 XRD spectrums of SF-containing textured surface after (a) 1 month and (b) 3 months exposure to 98% RH.

Unlike the surface textures made of plain cement paste and mortar that significantly deteriorated in a humid environment, SF-containing textures remained largely unchanged after 3 months exposure to 98% RH (Figure 6.12). Large calcium carbonate crystals were not observed on the surface and XRD spectrum of the surface showed much weaker calcite peaks than those of plain cement counterpart (Figure 6.13). This indicates the presence of small efflorescent deposits exist on the mortar surfaces, and that this has a minor influence on the surface topography.

Surface textures made of SF-containing mortar were much more durable than those made of plain mortar. This could be due to two reasons: a) The influence of continuous hydration was reduced as 10% of cement was replaced with SF and the samples were cured for longer period before exposure to high humidity; and b) the pozzolanic reaction in SF mortar consumed part of calcium hydroxide, leading to a reduction in leachable calcium ions in cement matrix. In addition, the refined pore structure of SF-containing mortar caused less opportunity for moisture and ionic movement (Lewis & Fidjestol, 2019).

Table 6.2 Summary of water contact angles of textured surfaces subjected to different exposure time to 98% RH.

	Water contact angle (°)		
	Initial	*1 month*	*3 months*
P-L-0%H-0%SF-3d	*121.7 (2.17)*	*122.7 (2.24)*	*68.2 (6.44)*
P-T-0%H-0%SF-3d	*128 (2.34)*	*133.5 (2.35)*	*99 (5.76)*
P-MP-0%H-0%SF-3d	*114.3 (1.81)*	*113.3 (1.83)*	*100.7 (5.98)*
M-L-0%H-0%SF-3d	*120.7 (1.8)*	*118.6 (2.13)*	*107.6 (3.14)*
M-T-0%H-0%SF-3d	*127.3 (2.18)*	*129.4 (2.36)*	*115.9 (3.66)*
M-MP-0%H-0%SF-3d	*115.2 (2.24)*	*114.5 (1.97)*	*111.4 (2.73)*
M-L-0%H-10%SF-28d	*138.5(1.23)*	*137.3(1.12)*	*140.3(1.24)*
M-T-0%H-10%SF-28d	*138.1(0.98)*	*139.4(1.03)*	*139.1(1.15)*
M-MP-0%H-10%SF-28d	*132.7(0.93)*	*133.1(0.89)*	*132(0.81)*

In Table 6.2, static water contact angles measured from the deteriorated surfaces are shown. It can be found that the surface wettability was basically unaffected after exposure to the humid environment for 1 month as the change in water contact angle was less than 6°. Again, droplets were pinned on the textured surface with no sign of rolling in all cases. The SF-containing samples had their wettability unaffected by humid environment even after 3 months of exposure. However, a significant increase in surface wettability was observed on textured pastes. The deterioration resulted in a decrease in the water contact angle of P-T-0%H-0%SF and P-L-0%H-0%SF by 23% and 44% respectively. The wettability of textured mortar was less affected by efflorescence compared to the textured paste after 3 months of exposure, as M-T-0%H and M-L-0%H showed contact angles 9% and 11% lower than that before exposure, respectively. This is consistent with the observation of surface topography that a minor deterioration of surface texture would lead to a smaller reduction in water contact angle.

The question as to why the efflorescent deposits resulted in a large decrease in the hydrophobicity of micro textured surface can be answered by ‘sag transition’ described in the work of Whyman & Bormashenko (2011). The effective height to spacing ratio of surface texture was reduced because of the large efflorescent deposits that have developed on the base of texture. As a result, the water-air interface can easily reach the base due to sagging and this leads to an instant wetting transition. It is worth noting that the microgrid textured surface always showed the least reduction in contact angle compared to the plant textures. This is because the characteristic size of microgrid pattern is much larger than the plant textures, which makes it less sensitive to small changes in topography caused by

efflorescence. The efflorescence products were non-uniformly distribute over the surface, this led to surface wettability varying from place to place (as evidenced by large standard error of the measured mean), depending on the accident of the shape and the local density of the products.

6.7 Carbonation

Mortar samples (3 days old) with 0%, 4%, 8%, and 16% HPCC had carbonation depth of 6.1, 5.9, 6.2, and 6 mm after 1 month exposure to 3% CO_2 and 68% RH, indicating no apparent effect of HPCC on the carbonation of mortars. This is consistent with the results of gas diffusion (section 5.7) where the diffusivity of mortars was unaffected by HPCC addition, as carbonation is governed by gas diffusion.

Table 6.3 Water contact angles of textured mortars before and after carbonation.

	Water contact angle (°)	
	Before	After
M-L-0%H-0%SF-3d	121.4 (2.03)	123.9 (2.22)
M-T-0%H-0%SF-3d	121.9 (2.38)	124.3 (2.15)
M-MP-0%H-0%SF-3d	115.2 (2.24)	113 (1.99)
M-L-0%H-10%SF-28d	137.9 (0.74)	137 (1.07)
M-T-0%H-10%SF-28d	138.4 (1.01)	138.2 (0.83)
M-MP-0%H-10%SF-28d	132.5 (0.79)	130.4 (0.87)

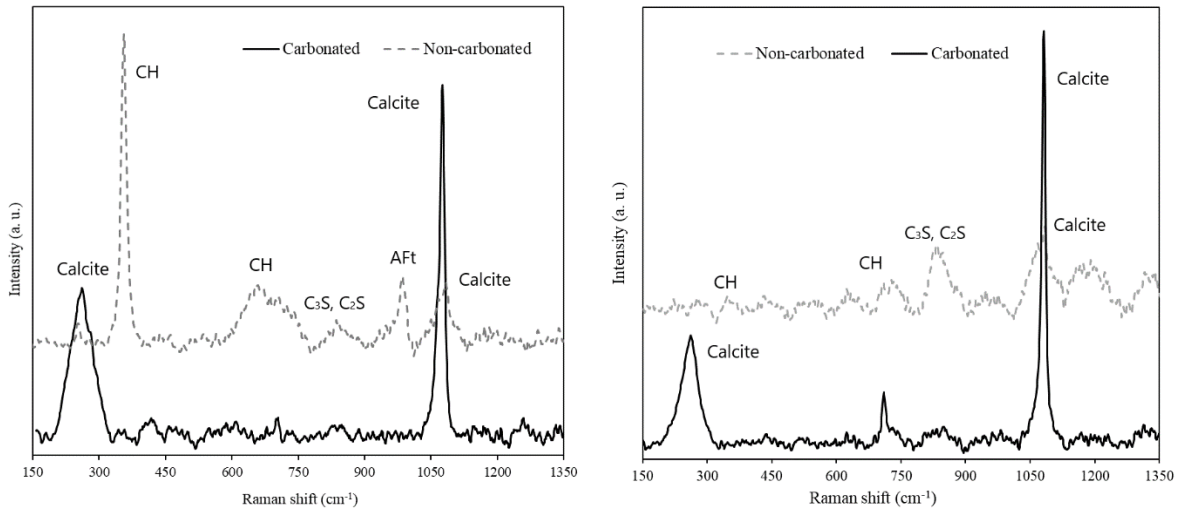


Figure 6.14 Raman spectrums of micro textured mortar surfaces before and after carbonation. Left: M-L-0%H-0%SF-3d; Right: M-L-0%H-10%SF-28d.

The Raman spectrums of surface before carbonation are showed in Figure 6.14. Pozzolanic reaction in SF-containing mortars that consume calcium hydroxide and generate C-S-H gel leads to a weaker calcium hydroxide intensity compared to that of plain mortars before carbonation. This would make the carbonation of textured samples containing SF to occur much faster due to the lack calcium hydroxide acting as a buffer to carbonation. Traces of calcite was found on the surfaces before placed into a carbonation incubator as carbonation took place quickly once removing the samples out of the CO_2 free environmental chamber (Figure 6.14). After 1 month of carbonation, the measured water contact angles on carbonated textured surfaces were nearly identical with that before carbonation in all cases (Table 6.3). Image analysis showed the surface topography remained unchanged after carbonation. Raman spectroscopy of carbonated surface showed that the surfaces were dominated by calcite, which indicated the surfaces were fully carbonated (Figure 6.14). Therefore, further exposure of the samples to CO_2 is unlikely to cause significant change in surface topography as well as surface wettability.

6.8 Conclusion

Abrasion resistance of micro textures was tested by pulling the samples on a 1200-grit SiC paper. Replacing 10% of cement with SF led to an increase in abrasion resistance compared to samples made of plain cement. Aggregate had virtually no influence on surface properties leaving the abrasion resistance of micro textures mainly reliant on the strength of cement matrix. Severe abrasion caused the top of surface textures to flatten out and the shortened textures lead to the loss of hydrophobicity. Microgrid pattern was more resistance to abrasion as its dimension was larger than the plant textures.

Cracks on surfaces would also lead to a significant loss of hydrophobicity for micro textures. Acid leaching removed calcium from the cement paste matrix, leaving a fragile silica rich gel that cracks during the drying process. Water droplets placed on such a leached surface were immediately spread out.

Micro textured samples subjected to cyclic wetting and drying had their sorptivity values increasing to close to those of nontextured samples, indicating that deterioration has occurred. Observation of the surfaces showed the surfaces suffered from shrinkage-induced cracking. Damages of this type would trigger the collapse of air cushion at surrounding areas and the cracks act as a convenient path for water to bypass the air cushion covered area. Paste samples showed more severe cracking than mortars due to the lack of aggregate to restrain the deformation of cement paste matrix. PDMS coated textured samples had durability far superior to the textured ones (uncoated) under cyclic wetting and drying test. The coating also

appeared durable enough to withstand the constant immersion and high temperature exposure.

Prolonged exposure to a humid environment (98% RH) resulted in a change in the morphology of textured surfaces due to efflorescence. The precipitated product were mainly calcium carbonate crystals, and they frequently developed on the base of surface textures, reducing the effective height to spacing ratio of surface textures. Contact angle measurements on these surfaces showed a loss of hydrophobicity to some extent, due to the large efflorescent deposits triggering a “sagging” transition, which occur when the meniscus reaches the top of the deposits between textures. Among the three types of surface textures, the wettability of microgrid patterned surface was the least affected by efflorescent deposits. Compared to pastes, mortar samples were less affected by efflorescence since 60% vol. of the cement paste matrix have been replaced with inert aggregate particles. There was no visible sign of deterioration on SF-containing textured samples, suggesting the avoidance of efflorescence mechanism due to pozzolanic reaction. Water contact angle of these textured mortar (with and without SF) remained fairly constant after 3 months of exposure to 98% RH.

Carbonation carried out in 3% CO_2 showed that HPCC did not affect carbonation resistance of mortars. In addition, the morphology of surface textures, as well as the surface wettability, did not alter during carbonation.

7 Conclusions and future work

7.1 General conclusions

The main aim of this work was to develop cementitious materials with hydrophobic micro textured surfaces, to investigate their effects on wettability and transport properties, and to establish their durability in a range of environments. The surface textures selected for this study were two natural micro textures derived from water repellent plant leaves, lotus and taro, and a synthetic microgrid pattern. The microgrid patterned surface consisted of an array of square posts and was designed to imitate natural hydrophobic textures. The main conclusions that can be drawn from this thesis are as follows:

- Soft lithography was found to be an effective approach for replicating the micro textures on to cementitious materials with a high degree of fidelity. The replicated micro textures (lotus, taro and microgrid) were found to be effective in reducing the wettability of cement-based materials. The addition of hydrophobic precipitated calcium carbonate (HPCC) and hydrophobic PDMS coating enhanced the effect of micro textures to a large degree.
- HPCC reduced both the wettability and water absorption of cementitious samples. The higher the amount of HPCC, the higher the degree of water repellency and the lower the deterioration under cyclic wetting-drying. The HPCC also led to the formation of entrapped air voids in paste samples, which facilitated gas transport and increased the oxygen diffusivity and oxygen permeability coefficients. However, the gas transport properties and porosity of mortar and concrete samples were largely unaffected by HPCC addition.
- Water droplets placed on lotus and taro textured surfaces showed contact angles of around 120°, which increased with increasing HPCC content. However, an energy input such as dropping from a height above the surface can cause the transition from Cassie to Wenzel state. In this case, the droplets will exhibit low water contact angle and be absorbed into the bulk sample.
- Textured cementitious surfaces showed a strong adhesion to water droplets to the extent that the droplets remained pinned even when the surfaces were rotated. Rolling of the droplets was observed when the droplets were released from a height onto inclined micro textured surfaces. In this case, the initial velocity combined with gravity acting on the droplets can overcome the adhesive forces.
- Casting fresh cement-based mixture against a nylon microgrid that has been pre-coated with PDMS was effective for creating the desired microgrid surface texture. The produced microgrid patterned surface consisted of an array of micro posts and displayed a water contact angle of 113°. Adding 16% HPCC increased the water contact angle to 134°,

indicating that this approach for producing hydrophobic cement-based materials was highly successful.

- Air cushion trapped between the surface texture under water was observed for the first time, by using optical microscopy. It was found that the stability of the trapped air cushion was related to the content of HPCC in the mixture. At low HPCC content (<8%), the trapped air cushion either did not form or quickly coalesced into larger air bubbles. At 16% HPCC, the stability of the trapped air cushion increased, and this led to a substantial decrease in water absorption. In most cases, the area of air cushion gradually decreased over time without coalescing into air bubbles.
- Durability studies found that micro textured surfaces can lose their hydrophobicity when subjected to abrasion. Efflorescence was another deterioration mechanism that can occur when textured samples were exposed to prolonged humid environment. Samples with microgrid patterned surface showed a considerable advantage in resisting such degradations and was less susceptible to morphological changes because of their larger texture size. The presence of aggregate particles and silica fume also played important roles in enhancing the durability of micro textures because they reduce the cement content and leachable calcium, thereby alleviating the degree of efflorescence over service life.
- Carbonation depth of mortar was unaffected in the presence of HPCC. Surface morphology and wettability of textured surfaces were largely unchanged after carbonation, indicating that carbonation had no major influence on the durability of surface textures.
- The hydrophobicity of textured cementitious surfaces was largely improved by coating the surfaces with a thin layer of PDMS. This was achieved by replacing 10% of cement with SF. The PDMS reacts with SF through a grafting reaction and becomes transferred onto the sample surface. The results showed that the grafted PDMS coating was permeable to water vapour but restricted the passage of liquid water. Furthermore, the PDMS coating significantly increased the stability of air cushion trapped between surface textures compared to uncoated samples when immersed under water. The PDMS coating remained effective and durable after being subjected to cyclic wetting and high temperature.

For the first time, the effects of hydrophobic surface textures on wettability and water transport properties of cement-based materials have been systematically explored. This research has showed that textured surfaces can not only decrease the surface wettability but also impede water ingress through trapping a layer of air on the surface. The performance of textured surface with regard to reducing water absorption was found more prominent in the presence of hydrophobic coating. In other words, producing a micro textured surface on cementitious samples can be viewed as a method to enhance the effect of hydrophobic coating. In practical

terms, this provides a novel method to deliver effective hydrophobic concrete materials. The change in the wetting behaviour on horizontal and inclined surfaces highlights that the huge effect the impact has on the hydrophobicity of the surfaces. Inclination angle of a micro textured surface is therefore an important factor that must be considered in application. Generally, large inclination angle should be adapted as it facilitates the rolling of droplets. The use of nylon microgrid to produce hydrophobic textured surfaces is a cost-effective approach compared to soft lithography, and it can be applied on to curved surfaces and over large surface areas. Whilst there is still a long way to delivering hydrophobic surface texture in construction practice, this research has demonstrated that micro textured cementitious surface is a viable approach and an important area that is worthy of further research. It is anticipated that the innovations arising from this research will enable wider development and application of hydrophobic surface textures on cementitious materials.

7.2 Opportunities for future work

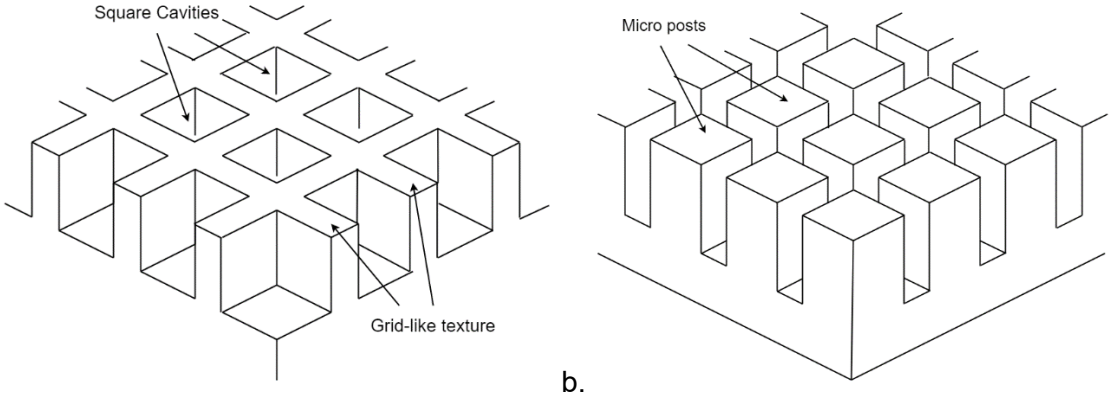
This research has largely focused on the effect of hydrophobic surface textures on the wettability and mass transport properties of cementitious samples, and the durability of such surface textures. The samples that were tested were prepared with paste or mortar with 60% vol. sand at w/c 0.4 and were by no means extensive. Mixture rheology is crucial to whether a surface texture can be produced (Liu *et al.,* 2017; Gao *et al.*, 2019). In practice, aggregate comprises 60% to 80% vol. of a typical concrete mix. High aggregate content can lead to a reduction in rheology, and therefore, may lead to a defective surface texture. Such a situation can also occur on stiff mixes, such as high strength concretes which are normally produced at very low w/c ratios of 0.13-0.26 (Shin *et al.*, 2019). Therefore, further research must be carried out on a wider range of concrete mixtures with various binder content, type, aggregate volume fraction, aggregate grading, and w/b ratio. This will give a better understanding of the applicability and limitations of lithography for producing micro textured cement-based materials.

This research showed that high dosage of HPCC or a thin PDMS coating enhanced the hydrophobicity of textured cement-based materials to a great extent through surface modification, suggesting that surface energy is as important as micro texture with regards to hydrophobicity. However, as reported by Wong *et al.* (2015) and Shahbazi *et al.* (2020), very high dosage of hydrophobic powder can have detrimental effects on compressive strength and mass transport properties, and whether or not the HPCC would affect the ITZ of cementitious materials requires deep investigation. Further research could test other types of hydrophobic additives which may deliver enhanced hydrophobicity but has less negative

influence on mechanical and transport properties. Fluid hydrophobic emulsion, such as fluoropolymers and hydrocarbons, may be a good alternative as they are likely to be dispersed easily over the micro textured surface, giving a uniform surface coating.

It has been shown that superhydrophobic cementitious surfaces can be produced by applying a thin hydrophobic coating onto the micro textured surface through grafting reaction. Further research is required to develop a method by which the hydrophobic coating can be repaired once deterioration occur during the service life of the structure, to preserve its designed surface properties, ideally without the need for reapplication of the hydrophobic agent. In addition, testing of contact angle hysteresis should be undertaken since the surface coating is likely to block capillary pores, which eliminates suction exerted on water droplets.

Producing surface textures to achieve hydrophobic cementitious materials is a relatively new subject. The work in Chapter 4 showed that a hydrophobic textured cementitious surface can be created through a nylon microgrid. A future possible development would be to attempt other hydrophobic surface geometries. Figure 7.1 (a) shows an example surface texture that is worth consideration for testing. This consists of a close packed array of micron sized square cavities. A water droplet placed on the surface would sit on top of the grid-like micro textures with gas within the cavities. When such a surface contacts with water, the expectation is that air trapped within the separated cavities should be more stable than the continuous air cushion as in the latter case, a collapse of air cushion will trigger the collapse of air cushion nearby. Moreover, the grid-like texture has larger solid fraction than square array of micro posts, which may make them more resistant to abrasion. However, the larger solid fraction may also lead to a decrease in water contact angle. Nevertheless, it would be very interesting to investigate the performance of such grid-like textures in terms of hydrophobicity and durability. Micro textures with inverted trapezoid cross sections are also worth investigating, as it has been shown that this type of surface texture promotes pinning of the water contact line (Cao, Hu & Gao, 2007; Liu *et al.*, 2007). Parameters that are potentially important to the performance of the surface are: side wall angle, area coverage, the height of trapezoid, and cavity mouth radius. However, these parameters have not been studied in great detail, therefore more effort needs to be put into determining the optimal surface geometry.



a. b.

Figure 7.1 Schematic illustration of (a) a grid-like micro texture and (b) the mold used to fabricate the desired surface.

Another area to focus on for further research is to develop reusable templates at a cost-effective manner, which can be used to create micro textured surfaces on a large scale. The template must be manufactured from hydrophobic materials because, as shown in Chapter 4, hydrophilic material facilitated the formation of water-rich regions at the mold-mixture interface, leading to a defective textured surface. In addition, templates that consist of an array of micro post are expected to be easier to clean compared to those consisting of micro cavities as cement residues left within the cavities are difficult to be removed, which then prevent the filling of cement paste during the subsequent casting, as shown in Section 4.4.1. If all the above is achieved, then this could lead to a new promising hydrophobic treatment that can be used in the field.

.

8 Reference

Adamson, A.W. & Gast, A.P. (1997) *Physical Chemistry of Surfaces*. 6th edition. New York: Chichester: Wiley.

Aitcin, P.-C. (2019) The Influence of Water/Cement Ratio on the Sustainability of Concrete. In: P; Hewlett & M; Liska (eds.). *Lea's Chemistry of Cement and Concrete*. fifth. Mathew Deans. p.

Al-kheetan, M.J., Rahman, M.M. & Chamberlain, D.A. (2019) Fundamental interaction of hydrophobic materials in concrete with different moisture contents in saline environment. *Construction and Building Materials*. [Online] 207, 122–135. Available from: doi:10.1016/j.conbuildmat.2019.02.119.

Al-kheetan, M.J., Rahman, M.M. & Chamberlain, D.A. (2020) Moisture evaluation of concrete pavement treated with hydrophobic surface impregnants. *International Journal of Pavement Engineering*. [Online] 21 (14), 1746–1754. Available from: doi:10.1080/10298436.2019.1567917.

Alvaro, Mata; Aaron J, Fleischman; Shuvo, R. (2005) Characterization of Polydimethylsiloxane (PDMS) Properties for Biomedical Micro/Nanosystems. *Mostra de Iniciação Científica, Pós-graduação, Pesquisa e Extensão*. [Online] 7 (4), 281–293. Available from: doi:10.18226/35353535.v5.2016.108.

Arunachalam, S., Ahmad, Z., Das, R. & Misha, H. (2020) *Counterintuitive Wetting Transitions in Doubly Reentrant Cavities as a Function of Surface Make-Up, Hydrostatic Pressure, and Cavity Aspect Ratio.pdf*.p.2001268.

Baker, P.G. & Bishop, P.L. (1997) Prediction of metal leaching rates from solidified / stabilized wastes using the shrinking u & eacted core leaching procedure. *Journal of Hazardous Materials*. 52, 311–333.

Baroghel-Bouny, V. (2007) Water vapour sorption experiments on hardened cementitious materials. Part I: essential tool for analysis of hygral behaviour and its relation to pore structure. *Cement and Concrete Research*. 37, 414–437.

Beaudoin, J. & Odler, I. (2019) Hydration, Setting and Hardening of Portland Cement. In: Peter Hewlett & Martin Liska (eds.). *Lea's Chemistry of Cement and Concrete*. fifth. Mathew Deans. pp. 157–250.

Berg, J. (2010) *An introduction to interfaces & colloids: the bridge to nanoscience*.

Singapore; Hackensack, NJ: World Scientific.

Berthier, J. (2013) The Physics of Droplets. In: *Micro-Drops and Digital Microfluidics*. Second. William Andrew. pp. 75–160.

Bico, J., Thiele, U. & Quéré, D. (2002) Wetting of textured surfaces. *Colloids and Surfaces A: Physicochemical and Engineering Aspects*. [Online] 206 (1–3), 41–46. Available from: doi:10.1016/S0927-7757(02)00061-4.

Bormashenko, E. (2015) Progress in understanding wetting transitions on rough surfaces. *Advances in Colloid and Interface Science*. [Online] 222, 92–103. Available from: doi:10.1016/j.cis.2014.02.009.

Bormashenko, E., Bormashenko, Y., Whyman, G., Pogreb, R., et al. (2006) Micrometrically scaled textured metallic hydrophobic interfaces validate the Cassie – Baxter wetting hypothesis. *Journal of Colloid and Interface Science*. [Online] 302, 308–311. Available from: doi:10.1016/j.jcis.2006.06.016.

Bye, G.. (1999) The nature of harden cement paste. In: *Portland Cement*. Second. London, Thomas Telford Publishing. pp. 131–161.

Callies, M., Chen, Y., Marty, F., Quere, D., et al. (2005) Microfabricated textured surfaces for super-hydrophobicity investigations. *Microelectronic Engineering*. [Online] 79, 100–105. Available from: doi:10.1016/j.mee.2004.12.093.

Camino, G., Lomakin, S.M. & Lazzari, M. (2001) Polydimethylsiloxane thermal degradation Part 1. Kinetic aspects.pdf. *Polymer*. 42, 2395–2402.

Cao, L., Hu, H. & Gao, D. (2007) Design and Fabrication of Micro-textures for Inducing a Superhydrophobic Behavior on Hydrophilic Materials. *Langmuir*. [Online] 23, 4310–4314. Available from: doi:10.1021/la063572r.

Carman, P.C. (1956) *Flow of gases through media*. New york, Academic Press.

Cha, T., Yi, J.W., Moon, M., Lee, K., et al. (2010) Nanoscale Patterning of Microtextured Surfaces to Control Superhydrophobic Robustness. *Langmuir*. [Online] 26 (11), 8319–8326. Available from: doi:10.1021/la9047402.

Chan, H.Y. (2018) *Super-Hydrophobic Concrete Surface*. Imperial college london.

Chandra, S. (1988) Hydrochloric Acid Attack on Cement Mortar-An Analytical Study. *Cement and Concrete Research*. 18, 193–203.

Cheng, Y.-T., Rodak, D.E., Angelopoulos, A. & Gacek, T. (2005) Microscopic observations of condensation of water on lotus leaves. *Applied Physics Letters*. [Online] 87, 1–4. Available from: doi:10.1063/1.2130392.

Cheng, Y.T., Rodak, D.E., Wong, C.A. & Hayden, C.A. (2006) Effects of micro- and nano-structures on the self-cleaning behaviour of lotus leaves. *Nanotechnology*. [Online] 17 (5), 1359–1362. Available from: doi:10.1088/0957-4484/17/5/032.

Crick, C.R. & Parkin, I.P. (2009) A single step route to superhydrophobic surfaces through aerosol assisted deposition of rough polymer surfaces : duplicating the lotus effect. *Journal of Materials Chemistry*. [Online] 19, 1074–1076. Available from: doi:10.1039/b820102c.

Dai, J., Akira, Y., Wittmann, F.H., Yokota, H., et al. (2010) Water repellent surface impregnation for extension of service life of reinforced concrete structures in marine environments : The role of cracks. *Cement and Concrete Composites*. [Online] 32, 101–109. Available from: doi:10.1016/j.cemconcomp.2009.11.001.

Dawood, M.K., Zheng, H. & Liew, T.H. (2011) Mimicking Both Petal and Lotus Effects on a Single Silicon Substrate by Tuning the Wettability of Nanostructured Surfaces. *Langmuir*. [Online] 27, 4126–4133. Available from: doi:10.1021/la1050783.

Devarajan, A., Khadar, M.A. & Chattopadhyay, K. (2007) Effect of ball milling on chemically synthesized nanoparticles of CaCO3. *Materials Science and Engineering A*. [Online] 452–453, 395–400. Available from: doi:10.1016/j.msea.2006.10.095.

Diamond, S. (1996) Delayed Ettringite Formation - Processes and Problems. *Cement and Concrete Composites*. 18, 205–215.

Dinakar, P., Sahoo, P.K. & Sriram, G. (2013) Effect of Metakaolin Content on the Properties of High Strength Concrete. *International Journal of Concrete Structures and Materials*. [Online] 7 (3), 215–223. Available from: doi:10.1007/s40069-013-0045-0.

Domingues, E.M., Arunachalam, S. & Mishra, H. (2017) Doubly Reentrant Cavities Prevent Catastrophic Wetting Transitions on Intrinsically Wetting Surfaces. *Applied Materials & Interfaces*. [Online] 9, 21532–21538. Available from: doi:10.1021/acsami.7b03526.

Domingues, E.M., Arunachalam, S., Nauruzbayeva, J. & Mishra, H. (2018) Biomimetic coating-free surfaces for long-term entrapment of air under wetting liquids. *Nature Communications*. [Online] 9 (3606), 1–11. Available from: doi:10.1038/s41467-018-05895-x.

Dow, C. & Glasser, F.P. (2003) Calcium carbonate efflorescence on Portland cement and building materials. *Cement and Concrete Research*. 33, 147–154.

Du, Y., Wei, M., Reddy, K.R., Liu, Z., et al. (2014) Effect of acid rain pH on leaching behavior of cement stabilized lead-contaminated soil. *Journal of Hazardous Materials*. [Online] 271, 131–140. Available from: doi:10.1016/j.jhazmat.2014.02.002.

Duan, H. (2017) Underwater Superhydrophobiciy : Fundamentals and Applications. *Procedia IUTAM*. [Online] 20, 128–135. Available from: doi:10.1016/j.piutam.2017.03.018.

Enevoldsen, J.N., Hansson, C.M. & Hope, B.B. (1994) The influence of internal relative humidity on the rate of corrosion of steel embedded in concrete and mortar. *Cement and Concrete Research*. 24 (7), 1373–1382.

Ensikat, H.J., Ditsche-Kuru, P., Neinhuis, C. & Barthlott, W. (2011) Superhydrophobicity in perfection: The outstanding properties of the lotus leaf. *Beilstein Journal of Nanotechnology*. [Online] 2 (1), 152–161. Available from: doi:10.3762/bjnano.2.19.

Extrand, C.W. (2004) Criteria for Ultralyophobic Surfaces. *Langmuir*. 20, 5013–5018.

Facio, D.S. & Mosquera, J. (2013) Simple strategy for producing superhydrophobic nanocomposite coatings in situ on a building substrate. *Applied Materials & Interfaces*. 5, 7517–7526.

Faraji, G., Kim, H.S. & Kashi, H.T. (2018) *Severe Plastic Deformation*. Elsevier.

Fattuhi, N.I.. & Hughes, B.P.. (1988) The Performance of Cement Paste and Concrete Subjected to Sulphuric Acid Attack. *Cement and Concrete Research*. 18, 545–543.

Fekete, E., Pukánszky, B., Tóth, A. & Bertóti, I. (1990) Surface modification and characterization of particulate mineral fillers. *Journal of Colloid And Interface Science*. [Online] 135 (1), 200–208. Available from: doi:10.1016/0021-9797(90)90300-D.

Flatt, R.J., Scherer, G.W. & Bullard, J.W. (2011) Why alite stops hydrating below 80 % relative humidity. *Cement and Concrete Research*. [Online] 41, 987–992. Available from: doi:10.1016/j.cemconres.2011.06.001.

Flores-vivian, I., Hejazi, V., Kozhukhova, M.I., Nosonovsky, M., et al. (2013) Self-Assembling Particle-Siloxane Coatings for Superhydrophobic Concrete. *Applied Materials & Interfaces*. 5, 13284–03294.

Frankel, G.S. (1998) Pitting Corrosion of Metals : A Review of the Critical Factors. *Journal of The Electrochmical Society*. 145 (6), 2186–2198.

Gajewicz, A.M., Gartner, E., Kang, K., McDonald, P.J., et al. (2016) A H NMR relaxometry investigation of gel-pore drying shrinkage in cement pastes. *Cement and Concrete Research*. 86, 12–19.

Galan, I., Glasser, F.P. & Andrade, C. (2013) Calcium carbonate decomposition. *Journal of Thermal Analysis and Calorimetry*. 111 (2), 1197–1202.

Gao, D., Yang, L., Pang, Y., Li, Z., et al. (2022) Effects of a novel hydrophobic admixture on the sulfate attack resistance of the mortar in the wet-dry cycling environment. *Construction and Building Materials*. [Online] 344, 128148. Available from: doi:10.1016/j.conbuildmat.2022.128148.

Gao, L. & Mccarthy, T.J. (2006) *Contact Angle Hysteresis Explained*. [Online] (22), 6234–6237. Available from: doi:10.1021/la060254j.

Gao, Y., Qu, L., He, B., Dai, K., et al. (2018) Study on effectiveness of anti-icing and deicing performance of super-hydrophobic asphalt concrete. *Construction and Building Materials*. [Online] 191, 270–280. Available from: doi:10.1016/j.conbuildmat.2018.10.009.

Gao, Y., Wang, F., Liu, P., Zhang, W., et al. (2019) Superhydrophobic behavior of magnesium oxychloride cement surface with a dual-level fractal structure. *Construction and Building Materials*. [Online] 210, 132–139. Available from: doi:10.1016/j.conbuildmat.2019.03.158.

Geissler, M. (2011) Sub-Micrometer Patterning Using Soft Lithography. In: *Comprehensive Nanoscience and Technology*. Elsevier. pp. 63–81.

Gilbert, M., Sutherland, I. & Guest, A. (2000) Characterization of coated particulate fillers. *Journal of Materials Science*. [Online] 35 (2), 391–397. Available from: doi:10.1023/A:1004759115462.

Green, W.H. & Ampt, G.A. (1911) STUDIES ON SOIL PHYSICS. *The journal of agricultural science*. 4 (1), 1–24.

Groves, G.W., Rodway, D.I. & Richardson, I.G. (1990) The carbonation of hardened cement pastes. *Advances in Cement Research*. 3 (11), 117–125.

Guo, Z., Liu, W. & Su, B. (2011) Superhydrophobic surfaces: From natural to biomimetic to functional. *Journal of Colloid And Interface Science*. [Online] 353, 335–355. Available from: doi:10.1016/j.jcis.2010.08.047.

Hall, C. (1989) The water soprtivity of mortars and concretes: a review. *Magazine Concrete Research*. 41 (147), 51–61.

Hall, C. (1981) Water Movement in Porous Building Materials--IV. The Initial Surface Absorption and the Sorptivity. *Building and Environment*. 16 (3), 201–207.

Hall, C. & Hoff, W.. (2007) Rising damp: capillary rise dynamics in walls. *Proceedings of the Royal Society A*. [Online] 463, 1871–1884. Available from: doi:10.1098/rspa.2007.1855.

Hall, C. & Hoff, W.D. (2012a) Flow in porous materials. In: *Water transport in brick, stone and concrete*. Second edi. New york, Spon Press. pp. 64–101.

Hall, C. & Hoff, W.D. (2012b) Topics in water transport. In: *Water transport in brick, stone and concrete*. second edi. Abingdon, Spon Press. pp. 221–279.

Hall, C. & Hoff, W.D. (2012c) Unsaturated flow. In: *Water transport in brick, stone and concrete*. second edi. Oxford, Spon Press. pp. 102–145.

Hall, C. & Hoff, W.D. (2012d) Water in porous materials. In: *Water transport in brick, stone and concrete*. Second. Abingdon. pp. 30–63.

Hang, T., Hu, A., Ling, H., Li, M., et al. (2010) Super-hydrophobic nickel films with micro-nano hierarchical structure prepared by electrodeposition. *Applied Surface Science*. [Online] 256, 2400–2404. Available from: doi:10.1016/j.apsusc.2009.10.074.

Hansen, G., Hamouda, A.A. & Denoyel, R. (2000) The effect of pressure on contact angles and wettability in the mica/water/n-decane system and the calcite+stearic acid/water/n-decane system. *Colloids and Surfaces A: Physicochemical and Engineering Aspects*. [Online] 172 (1–3), 7–16. Available from: doi:10.1016/S0927-7757(99)00498-7.

He, Y., Jiang, C., Wang, S., Yin, H., et al. (2013) Control wetting state transition by micro-rod geometry. *Applied Surface Science*. [Online] 285, 682–687. Available from: doi:10.1016/j.apsusc.2013.08.110.

Hensel, R., Finn, A., Helbig, R., Braun, H., et al. (2014) Biologically Inspired Omniphobic Surfaces by Reverse Imprint Lithography. *Advanced materials*. [Online] 26, 2029–2033. Available from: doi:10.1002/adma.201305408.

Herminghaus, S. (2000) Roughness-induced non-wetting. *Europhysics Letters*. 52 (2), 165–170.

Hewlett, P.C., Justnes, H. & Edmeades, R.M. (2019) Cement and Concrete Admixtures. In: Peter C Hewlett & Martin Liska (eds.). *Lea's Chemistry of Cement and Concrete*. Fifth

Edit. Oxford, Mathew Deans. pp. 641–698.

Higham, C. (2023) Surface tension. Available at: https://fluid-dynamics.leeds.ac.uk/research/outreach/surface-tension/

Hinsenveld, M. & Bishop, P.L. (1996) Use of the Shrinking core/exposure model to describe the leachability from cement stabilized wastes. In: T. Michael; Gilliam & Carlton C Wiles (eds.). *Stabilization and Solidification of Hazardous, Radioactive, and Mixed Wastes: 3rd Volume, ASTM STP 1240*. American Society for Testing and Materials. pp. 528–539.

Horgnies, M. & Chen, J.J. (2014) Superhydrophobic concrete surfaces with integrated microtexture. *Cement and Concrete Composites*. [Online] 52, 81–90. Available from: doi:10.1016/j.cemconcomp.2014.05.010.

Horne, A.T., Richardson, I.G. & Brydson, R.M.D. (2007) Quantitative analysis of the microstructure of interfaces in steel reinforced concrete. *Cement and Concrete Research*. 37, 1613–1623.

Hu, J., Deng, T., Beck, R.G., Westervelt, R.M., et al. (1999) Fabrication of arrays of Schottky diodes using microtransfer molding. *Sensors and Actuators A*. 75, 65–69.

Hu, Z., Zen, X., Gong, J. & Deng, Y. (2009) Water resistance improvement of paper by superhydrophobic modification with microsized CaCO3 and fatty acid coating. *Colloids and Surfaces A: Physicochemical and Engineering Aspects*. [Online] 351 (1–3), 65–70. Available from: doi:10.1016/j.colsurfa.2009.09.036.

Husni, H., Nazari, M.R., Yee, H.M., Rohim, R., et al. (2017) Superhydrophobic rice husk ash coating on concrete. *Construction and Building Materials*. [Online] 144, 385–391. Available from: doi:10.1016/j.conbuildmat.2017.03.078.

Ioannou, I., Andreou, A., Tsikouras, B. & Hatzipanagiotou, K. (2009) Application of the Sharp Front Model to capillary absorption in a vuggy limestone. *Engineering Geology*. [Online] 105, 20–23. Available from: doi:10.1016/j.enggeo.2008.12.008.

Ioannou, I., Hall, C., Wilson, M.A., Hoff, W.D., et al. (2003) Direct measurement of the wetting front capillary pressure in a clay brick ceramic. *Journal of Physics D: Applied Physics*. 36, 3176–3182.

Ioannou, I., Hamilton, A. & Hall, C. (2008) Capillary absorption of water and n -decane by autoclaved aerated concrete. *Cement and Concrete Research*. [Online] 38, 766–771.

Available from: doi:10.1016/j.cemconres.2008.01.013.

Ishino, C., Okumura, K. & Quéré, D. (2004) Wetting transitions on rough surfaces. *Europhysics Letters*. [Online] 68 (3), 419–425. Available from: doi:10.1209/epl/i2004-10206-6.

Israelachvili, J.N. (2011) *Intermolecular and surface forces*. 3rd edition. Burlington, Massachusetts: Academic Press.

Jafari, R. & Farzaneh, M. (2013) Development a simple method to create the superhydrophobic composite coatings. *Journal of Composite Materials*. [Online] 47 (25), 3125–3129. Available from: doi:10.1177/0021998312462429.

Jennings, H.M., Kumar, A. & Sant, G. (2015) Quantitative discrimination of the nano-pore structure of cement paste during drying: new insights from water sorption isotherms. *Cement and Concrete Research*. 76, 26–36.

Johnson, L.M., Gao, L., Shields IV, C.W., Smith, M., et al. (2013) Elastomeric microparticles for acoustic mediated bioseparations. *Journal of nanobiotechnology*. 11 (22), 1–8.

Jones, M.R.., Dhir, R.K.. & GIll, J.P.. (1995) Concrete Surface Treatment: Effect of Exposure Temperature on Chloride Diffusion Resistance. *Cement and Concrete Research*. 25 (1), 197–208.

Kaufman, Y., Chen, S., Mishra, H., Schrader, A.M., et al. (2017) Simple-to-Apply Wetting Model to Predict Thermodynamically Stable and Metastable Contact Angles on Textured / Rough / Patterned Surfaces. *The Journal of Physical Chemistry*. [Online] 121, 5642–5656. Available from: doi:10.1021/acs.jpcc.7b00003.

Khoo, J.Y.H. & Lim, J.V. (2017) *A feasibility study on eggshells as a viable substitute for calcium carbonate in the fabrication of superhydrophobic coatings*. Imperial College London.

Khorasani, M.T., Mirzadeh, H. & Kermani, Z. (2005) Wettability of porous polydimethylsiloxane surface: Morphology study. *Applied Surface Science*. [Online] 242 (3–4), 339–345. Available from: doi:10.1016/j.apsusc.2004.08.035.

Kim, Y., Lee, K., Bang, J. & Kwon, S. (2014) Effect of W/C Ratio on Durability and Porosity in Cement Mortar with Constant Cement Amount. *Advances in Materials Science and Engineering*. (273460).

Klinkenberg, L.J. (1941) *The permeability of porous media to liquids and gases*.

Koch, K. & Barthlott, W. (2009) Superhydrophobic and superhydrophilic plant surfaces: An inspiration for biomimetic materials. *Philosophical Transactions of the Royal Society A: Mathematical, Physical and Engineering Sciences*. [Online] 367 (1893), 1487–1509. Available from: doi:10.1098/rsta.2009.0022.

Kokkinis, P. (2017) *Durability of superhydrophobic coatings from recycled materials*. Imperial College London.

Künzel, H.M. (1995) *Simultaneous Heat and Moisture Transport in Building Components*.

Lai, Y., Gao, X., Zhuang, H., Huang, J., et al. (2009) Designing Superhydrophobic Porous Nanostructures with Tunable Water Adhesion. *Advanced Material*. 21, 3799–3803.

Lam, J. & Lutsko, J.F. (2017) Solute particle near a nanopore: influence of size and surface properties on the solvent-mediated force. *Nanoscale*. 9, 17099-17108

Lawrence, C.D. (1984) Transport of oxygen through concrete. In: F.P. Glasser (ed.). *The Chemistry and Chemically-Related Properties of Cement*. 1984 British Ceramic Society Proceeding,35. pp. 277–293.

Lemoisson, F. & Froyen, L. (2005) Understanding and improving powder metallurgical processes. In: Seshadri Seetharaman (ed.). *Fundamentals of Metallurgy*. Cambridge, Woodhead. pp. 471–502.

Leung, H.Y.., Kim, J.., Nadeem, A.., Jaganathan, J., et al. (2016) Sorptivity of self-compacting concrete containing fly ash and silica fume. *Construction and Building Materials*. 113, 369–375.

Levy, S.M. (2012) Calculations Relating to Concrete and Masonry. In: *Construction Calculations Manual*. Elsevier Inc. pp. 211–264.

Lewis, R. & Fidjestol, P. (2019) Microsilica as an Addition. In: Martin Hewlett, Peter Clive; Liska (ed.). *Lea's Chemistry of Cement and Concrete*. Elsevier Inc. pp. 509–535.

Li, G., Huang, X., Lin, J., Jiang, X., et al. (2019) Activated chemicals of cementitious capillary crystalline waterproofing materials and their self-healing behaviour. *Construction and Building Materials*. [Online] 200, 36–45. Available from: doi:10.1016/j.conbuildmat.2018.12.093.

Lisco, F., Bukhari, F., Ulicna, S., Kenan, I., et al. (2020) Degradation of Hydrophobic, Anti-Soiling Coatings for Solar Module Cover Glass. *Energies*. 13 (3811), 1–15.

Liu, B., He, Y., Fan, Y. & Wang, X. (2006) Fabricating Super-Hydrophobic Lotus-Leaf-Like

Surfaces through Soft-Lithographic Imprinting. *Macromolecular Rapid Communications*. [Online] 27, 1859–1864. Available from: doi:10.1002/marc.200600492.

Liu, J., Feng, X., Wang, G. & Yu, S. (2007) Mechanisms of superhydrophobicity on hydrophilic substrates. *Journal of Physics: Condensed Matter*. [Online] 19 (35), 1–12. Available from: doi:10.1088/0953-8984/19/35/356002.

Liu, M. & Jiang, L. (2010) Switchable Adhesion on Liquid / Solid Interfaces. *Advanced Functional Materials*. [Online] 20, 3753–3764. Available from: doi:10.1002/adfm.201001208.

Liu, P., Gao, Y., Wang, F., Yang, J., et al. (2017) Superhydrophobic and self-cleaning behavior of Portland cement with lotus-leaf-like microstructure. *Journal of Cleaner Production*. [Online] 156, 775–785. Available from: doi:10.1016/j.jclepro.2017.03.211.

Liu, Y. & Choi, C. (2013) Condensation-induced wetting state and contact angle hysteresis on superhydrophobic lotus leaves. *Colloid Polym Sci*. [Online] 291, 437–445. Available from: doi:10.1007/s00396-012-2751-6.

Lloyd, B.P. (2015) *Wetting of Textured Surfaces and their application to drag and friction reduction*. University of Southampton.

Lu, Z., Xu, L., He, Y. & Zhou, J. (2019) One-step facile route to fabricate functionalized nano-silica and silicone sealant based transparent superhydrophobic coating. *Thin Solid Films*. 692, 137560.

Lv, P., Xue, Y., Liu, H., Shi, Y., et al. (2015) Symmetric and Asymmetric Meniscus Collapse in Wetting Transition on Submerged Structured Surfaces. *Langmuir*. [Online] 31 (4), 1248–1254. Available from: doi:10.1021/la503465q.

Malakopoulos, A., Chatzigeorgiou, M., Boukos, N. & Salifoglou, A. (2021) Durability performance of Portland limestone cement mortar containing butyl and zinc stearate admixtures. *Materials and Structures*. [Online] 54:60, 1–17. Available from: doi:10.1617/s11527-021-01638-5.

Malone, P.G. (1999) *Use of Permeable Formwork in Placing by*. (October).

Margi, E. (1998) Resistance of Concrete to destructive agencies. In: *Lea's Chemistry of Cement and Concrete*. fourth. London, Arnold. p. 299.

Marinova, K.G., Christova, D., Tcholakova, S., Efremov, E., et al. (2005) Hydrophobization of Glass Surface by Adsorption of Poly (dimethylsiloxane). *Langmuir*. 21, 11729–11737.

Masoodi, R. & Pillai, K.M. (2013) *Wicking in Porous Materials: Traditional and Modern Modeling Approaches*. New york, CRC Press.

Massazza, F. (1998) Pozzolana and pozzolanic Cements. In: Peter Clive Hewlett (ed.). *Lea's Chemistry of Cement and Concrete*. Foruth. Arnold. pp. 471–632.

Mauseth, J.D. (2008) *Plant Anatomy*. Blackburn Press.

McCarter, W.J. (1996) Assessing the protective qualities of treated and untreated concrete surfaces under cyclic wetting and drying. *Building and Environment*. 31 (6), 551–556.

McCarter, W.J. & Watson, D. (1997) Wetting and drying of cover-zone concrete. *Proceedings of the Institution of Civil Engineers - Structures and Buildings*. 112 (2), 227–236.

McCarthy, M.J. & Dyer, T.D. (2019) Pozzolanas and Pozzolanic Materials. In: Hewlwtt Peter C & Liska Martin (eds.). *Lea's Chemistry od Cement and Concrete*. Mathew Deans. p. 363.

McHale, G., Shirtcliffe, N.J. & Newton, M.I. (2004) Contact-Angle Hysteresis on Super-Hydrophobic Surface. *Langmuir*. 20, 10146–10149.

Medeiros, M. & Helene, P. (2008) Efficacy of surface hydrophobic agents in reducing water and chloride ion penetration in concrete. *Materials and Structures*. [Online] 41, 59–71. Available from: doi:10.1617/s11527-006-9218-5.

Medeiros, M.H.F. & Helene, P. (2009) Surface treatment of reinforced concrete in marine environment : Influence on chloride diffusion coefficient and capillary water absorption. *Construction and Building Materials*. [Online] 23 (3), 1476–1484. Available from: doi:10.1016/j.conbuildmat.2008.06.013.

Micha, D.A. (2020) Interaction of Molecules with Surfaces. In: *Molecular Interactions: Concepts and Methods*. JohnWiley & Sons. pp. 309–366.

Mihajlović, S.R., Vučinić, D.R., Sekulić, Ž.T., Milićević, S.Z., et al. (2013) Mechanism of stearic acid adsorption to calcite. *Powder Technology*. [Online] 245, 208–216. Available from: doi:10.1016/j.powtec.2013.04.041.

Mindess, S. (2019) Resistance of Concrete to destructive angencies. In: Peter Hewlett & Martin Liska (eds.). *Lea's Chemistry of Cement and Concrete*. fifth. Oxford, Mathew Deans. pp. 251–285.

Moon, H.Y., Shin, D.G. & Choi, D.S. (2007) Evaluation of the durability of mortar and

concrete applied with inorganic coating material and surface treatment system. *Construction and Building Materials*. [Online] 21, 362–369. Available from: doi:10.1016/j.conbuildmat.2005.08.012.

Di Mundo, R., Petrella, A. & Notarnicola, M. (2018) Surface and bulk hydrophobic cement composites by tyre rubber addition. *Construction and Building Materials*. [Online] 172, 176–184. Available from: doi:10.1016/j.conbuildmat.2018.03.233.

Muzenski, S., Flores-vivian, I. & Sobolev, K. (2015) Hydrophobic engineered cementitious composites for highway applications. *Cement and Concrete Composites*. [Online] 57, 68–74. Available from: doi:10.1016/j.cemconcomp.2014.12.009.

Neinhuis, C. & Barthlott, W. (1997a) Characterization and Distribution of Water-repellent, Self-cleaning Plant Surfaces. *Annals of Botany*. [Online] 79, 667–677. Available from: doi:10.1006/anbo.1997.0400.

Neinhuis, C. & Barthlott, W. (1997b) Purity of the sacred lotus, or escape from contamination in biological surfaces. *Planta*. 202, 1–8.

Ng, M., Saxena, I., Ehmann, K.F. & Cao, J. (2016) Improving Surface Hydrophobicity by Microrolling- Based Texturing. *Journal of Micro- and Nano Manufacturing*. [Online] 4, 1–8. Available from: doi:10.1115/1.4033680.

Ng, W.M. & Shah, V. (2016) *A simple production method for durable superhydrophobic calcium carbonate coatings *. Imperial College London.

Nosonovsky, M. & Bhushan, B. (2007) Hierarchical roughness makes superhydrophobic states stable. *Microelectronic Engineering*. [Online] 84, 382–386. Available from: doi:10.1016/j.mee.2006.10.054.

Nosonovsky, M. & Ramachandran, R. (2015) Geometric Interpretation of Surface Tension Equilibrium in Superhydrophobic Systems. *Entropy*. [Online] 17, 4684–4700. Available from: doi:10.3390/e17074684.

Nunes, C. & Slízkova, Z. (2014) Cement and Concrete Research Hydrophobic lime based mortars with linseed oil : Characterization and durability assessment. *Cement and Concrete Research*. [Online] 62, 28–39. Available from: doi:10.1016/j.cemconres.2014.03.011.

Olufemi Samuel, F. (2012) Sorptivity Of Cement Combination Concretes Containing Portland Cement, Fly Ash And Metakaolin. *International Journal of Engineering Research and*

Applications. 2 (5), 1953–1959.

Oner, D. & Mccarthy, T.J. (2000) Ultrahydrophobic Surfaces . Effects of Topography Length Scales on Wettability. *Langmuir*. 16 (20), 7777–7782.

Pan, X., Shi, Z., Shi, C., Ling, T., et al. (2017) A review on concrete surface treatment Part I : Types and mechanisms. *Construction and Building Materials*. [Online] 132, 578–590. Available from: doi:10.1016/j.conbuildmat.2016.12.025.

Pandey, A. & Kumar, B. (2019) Evaluation of water absorption and chloride ion penetration of rice straw ash and microsilica admixed pavement quality concrete. *Heliyon*. [Online] 5 (e02256). Available from: doi:10.1016/j.heliyon.2019.e02256.

Patankar, N.A. (2010) Consolidation of Hydrophobic Transition Criteria by Using an Approximate Energy Minimization Approach. *Langmuir*. [Online] 26 (11), 8941–8945. Available from: doi:10.1021/la9047424.

Qian, B. & Shen, Z. (2005) Fabrication of Superhydrophobic Surfaces by Dislocation-Selective Chemical Etching on Aluminum , Copper , and Zinc Substrates. *Langmuir*. (21), 9007–9009.

Qin, D., Xia, Y. & Whitesides, G.M. (2010) Soft lithography for micro- and nanoscale patterning. *Nature Protocols*. [Online] 5 (3), 491–502. Available from: doi:10.1038/nprot.2009.234.

Qu, Z.Y. & Yu, Q.L. (2018) Synthesizing super-hydrophobic ground granulated blast furnace slag to enhance the transport property of lightweight aggregate concrete. *Construction and Building Materials*. [Online] 191, 176–186. Available from: doi:10.1016/j.conbuildmat.2018.10.018.

Quéré, D. (2008) Wetting and Roughness. *Annual Review of Materials Research*. [Online] 38 (1), 71–99. Available from: doi:10.1146/annurev.matsci.38.060407.132434.

Rabi'atu, T. (2016) *Durability of hydrophboic coating from paper sludge ash and calcium carbonate*. Imperial College London.

Ramezanianpour, A.A.. & Malhotra, V.M. (1995) Effect of Curing on the Compressive Strength , Resistance to Chloride-Ion Penetration and Porosity of Concretes Incorporating Slag , Fly Ash or Silica Fume. *Cement and Concrete Composites*. 17, 125–133.

Razak, H.A., Chai, H.K. & Wong, H.S. (2004) Near surface characteristics of concrete

containing supplementary cementing materials. *Cement and Concrete Composites*. [Online] 26, 883–889. Available from: doi:10.1016/j.cemconcomp.2003.10.001.

Rezaei Gomari, K.A., Denoyel, R. & Hamouda, A.A. (2006) Wettability of calcite and mica modified by different long-chain fatty acids (C18 acids). *Journal of Colloid and Interface Science*. [Online] 297 (2), 470–479. Available from: doi:10.1016/j.jcis.2005.11.036.

Richardson, I.G. (2004) Tobermorite/jennite- and tobermorite/calcium hydroxide-based models for the structure of C-S-H: applicability to hardened pastes of tricalcium silicate, β-dicalcium silicate, Portland cement, and blends of Portland cement with blast-furnace slag, metakaol. *Cement and Concrete Research*. 34, 1733–1777.

Rodrigues, R., Gaboreau, S., Gance, J., Ignatiadis, I., et al. (2021) Reinforced concrete structures: A review of corrosion mechanisms and advances in electrical methods for corrosion monitoring. *Construction and Building Materials*. [Online] 269, 121240. Available from: doi:10.1016/j.conbuildmat.2020.121240.

Russ, J.C.. & Dehoff, R.T.. (1999) *Practical Stereology*. Second edi. New york, Plenum Press.

Sadrmomtazi, A., Khoshkbijari, R.K. & Tahmouresi, B. (2018) Effect of fly ash and silica fume on transition zone , pore structure and permeability of concrete. *Magazine of Concrete Research*. 70 (10), 519–532.

Sahoo, S., Parhi, P.K. & Panda, B.C. (2021) Durability properties of concrete with silica fume and rice husk ash. *Cleaner Engineering and Technology*. 2, 100067.

Sakr, M.R. & Bassuoni, M.T. (2018) Surface Treatments for Concrete under Physical Salt Attack. *Sixth International Conference on Durability of Concrete Structures*. (July), 633–640.

Scherer, G.W. (1990) Theory of drying. *Journal of American Ceramic Society*. 73 (1), 3–14.

Seo, D., Schrader, A.M., Chen, S., Kaufman, Y., et al. (2018) Rates of cavity filling by liquids. *Proceedings of the National Academy of Sciences*. [Online] 115 (32), 8070–8075. Available from: doi:10.1073/pnas.1804437115.

Shahbazi, R., Korayem, A.H., Razmjou, A., Duan, W.H., et al. (2020) Integrally hydrophobic cementitious composites made with waste amorphous carbon powder. *Construction and Building Materials*. [Online] 233, 1–12. Available from: doi:10.1016/j.conbuildmat.2019.117238.

Shaw, L., Zawrah, M., Villegas, J., Luo, H., et al. (2003) Effects of Process-Control Agents on Mechanical Alloying of Nanostructured Aluminum Alloys. *Metallurgical and Materials Transactions A*. 34, 159–170.

She, W., Yang, J., Hong, J., Sun, D., et al. (2020) Superhydrophobic concrete with enhanced mechanical robustness : Nanohybrid composites , strengthen mechanism and durability evaluation. *Construction and Building Materials*. [Online] 247, 118563. Available from: doi:10.1016/j.conbuildmat.2020.118563.

Shi, X., Rosa, R. & Lazzeri, A. (2010) On the coating of precipitated calcium carbonate with stearic acid in aqueous medium. *Langmuir*. [Online] 26 (11), 8474–8482. Available from: doi:10.1021/la904914h.

Shin, H., Yoo, D., Lee, J., Lee, S., et al. (2019) Optimized mix design for 180 MPa ultra-high-strength concrete. *Journal of Materials Research and Technology*. [Online] 8 (5), 4182–4197. Available from: doi:10.1016/j.jmrt.2019.07.027.

Sims, I., Lay, J. & Ferrari, J. (2019) Concrete Aggregate. In: P.C. Hewlett & M Liska (eds.). *Lea's Chemistry of Cement and Concrete*. fifth. Mathew Deans. p. 699.

Singh, S., Housto, J., Van Swol, F. & Brinker, C.J. (2006) Drying transition of confined water. *Nature*. [Online] 442 (3), 526. Available from: doi:10.1038/442526a.

Snyder, K.A. & Bentz, D.P. (2004) Suspended hydration and loss of freezable water in cement pastes exposed to 90 % relative humidity. *Cement and Concrete Research*. [Online] 34, 2045–2056. Available from: doi:10.1016/j.cemconres.2004.03.007.

Spathi, C., Young, N., Heng, J.Y.Y., Vandeperre, L.J.M., et al. (2015) A simple method for preparing super-hydrophobic powder from paper sludge ash. *Materials Letters*. [Online] 142, 80–83. Available from: doi:10.1016/j.matlet.2014.11.123.

Subbiah, K., Park, D., Su, Y., Velu, S., et al. (2018) Development of water-repellent cement mortar using silane enriched with nanomaterials. *Progress in Organic Coatings*. [Online] 125, 48–60. Available from: doi:10.1016/j.porgcoat.2018.08.021.

Sun, M., Luo, C., Xu, L., Ji, H., et al. (2005) Artificial Lotus Leaf by Nanocasting. *Langmuir*. [Online] 21, 8978–8981. Available from: doi:10.1021/la050316q.

Surahyo, A. (2019) Constituent Materials. In: *Concrete Construction: Practical Problems and Solutions*. Cham, Springer International Publishing. pp. 21–60.

Taylor, H.F.W., Famy, C. & Scrivener, K.L. (2001) Delayed ettringite formation. *Cement and*

Concrete Research. 31, 683–693.

Teisala, H., Baumli, P., Weber, S.A.L., Vollmer, D., et al. (2020) Grafting Silicone at Room Temperature ---a Transparent, Scratch- resistant Nonstick Molecular Coating. *Langmuir*. [Online] 36, 4416–4431. Available from: doi:10.1021/acs.langmuir.9b03223.

The Concrete Society (2013) *CS TR174 Integral water resisting admixtures on concrete durability*.

The Concrete Society (2008) *Guide to the design of concrete structures in the Arabian Peninsula*.

Thomas, M.D.A. (2007) Optimizing the Use of Fly Ash in Concrete. In: *Portland Cement Association*. Skokie, IL, USA. p.

Thomas, T.H. & Kendrick, T.C. (1969) Thermal Analysis of Polydimethylsiloxanes. I. Thermal Degradation in Controlled Atmospheres. *Journal of Polymer Science*. 7, 537–549.

Tittarelli, F. (2009) Oxygen diffusion through hydrophobic cement-based materials. *Cement and Concrete Research*. [Online] 39, 924–928. Available from: doi:10.1016/j.cemconres.2009.06.021.

Tittarelli, F. & Moriconi, G. (2011) Comparison between surface and bulk hydrophobic treatment against corrosion of galvanized reinforcing steel in concrete. *Cement and Concrete Research*. [Online] 41, 609–614. Available from: doi:10.1016/j.cemconres.2011.03.011.

Torres, A., Souza, L., Silva, M. & Silva, F. (2019) Concrete degredation mechanisms by sulfuric acid attack. *Magazine of Concrete Research*. 71 (7), 349–361.

Tsutsumi, Y., Nishikata, A. & Tsuru, T. (2007) Pitting corrosion mechanism of Type 304 stainless steel under a droplet of chloride solutions. *Corrosion science*. [Online] 49, 1394–1407. Available from: doi:10.1016/j.corsci.2006.08.016.

Turk, K., Karatas, M. & Gonen, T. (2013) Effect of Fly Ash and Silica Fume on Compressive Strength, Sorptivity and Carbonation of SCC. *KSCE Journal of Civil Engineering*. 17 (1), 202–209.

Wagner, P., Fürstner, R., Barthlott, W. & Neinhuis, C. (2003) Quantitative assessment to the structural basis of water repellency in natural and technical surfaces. *Journal of Experimental Botany*. [Online] 54 (385), 1295–1303. Available from: doi:10.1093/jxb/erg127.

Wang, S., Feng, L., Liu, H., Sun, T., et al. (2005) Manipulation of surface wettability between superhydrophobicity and superhydrophilicity on copper films. *ChemPhysChem*. [Online] 6 (8), 1475–1478. Available from: doi:10.1002/cphc.200500204.

Webster, M.T. & Loehr, R.C. (1996) LONG-TERM LEACHING OF METALS FROM CONCRETE PRODUCTS. *Journal of environmental engineering*. 122 (8), 714–721.

Wenzel, R.N. (1936) Resistance of solid surfaces to wetting by water. *Industrial and Engineering Chemistry*. [Online] 28 (8), 988–994. Available from: doi:10.1021/ie50320a024.

Whyman, G. & Bormashenko, E. (2011) *How to Make the Cassie Wetting State Stable ?* [Online] 8171–8176. Available from: doi:10.1021/la2011869.

Whyman, G. & Bormashenko, E. (2012) Wetting Transitions on Rough Substrates : General Considerations. *Journal of Adhesion science and Technology*. [Online] 26, 207–220. Available from: doi:10.1163/016942411X574844.

Wier, K.A. & Mccarthy, T.J. (2006) Condensation on Ultrahydrophobic Surfaces and Its Effect on Droplet Mobility : Ultrahydrophobic Surfaces Are Not Always Water Repellant. *Langmuir*. [Online] 22, 2433–2436. Available from: doi:10.1021/la0525877.

Wong, H.S.., Pappas, A.M.., Zimmerman, R.W.. & Buenfeld, N.R.. (2011) Effect of entrained air voids on the microstructure and mass transport properties of concrete. *Cement and Concrete Research*. 41 (10), 1067–1077.

Wong, H.S. (2006) *Quantifying the pore structure of cement- based materials using backscattered electron*. Imperial College London.

Wong, H.S., Barakat, R., Alhilali, A., Saleh, M., et al. (2015) Hydrophobic concrete using waste paper sludge ash. *Cement and Concrete Research*. [Online] 70, 9–20. Available from: doi:10.1016/j.cemconres.2015.01.005.

Wong, H.S. & Buenfeld, N.R. (2006) Patch microstructure in cement-based materials : Fact or artefact ? *Cement and Concrete Research*. [Online] 36, 990–997. Available from: doi:10.1016/j.cemconres.2006.02.008.

Wong, H.S., Head, M.K. & Buenfeld, N.R. (2006) Pore segmentation of cement-based materials from backscattered electron images. *Cement and Concrete Research*. [Online] 36, 1083–1090. Available from: doi:10.1016/j.cemconres.2005.10.006.

Wong, H.S., Zobel, M., Buenfeld, N.R. & Zimmerman, R.W. (2009) Influence of the

interfacial transition zone and microcracking on the diffusivity , permeability and sorptivity of cement-based materials after drying. *Magazine of Concrete Research*. 61 (8), 571–589.

Wu, K., Han, H., Li, H., Dong, B., et al. (2021) Experimental study on concurrent factors influencing the ITZ effect on mass transport in concrete. *Cement and Concrete Composites*. [Online] 123, 104215. Available from: doi:10.1016/j.cemconcomp.2021.104215.

Wu, Z., Wong, H.S. & Buenfeld, N.R. (2015) Influence of drying-induced microcracking and related size effects on mass transport properties of concrete. *Cement and*. [Online] 68, 35–48. Available from: doi:10.1016/j.cemconres.2014.10.018.

Wu, Z., Wong, H.S., Chen, C. & Buenfeld, N.R. (2019) Anomalous water absorption in cement-based materials caused by drying shrinkage induced microcracks. *Cement and Concrete Research*. [Online] 115, 90–104. Available from: doi:10.1016/j.cemconres.2018.10.006.

Xi, Y., Bazan, Z.P. & Jennings, H.M. (1994) Moisture Diffusion in Cementitious Materials Adsorption Isotherms. *Advanced Cement Based Materials*. 1 (6), 248–257.

Xia, Y. & Whitesides, G.M. (1998) Soft Lithography. *Angewandte Chemie*. [Online] 37, 550–575. Available from: doi:10.1146/annurev.matsci.28.1.153.

Young, T. (1805) An Essay on the Cohesion of Fluids. *Proceedings of the Royal Society of London*. [Online] 95 (0), 65–87. Available from: doi:10.1098/rspl.1800.0095.

Zhang, K. (2022) *Assessing long-term carbonation resistance of blended concretes from short-term natural exposure*. Imperial College London.

Zhang, L. & Guo, X. (2018) Effects of Process Control Agents on the Mechanical Alloying Behavior of Nb-Ti-Si Based Alloy. *Materials Transactions*. 59 (4), 528–537.

Zhang, W., Zhang, R., Jiang, C. & Wu, C. (2017) Effect of pillar height on the wettability of micro-textured surface : Volume-of- fluid simulations. *International Journal of Adhesion and Adhesives*. [Online] 74, 64–69. Available from: doi:10.1016/j.ijadhadh.2016.12.011.

Zhao, X., Xia, Y. & Whitesides, G.M.. (1997) Soft lithographic methods for nano-fabrication. *Journal of Materials Chemistry*. [Online] 7 (7), 1069–1074. Available from: doi:10.1039/a700145b.

Zheng, Q. & Lü, C. (2013) Size effects of surface roughness to superhydrophobicity.

Procedia IUTAM. [Online] 10, 462–475. Available from: doi:10.1016/j.piutam.2014.01.041.

Zheng, Q.S., Yu, Y. & Zhao, Z.H. (2005) Effects of Hydraulic Pressure on the Stability and Transition of Wetting Modes of Superhydrophobic Surfaces.pdf. *Langmuir*. 21, 12207–12212.

Zhu, L., Feng, Y., Ye, X. & Zhou, Z. (2006) Tuning wettability and getting superhydrophobic surface by controlling surface roughness with well-designed microstructures. *Sensors and Actuators A*. [Online] 131, 595–600. Available from: doi:10.1016/j.sna.2005.12.005.

Appendix I

Calculation for water pressure required to transform the Cassie-Baxter state to the Wenzel state

This section provides a theoretical calculation for the minimum water pressure required for the transition from the Cassie-Baxter state to the Wenzel state for a PDMS coated lotus textured surface. The method is based on the one used by Zheng, *et al.* (2005), in which the underlying assumption was that the work done by external force was totally converted into the increase in interfacial energy.

As shown in the SEM image (Figure 4.1), the side view of a papilla is similar to a sinusoidal waveform over half a cycle. Therefore, it is justifiable and useful to represent the reproduced lotus leaf texture as a sinusoidal profile. A two-dimensional illustration which geometrically describes the profile of a papilla is shown in Figure A-1, which has a 20 μm wavelength and 11 μm amplitude. These values were average dimensions of reproduced papillae on a lotus textured mortar as described in the Chapter 4. Based on the geometrical shape of papilla, the sinusoidal equation of the cross section of papilla can be identified. By using the approximate outline profile, I can obtain a relatively simple mathematical formula to describe the pressure required throughout a wetting process. Here, for simplicity, smaller scale roughness characteristics on papillae are ignored.

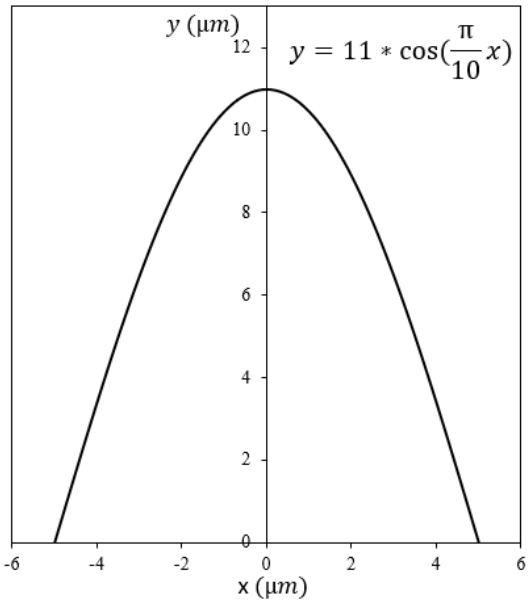


Figure A.0.1 Two-dimensional sinusoidal profile of a papilla (side view). The equation at the top right corner defines the sinusoidal waveform.

The three-dimensional shape of a papilla is defined by rotating the sinusoidal waveform around the axis of amplitude. This means that no matter where it is sliced along the amplitude axis, the cross section is circular but of different size.

To deduce the pressure needed to cause the penetration of water, it is assumed that the initial position of the water-gas interface (zero penetration) is at the top of papillae and the advance of contact line can be treated as having a unified movement in an isothermal process. Gas pressure generated by compression ahead of the water front and the effect of gas dissolution into water are ignored. I mean by this that the work of pressure is completely transferred into the increase of free energy with respect to the variation of interfacial area. Consider the change in free energy associated with the advancement of the water-gas interface as illustrated in Figure A-2. As the water-gas interface moves downward along the side of papillae, the contact angle maintains the true contact angle θ_Y, which is given by the Young's equation, against the side of papillae. The change in free energy due to an infinitively small movement of interline along the arc of sinusoidal profile, ds, is:

$$\Delta G = \gamma_{sl} ds - \gamma_{lg} ds' - \gamma_{sg} ds \qquad \text{(eqn. A-1)}$$

In which γ_{sl}, γ_{sg} and γ_{lg} denote solid-liquid interfacial energy, solid-gas interfacial energy, and liquid-gas interfacial energy respectively. ds' is the variation of liquid-gas interfacial area corresponding to the movement of interline.

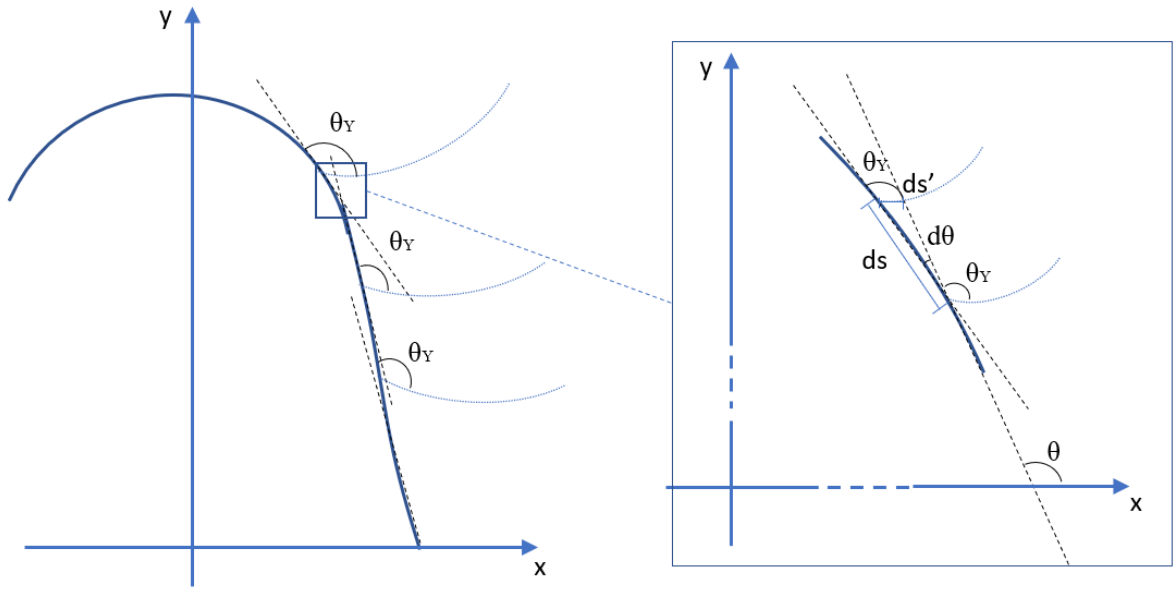


Figure A.0.2 Progressive penetration of liquid. The contact angle maintains θ_Y against the side of papillae throughout the whole wetting process. Solid line represents the outline of papillae. Dashed lines represent tangents. Dotted lines represent the water-gas interface. The insert

on the right shows that the water front moves downward by a distance of ds. Correspondingly, the water-gas interfacial area decreases ds'.

From geometry, an infinitively small change in s', which is the area of water-gas interface, corresponds to a differential plane angle dθ as the contact line moves by a distance ds. dθ is the change in the angle of inclination of the tangent with respect to the positive x-axis (Figure A-2). Therefore, the unknown ds' can be expressed as a function of dθ:

$$\frac{ds\prime}{\sin d\theta} = \frac{ds}{\sin(\theta_Y - d\theta)} \qquad \text{(eqn. A-2)}$$

Where θ_Y stands for the Young's contact angle. Other terms are explained in the text.

Combining equation A-1 with equation A-2 we obtain:

$$\Delta G = (\gamma_{sl} - \gamma_{sg})ds - \gamma_{lg} ds \frac{\sin d\theta}{\sin(\theta_Y - d\theta)} \qquad \text{(eqn. A-3)}$$

Since the increment of free energy equals to the work done by an external force, p, equation A-3 may be written as:

$$(\gamma_{sl} - \gamma_{sg})ds - \gamma_{lg} ds \frac{\sin d\theta}{\sin(\theta_Y - d\theta)} = \mathrm{p}ds \sin(\pi - \theta) \qquad \text{(eqn. A-4)}$$

Where θ denotes the angle of inclination of tangent to the positive x-axis as in Figure A-2. p*sin(π-θ) is a spreading force tangential to the surface.

Since the variation of the water-gas interface, ds', depends only on dθ, it is more convenient to express dθ in terms of x rather than θ. As shown in Figure A-2, at any given point on the sinusoidal waveform, the included angle of tangent to positive x-axis can be expressed as

$$\theta = \tan^{-1}(-\frac{11\pi}{10}\sin(\frac{\pi}{10}x)) \qquad \text{(eqn. A-5)}$$

subject to a restricted domain of $0 \leq x \leq 5$. In equation A-4, as dθ goes to zero, the limit of numerator is zero while the limit of denominator is sin θ_Y. Therefore, the term corresponding to the change in the water-gas interfacial area is zero. Simplifying equation A-4 by rearranging:

$$\mathrm{p} = \frac{\gamma_{sl} - \gamma_{sg}}{\sin\tan^{-1}(-\frac{11\pi}{10}\sin(\frac{\pi}{10}x))} \qquad \text{(eqn. A-6)}$$

It is reasonable to assume the PDMS coating has a very high surface coverage as the trace of PDMS was detected at all random positions over a coated surface (Section 4.5.1) Therefore, the solid phase in equation A-6 refers to PDMS. From Young's equation and simplifying the denominator, we may write equation A-6 in the form:

$$\mathrm{p} = \frac{\gamma_{lg}\cos\theta_Y}{-\sqrt{\frac{\pi^2\sin\left(\frac{\pi}{10}x\right)^2}{\frac{100}{121}+\pi^2\sin\left(\frac{\pi}{10}x\right)^2}}} \qquad \text{(eqn. A-7)}$$

Equation A-7 is an important result. It refers to the force required to push one unit length of interline of liquid downward. Since the length of contact line varies with the depth of penetration for geometrical reason, the pressure needed per unit area is given by:

$$P = \frac{\gamma_{lg}\cos\theta_Y}{-\sqrt{\frac{\pi^2\sin\left(\frac{\pi}{10}x\right)^2}{\frac{100}{121}+\pi^2\sin\left(\frac{\pi}{10}x\right)^2}}}\ 3500 * 2\pi\mathrm{x} \qquad \text{(eqn. A-8)}$$

In which 3500 refers to the area density of papillae on the surface of lotus leaf. Within the domain of $0 \leq \mathrm{x} \leq 5$, the equation is monotonic increasing, with the maximum value of 2133 Pa. Therefore, the maximum pressure the air cushion can withstand before transiting to the Wenzel state is 2133 Pa, which corresponds to around 22 cm of water.